Lehrstuhl für Elektrische Energiespeichertechnik
Fakultät für Elektrotechnik und Informationstechnik
Technische Universität München

System Simulation of Utility-Scale Lithium-Ion Battery Energy Storage Systems

An Assessment of the Energy Efficiency, the Battery Degradation, and the Economics of System Operation

Michael R. Schimpe M.Sc.

Vollständiger Abdruck der von der Fakultät für Elektrotechnik und Informationstechnik der Technischen Universität München zur Erlangung des akademischen Grades eines

Doktor-Ingenieurs (Dr.-Ing.)

genehmigten Dissertation.

Vorsitzender:		Prof. Dr.-Ing. Bernhard Seeber
Prüfer der Dissertation:	1.	Prof. Dr.-Ing. Andreas Jossen
	2.	Prof. Dr. rer. nat. Thomas Hamacher

Die Dissertation wurde am 30.10.2018 bei der Technischen Universität München eingereicht und durch die Fakultät für Elektrotechnik und Informationstechnik am 27.06.2019 angenommen.

Zusammenfassung

Der Klimawandel erfordert einen Wandel des Energiesystems zu Technologien mit geringem CO_2-Ausstoß. Zukünftige Energiesysteme basieren daher auf einer verstärkten Nutzung von volatil einspeisenden Energiequellen wie der Wind- und der Solarenergie. Batteriespeichersysteme sind eine Option, um bei hohen Anteilen volatiler Einspeisung eine stabile Energieversorgung durch die Entkopplung von Produktion und Bedarf elektrischer Leistung zu gewährleisten.

Um sowohl ökologisch als auch ökonomisch einen positiven Beitrag zum Energiesystem beizutragen, müssen Batteriespeicher eine hohe Energieeffizienz und eine lange Lebensdauer aufweisen. In dieser Arbeit wird eine detaillierte Analyse dieser zwei Schlüsselmetriken für Lithium-Ionen Großbatteriespeichersysteme durchgeführt.

Die Energieeffizienz von Batteriespeichersystemen wird detailliert anhand des Referenzsystems *Energy Neighbor* analysiert. Die Ergebnisse zeigen deutlich variierende Effizienzkennzahlen für verschiedene Systemanwendungen. Weiterhin zeigt sich, dass die Leistungselektronik zur Anbindung der Batterien an das elektrische Netz eine Hauptursache für energetische Verluste ist.
In der folgenden Analyse werden fokussiert verschiedene Netzebenen und Leistungselektroniktopologien in Bezug auf die Energieeffizienz analysiert. Die Resultate zeigen, dass die Auswahl der Netzanbindungstopologie die Energieeffizienz deutlich beeinflusst und spezifisch für die Systemanwendung ausgewählt werden muss.
Eine weitere Möglichkeit zur Verringerung der energetischen Verluste in der Leistungselektronik ergibt sich über das Management der Verteilung der Leistungsflüsse im System. Dazu wird eine Lastverteilungsstrategie entwickelt und in einem industriellen Großbatteriespeicher implementiert und getestet. Die Ergebnisse zeigen einen stabilen Betrieb und eine deutliche Reduktion der energetischen Verluste.
Für die Analyse der Batterielebensdauer wird ein umfangreiches Lagerungs- und Zyklisierungsexperiment mit Fokus auf den Einfluss der Temperatur auf die zyklische Batteriealterung durchgeführt. Als Testobjekt wird eine Lithium-Eisenphosphat/Graphit Zelle verwendet. Auf Basis der experimentellen Daten wird ein semi-empirisches Model entwickelt, das unterschiedliche Degradationsmechanismen berechnet. Das Model wird durch zusätzliche anwendungsorientierte Tests validiert.
Um den Einfluss der energetischen Verluste und der Batteriedegradation auf die Wirtschaftlichkeit des Betriebs von Batteriespeichern, auch Grenzkosten des Betriebs genannt, zu bewerten, wird ein kombinierter Ansatz verwendet. Dabei werden Kosten für energetische Verluste des Systems und für Kapazitätsverluste der Batterie berechnet und analysiert. Die Ergebnisse zeigen optimale Betriebspunkte, welche in einer profitoptimierten Betriebsstrategie für Batteriespeicher in Energiehandelsapplikationen angewendet werden. Dabei zeigt sich ein deutliches Potential für einen erhöhten Profit.

Zusammenfassend benötigen die Schlüsselmetriken Energieeffizienz und Batterielebensdauer detaillierte Betrachtungen im Systemdesign. Weiterhin können mit optimierten Betriebsstrategien im Betrieb deutliche Verbesserungen erzielt werden.

Abstract

Climate change requires a transition to a low-carbon energy supply, which often includes intensified use of renewable volatile energy sources such as wind and solar. For a stable energy supply with high shares of volatile renewable energy sources, battery energy storage systems (BESS) are a technically possible option to decouple electricity production and demand.

To benefit the power system both ecologically and economically, BESS are required to provide a high energy efficiency and long battery lifetime. This work presents a detailed analysis of the two key metrics, energy efficiency and battery lifetime, for utility-scale lithium-ion BESS.

Energy efficiency of BESS is analyzed in detail for the reference system *Energy Neighbor*. Results reveal strongly varying energy efficiency values for different systems applications. Furthermore, the power electronics connecting the battery to the electrical grid are found to be a major source of energy losses. Consequently, grid connection topologies consisting of different power electronics topologies and grid levels are analyzed in detail regarding their energy efficiency. Here, results show that the choice of topology can strongly affect the energy efficiency and has to be considered specifically for each grid application. As a second approach to reduce power electronics losses, a software-based power flow distribution strategy is proposed and developed. The strategy is tested in an industrial utility-scale system and shows stable operation as well as a strong reduction of energy losses.
Regarding battery lifetime, a comprehensive storage and cycle test experiment with a focus on the effect of battery temperature on the cycle-induced battery degradation is conducted with lithium iron phosphate/graphite cells. Based on experimental data, a semi-empirical model that captures separate degradation mechanisms is developed and validated via application-oriented experiments.
To evaluate and compare the impact of the energy losses and battery degradation on the economics of BESS operation, specifically their marginal costs of operation, a new combined approach is developed. Costs for energy losses and battery capacity degradation are calculated and evaluated, revealing optimum operating points. The results are evaluated in a profit-optimized control strategy for BESS in energy arbitrage, showing large potential for an increased profit.

In summary, both energy efficiency and battery degradation are key parameters for BESS requiring detailed consideration during system design. Operational control strategies offer opportunities for noticeable improvement.

List of Publications

Peer-Reviewed Journal Paper Contributions (Lead Author)

I Schimpe, M.; Naumann, M.; Truong, N.; Hesse, H.C.; Santhanagopalan, S.; Saxon, A.; Jossen, A.: *Energy efficiency evaluation of a stationary lithium-ion battery container storage system via electro-thermal modeling and detailed component analysis*, in: *Applied Energy 210*, pp. 211–229, 2018

II Schimpe, M.; von Kuepach, M. E.; Naumann, M.; Hesse, H.C.; Smith, K.; Jossen, A.: *Comprehensive Modeling of Temperature-Dependent Degradation Mechanisms in Lithium Iron Phosphate Batteries*, in: *Journal of The Electrochemical Society 165 (2)*, pp. A181–A193, 2018

III Schimpe, M.; Piesch, C.; Hesse, H.C.; Paß, J.; Ritter, S.; Jossen, A.: *Power Flow Distribution Strategy for Improved Power Electronics Energy Efficiency in Battery Storage Systems: Development and Implementation in a Utility-Scale System*, in: *Energies 11 (3)*, 533, 2018

IV Schimpe, M.; Becker, N.; Lahlou, T.; Hesse, H.C.; Herzog, H.-G.; Jossen, A.: *Energy efficiency evaluation of grid connection scenarios for stationary battery storage systems*, in: *Energy Procedia 155*, pp. 77-101, 2018

Peer-Reviewed Conference Paper Contributions (Lead Author)

I Schimpe, M.; Truong, C.N.; Naumann, M.; Jossen, A.; Hesse, H.C.; Reniers, J.M.; Howey, D.A.: *Marginal Costs of Battery System Operation in Energy Arbitrage based on Energy Losses and Cell Degradation*, in: *Proceedings of 2018 IEEE International Conference on Environment and Electrical Engineering and 2018 IEEE Industrial and Commercial Power Systems Europe*, 2018

Self-written sections of peer-reviewed lead author journal/conference paper contributions are partially contained in this doctoral thesis without further reference in the text. Figures are continuously referenced.

Peer-Reviewed Journal Paper Contributions (Co-Author)

I Göbel, C.; Hesse, H.C.; Schimpe, M.; Jossen, A.; Jacobsen, H.-A.: *Model-based Dispatch Strategies for Lithium-Ion Battery Energy Storage applied to Pay-as-Bid Markets for Secondary Reserve*, in: *IEEE Transactions on Smart Grid 32.4*, pp. 2724–2734, 2017

II Hesse, H.C.; Schimpe, M.; Kucevic, D.; Jossen, A.: *Lithium-Ion Battery Storage for the Grid—A Review of Stationary Battery Storage System Design Tailored for Applications in Modern Power Grids*, in: *Energies 10 (12)*, 2107, 2018

III Naumann, M.; Schimpe, M.; Keil, P.; Hesse, H.C.; Jossen, A.: *Analysis and modeling of calendar aging of a commercial LiFePO4/graphite cell*, in: *Journal of Energy Storage (17)*, pp. 211–229, 2018

Selection of Conference Presentations

I Schimpe, M.; Naumann, M.; Müller, M.; Truong, C.N.; Hesse, H.C.; Jossen, A.: *System Simulation of a Large Stationary Battery System with Thermal Management*, *Kraftwerk Batterie 2016*, Münster, 2016

II Schimpe, M.; Naumann, M.; Müller, M.; Truong, C.N.; Hesse, H.C.; Jossen, A.: *Model-based Energy Efficiency Evaluation of the 200 kWh Stationary Lithium-Ion Battery System "Energy Neighbor"*, *Batterieforum Deutschland 2017*, Berlin, 2017

III Schimpe, M.; Kuepach, M. E. v.; Naumann, M.; Hesse, H.C.; Jossen, A.: *Semi-Empirical Modeling of Temperature-Dependent Degradation Mechanisms in Lithium-Ion Batteries*, *232nd ECS Meeting*, National Harbor (MD, USA), 2017

IV Schimpe, M.; Piesch, C.; Hesse, H.C.; Paß, J.; Ritter, S.; Jossen, A.: *Operational Strategy for Improved Energy Efficiency of Battery Storage Systems: Development and Implementation in a Large-Scale Second-Use Battery System*, *International Renewable Energy Storage Conference 2018*, Düsseldorf, 2018

V Schimpe, M.; Truong, C.N.; Naumann, M.; Jossen, A.; Hesse, H.C.; Reniers, J.M.; Howey, D.A.: *Marginal Costs of Battery System Operation in Energy Arbitrage based on Energy Losses and Cell Degradation*, *2018 IEEE International Conference on Environment and Electrical Engineering and 2018 IEEE Industrial and Commercial Power Systems Europe*, Palermo, 2018

Peer-Reviewed Conference Contributions (Co-Author)

I Smith, K.; Baggu, M.; Friedl, A.; Bialek, T.; Schimpe, M.R.: *Performance and Health Test Procedure for Grid Energy Storage Systems*, in: *Proceedings of the IEEE Power Engineer Society General Meeting 2017*, Chicago, 2017

II Truong, C.N.; Viernstein, L.; Schimpe, M.; Witzmann, R.; Jossen, A.; Hesse, H.C.: *Maximizing Solar Home Battery System's Contribution to the Energy Transition of the Power System*, in: *Proceedings of the Conference NEIS 2017 - Conference on Sustainable Energy Supply and Energy Storage Systems*, Hamburg, 2017

III Truong, C.N.; Schimpe, M.; Naumann, M.; Jossen, A.; Hesse, H.C.: *Impact of Sub-Components on the Overall Performance of Stationary Battery Systems. Insights on the Prototype Energy Neighbor*, in: *Proceedings of the International ETG Congress 2017*, Bonn, 2017

IV Naumann, M.; Truong, C.N.; Schimpe, M.; Kucevic, D.; Jossen, A.; Hesse, H.C.: *SimSES: Software for techno-economic Simulation of Stationary Energy Storage Systems*, in: *Proceedings of the International ETG Congress 2017*, Bonn, 2017

Contents

Abbreviations

Please note that the list below is based on the main part of this thesis and does not fully cover the included papers. Each paper itself includes a complete individual definition.

AC	Alternating Current
B-TMS	Battery Thermal Management System
BESS	Battery Energy Storage System(s)
BMS	Battery Management System
BOL	Begin of Life
CC	Constant Current
CV	Constant Voltage
DC	Direct Current
EIS	Electrical Impedance Spectroscopy
EMS	Energy Management System
EOL	End of Life
FEC	Full Equivalent Cycles
LFP	Lithium Iron Phosphate
LFP-C	Lithium Iron Phosphate/Graphite
LV	Low-Voltage
MV	Medium-Voltage
OCV	Open Circuit Voltage
PCR	Primary Control Reserve
PE	Power Electronics
PFDS	Power Flow Distribution Strategy
PV-BESS	Photovoltaic Buffer Battery Energy Storage System

RPT . . . . . Reference Performance Test

S-TMS . . . . . System Thermal Management System

SCADA . . . . . Supervisory Control and Data Acquisition

SCR . . . . . Secondary Control Reserve

SEI . . . . . Solid Electrolyte Interphase

SOC . . . . . State of Charge

SOH . . . . . State of Health

TMS . . . . . Thermal Management System

TU . . . . . Technical Unit

Symbols

Please note that the list below is based on the main part of this thesis and does not fully cover the included papers. Each paper itself includes a complete individual definition.

A . . . . . Surface interface area in m^2

C_{actual} . . . . . Actual battery capacity in Ah

c_{Capacity} . . . . . Capacity costs in €/kWh

$c_{\text{Capacity Loss}}$ . . . Marginal costs through battery capacity losses in €/kWh

c_{Energy} . . . . . Energy costs in €/kWh

$c_{\text{Energy Loss}}$ . . . . Marginal costs through energy losses in €/kWh

c_{Marginal} . . . . . Total marginal costs of operation in €/kWh

C_{Nominal} . . . . . Nominal battery capacity in Ah

COP . . . . . Coefficient of Performance (no unit)

$c_{p,\text{Air}}$ . . . . . Specific heat capacity of air in J/kg/K

$C_{\text{th,Cell}}$ . . . . . Cell thermal heat capacity in J/K

ΔS . . . . . Reaction entropy in J/K/mol

ΔT . . . . . Temperature difference in K

ΔU . . . . . Overvoltage in V

$\dot{V}$ . . . . . Volumetric air flow rate in m^3/s

$E_{\text{Charge,AC}}$ . . . . Charged energy (AC-side measurement) in kWh

$E_{\text{Discharge,AC}}$ . . . Discharged energy (AC-side measurement) in kWh

$E_{\text{Loss,i}}$ . . . . . Energy loss of mechanism i in kWh

e_{Loss} . . . . . Specific energy losses in kWh/kWh

$E_{\text{System Consumption}}$ Auxiliary system energy consumption in kWh

$\eta_{\text{Conversion}}$ . . . . Conversion round-trip efficiency in %

η_{Total} . . . . . Total round-trip efficiency in %

F . . . . . Faraday's constant, 96 485 C/mol

I . . . . . Current in A

n . . . . . Number of participating electrons

$P_{\text{AC,Req.}}$ . . . . . Required system power (AC-side) in W

P_{AirC} . . . . . Power consumption of the active cooling/heating in W

$P_{\text{C\&M}}$ . . . . . Power consumption of control & monitoring components in W

P_{DC} . . . . . Power DC-side in W

ϕ . . . . . Relative energy loss of mechanism i in %

$P_{\text{Loss,Batt}}$ . . . . . Power loss of battery in W

$P_{\text{Loss,DC-DC}}$ . . . Power loss of DC-DC converter in W

$P_{\text{Loss,Diode,Cond}}$ . . Diode conduction power loss in W

$P_{\text{Loss,Diode,Switch}}$. Diode switching power loss in W

$P_{\text{Loss,GridCon}}$ . . . Power loss of grid connection in W

$P_{\text{Loss,IGBT,Cond}}$ . . IGBT conduction power loss in W

$P_{\text{Loss,IGBT,Switch}}$. IGBT switching power loss in W

$P_{\text{Loss,Inv./Rect.}}$ . . Power loss of inverter/rectifier in W

$P_{\text{Loss,Inv./Rect. Unit}}$ Power loss of inverter/rectifier unit in W

$P_{\text{Loss,LCL}}$ . . . . . Power loss of LCL-filter in W

$P_{\text{Loss,LCL,Cond}}$ . . Conduction power loss of LCL-filter in W

$P_{\text{Loss,LCL,Core}}$ . . Core power loss of LCL-filter in W

$P_{\text{Loss,PE}}$ . . . . . Power loss of power electronics in W

$P_{\text{Loss,Transformer}}$. Power loss of transformer in W

$P_{\text{Loss,TR,Cond}}$ . . . Conduction power loss of transformer in W

$P_{\text{Loss,TR,Core}}$ . . . Core power loss of transformer in W

$P_{\text{Thml. Mgt.}}$ . . . . Power consumption of thermal management in W

P_{TU} . . . . . Power of Technical Unit (string) in kW

$\dot{Q}_{\text{AirC}}$ . . . . . Heat flow rate Air-Conditioning in W

$\dot{Q}_{\text{Cell}}$ . . . . . Cell heat source rate in W

$\dot{Q}_{\text{Cell-Amb}}$ . . . . Cell heat exchange rate to ambient in W

$Q_{\text{L,Cal}}$ . . . . . Calendar aging capacity loss in Ah or in %

$Q_{\text{L,Cyc}}$ . . . . . Cycle-induced capacity loss in Ah or in %

$Q_{\text{L,Cyc,High T}}$ . . . High temperature cycle-induced capacity loss in Ah or in %

$Q_{\text{L,Cyc,LowT HighSOC}}$ Low temperature, high SOC cycle-induced capacity loss in Ah or in %

$Q_{\mathrm{L,Cyc,Low\ T}}$ . . . Low temperature cycle-induced capacity loss in Ah or in %

q_{Loss} . . . . . Specific capacity losses in %

$Q_{\mathrm{Loss},i}$ . . . . . Capacity loss of the cell in Ah or in %

$Q_{\mathrm{Throughput}}$ . . . Charge throughput in Ah

$P_{\mathrm{AC,R}}/P_{\mathrm{AC,N,R}}$ . . Relative rack power in %

$P_{\mathrm{AC,Sys}}/P_{\mathrm{AC,N,Sys}}$ Relative system power in %

ρ_{Air} . . . . . Density of air in kg/m^3

R_{i} . . . . . Series resistance in Ω

R_{th} . . . . . Thermal resistance in m$^2\cdot$ K/W

s . . . . . Self-discharge rate in %/30d

SOC . . . . . State of Charge in %

SOH . . . . . State of Health in %

T . . . . . Temperature in K

$T_{\mathrm{Amb,Batt}}$ . . . . . Air temperature ambient to battery in K

$T_{\mathrm{Amb,PE}}$ . . . . . Air temperature ambient to power electronics in K

τ_{Q} . . . . . Charge-based system utilization in %

τ_{t} . . . . . Temporal system utilization in %

T_{Cell} . . . . . Cell temperature in K

$t_{\mathrm{Operation}}$ . . . . . Cumulated time of system in operation in h

t_{Profile} . . . . . Duration of load profile in h

T_{Outdoor} . . . . . Ambient outdoor temperature in K

T_{Ref} . . . . . Reference temperature in K

U_{DC} . . . . . Voltage DC-side in V

U_{Hys} . . . . . Cell hysteresis voltage in V

U_{OCV} . . . . . Open circuit voltage in V

$U_{\mathrm{OCV,Ref}}$ . . . . . Open circuit voltage at reference temperature in V

U_{T} . . . . . Terminal voltage in V

1 Introduction

The majority of human-induced carbon dioxide emissions stem from fossil fuels, which today still provide 80 % of global primary energy demand [1]. Climate change requires a transition to a low-carbon energy supply, which often includes the intensified use of renewable energy sources such as wind and solar [2]. As wind and solar are volatile energy sources, the issue of decoupled production and demand load arises. Flexibility options such as variable generation, demand-side management, and grid expansion can support the reduction of unbalanced production and load. For a stable energy supply with high shares of volatile renewable energy sources, energy storage at large-scales for short and long-term is a technically possible option [3, 4].

Recently, lithium-ion batteries have achieved significant cost reductions as well as increases in power/energy capacity and lifetime [5, 6]. Thus, they are now being increasingly installed in stationary Battery Energy Storage System(s) (BESS). System sizes for lithium-ion BESS range from small (under 20 kWh of nominal energy) for residential BESS, towards medium utility-scale size (under 1 MWh) for local grid applications [7], to large utility-scale size (over 1 MWh) for grid ancillary services [8, 9]. Lately, more and more systems of large sizes are being built and aid the transition to a renewable-based energy system [10].

To benefit the power system both ecologically and economically, BESS are required to provide a high *energy efficiency* and long *battery lifetime*. This work presents a detailed analysis of these two key metrics for utility-scale lithium-ion BESS.

In Section 1.1 the scope of this work is further detailed. Following in Section 1.2 the outline of the dissertation is presented.

1.1 Scope of this work

The energy efficiency of BESS can only be evaluated to a high degree of accuracy if all relevant energy loss mechanisms are covered. Losses of BESS include conversion losses and additionally auxiliary system power consumption. A holistic evaluation approach should include both mechanisms.
Energy efficiency of BESS is analyzed in detail for a reference system, the *Energy Neighbor*, to achieve a breakdown of the energy losses. As the model parameters derived and used herein are based on an actual BESS and the evaluated application scenarios are typical BESS applications, the simulations give realistic results for the performance of lithium-ion BESS.
As results reveal the Power Electronics (PE) connecting the battery to the electrical grid to be a major source of energy losses, a focus is put on the grid connection of BESS. Grid connection topologies consisting of different PE topologies and grid levels are compared regarding their energy efficiency. Furthermore, a software-based Power Flow Distribution Strategy (PFDS) for reducing PE losses is proposed, developed and tested in an industrial utility-scale system.

Regarding battery lifetime, a comprehensive storage and cycle test experiment with a focus on the effect of battery temperature on the cycle-induced battery degradation is conducted with Lithium Iron Phosphate/Graphite (LFP-C) cells. Based on experimental data, a semi-empirical model that captures separate degradation mechanisms is developed.

For an evaluation of the impact of energy losses and battery degradation on the economics of BESS operation, specifically their marginal costs of operation, a combined approach is presented. The marginal costs can be defined as additional costs occurring specifically through the BESS operation for charging and discharging. Considered incurring costs are energy losses during the operation and cycle-induced battery capacity degradation. Combined results are calculated and evaluated to identify optimum operating points. The results are evaluated in a profit-optimized control strategy for BESS in energy arbitrage.

1.2 Thesis outline

The main part of the dissertation largely references five research papers. Figure 1.1 presents an overview of the topics covered by these papers.

Chapter 2 gives an overview of the utilized methods for investigations on stationary lithium-ion BESS. The papers are each reproduced in the subsequent chapters. The Chapters 3-5 cover energy efficiency, Chapter 6 focusses on battery degradation, and Chapter 7 combines the evaluation of energy efficiency and battery degradation through an analysis of their impact on the marginal costs of operation.

Chapter 3 introduces the foundation for energy efficiency evaluations through holistic system simulation for a reference prototype system, the *Energy Neighbor*. The simulations reveal a detailed breakdown of the energy losses, as well as the grid connection to be major source of energy losses in BESS. The chapter references the paper *Energy efficiency evaluation of a stationary lithium-ion battery container storage system via electro-thermal modeling and detailed component analysis* [11]. The following two Chapters 4-5 consequently cover a more detailed analysis of the grid connection.

Chapter 4 presents an analysis of various grid connection topologies for BESS with focus on the reduction of losses in the PE. Results reveal that the choice of topology can strongly affect the energy efficiency and has to be considered specifically for each grid application. The chapter references the paper *Energy efficiency evaluation of grid connection scenarios for stationary battery storage systems* [12].

Chapter 5 then shows a second approach for PE energy loss reduction based on an improved control strategy. The developed control strategy is tested in an industrial utility-scale BESS and shows stable operation as well as a strong reduction of energy losses. The chapter references the paper *Power Flow Distribution Strategy for Improved Power Electronics Energy Efficiency in Battery Storage Systems: Development and Implementation in a Utility-Scale System* [13].

Towards battery degradation, Chapter 6 presents the developed battery degradation model with a focus on the effect of battery temperature on the cycle-induced battery degradation. The model is successfully validated against application-oriented experiments and correctly predicts the optimum operating temperature for battery cells regarding degradation. The chapter references the paper *Comprehensive Modeling of Temperature-Dependent Degradation Mechanisms in Lithium Iron Phosphate Batteries* [14].

Chapter 7 presents an economics-based approach regarding a multi-objective optimized control strategy respective to energy losses and battery degradation. For the energy loss calculation the methods and parameters presented in Chapter 3 are used, whereas for the battery degradation the model presented in Chapter 6 is utilized. The chapter references the paper *Marginal Costs of Battery System Operation in Energy Arbitrage based on Energy Losses and Cell Degradation* [15].

Finally, Chapter 8 summarizes the key findings of the dissertation and gives an outlook regarding the application of the results, as well as future research tasks.

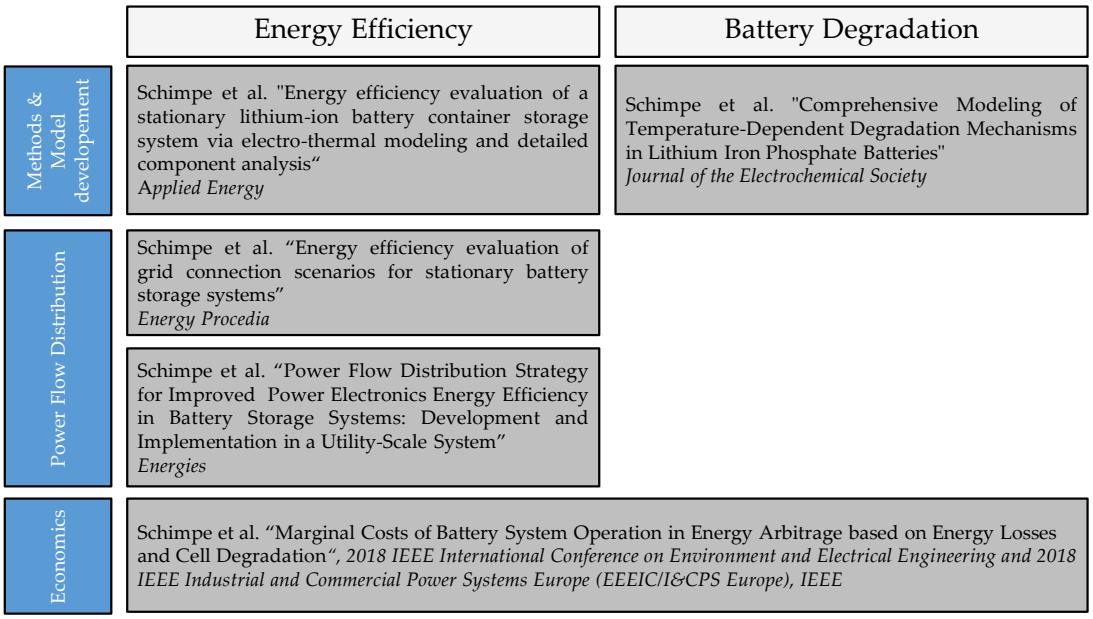

Figure 1.1: Overview of the thesis.

2 Stationary lithium-ion battery energy storage systems

This chapter presents the investigation methods and objects. First, Section 2.1 gives a short introduction into BESS, typical grid applications, and their important metrics to quantify system application and performance. Section 2.2 then introduces the two BESS used as a reference and as test-bed in this work. Finally, Section 2.3 presents the developed and utilized methods, both experimental and simulation-based. As the following methods are described based on the papers [11–15], the sections are based on the respective papers without further reference.

2.1 System applications and operation metrics

Figure 2.1 shows a schematic drawing of a BESS with power system coupling and grid interface components. Keywords highlight technically and economically relevant aspects for the design and operation of stationary BESS.

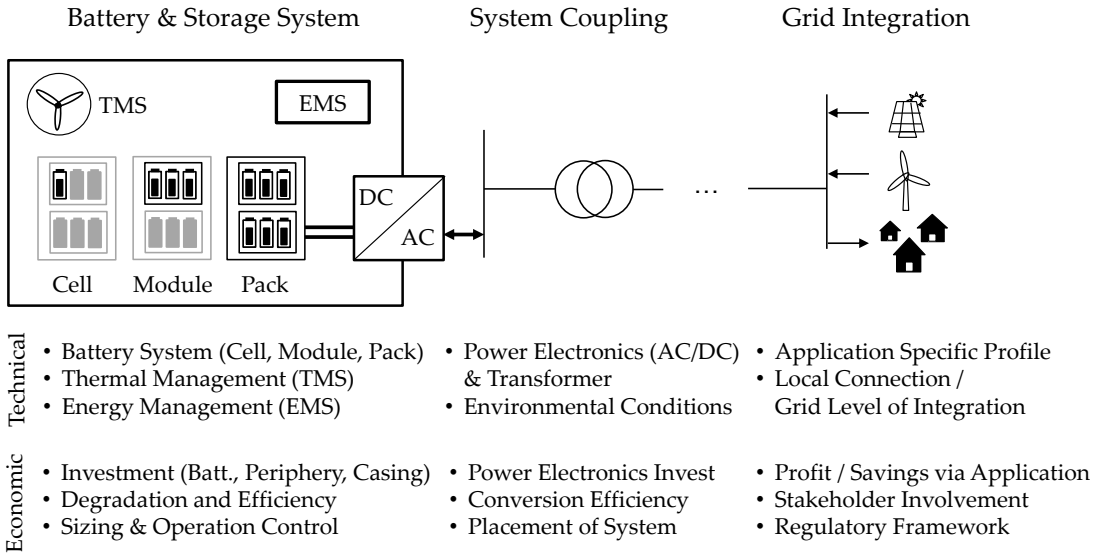

Figure 2.1: Formalized schematic drawing of a BESS, power system coupling and grid interface components. Keywords highlight technically and economically relevant aspects for the design and operation of stationary BESS. Reproduced from [5].

BESS can be used for various grid application scenarios, which can differ strongly in terms of load. Figure 2.2 shows the time-based distribution for the State of Charge (SOC) and the C-Rate (A 1 C rate means that the current will charge/discharge the nominal battery capacity in 1 hour) for three grid applications: Primary Control Reserve (PCR) (a,d), peak shaving (b,e), and the application as Photovoltaic Buffer Battery Energy Storage System (PV-BESS) (c,f).

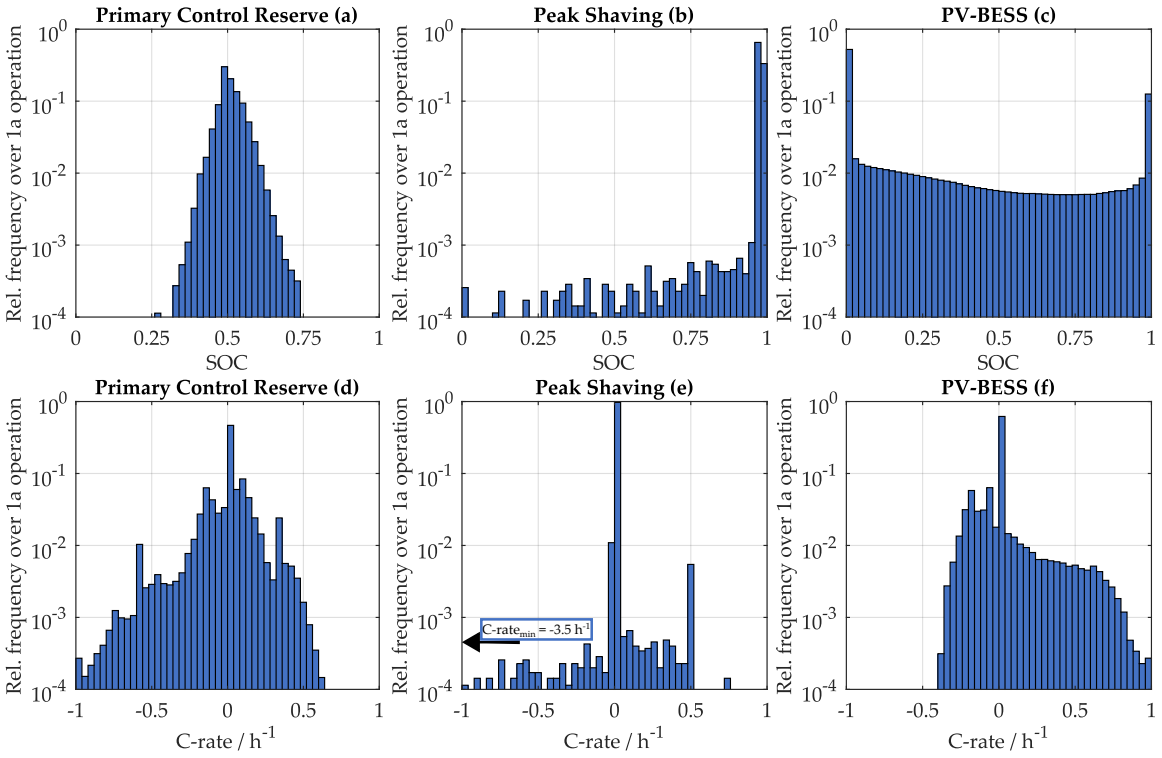

Figure 2.2: a-c) Distribution of SOC and d-f) C-rate for selected BESS applications: PCR, peak shaving, PV-BESS. Reproduced from [5].

To compare different application scenario load profiles quantitatively, utilization ratios are defined. The temporal utilization τ_t is the ratio of the time in which the simulation is in operation $t_\mathrm{Operation}$ (system power $\neq 0$) to the evaluated duration of the profile t_Profile :

$$\tau_\mathrm{t} = \frac{t_\mathrm{Operation}}{t_\mathrm{Profile}} \tag{2.1}$$

The charge-based utilization τ_Q is the ratio of the charge-throughput of the battery $Q_\mathrm{Throughput}$ to the theoretically possible maximum throughput during the profile duration $Q_\mathrm{Throughput,theoretical\,max.}$ at cycling the system at the maximum battery current:

$$\tau_\mathrm{Q} = \frac{Q_\mathrm{Throughput}}{Q_\mathrm{Throughput,theoretical\,max.}} \tag{2.2}$$

The utilization metrics will be used the Chapters 3-4 for the comparison of system application scenarios.

For the evaluation of the system efficiency, two round-trip efficiencies are defined, which give average values for an operation duration. The conversion round-trip efficiency $\eta_{\text{Conversion}}$ considers losses which occur on the conversion path from the energy charged, $E_{\text{Charge,AC}}$, and the energy discharged, $E_{\text{Discharge,AC}}$, from/to the grid. It includes only the conversion losses in the battery and PE, but not the auxiliary system power consumption. In the given simplified defintions of the efficiency calculation, the SOC at the start and end of the evaluation has to be identical:

$$\eta_{\text{Conversion}} = \frac{E_{\text{Discharge,AC}}}{E_{\text{Charge,AC}}} \tag{2.3}$$

The total round-trip efficiency η_{Total} further includes the auxiliary system energy consumption $E_{\text{System Consumption}}$:

$$\eta_{\text{Total}} = \frac{E_{\text{Discharge,AC}}}{E_{\text{Charge,AC}} + E_{\text{System Consumption}}} \tag{2.4}$$

To evaluate energy losses of various components in a system in detail, the relative loss ϕ of mechanism i is calculated through the ratio of the energy loss $E_{\text{Loss,i}}$ to the total energy input:

$$\phi_i = \frac{E_{\text{Loss},i}}{E_{\text{Charge,AC}} + E_{\text{System Consumption}}} \tag{2.5}$$

The efficiency metrics will be used the Chapters 3-5 for the evaluation of the energy efficiency in various applications and systems.

To evaluate the battery degradation, the actual battery capacity C_{actual} can be measured through capacity measurements, which are typically a full cycle of the battery. The achieved values can be put into comparison to the nominal cell capacity C_{Nominal}, which is specified by the manufacturer in the datasheet. In ideal conditions, the nominal capacity is identical to the actual capacity of a new battery. The metric SOH representing the battery State of Health (SOH) regarding the capacity loss can finally be calculated:

$$SOH = \frac{C_{\text{actual}}}{C_{\text{Nominal}}} \tag{2.6}$$

The metric will be intensively used in Chapter 6 to evaluate the battery degradation under various conditions.

To compare the economic impact of energy losses and battery capacity losses quantitatively, the marginal costs of operating the battery c_{Marginal} can be calculated. They are defined as costs in Euro for a full cycle per installed kWh of nominal energy capacity. In this work, they comprise costs for energy conversion losses and for battery degradation. The costs for the energy losses $c_{\text{Energy Loss}}$ are calculated from the specific lost energy e_{Loss}, which is derived from electrical cell models further detailed in Section 2.3.2, and the costs for energy c_{Energy} in €/kWh:

$$c_{\text{Energy Loss}} = e_{\text{Loss}} \cdot c_{\text{Energy}} \tag{2.7}$$

Costs for the capacity losses $c_{\text{Capacity Loss}}$ are calculated from the specific lost capacity q_{Loss}, which is derived from degradation models further detailed in Chapter 6, and the specific investment costs for battery capacity c_{Capacity} in €/kWh:

$$c_{\text{Capacity Loss}} = q_{\text{Loss}} \cdot c_{\text{Capacity}} \tag{2.8}$$

Together they comprise total marginal costs c_{Marginal}. This metric will be used in Chapter 7.

$$c_{\text{Marginal}} = c_{\text{Energy Loss}} + c_{\text{Capacity Loss}} \tag{2.9}$$

2.2 Battery energy storage systems investigated in this work

Two BESS are used in the studies of this work: The prototye system *Energy Neighbor* developed at the Technical University of Munich and the Second-Life system operated by the company *The Mobility House*. Section 2.2.1 presents the reference system, the *Energy Neighbor*. The system is used as a reference object in the studies on energy efficiency in Chapter 3 and 4. Further, the battery cell of the system is evaluated regarding battery degradation in the paper presented in Chapter 6. Finally, the study combining energy efficiency and battery degradation in Chapter 7 through the marginal cost calculation is also based on the reference system and the respective battery cell.
Section 2.2.2 presents the second BESS, the system operated by *The Mobility House*. The system is used to test the developed PFDS improving the energy efficiency, presented in Chapter 5, in a system in the commercial application.

2.2.1 Reference system: Prototype system *Energy Neighbor*

The system *Energy Neighbor* is a 192 kWh, 248 kW 20-foot container prototype BESS. The system was developed by the Technical University of Munich in the research project *EEBatt* in cooperation with Varta Storage and the Bavarian Centre for Applied Energy Research (ZAE Bayern) [7].

For thermal management, the system features a two-zone climate system for separate and energy-efficient temperature control of the battery racks and the PE, which are both air cooled. Figure 2.3 shows the structure of the system with battery racks, PE, and thermal management highlighted. More information on the system can be found in [16].

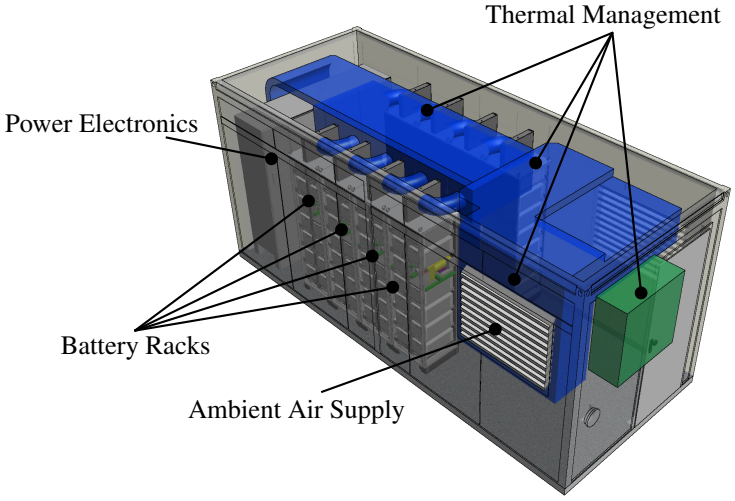

Figure 2.3: Structure of the stationary BESS *Energy Neighbor*. Reproduced from [11].

The system features eight battery racks which are each coupled to the Low-Voltage (LV) grid via bidirectional PE establishing the conversion between Alternating Current (AC) and Direct Current (DC) based power flow. Figure 2.4 shows the electrical system layout of the *Energy Neighbor* connecting the eight battery racks to the grid.

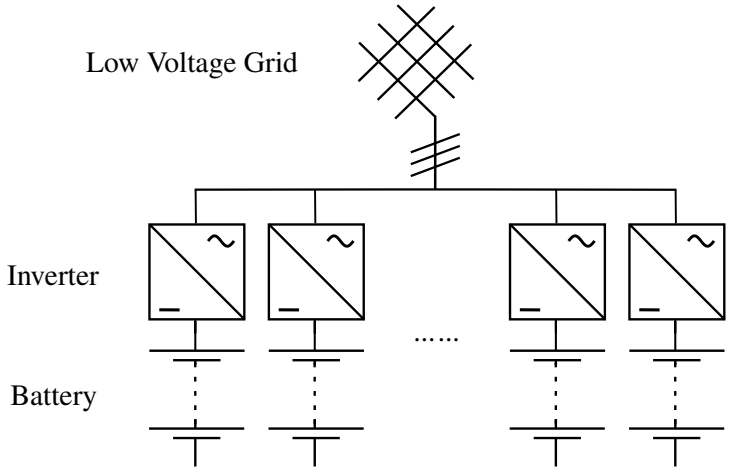

Figure 2.4: Electrical system layout of the *Energy Neighbor* connecting the eight battery racks to the LV grid. Reproduced from [11].

The battery racks are based on the 26650-format LFP-C cell manufactured by Sony under brand name US26650FTC1. The cell is designed for stationary applications [17]. Figure 2.5 shows a photo of a single cylindrical cell.

Figure 2.5: Photo of 26650-format cell Sony US26650FTC1. Reproduced from [18].

The datasheet parameters of the cell with notes for this work are given in Table 2.1.

Table 2.1: Datasheet parameters of cell Sony US26650FTC1 with notes for this work. Data from [19]. Reproduced from [14].

Parameter	Value	Notes
Nominal Voltage	3.2 V	
Nominal Capacity	3000 mAh	Rated Capacity is 2850 mAh. Capacity 3000 mAh is denoted as nominal in this work, as all tested new cells have approximately this capacity.
Charge Voltage	3.60 V ± 0.05 V	3.60 V is used in this work.
Discharge Voltage	2.00 V	
Continuous Max. Charge Current	2.85 A	Continuous max. charge current of 1 C (3.00 A) is used in this work, based on the new cell capacity of 3000 mAh.
Continuous Max. Discharge Current	20 A	
Temperature Range Charge	0 to + 45 °C	Max. surface temperature is +60 °C.
Temperature Range Discharge	-20 to + 60 °C	Max. surface temperature is +80 °C.

Table 2.2 gives the interconnection setup as well as the resulting capacities and voltages for a battery cell, cell block, module and rack of the *Energy Neighbor*.

Table 2.2: Battery parameters for battery cell, cell block, module and rack of the *Energy Neighbor*. Reproduced from [11].

	Interconnection	Nominal Voltage	Nominal Capacity	Nominal Energy	Minimum Voltage	Maximum Voltage
Cell	1s1p	3.2 V	3 Ah	9.6 Wh	2.0 V	3.6 V
Block	1s12p	3.2 V	36 Ah	115 Wh	2.0 V	3.6 V
Module	16s12p	51.2 V	36 Ah	1.8 kWh	32.0 V	57.6 V
Rack	13s x 16s12p	665.6 V	36 Ah	24 kWh	416.0 V	748.8 V

The system was installed in the German village Moosham in Bavaria in the LV grid to enable local grid applications such as load reduction of the local transformer [7]. It further serves as a test platform for various grid applications. As it has been developed as part of a research cooperation of industry and academia, it is up to date with current industry standards and at the same time enables the availability of the necessary system information for a detailed study.

2.2.2 Test system: Second-Life system operated by *The Mobility House*

The system used for testing of the PFDS is a Second-Life BESS, operated by *The Mobility House* in cooperation with *GETEC* and *REMONDIS* in Lünen, Germany [20]. The system has a nominal capacity and power of 3.3 MWh and 3 MW, respectively. Second-Life here refers to the second application of automotive batteries that were first used in electrical battery-powered vehicles. The system is thus set up from used battery packs from electric cars sold under brand name *Smart electric drive* by *Daimler*. The stationary application for the battery packs extends their usage beyond their initial mobile application. The concept is a promising approach to reduce the high costs associated with the

battery packs for a BESS, and thus improves the economic viability of BESS and their applications. As one of the first systems and at time of installation in 2016 the largest Second-Life system in the world, the system in this work also shows the technical feasibility of Second-Life concepts.
Figure 2.6 gives a schematic overview of the system, which consists of six Technical Unit (TU), the auxiliary system components, and the grid connection.

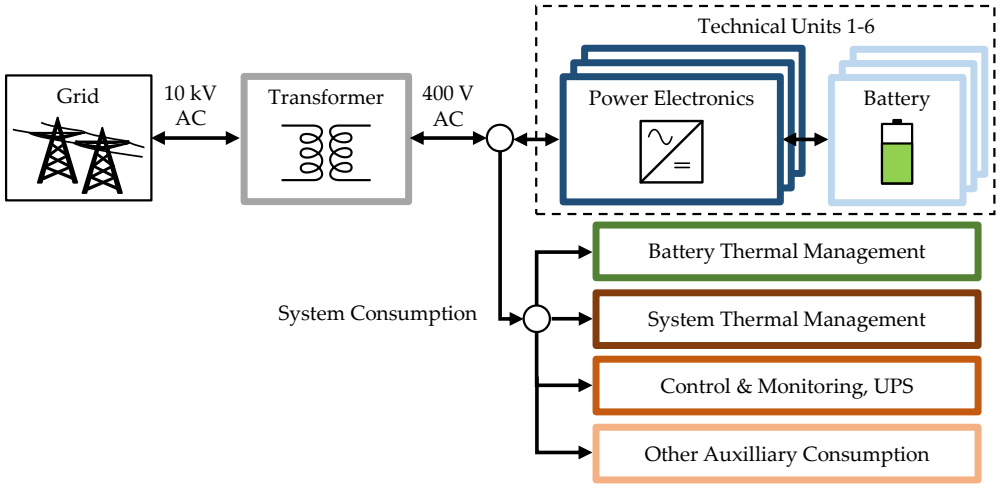

Figure 2.6: Overview of the Second-Life system operated by *The Mobility House* with six TU, the grid connection, and auxiliary components. Adapted from [13].

The TU each consist of batteries with dedicated PE, however vary in terms of topology, power and capacity. The auxiliary components are required for the operation of the overall system. A transformer connects the system-internal 400 V AC low-voltage to the 10 kV Medium-Voltage (MV) grid. The TU, as well as the auxiliary components, are connected to the LV level within the system.
Figure 2.7 shows the schematic overview for a TU with a specific topology that features two internal power strings, which both have the same nominal battery capacity/power. The total unit power P_{TU} is distributed to the power strings $P_{\mathrm{TU},1}$ and $P_{\mathrm{TU},2}$. The topology of a TU consisting of two independent power strings enables flexible distribution of the total TU power between the two power strings. This flexibility is required for the developed PFDS presented in Chapter 5.

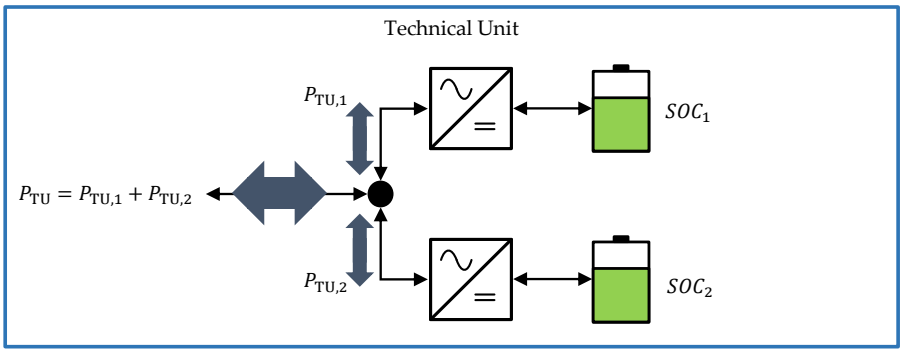

Figure 2.7: Schematic overview of a TU consisting of two power strings. Adapted from [13].

2.3 Methods for evaluation of energy efficiency and battery lifetime

This section presents the developed and utilized methods for the evaluation of the energy efficiency and the battery lifetime of BESS, both experimental and simulation-based. In the dissertation, a holistic system simulation approach to analyze BESS is developed, which is presented in Section 2.3.1. To evaluate the energy efficiency of sub-systems in BESS, detailed component models are utilized. Section 2.3.2 presents the methods for electrical-thermal battery modeling and their parameterization methods. Section 2.3.3 then gives an overview of the calculation of energy losses in the grid connection. Finally, Section 2.3.4 presents the calculation methods for the auxiliary power consumption of the system, with a focus on the system thermal management.
To evaluate field-deployed BESS for their energy efficiency, Section 2.3.5 gives an overview regarding the required measurements and calculation protocols.
Regarding battery degradation, Section 2.3.6 presents an overview of the methods for aging experiments and the development of semi-empirical battery degradation models.

2.3.1 Holistic system simulation

To evaluate the energy efficiency in a simulation, all relevant energy loss mechanisms have to be quantified in the system model. Most studies so far focus on specific system issues, i.e. thermal management [21–25], PE [26, 27], or the battery [21, 28]. Other studies focussed more on the overall performance of the system in terms of economic performance [29–34]. The new contribution in this work is that the system simulation features a breakdown of the energy losses and that all components relevant to the system energy efficiency are included.
An analysis of the system setup of the *Energy Neighbor* is conducted to include all relevant components. Figure 2.8 shows the identified mechanisms, grouped in the respective categories which are also calculated in the system model. In total, 18 different types of loss mechanisms are defined and quantified. As the energy loss model is built bottom-up, only the major loss mechanisms are considered. E.g. in the inverter/rectifier unit no coil losses besides in the LCL-filter are included as they are expected to be negligible.

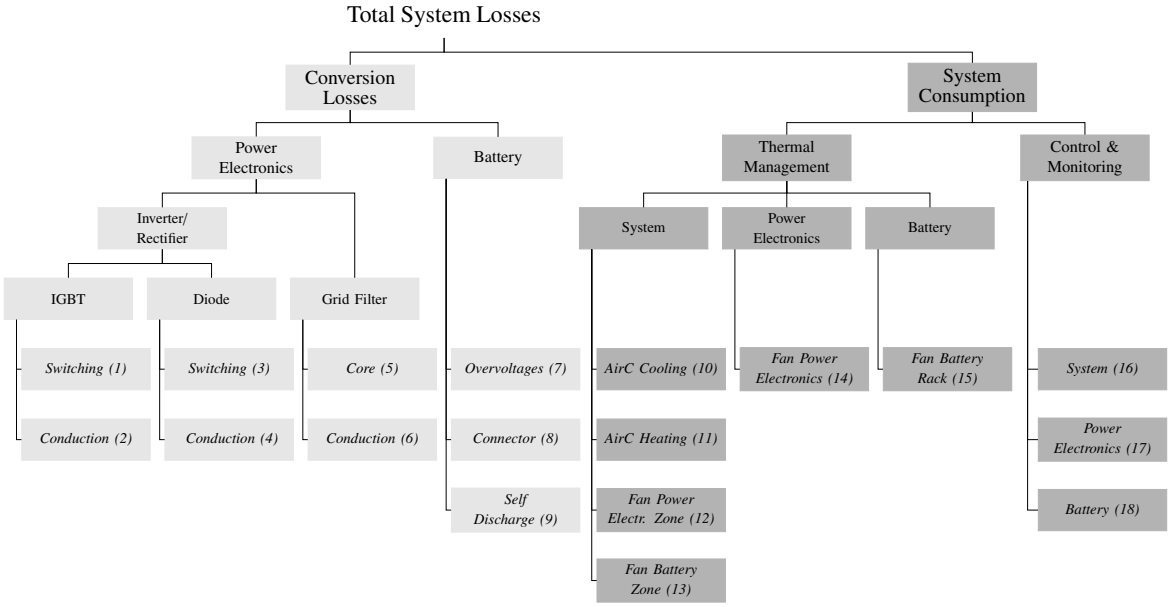

Figure 2.8: Overview of the 18 energy loss mechanisms calculated in the system model. Reproduced from [11].

Figure 2.9 shows the schematics of the developed system model. The system model consists of four coupled component models, which are: *Battery*, *Power Electronics*, *Thermal Management*, and *Control & Monitoring*. The component models are coupled via temperatures, voltage levels, and power/heat flows. Input variables are the ambient outdoor temperature derived from weather data T_{Outdoor} and the AC-side power value of the load profile $P_{\mathrm{AC,Req.}}$.

The component models for the *Battery* and *Power Electronics* take into account conversion losses $P_{\mathrm{Loss,PE}}$ and $P_{\mathrm{Loss,Batt}}$, whereas power consumption related to thermal management $P_{\mathrm{Thml.\ Mgt.}}$, and control electronics $P_{\mathrm{C\&M}}$ is covered in the respective separate models *Thermal Management* and *Control & Monitoring*. The sub-models are coupled to accurately represent the component interdependencies. Battery and PE are coupled through the DC-link voltage U_{DC} and the DC-link power P_{DC}. For the coupling of the thermal aspects, the system temperature ambient to the battery and the PE, $T_{\mathrm{Amb,Batt}}$ and $T_{\mathrm{Amb,PE}}$ respectively, are taken into consideration.

This holistic system model is used in the studies covering the overall system efficiency in Chapters 3 and 5. The study in Chapter 4 focussing on the energy efficiency of the grid connection as well as the marginal cost study in Chapter 7 use a reduced version of the system model.

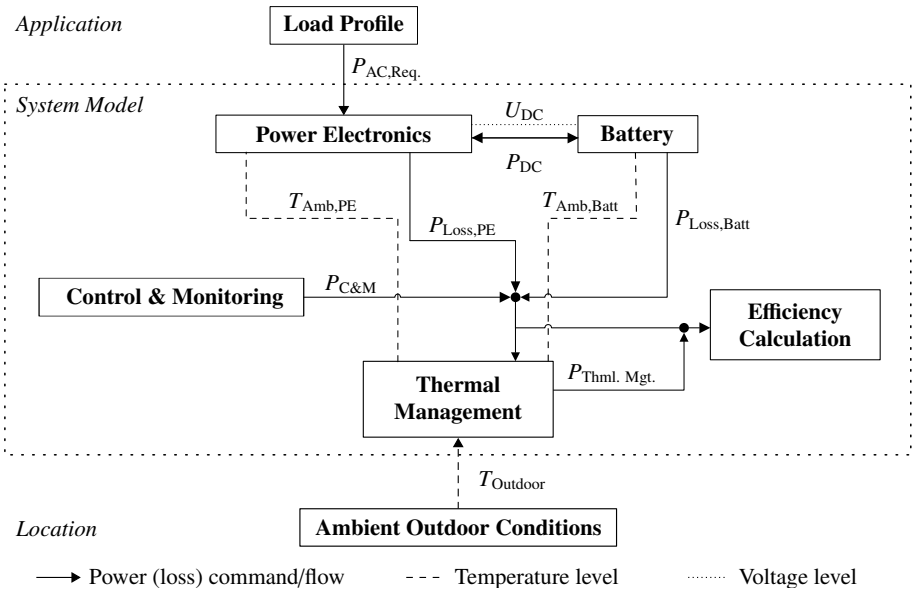

Figure 2.9: System model overview: Schematics of component model coupling via temperature, voltage levels, and power/heat flows. Reproduced from [11].

2.3.2 Equivalent circuit battery models

All battery simulations in this dissertation are based on equivalent circuit battery models. The battery single-cell model is based on full-cell characterization. Figure 2.10 shows the schematic of the model featuring a voltage source for the cell Open Circuit Voltage (OCV) and a single resistor for cell overvoltages. Further modeled cell characteristics which are not shown in the schematic figure are voltage hysteresis, reaction entropy in both electrodes of the cell, and self-discharge.

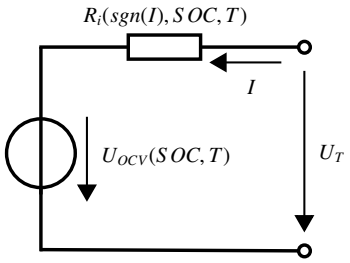

Figure 2.10: Equivalent circuit of electrical battery model. Current direction for charging is positive.

Terminal voltage U_T is calculated from the OCV U_OCV, overvoltages ΔU across the series resistance R_i and a cell hysteresis voltage U_Hys.
The OCV of the cell can be measured through stepwise incremental OCV measurements at specific SOC or through low-current charge/discharge voltage profile measurements. The methods differ in terms of measurement time, SOC resolution and accuracy [35, 36]. In this work, the low-current charge/discharge method is utilized to achieve a continous voltage profile over the SOC.
The OCV voltage U_OCV at reference conditions of $T_\mathrm{Ref} = 25\,^\circ\mathrm{C}$ over the SOC is measured by charging and discharging the cell at a low current rate of C/50 and averaging both voltage curves to compensate for remaining overvoltages and hysteresis effects. Figure 2.11 shows the experimental results for charge and discharge over the cell SOC as well as the calculated averaged voltage. Results are implemented in the model as $U_\mathrm{OCV,Ref}(SOC)$, which is shown in Figure 2.12a.

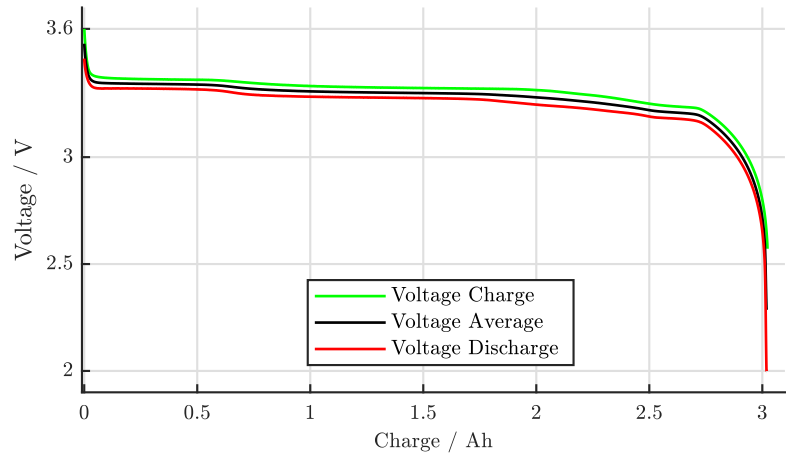

Figure 2.11: Low-current charge/discharge test at current rate C/50 for OCV characterization. $T = 25\,°\mathrm{C}$.

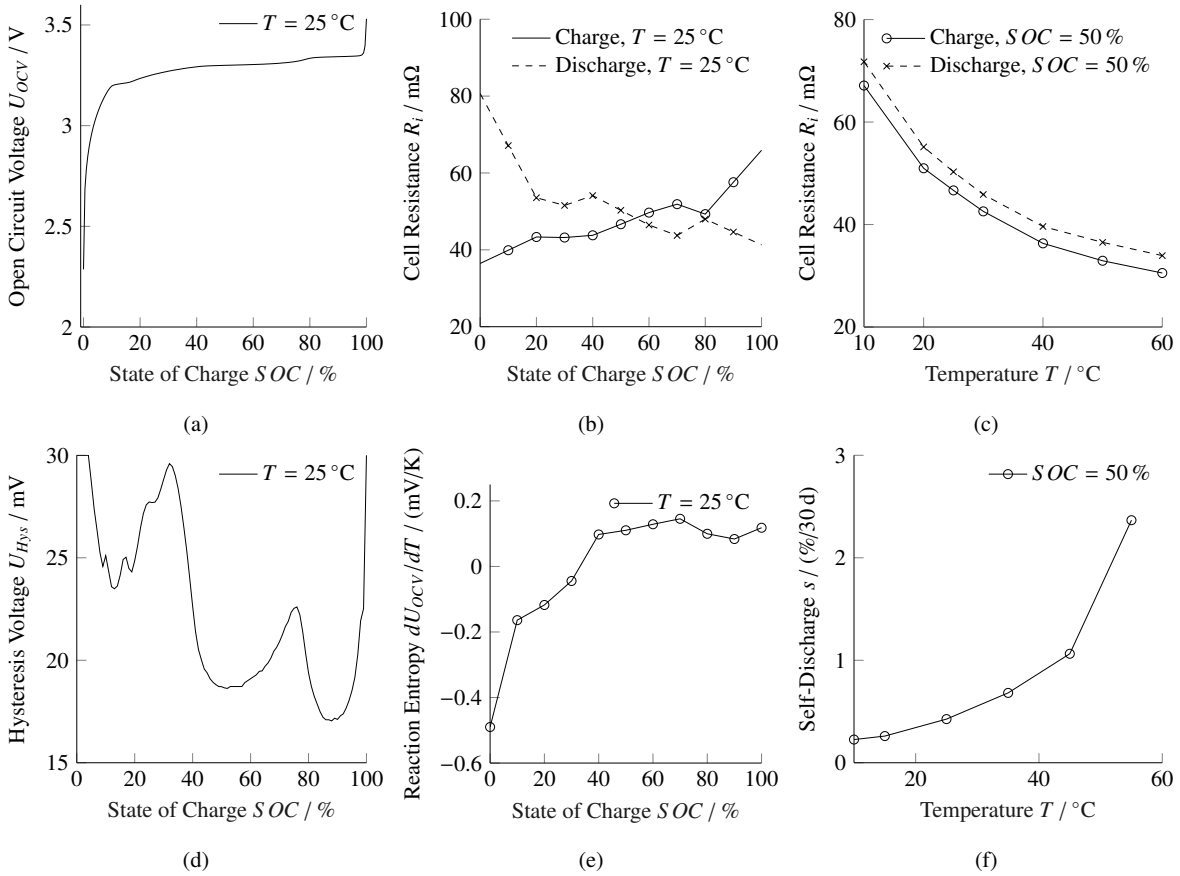

Figure 2.12: Battery model parametrization for the LFP-C cell: a) OCV over SOC at $T = 25\,°\mathrm{C}$, b) Cell resistance (Pulse 1 C, 6 min) over SOC at $T = 25\,°\mathrm{C}$, c) Cell resistance (Pulse 1 C, 6 min) over temperature at $SOC = 50\,\%$, d) Cell hysteresis voltage over SOC at $T = 25\,°\mathrm{C}$, e) Reaction entropy over SOC at $T = 25\,°\mathrm{C}$, f) Self-discharge rate over temperature at $SOC = 50\,\%$. Adapted from [11].

Parameters for the series resistance R_i are collected through pulse tests over the entire SOC range with a current rate of 1 C in both charge and discharge direction in 10 % (6 min) SOC-steps. The series resistance is calculated from the cell overvoltage at the end of a pulse, defined as voltage difference between the end of the pulse and the end of the following relaxation phase, and the pulse current. Relaxation time after each pulse is 6 h.
Figure 2.13 shows the test procedure for the discharge pulse test at $SOC = 50\,\%$. The 10 % (6 min) SOC-step pulse starts at $SOC = 60\%$ followed by the relaxation time for calculation of the overvoltage at the end of the pulse from the measured terminal voltage U_T.

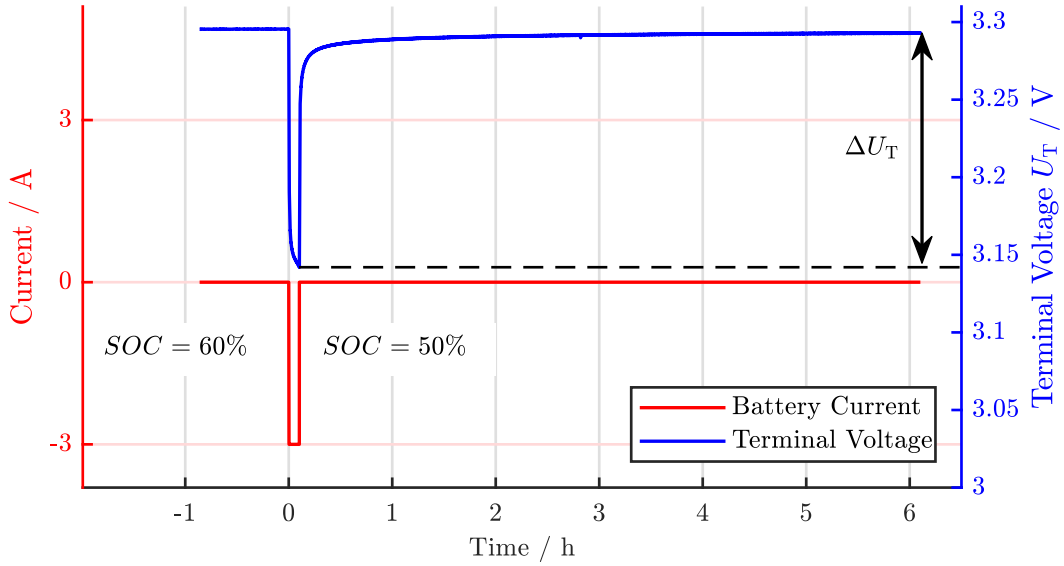

Figure 2.13: Pulse test for cell resistance: Measured terminal voltage U_T and battery current (Discharge, measurement for $SOC = 50\%$, $T = 25\,^\circ\mathrm{C}$).

Results shown in Figure 2.12b for tests at a climate chamber temperature of 25 °C indicate that values for charge and discharge are not identical and tend to higher values towards the end for both charge and discharge.
The pulse characterization over the SOC range is conducted at climate chamber temperatures from 10 °C to 60 °C in steps of 10 °C and additionally at 25 °C. Results for a SOC of 50 % at various temperatures are shown in Figure 2.12c. As expected for lithium-ion batteries, resistances increase with decreasing temperature due to the slow-down of electrochemical and physical processes.

Dedicated modeling of the voltage hysteresis, which is prominent in Lithium Iron Phosphate (LFP) electrodes [37–39], is necessary for accurate equivalent circuit modeling of the cell [40]. A time-independent hysteresis model for the voltage hysteresis U_Hys is implemented as a function of the SOC based on the C/50 charge and discharge curves from OCV measurements, while accounting for the overvoltage through the previously determined series resistance R_i:

$$U_\mathrm{Hys}(SOC) = \frac{(U_\mathrm{T,Charge}(SOC) - R_\mathrm{i} \cdot I) - (U_\mathrm{T,Discharge}(SOC) + R_\mathrm{i} \cdot I)}{2} \tag{2.10}$$

Results are shown in Figure 2.12d.

The overvoltage ΔU, the difference between the cell terminal voltage and the OCV, is thus calculated through the ohmic losses in the series resistance at current I and the hysteresis voltage:

$$\Delta U = U_{\mathrm{T}} - U_{\mathrm{OCV}} = I \cdot R_{\mathrm{i}}(SOC, T) + \mathrm{sgn}(I) \cdot U_{\mathrm{Hys}}(SOC) \tag{2.11}$$

As both the OCV of the cell and reversible heat production are a function of the reaction entropy ΔS [41–43], the reaction entropy profile for the cell is taken through potentiometric measurements. The SOC is changed from 0 % to 100 % in 10 % steps using a C/20 current at 25 °C and the battery is subsequently allowed to relax for 13 h at the same temperature, followed by a thermal cycle: Temperature change to +60 °C; Relaxation for 3 h; Temperature change to 10 °C; Relaxation for 3 h. Reaction entropy ΔS is calculated as dU_{OCV}/dT from cell voltages after relaxation at +60°C and -10°C, where n is the number of electrons participating in the reaction and F is the Faraday constant:

$$\Delta S = n \cdot F \cdot \frac{U_{\mathrm{T}}(T = +60°\mathrm{C}) - U_{\mathrm{T}}(T = -10°\mathrm{C})}{+60°\mathrm{C} - (-10°\mathrm{C})} \tag{2.12}$$

Results are shown in Figure 2.12e.
The temperature-dependent OCV of the cell can then be approximated by first order expansion around the reference temperature of 25 °C:

$$U_{\mathrm{OCV}}(T, SOC) = U_{\mathrm{OCV,Ref}}(SOC) + (T - T_{\mathrm{Ref}}) \cdot \left.\frac{dU_{\mathrm{OCV}}(SOC)}{dT}\right|_{T=T_{\mathrm{Ref}}} \tag{2.13}$$

Neglecting slow side-reactions due to cell aging or self-discharge and further the heat of mixing due to concentration gradients within the cell, which can generally be neglected for typical loads for lithium-ion cells [44, 45], the heat source in the cell $\dot{Q}_{\mathrm{Cell}}$ cell can be calculated as the sum of irreversible energy losses and the reversible heat production:

$$\dot{Q}_{\mathrm{Cell}} = I \cdot \left(\Delta U + T \cdot \left.\frac{dU_{\mathrm{OCV}}(SOC)}{dT}\right|_{T=T_{\mathrm{Ref}}} \right) \tag{2.14}$$

Cell self-discharge rate s is measured via a separate experiment. Self-discharge can be measured through open circuit measurements, where the cell is stored and the change in remaining capacity is determined afterwards, or through floating voltage measurements, where the voltage is kept constant through recharging the battery. Both methods suffer from the difficulty of differentiating between self-discharge and battery aging [36, 46, 47]. In this work, open circuit measurements were conducted as they don't require the extensive use of high-precision current sensors.
Cells are fully discharged at 25 °C, charged to 50 % SOC, rested for one month and again fully discharged at 25 °C. The difference between charged capacity and discharged capacity after storage is taken as constant self-discharge as a function of temperature for the simulation. Storage temperatures are 10 °C, 15 °C, 25 °C, 35 °C, 45 °C and 55 °C. Results are shown in Figure 2.12f, indicating a strong increase at higher temperatures.
As self-discharge is covered through the measured self-discharge rate s, the coulombic efficiency in the simulations is implemented as 100 %.

Thermal battery models range from simple approaches, e.g. constant cell temperature assumptions based on ideal cooling, to more advanced methods, e.g. to 0D, 1D, 2D and 3D thermal models [44, 48, 49]. In this work, the cell temperature T_{Cell} of the single-cell is implemented as 0D lumped thermal capacity, with cell heat capacity $C_{\text{th,Cell}}$, for computational efficiency and as low cell-internal thermal gradients are expected for the low current loads of stationary battery applications. The thermal model is then extended for simulation of a cell block, and then to the module and the whole rack.

Exemplarly, the heat balance for a cell is based on the heat rate of the cell $\dot{Q}_{\text{Cell}}$ and the heat exchange rate to ambient $\dot{Q}_{\text{Cell-Amb}}$:

$$C_{\text{th,Cell}} \frac{dT_{\text{Cell}}}{dt} = \dot{Q}_{\text{Cell}} - \dot{Q}_{\text{Cell-Amb}} \tag{2.15}$$

2.3.3 Grid connection power loss calculation

The grid connection of BESS can vary strongly in terms of different PE topologies, number of PE units depending on the system size, and the voltage level of the grid. Various methods for the power loss calculation of PE are proposed in [26, 50–52]. Different grid connection topologies have been compared in [27, 53]. The novel contribution in this work is that the typical grid connection scenarios based on industry components and their respectively validated component models are compared with respect to their energy efficiency, resulting application-oriented results.

The considered grid connection topologies in this work all consist of several inverter/rectifier units with optionally a DC-DC converter and/or a transformer. Consequently in the simulation, the total grid connection power loss $P_{\mathrm{Loss,GridCon}}$ is calculated through the sum of the power losses of each component, i.e. of the DC-DC converter $P_{\mathrm{Loss,DC\text{-}DC}}$, the inverter/rectifier unit $P_{\mathrm{Loss,Inv./Rect.\ Unit}}$, and the transformer $P_{\mathrm{Loss,Transformer}}$:

$$P_{\mathrm{Loss,GridCon}} = \sum P_{\mathrm{Loss,DC\text{-}DC}} + \sum P_{\mathrm{Loss,Inv./Rect.\ Unit}} + P_{\mathrm{Loss,Transformer}} \tag{2.16}$$

The sub-component models are simulated in MATLAB Simulink. The step-widths in the component models are in the range of microseconds to resolve semiconductor switching operation, as well as the sinusoidal voltage and current. The simulation of the typically year-long grid application scenarios uses reduced component models. These are created by simulating the component models until steady-state conditions are reached. Then, time-averaged values are calculated for varying parameters, i.e. DC-voltage and unit power. The topologies are then simulated by combining the steady-state time-averaged component models.

Exemplary, Figure 2.14 shows the structure of an inverter/rectifier unit including the LCL-filter.

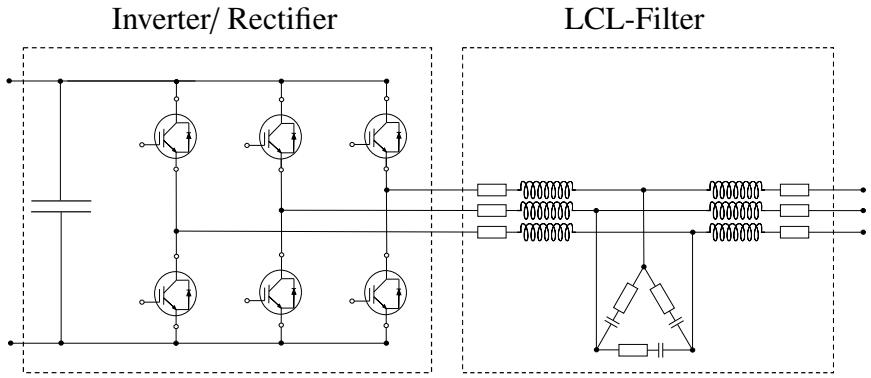

Figure 2.14: Structure of an inverter/rectifier unit. Reproduced from [12].

For the respective power loss calculation of the complete unit the losses in the inverter/rectifier part, $P_{\mathrm{Loss,Inv./Rect.}}$, and in the LCL-filter module, $P_{\mathrm{Loss,LCL}}$ are included:

$$P_{\mathrm{Loss,Inv./Rect.\ Unit}} = P_{\mathrm{Loss,Inv./Rect.}} + P_{\mathrm{Loss,LCL}} \tag{2.17}$$

The loss calculation in the inverter/rectifier unit calculates the conduction losses and switching losses in both the IGBT and the freewheeling diodes, i.e. $P_{\text{Loss,IGBT,Switch}}$, $P_{\text{Loss,IGBT,Cond}}$, $P_{\text{Loss,Diode,Switch}}$, and $P_{\text{Loss,Diode,Cond}}$:

$$P_{\text{Loss,Inv./Rect.}} = P_{\text{Loss,IGBT,Switch}} + P_{\text{Loss,IGBT,Cond}} + P_{\text{Loss,Diode,Switch}} + P_{\text{Loss,Diode,Cond}} \tag{2.18}$$

The losses in the LCL-filter are calculated separately as core losses, $P_{\text{Loss,LCL,Core}}$, and conduction losses $P_{\text{Loss,LCL,Cond}}$:

$$P_{\text{Loss,LCL}} = P_{\text{Loss,LCL,Core}} + P_{\text{Loss,LCL,Cond}} \tag{2.19}$$

The DC-DC converter power losses are calculated in the same fashion as in the inverter/rectifier model.

The transformer power losses are the sum of the load-independent core losses due to hysteresis and eddy current losses $P_{\text{Loss,TR,Core}}$, and of the load-dependent conduction losses occurring in the transformer windings $P_{\text{Loss,TR,Cond}}$:

$$P_{\text{Loss,Transformer}} = P_{\text{Loss,TR,Core}} + P_{\text{Loss,TR,Cond}} \tag{2.20}$$

2.3.4 Auxiliary system power consumption

For simulation of the auxiliary components power consumption different approaches are used based on the components in the system. Most components have a constant power consumption or different states of operation, e.g. standby and operation, in which the power consumption is again relatively constant.
Other components, however, which are variably controlled such as the thermal management require more detailed simulation approaches. Simple models directly calculate the thermal management power consumption from the power losses in the system without accounting for thermal dynamics or gradients of the system [21, 24, 25]. More advanced approaches use thermal resistor networks fitted to measurements or approximated parameters [22, 23]. The new contribution in this work is that thermal resistor networks are developed based on an prototype system and its actual structure and are accurately parametrized to component data.

Figure 2.15 shows the system thermal management model overview for the prototype system *Energy Neighbor*, studied in detail in Chapter 3. The model is based on a thermal resistance network of the container system representing the two-climate zones as well as the possibility of air conditioning through the ambient outdoor air or active cooling/heating.

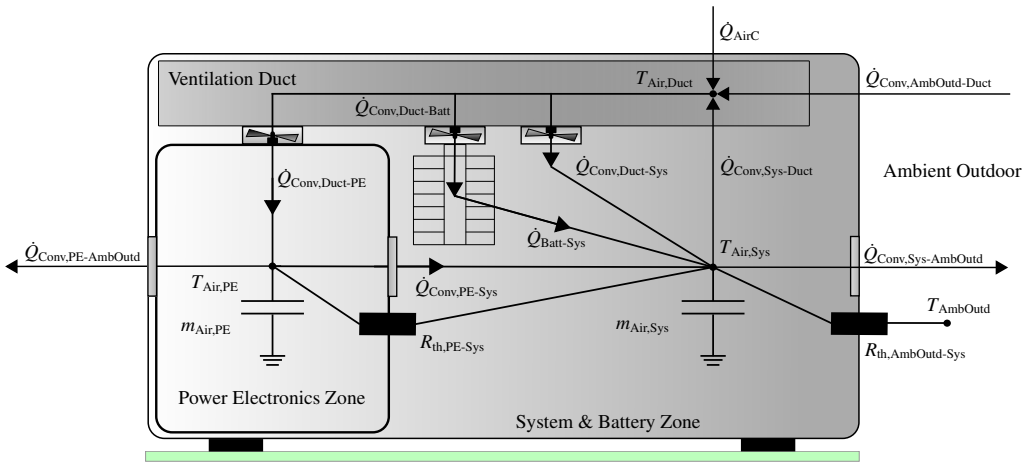

Figure 2.15: System thermal management model overview: Thermal resistance network of the container system with two-climate zones, air-conditioned by ambient outdoor air and active cooling/heating. Reproduced from [11].

Convective heat flows of a volumetric air flow rate $\dot{V}$, with a specific heat capacity $c_{p,\mathrm{Air}}$, density ρ_{Air}, at a temperature T are calculated in the thermal system model as follows:

$$\dot{Q}_{\mathrm{Conv}} = \dot{V} \cdot c_{p,\mathrm{Air}} \cdot \rho_{\mathrm{Air}} \cdot T \tag{2.21}$$

Conductive heat flows between two objects are calculated with the interface area A , the temperature difference ΔT and the thermal resistance R_{th}:

$$\dot{Q}_{\mathrm{Cond}} = A \cdot \frac{\Delta T}{R_{\mathrm{th}}} \tag{2.22}$$

For a more detailed explanation of the thermal system model it is here refered to Chapter 3.

Towards the power consumption of the thermal management, e.g. the power consumption of the active cooling/heating with the split-inverter unit P_{AirC} at a heat flow rate $\dot{Q}_{\mathrm{AirC}}$ is calculated with the Coefficient of Performance COP:

$$P_{\mathrm{AirC}} = COP \cdot \dot{Q}_{\mathrm{AirC}} \tag{2.23}$$

The alternative to detailed simulation or component analysis is the use of measured loads for the respective components for an analysis. Such analyses are of value to understand known operation scenarios, but accuracy is typically to low for evaluation of novel or future applications of the system, where the auxiliary power consumption might differ. Nevertheless, this approach is used in Chapter 5, where detailed power consumption measurements are taken for a whole month to study the loss distribution of the system in its actual application. The following Section 2.3.5 gives further insights into the setup of field-test measurements.

2.3.5 Field-test measurements

For the evaluation of field-deployed BESS regarding their metrics, specific measurements and test protocols are required. A performance and health test procedure for BESS was presented in detail in [54]. Regarding energy efficiency of BESS, Figure 2.16 gives an overview of the functional blocks of a utility-scale BESS. Here grey lines indicate auxiliary power supply, black lines indicate main power flows.

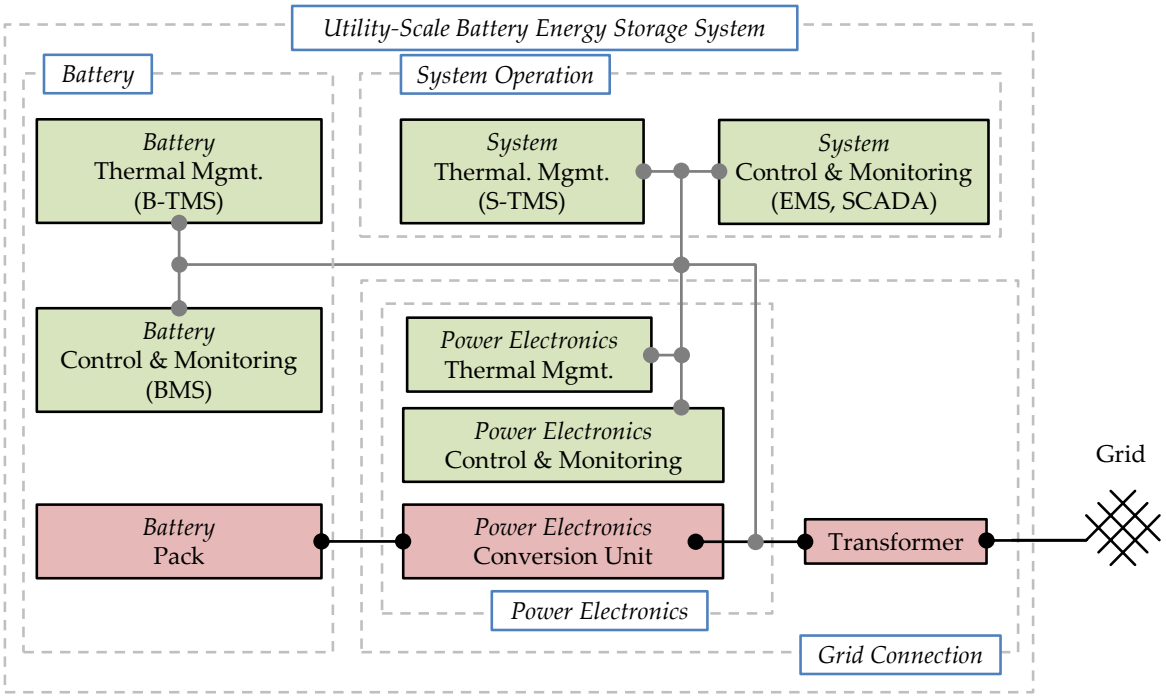

Figure 2.16: Overview to functional blocks of a utility-scale BESS. Grey lines indicate auxiliary power supply, black lines indicate main power flows. Reproduced from [5].

All relevant power flows in the BESS should be measured to quantify the system efficiency. If possible, power consumptions should be instrumented individually, e.g. for the Thermal Management System (TMS) separately the power consumption of the Battery Thermal Management System (B-TMS) and the System Thermal Management System (S-TMS). However, power flows can also be grouped to measure more conveniently. Further typical grouped power consumptions are the Energy Management System (EMS), Supervisory Control and Data Acquisition (SCADA), and the Battery Management System (BMS).

Energy flow measurements require large numbers of high-frequency measurements of main power flows to resolve fast transitions in power. The required frequency for the measurements depends on the dynamics of the system power, e.g. how fast the system power changes typically, and should be validated through a comparison of the results to cumulated energy measurements. The frequency is limited trough the amount of data resulting from high-frequency measurements over long periods of time and through the maximum frequency of the measurement equipment.

A derivation of the presented measurement procedure is used in Chapter 5 for the study of the commercial Second-Life system in its application.

2.3.6 Battery degradation analysis and modeling

For reliable lifetime predictions, battery degradation models are necessary. Different modelling approaches exist, which vary in terms of input parameters, computational expense and accuracy. Physicochemical models are based on an extensive set of parameters, computationally costly and require experimental parameterization of degradation rates [26, 55, 56]. Purely empirical models can be parameterized without knowledge of the cell setup through testing. Several purely empirical models capture calendar aging [57–59] or cycle aging [60, 61] separately. Through superposition, some empirical model approaches combine calendar and cycle aging [62–65].
The purely empirically based models so far lump multiple degradation effects into single functions. For an improved understanding of cell degradation, model development should aim for a separation of the degradation mechanisms wherever possible. E.g. for cycle aging, Waldmann et al. reported a transition of dominating aging mechanisms at 25 °C [66]. The aging for temperatures above 25 °C was attributed to the Solid Electrolyte Interphase (SEI) growth and cathode degradation, while below 25 °C the aging was attributed to lithium plating. The respective mechanisms can then be modeled through functions that are suitable for the degradation driving factors. In this work, a comprehensive semi-empirical capacity loss model for lithium-ion cells is introduced. Various capacity loss mechanisms for calendar and cycle aging are captured separately in an empirical, yet physically supported approach.

The semi-empirical models in this work still require experimental data for parametrization. The flow diagram of an experimental battery lifetime study starting from Begin of Life (BOL) (new cell) to End of Life (EOL) is shown in Figure 2.17.
At the begin of the experiment, each new cell is tested in a Reference Performance Test (RPT) at 25 °C to measure impedance and capacity. After the RPT, cells are subjected to the test conditions, i.e. various cycle tests or storage tests, for which the storage SOC has to be set. Regular RPT are performed at 25 °C to allow for comparison between different test conditions. The first RPT after begin of testing is performed after one week. Afterward, the RPT frequency is increased with increased duration of the testing for cells.
The procedure of the RPT is shown in Figure 2.18 through current and voltage measurements. The RPT consists of two capacity measurement cycles and 10 s discharge/charge pulses tests for impedance characterization. To accurately determine cell capacity regardless of impedance increases, two full charge-discharge Constant Current (CC)-Constant Voltage (CV) cycles are conducted for measuring the cell capacity (CC rate 1 C, current cut-off rate C/50), after an initial CC-CV discharge. For cell impedance, 10 s current pulses and Electrical Impedance Spectroscopy (EIS) tests are conducted, both at $SOC = 50\,\%$, after a relaxation time of 1 h and 12 h respectively.

If a cell reaches the EOL criteria of a SOH of 80 %, testing is stopped [62, 67, 68].

The experiments revealed the capacity loss to be the primary EOL criterion for all cells under test, e.g. CC cycling at ambient temperature of 45 °C with 1 C showed a capacity loss of 12 % but only a moderate increase in the 10 s pulse resistance of 4 % after 2800 Full Equivalent Cycles (FEC) (1 FEC = 6 Ah throughput). Therefore, the focus of this work is the capacity loss of the cells, for which the methods and exemplary results are presented in the following.

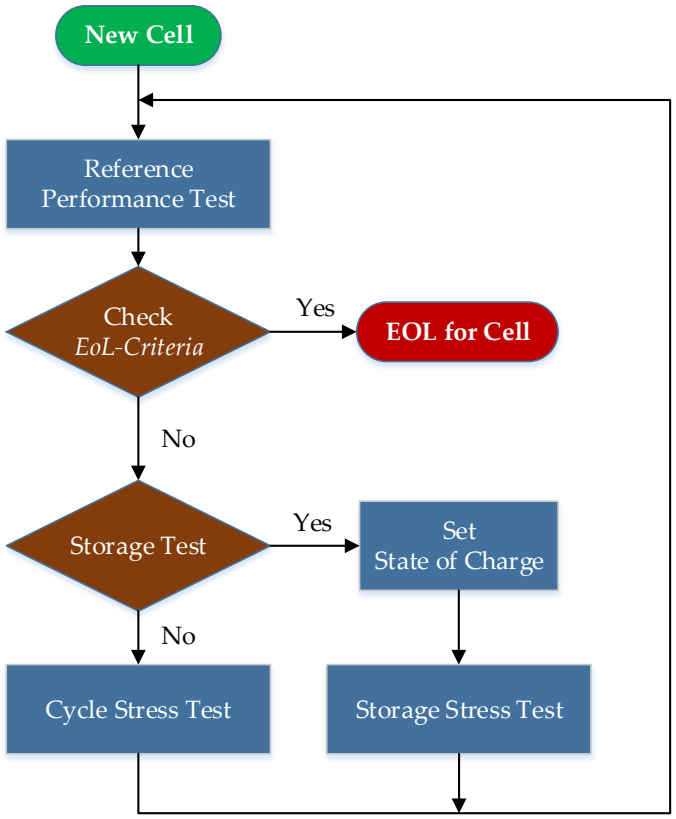

Figure 2.17: Flow diagram of an experimental battery aging experiment from BOL to EOL. Figure based on [69].

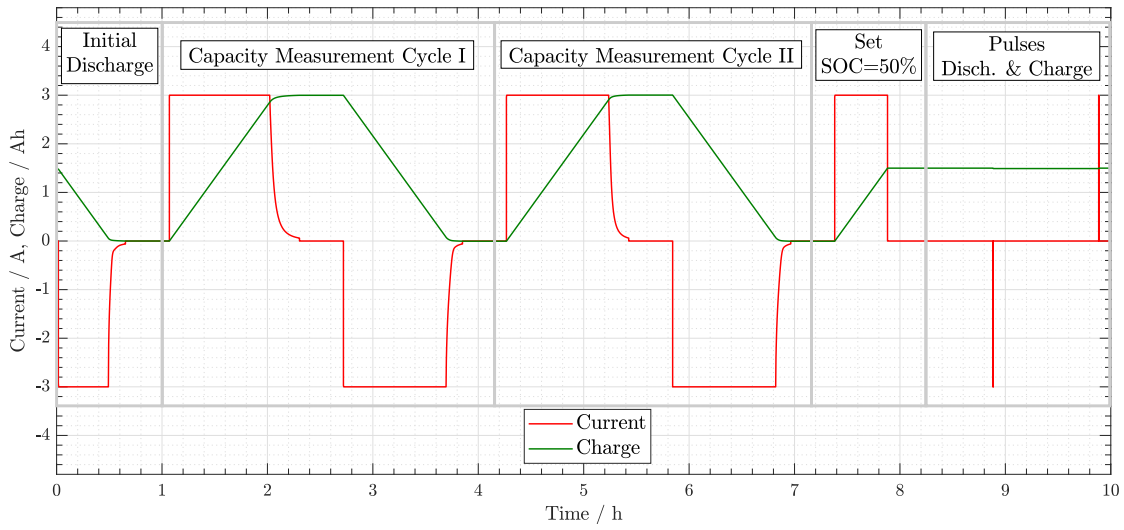

Figure 2.18: Current and voltage measurements of a RPT consisting of two capacity measurement cycles and 10 s discharge/charge pulses tests for impedance characterization. Figure based on [69].

The experimentally measured capacity loss of the cell, $Q_{\mathrm{Loss},i}$ in the RPT numbered i is calculated by averaging over two subsequent cycles in the RPT: $Q_{\mathrm{Disch},i,1}$ and $Q_{\mathrm{Disch},i,2}$. As a reference, the first RPT of the cell before the tests, $Q_{\mathrm{Disch},0}$ is used.

$$Q_{\mathrm{Loss},i} = Q_{\mathrm{Disch},0} - (Q_{\mathrm{Disch},i,1} + Q_{\mathrm{Disch},i,2})/2 \tag{2.24}$$

For better visualization though, the capacity loss in this work is not given through the value for the actual capacity (Unit: Ah), but normalized to the original cell capacity in the first RPT before the tests, $Q_{\mathrm{Disch},0}$.

Standard cycle and storage tests are used for degradation analysis and parametrization of degradation models. For the model validation in application-oriented settings, a dynamic profile for application in a residential PV-BESS in Germany is additionally tested. The profile data was provided by the Fraunhofer Institute for Solar Energy Systems from Project *ESPEN* and scaled to the nominal cell capacity [70]. Figure 2.19 shows the battery current profile.

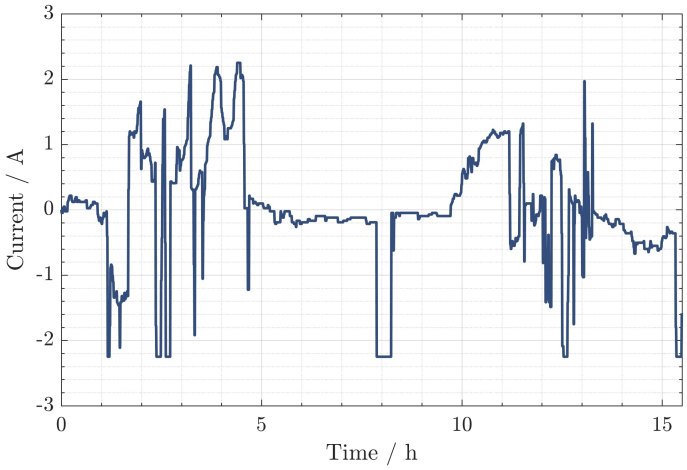

Figure 2.19: Current profile for validation cycle tests representing a residential PV-BESS application of the cell. Current direction for charging is positive. Figure reproduced from [14].

The profile is defined as the operation of a representative summer day and a representative winter day. Rest durations are excluded for acceleration of the test results, leading to a profile duration of 15.5 h. As the profile defines the battery current and features a coulombic efficiency of 100 %, the profile can be repeated permanently. However, due to measurement errors of the battery current, a drift of the SOC may occur and the experiment has to be restarted from a defined SOC. In this work the SOC is reset at every RPT.

Table 2.3 gives further parameters of the profile. All parameters relative to the cell capacity (Charge throughput, average/max. C-Rate, SOC values) are calculated with the nominal capacity of the cells (3 Ah).

Table 2.3: Parameters of the validation battery current profile representing a residential PV-BESS application of the cell. Table reproduced from [14].

Parameter	Value	Parameter	Value
Profile Duration	15.5 h	Time Resolution	60 s
Charge Throughput per Cycle relative to Nominal Cell Capacity (Charge)	1.56	Charge Throughput per Cycle relative to Nominal Cell Capacity (Discharge)	1.56
Time-averaged C-Rate (Charge)	+0.24C	Time-averaged C-Rate (Discharge)	-0.17C
Max. C-Rate (Charge)	+0.75C	Max. C-Rate (Discharge)	-0.75C
Start SOC of Profile	28 %	Average SOC	51.4 %
Min. SOC	5.4 %	Max. SOC	80 %

Exemplary results which are derived from the storage tests are shown in Figure 2.20 through the capacity loss evaluation over time. Data points represent the measurements taken in the RPT. A trend line is fitted for each test condition and shown for visualization purposes.

Figure 2.20a shows the influence of temperature through a comparison of test points for temperatures ranging from 10 °C to 55 °C, with a constant $SOC = 100\,\%$. Figure 2.20b shows the influence of the SOC during storage through a comparison of test points for SOC from 0 % to 100 %, with constant temperature $SOC = 45\,°C$.

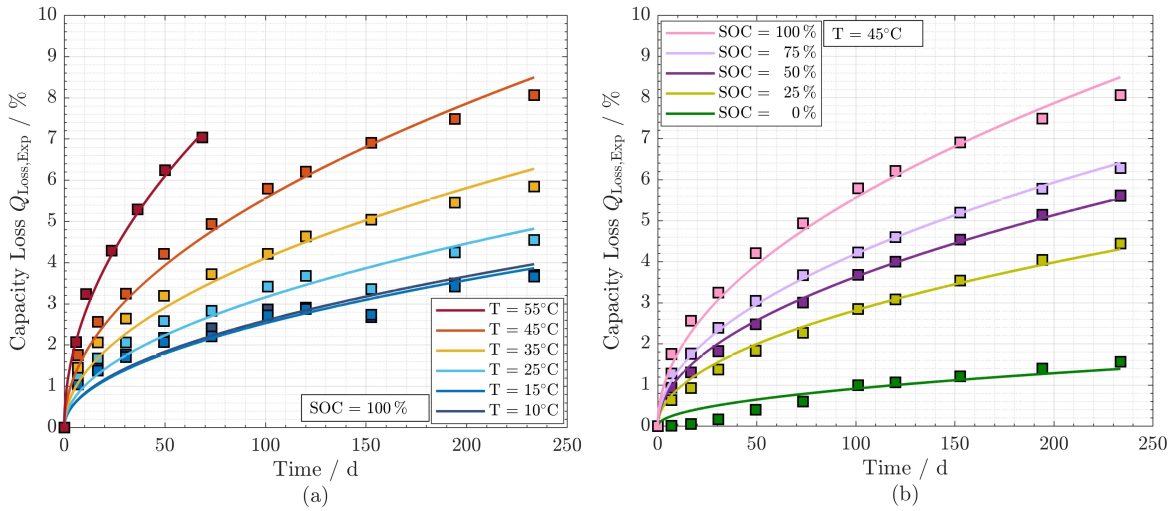

Figure 2.20: Capacity loss evaluation during storage tests: a) Influence of storage temperature at $SOC = 100\,\%$, b) Influence of SOC at $T = 45\,°C$. Trend lines are fitted for each test condition for visualization. Figure reproduced from [14].

Figure 2.21 shows the results for the CC cycle tests at 1 C without CV-phase for various ambient temperatures over FEC of cycling. Low temperatures ($T = 25\,°C$ and lower) are shown on the left hand side, high temperatures ($T = 25\,°C$ and higher) on the right hand side. The temperature influence on the cycle-induced degradation motivates a dedicated modelling of the temperature dependence.

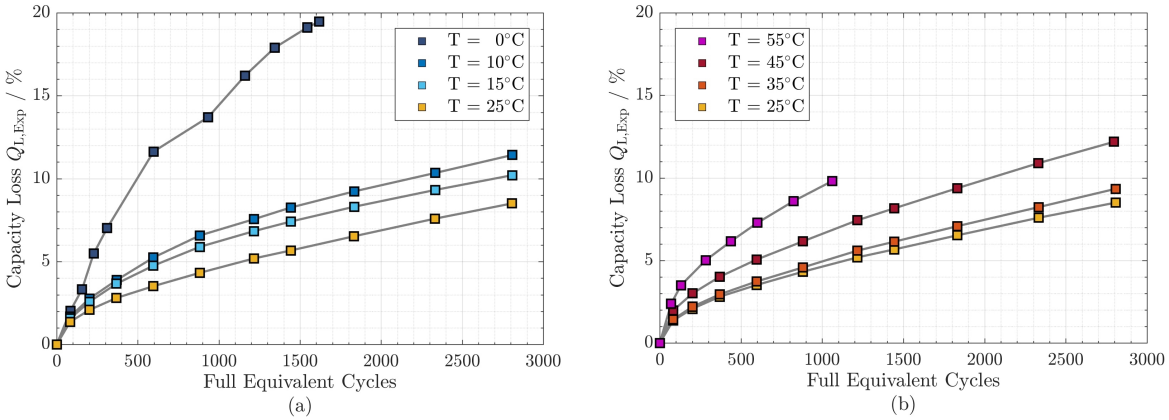

Figure 2.21: Capacity loss evaluation during CC cycle tests at 1 C, with focus on the temperature effect: a) Experimental capacity loss measurements at low temperatures (0 °C to 25 °C), b) Experimental capacity loss measurements at high temperatures (25 °C to 55 °C). Figure adapted from [14].

Figure 2.22 shows the cycle-induced degradation for the CC cycle tests with/without CV-phase at the end of charging for various C-rates over FEC of cycling. Low temperature ($T = 0\,°C$) is shown on the left hand side, high temperature ($T = 55\,°C$) on the right hand side.
Charging the cells to a high SOC through the CV-phase at low temperatures has a strong impact on degradation, which increases with higher current rate and thus also motivates a dedicated modelling approach.

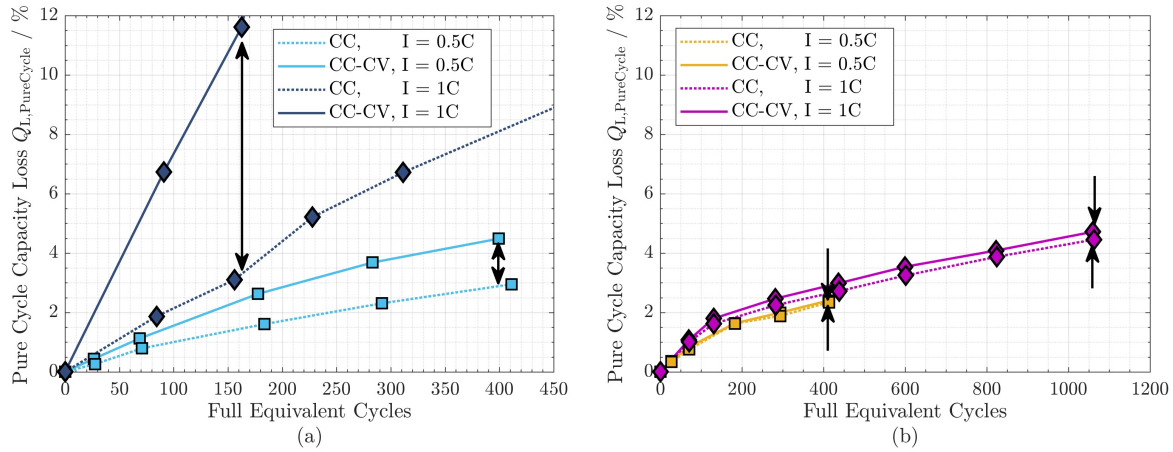

Figure 2.22: Influence of high SOC operation through CV-Phase at end of charge: a) $T = 0\,°C$, b) $T = 55\,°C$. Arrows are added for visualization of strong/weak variation at low/high temperatures. Figure reproduced from [14].

Towards battery degradation modeling, the capacity loss resulting from calendar aging effects $Q_{L,Cal}$ and cycle-induced aging effects $Q_{L,Cyc}$ can be evaluated through superposition [62]:

$$Q_{Loss} = Q_{L,Cal} + Q_{L,Cyc} \tag{2.25}$$

As different cycle aging mechanisms are identified in the experimental results, three sub-mechanisms are defined:

- High Temperature $Q_{\mathrm{L,Cyc,High\ T}}$
- Low Temperature $Q_{\mathrm{L,Cyc,Low\ T}}$
- Low Temperature, High SOC $Q_{\mathrm{L,Cyc,LowT\ HighSOC}}$

Again they can be evaluated through superposition, resulting in the overall model:

$$Q_{\mathrm{Loss}} = Q_{\mathrm{L,Cal}} + Q_{\mathrm{L,Cyc,High\,T}} + Q_{\mathrm{L,Cyc,Low\,T}} + Q_{\mathrm{L,Cyc,Low\,T\,HighSOC}} \tag{2.26}$$

The presented model is then fitted to experimental data with various input parameters, i.e. time, battery current, SOC, temperature, and charge throughput.

3 Energy efficiency evaluation of a stationary lithium-ion battery container storage system via electro-thermal modeling and detailed component analysis

This section introduces the paper *Energy efficiency evaluation of a stationary lithium-ion battery container storage system via electro-thermal modeling and detailed component analysis* and is based on the paper without further reference.

Section 2.1 previously introduced system metrics for efficiency, which are now quantified for grid application scenarios for the reference system *Energy Neighbor*, which has been described in Section 2.2.1.

In this paper, a system model of a stationary lithium-ion BESS is created for a use-case specific analysis of the system energy efficiency. The model offers a holistic approach by including conversion losses and auxiliary power consumption. Fundamentals for the model development have been briefly described in Section 2.3.1-2.3.4. The model is parameterized based on the system *Energy Neighbor*.

Component models for the battery, PE, thermal management, and the control and monitoring components are developed and coupled. The key loss mechanisms are identified and modeled. In total, 18 loss mechanisms are analyzed in detail. Both battery and PE loss calculation are validated against experimental data. The thermal management model features the calculation of the power consumption related to the battery, the PE, and the overall system. For the system model, a thermal resistance network is coupled with ambient data. All relevant control and monitoring components are included in the calculation of system power consumption.
The model is then evaluated using generic profiles which vary in terms of system power, operation time and average SOC. Results show that low power operation ($< 10\,\%$ of system power) should be avoided due to relatively high losses in the PE. A high temporal utilization of the system is only beneficial if it leads to an increased charge throughput. The energy efficiency is shown to be relatively stable over the middle SOC range. Peak conversion energy efficiency is shown to be $87\,\%$ under constant cycling with partial load at a charge-based system utilization of $41\,\%$. At full nominal power and constant cycling, conversion energy efficiency is $85\,\%$. Total system energy efficiency including auxiliary energy consumption reaches its peak value of $81\,\%$ at full nominal power and constant cycling, as auxiliary energy consumption is smallest relative to the high energy throughput of the system in this case.
The exemplary load profiles derived from the grid applications PCR, Secondary Control Reserve (SCR) and PV-BESS are evaluated with regards to the resulting performance. The simulations of grid applications confirm the results of the generic profiles. Conversion round-trip efficiency is in the range of $70\,\%$ to $80\,\%$ for all scenarios. Overall system efficiency, which also considers system power consumption, is 8 to 13 percentage points lower for PCR and the PV-BESS application. However, for SCR, the total round-trip efficiency is found to be extremely low at $23\,\%$, and thus 47 percentage points lower due to the low charge throughput.

Author contribution The system model was initiated, developed and evaluated by the author of this thesis. The paper draft was also written by the author of this thesis.
Nick Becker worked on the PE model in his master's thesis. The isothermal calorimetry measurements were conducted by Aron Saxon at the National Renewable Energy Laboratory (Colorado, USA), which the author of this thesis visited through a research exchange.
The results have also been presented at the conferences *Kraftwerk Batterie 2016* and *Batterieforum Deutschland 2017* by the author of this thesis.

Energy efficiency evaluation of a stationary lithium-ion battery container storage system via electro-thermal modeling and detailed component analysis

Michael Schimpe, Maik Naumann, Nam Truong, Holger C. Hesse, Shriram Santhanagopalan, Aron Saxon, Andreas Jossen

Applied Energy 210, pp. 211–229, 2018

Permanent weblink:
https://doi.org/10.1016/j.apenergy.2017.10.129

Reproduced by permission of Elsevier

Applied Energy 210 (2018) 211–229

Contents lists available at ScienceDirect

Applied Energy

journal homepage: www.elsevier.com/locate/apenergy

Energy efficiency evaluation of a stationary lithium-ion battery container storage system via electro-thermal modeling and detailed component analysis

Michael Schimpe[a,*], Maik Naumann[a], Nam Truong[a], Holger C. Hesse[a], Shriram Santhanagopalan[b], Aron Saxon[b], Andreas Jossen[a]

[a] Technical University of Munich (TUM), Institute for Electrical Energy Storage Technology (EES), Arcisstr. 21, 80333 Munich, Germany
[b] National Renewable Energy Laboratory, Transportation and Hydrogen Systems Center, Golden, CO 80401, USA

HIGHLIGHTS

- A holistic model for stationary battery systems is developed.
- In total 18 energy loss mechanisms in the system are analyzed and modelled.
- The model is parametrized based on an existing prototype battery system.
- Different grid applications are simulated for estimation of real-world performance.
- A detailed analysis of the battery system energy efficiency is given.

ARTICLE INFO

Keywords:
Energy efficiency
Battery storage system
Lithium-ion
Container system
Energy loss mechanism analysis
Thermal network model

ABSTRACT

Energy efficiency is a key performance indicator for battery storage systems. A detailed electro-thermal model of a stationary lithium-ion battery system is developed and an evaluation of its energy efficiency is conducted. The model offers a holistic approach to calculating conversion losses and auxiliary power consumption. Sub-models for battery rack, power electronics, thermal management as well as the control and monitoring components are developed and coupled to a comprehensive model. The simulation is parametrized based on a prototype 192 kWh system using lithium iron phosphate batteries connected to the low voltage grid. The key loss mechanisms are identified, thoroughly analyzed and modeled. Generic profiles featuring various system operation modes are evaluated to show the characteristics of stationary battery systems. Typically the losses in the power electronics outweigh the losses in the battery at low power operating points. The auxiliary power consumption dominates for low system utilization rates. For estimation of real-world performance, the grid applications Primary Control Reserve, Secondary Control Reserve and the storage of surplus photovoltaic power are evaluated. Conversion round-trip efficiency is in the range of 70–80%. Overall system efficiency, which also considers system power consumption, is 8–13 percentage points lower for Primary Control Reserve and the photovoltaic-battery application. However, for Secondary Control Reserve, the total round-trip efficiency is found to be extremely low at 23% due to the low energy throughput of this application type.

1. Introduction

The majority of human-induced carbon dioxide emissions come from fossil fuels that today still provide 80% of global primary energy demand [1]. Climate change requires a transition to a low-carbon energy supply, which often includes the intensified use of renewable energy sources such as wind and solar [2]. As wind and solar are volatile energy sources, the issue of decoupled production and demand load arises. Flexibility options such as variable generation, demand-side management, and grid expansion can support the reduction of unbalanced production and load. For a stable energy supply with high shares of volatile renewable energy sources, energy storage at large-scales for short and long-term is a technically possible option [3–5].

Recently, lithium-ion batteries have achieved significant cost

* Corresponding author.
E-mail address: michael.schimpe@tum.de (M. Schimpe).
URL: http://www.ees.ei.tum.de/en/ (M. Schimpe).

https://doi.org/10.1016/j.apenergy.2017.10.129
Received 27 June 2017; Received in revised form 17 October 2017; Accepted 31 October 2017
0306-2619/ © 2017 Elsevier Ltd. All rights reserved.

Nomenclature

Abbreviations

AC	alternating current
AirC	air conditioning
C & M	control & monitoring
DC	direct current
IGBT	insulated-gate bipolar transistor
OCV	open circuit voltage
PCR	primary control reserve
PE	power electronics
PV-B	photovoltaic-battery
RMS	root mean square
SCR	secondary control reserve
SOC	state of charge

Parameters & variables

ΔU	battery overvoltages
ΔT	temperature difference in thermal network
$\eta_{\text{Conversion}}$	round-trip conversion efficiency
η_{Total}	round-trip total efficiency
ϕ_i	relative losses of mechanism i
τ_t	temporal utilization of system
τ_Q	charge-based utilization of system
A	interface area in thermal network
$c_{p,\text{Air}}$	specific heat capacity of air
$c_{p,\text{Cell}}$	specific heat capacity of cell
C_{Nom}	nominal capacity of battery
$C_{\text{th,Block}}$	heat capacity of cell block
$C_{\text{th,Cell}}$	heat capacity of cell
COP	coefficient of performance for cooling/heating
$E_{\text{Charge,AC}}$	total system energy input (grid-side)
$E_{\text{Discharge,AC}}$	total system energy output (grid-side)
	energy loss of mechanism i
E_{Nom}	nominal energy of battery
E_{Off}	turn-off energy of IGBT
E_{On}	turn-on energy of IGBT
E_{Rec}	recovery energy of diode
$E_{\text{System Consumption}}$	total system energy consumption for auxiliary components
f_{Grid}	grid frequency
f_{Switch}	switching frequency
i_{C}	collector current
i_{CE}	collector-emitter current
i_{F}	forward current
i_{Grid}	grid-side current of LCL-filter
I	battery current
$\dot{m}_{Air,Module}$	air mass flow rate in the battery module
$m_{\text{Air,PE}}$	air mass in power electronics zone
$m_{\text{air,Sys}}$	air mass in battery zone
m_{Cell}	battery cell mass
$m_{\text{Connector,Block}}$	battery cell block connector mass
P_{AirC}	power consumption air conditioning
$P_{\text{C\&M,Batt}}$	power consumption C & M battery
$P_{\text{C\&M,PE}}$	power consumption C & M power electronics
$P_{\text{C\&M,Sys}}$	power consumption C & M system
$P_{\text{Fan,Nom}}$	nominal power fan
$\overline{P}_{\text{Loss,Block}}$	average experimental power losses in cell block
$P_{\text{Loss,Diode,Cond}}$	conduction losses in diode
$P_{\text{Loss,Diode,Switch}}$	switching losses in diode
$P_{\text{Loss,IGBT,Cond}}$	conduction losses in IGBT
$P_{\text{Loss,IGBT,Switch}}$	switching losses in IGBT
$P_{\text{Loss,Interface}}$	losses in interface module
$P_{\text{Loss,LCL,Cond}}$	conduction losses in LCL-filter
$P_{\text{Loss,LCL,Core}}$	core losses in LCL-filter
$P_{\text{Loss,PE}}$	conversion losses power electronics
$\dot{Q}_{\text{AirC}}$	heat flow of air conditioning unit into ventilation duct
$\dot{Q}_{\text{Batt-Sys}}$	(overall) heat input from battery rack to battery zone
$\dot{Q}_{\text{Block}}$	heat input from cell operation into cell block
$\dot{Q}_{\text{Block-AmbMod}}$	heat exchange of cell block to air in battery module
$\dot{Q}_{\text{Cell}}$	heat input from cell operation into cell
$\dot{Q}_{\text{Cond,PE-Sys}}$	conductive heat flow from power electronics zone to battery zone
$\dot{Q}_{\text{Cond,AmbOutd-Sys}}$	conductive heat flow from ambient outdoor to battery zone
$\dot{Q}_{\text{Conv,AmbOutd-Duct}}$	convective heat flow from ambient outdoor to ventilation duct
$\dot{Q}_{\text{Conv,Duct-Batt}}$	convective heat flow from ventilation duct to battery rack
$\dot{Q}_{\text{Conv,Duct-PE}}$	convective heat flow from ventilation duct to PE zone
$\dot{Q}_{\text{Conv,Duct-Sys}}$	convective heat flow directly from ventilation duct to battery zone
$\dot{Q}_{\text{Conv,PE-Sys}}$	convective heat flow from PE zone to battery zone
$\dot{Q}_{\text{Conv,PE-AmbOutd}}$	convective heat flow from PE zone to ambient outdoor
$\dot{Q}_{\text{Conv,Sys-AmbOutd}}$	convective heat flow from battery zone to ambient outdoor
$\dot{Q}_{\text{Conv,Sys-Duct}}$	convective heat flow from battery zone to ventilation duct
$Q_{\text{Throughput}}$	charge-throughput of battery
$Q_{\text{Throughput,theoretical max.}}$	theoretical maximum charge-throughput of battery
R_{i}	battery resistance cell model
R_{th}	thermal heat transfer resistance
$R_{\text{th,Block-AmbientMod}}$	thermal heat transfer resistance cell block to ambient air in module
R_{Contact}	electrical contact resistance
$R_{\text{DC10s,Exp}}$	experimental battery resistance derived from 10 s pulse
$R_{\text{DC10s,Scaled}}$	calculated battery resistance derived from 10 s pulse
$R_{\text{LCL,total}}$	total inductor resistance of LCL-filter
s	battery self-discharge rate
S	battery entropy
SOC	state of charge
$t_{\text{Operation}}$	total time of system in operation
$t_{\text{Simulation}}$	total duration of simulation
$T_{\text{Air,Duct}}$	air temperature ventilation duct
$T_{\text{Air,PE}}$	air temperature PE zone
$T_{\text{air,Sys}}$	air temperature battery zone
$T_{\text{AmbientMod,Row}k}$	air temperature in module in row k
T_{Block}	cell block temperature
T_{J}	junction temperature
T_{Ref}	reference temperature battery model
U_{CE}	collector-emitter voltage in IGBT
U_{DC}	blocking voltage in IGBT
U_{F}	forward voltage diode
U_{Grid}	grid voltage
U_{Hys}	battery hysteresis voltage
U_{Max}	maximum battery voltage
U_{Min}	minimum battery voltage
U_{Nom}	nominal battery voltage
U_{OCV}	open circuit battery voltage
$U_{\text{OCV,Ref}}$	open circuit battery voltage at reference temperature
U_{T}	terminal battery voltage
$\dot{V}_{\text{Fan}}$	fan volumetric flow rate
$V_{\text{Fan,Nom}}$	nominal fan volumetric flow rate

reductions as well as increases in power and lifetime [6]. Thus, they are now being increasingly installed in stationary battery systems. System sizes range from small (under 20 kWh of nominal energy), for residential storage systems which store excess electricity from photovoltaic systems, and medium (under 1 MWh), for local grid applications [7], to large (over 1 MWh), which are often used for grid ancillary services [8,9]. Lately, more and more systems of intermediate and large sizes are being built and aid the transition to a renewable-based energy system [10].

To evaluate a battery system for a specific application scenario, simulations can be used to calculate the system's expected performance and efficiency. Holistic simulation of a battery storage system is required to capture its overall performance, without neglecting key-dependencies. Thereby the inter-dependencies of the components, i.e. electrical coupling or thermal interconnections can be evaluated in a simultaneous approach, which can reveal that effects reinforce or mitigate each other.

A key result of a holistic system simulation is the energy efficiency, which can only accurately be evaluated if all relevant energy loss mechanisms are covered in the simulation. Losses of battery storage systems include conversion losses and the auxiliary system power consumption. An accurate model should, therefore, include both mechanisms. The conversion losses are related to the conversion and storage of energy in the power electronics and battery respectively, whereas the auxiliary power consumption is the additionally necessary power for the operation of the system, namely thermal management as well as the control and monitoring components.

This work aims to create a holistic simulation model to perform an accurate energy efficiency analysis of stationary lithium-ion battery systems. A detailed breakdown of the energy losses is given. As the model parameters derived and used herein are based on an actual battery system and the evaluated application scenarios are typical battery system applications, the simulations give realistic results for the performance of lithium-ion battery systems.

The remainder of this contribution is structured as follows: Section 1.1 gives a literature review on system simulation of battery systems. The novelty and specific contributions of this study are presented and compared to the literature review in Section 1.2. Section 1.3 describes the battery system which will be used for this work as a reference case. In Section 2, the system model, the component models, and the parametrization through experiments and literature are described. Results of generic and application-oriented simulations are given and discussed in Section 3. Section 4 concludes the key findings of the component and system modeling and Section 5 gives an outlook on the implications for the design and operation of battery systems.

1.1. Literature

Existing stationary battery system simulations can be categorized into the following types: *Cell focused*, *System operation focused* and *Holistic approaches*.

Cell focused approaches mostly consider a system as a scaled up single cell and partially combine the cell model with literature-based efficiencies for the power electronics [11–13]. The emphasis on the cell is mostly motivated with the bigger uncertainties for lithium-ion cell operation in comparison to the power electronics and the large share of system costs for the battery. The studies, therefore, neglect most other components in the system and results are limited to the battery itself. *System operation focused approaches* evaluate specific battery use cases regarding sizing, suitability, economics [14–19] or operational strategy [20–26], mostly using literature-based values for overall system efficiency. Such approaches are sufficient for the respective goal, i.e. system sizing but cannot differentiate between different types of battery cells, system setups and do not include the auxiliary power consumption of the system. As constant literature based efficiency values are often used, the models do not enable an accurate calculation or a breakdown of the energy losses.

Holistic approaches evaluate the technical inter-dependencies of multiple system components and can, therefore, give a detailed insight into system performance [27–38] which will be discussed in the following:

Patsios et al. [27] evaluated a storage system simulation in a local grid application, which encompassed a single-particle cell model, a discrete time power electronics model based on a single IGBT, and further included load-free transformer losses. The battery model was reduced to a single-cell simulation and validated against experimental data. The system model was implemented in a grid simulation to evaluate the application scenario *transformer stress relief*. Results showed that a higher time-averaged state of charge increased the rate of battery degradation, whereas a shift to a lower state of charge decreased the energy efficiency. They attributed most of the losses to the power electronics.

Neubauer et al. [28,29] analyzed the thermal behavior of stationary battery systems based on representative thermal parameters. They included weather data representing different climate zones. The thermal system model reduces the battery as well as the complete thermal mass of the system to a lumped thermal capacity. The simulation considers cooling via active air conditioning only. The simulations showed that solar effects can increase battery degradation in warm and sunny climates when the ambient climate has an impact on the system temperature through insufficient thermal management. They also showed that for the application scenario *Peak Shaving*, constraining inverter power could pose an economic alternative to control the system temperature with minimal impact on the performance of the application.

Magnor et al. [30] simulated a residential photovoltaic battery system with a focus on the model dynamics. The battery model was based on equivalent circuit modeling. For the power electronics, they simulated controller dynamics and the converter dynamic to evaluate the transient behavior. Simulations showed that neglecting the high-frequency current components induced by the action of converter switches leads to an underestimation of the effective current. However, due to the low pass filter characteristic of the battery impedance, this only leads to minor errors regarding power losses. Furthermore, the controller dynamics of the power electronics also showed little impact due to the fast response behavior. They showed that neglecting the switching operation of the converter's IGBTs strongly improved the simulation speed and was recommended.

Tjaden et al. developed an open-source simulation model for residential small-scale photovoltaic battery storage systems [31,32]. Battery and power electronics losses are modeled based on full system characterization tests. In a subsequent work, the influence of system location within Germany on the photovoltaic power production and of the user behavior on the load profile was evaluated [33]. In [34] they compared various indicators for performance, which included energy loss mechanisms due to conversion and system standby power consumption. They further analyzed the influence of inverter dimensioning, non-ideal power flow control and the energy management system. In their contributions, the focus is on general system performance and power flow for an optimal operation in terms of economics, grid independence and photovoltaic power self-consumption.

Gatta et al. [35] simulated a lithium-ion battery storage system in order to evaluate the overall system efficiency by including the power consumption of the battery management system and of the thermal management. The power consumption of the thermal management was calculated by applying a coefficient of performance directly to the internal losses of the battery. The power electronics losses were not further described. For thermal system model, the cabinet temperature was calculated as a lumped thermal capacitance. Results for the application scenarios *load leveling* and *frequency control* showed that auxiliary consumptions can greatly decrease overall efficiency. The total energy losses increase with the battery utilization rate but overall efficiency nonetheless increases. The auxiliary consumption increases with higher

utilization. In [36], they applied the model of [35] to the application scenario *frequency control*. Results showed that allowing higher current rates in the control strategy leads to higher charge throughput, higher overall efficiency, and increased mean cell temperature. Values varied from 60% to 75% for the overall system efficiency.

Rydh et al. [37,38] described a method for the calculation of conversion and overall efficiency of battery systems by including the effect of the air conditioning system, different battery temperatures, and inverter losses. Constant values with parameter variation for sensitivity analysis were used and resulted in a maximum overall efficiency of 80% for lithium-ion battery systems.

The literature shows the importance of considering all system components in a coupled model and therefore the necessity of a more comprehensive approach.

1.2. Paper highlights

Our new contribution focusses on a breakdown of the energy losses through a detailed system simulation including all key components relevant to the system energy efficiency. No existing study includes all the relevant components in single simulation approach and evaluates their interdependencies. The most holistic approach by Gatta et al. [35] includes only the power consumption of the battery management system and features only a zero-dimensional thermal system model. For the first time, we present a model with high detail and accuracy through experimental validation. The previously described literature on system simulations of battery systems did not include an energy efficiency oriented validation of the battery or the power electronics model. The model is described in detail and can be used for different components, system setups or application scenarios. We base our work on an existing prototype battery system for realistic parametrization and validation purposes. The discussed studies are mostly based on theoretical systems and literature assumptions for the system setup. Gatta et al. [36] describe the evaluation of 1 MW test system in their work, however, the system model does not include a representation of the setup, except the installed battery cell.

In detail, for the battery cell model, we use an advanced model featuring self-discharge, temperature-dependent characterization and validate its performance for energy efficiency calculation through combining electrical measurements and isothermal calorimetry data, which is a parametrization and validation depth of detail not identified in the existing literature. By including an electrical and thermal module and battery rack model, we are able to include the effects of scaling a single cell to a high voltage battery rack, which is a depth of detail for both parametrization and validation that is not found in the existing literature. The power electronics model enables a detailed breakdown of losses which goes beyond commonly measured efficiency values for the whole power electronics setup or a simple model considering a single IGBT without filter components. Power consumption for the thermal management is included for component cooling of the battery and power electronics unit as well as for the container system through active cooling/heating and ambient outdoor air. The existing studies typically neglect this system component or consolidate it strongly through a lumped thermal system mass without detailed thermal network calculations. The total auxiliary power consumption is accurately represented through a detailed component analysis of the system. No existing work is based on a detailed system analysis and thus provides the depth of detail of this analysis. Finally, we evaluate real-world grid applications and therefore can give realistic and application-oriented results. None of the known studies evaluate the system operation through a breakdown of the energy losses in general over the operating range of the system as well as in the mentioned application scenarios.

1.3. Reference prototype battery storage system

The simulation is parametrized based on a 192 kWh, 248 kW 20-foot container battery system, named the *Energy Neighbor*. The system was developed by the Technical University of Munich in the research project *EEBatt* [39] in cooperation with Varta Storage.

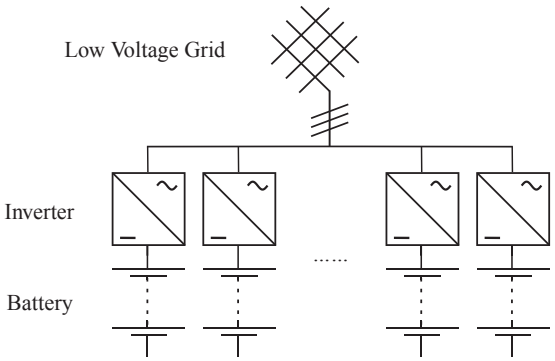

Fig. 1. Electrical system layout connecting the eight battery racks to the low voltage grid.

The system features eight battery racks which are each coupled to the low voltage grid via bidirectional power electronics establishing the conversion from alternating current (AC) to direct current (DC) based power flow. Fig. 1 shows the electrical layout of the battery system connecting the battery racks to the grid.

The battery management system uses dissipative balancing. For thermal management, the system features a two-zone climate system for separate and energy efficient temperature control of the battery racks and the power electronics, which are both air cooled. Fig. 2 shows the container system with the thermal management being highlighted.

Recently the system was installed in the German village Moosham in Bavaria [7,40] in the low voltage grid to enable local grid applications such as load reduction of the local transformer. It further serves as a test platform for various grid applications. As it has been developed as part of a research cooperation of industry and academia, it is up to date with current industry standards and at the same time enables the availability of the necessary information for a detailed system study.

2. Methodology

2.1. System overview and control

To evaluate the energy efficiency, all relevant energy loss mechanisms have to be quantified in the system model. An analysis of the system setup is conducted to include all relevant components. Fig. 3 shows the identified mechanisms, grouped in the respective categories which are also calculated in the system model. In total, 18 different types of loss mechanisms are defined for this study and will be explained in the respective sub-model sections.

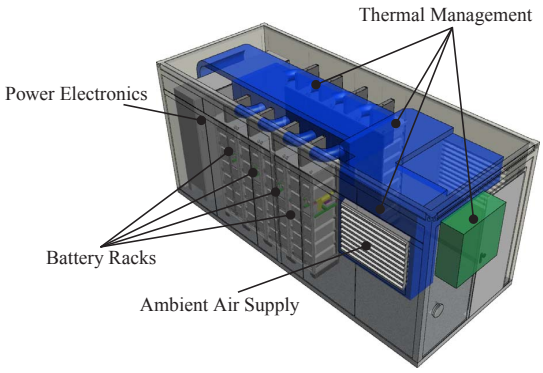

Fig. 2. Container storage system *Energy Neigbhor*. Picture from [39].

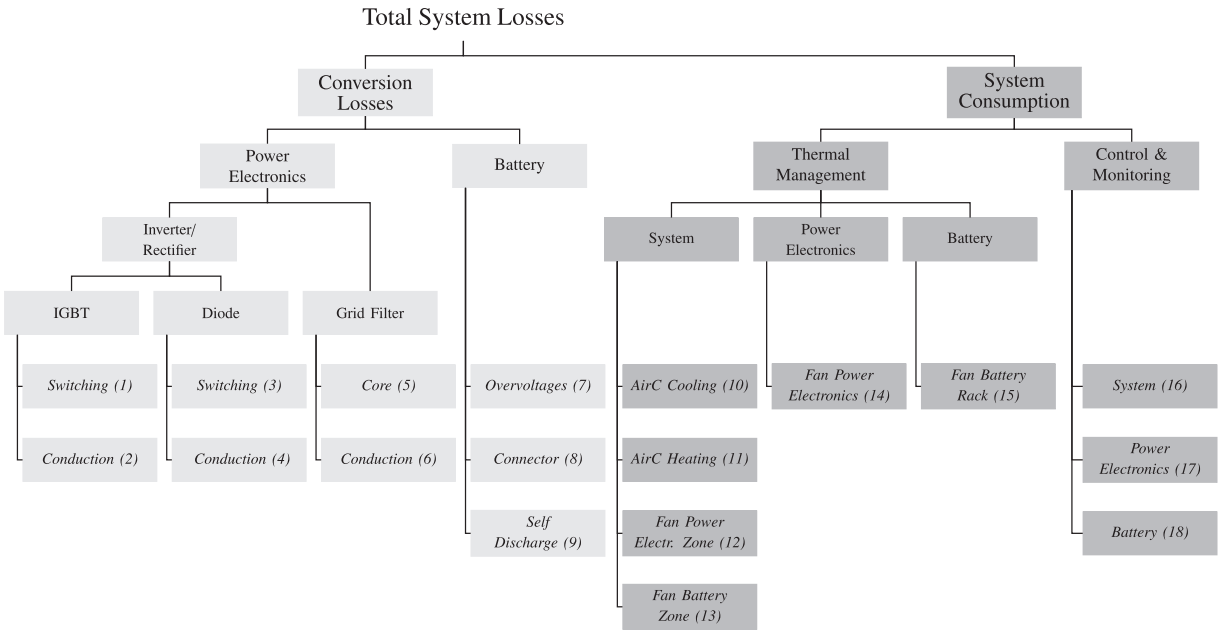

Fig. 3. Overview of the 18 energy loss mechanisms calculated in the system model.

The system model consists of four coupled component models, which are: *Battery*, *Power Electronics*, *Thermal Management* and *Control and Monitoring*. Input variables are the ambient outdoor temperature derived from weather data and the AC-side power request of the load profile. Fig. 4 shows the schematics of the system model which couples the input variables and the component models. In the component models for the *Battery* and *Power Electronics*, only the conversion losses are calculated, their power consumption related to thermal management or control electronics are covered in the respective separate models *Thermal Management* and *Control and Monitoring*.

We assume identical battery racks with evenly distributed power flow and reduce the simulation to a single rack.

The control for charging and discharging is derived from the AC-side power request of the load profile. After considering component model limits of the current maximum power states for the power electronics unit and the battery, system responses for DC and AC power are calculated. The power electronics units are turned off if no power is requested on the AC-side to reduce losses. In the following Sections

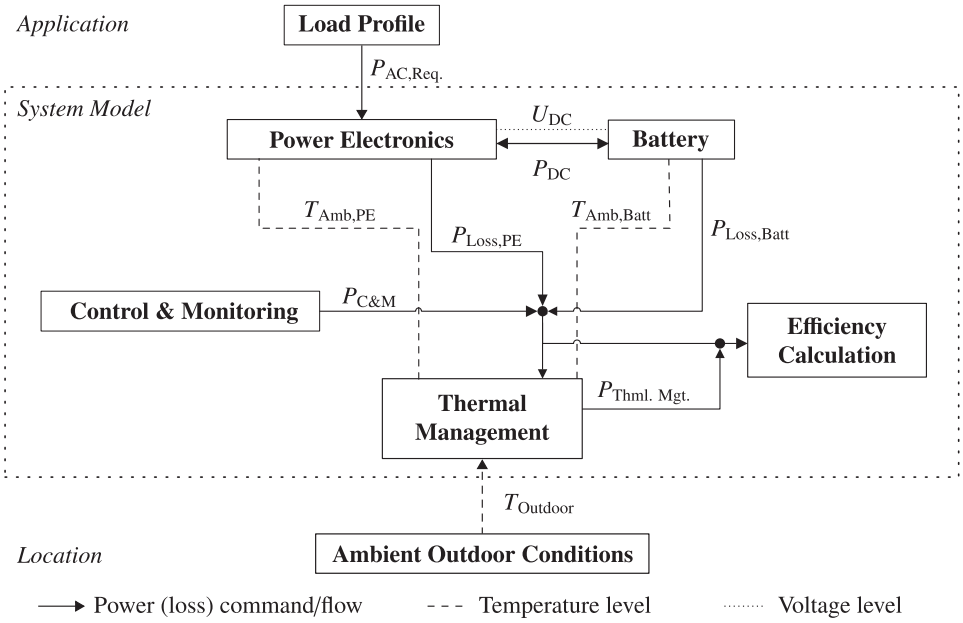

Fig. 4. System model overview: Schematics of component model coupling via temperature, voltage levels and power/heat flows.

Table 1
Battery parameters for battery cell, cell block, module and rack.

	U_{Nom}	C_{Nom}	E_{Nom}	U_{Min}	U_{Max}
Cell	3.2 V	3 Ah	9.6 Wh	2.0 V	3.6 V
Block	3.2 V	36 Ah	115 Wh	2.0 V	3.6 V
Module	51.2 V	36 Ah	1.8 kWh	32.0 V	57.6 V
Rack	665.6 V	36 Ah	24 kWh	416.0 V	748.8 V

2.2–2.5 the component setups and models are described. To compare different simulation results, various performance indicators are defined in Section 2.6.

2.2. Battery

The battery in the prototype system features eight identical battery racks which are each comprised of 13 battery modules connected in series; the battery modules each consist of 16 cell blocks connected in series, each cell block features 12 cylindrical cells connected in parallel.

The utilized 26650-format cell manufactured by Sony uses lithium iron phosphate and graphite for the electrodes. The cell is specified for a standard charge and discharge current rate of 1 C at room temperature. We define as 1 C as the maximum current rate in the simulations. Nominal voltage, capacity, and energy, as well as minimum and maximum voltages, are given in Table 1.

The battery model is based on a single-cell model, explained in Section 2.2.1, and scaled to the high-voltage rack through the implementation of a thermal rack model and resistances for cell connector and wiring, explained in Section 2.2.2.

2.2.1. Single-cell model

The single-cell model is an equivalent circuit model based on full-cell characterization. Terminal voltage U_T is calculated from the open circuit voltage (OCV) U_{OCV}, overvoltages ΔU across series resistance R_i and a cell hysteresis voltage U_{Hys}. Herein, we limit ourselves to a non-aged system, parameterize the simulation to a new battery cell and neglect further cell degradation effects. It is worth noting, that aging effects can increase cell resistance growth and capacity loss which can impair the system's energy efficiency in the long-term operation.

The open circuit voltage U_{OCV} at reference conditions of $T_{Ref} = 25$ °C over the state of charge (SOC) is measured by charging and discharging the cell at a low current rate of C/50 and averaging both voltage curves to compensate remaining overvoltages and hysteresis effects. Results are implemented in the model as $U_{OCV,Ref}(SOC)$, which is shown in Fig. 5a.

Parameters for the series resistance R_i are collected through pulse tests over the entire SOC range with 1 C in both charge and discharge direction in 10% (6 min) SOC-steps. The series resistance is calculated from the cell overvoltage at the end of a pulse and the pulse current. Relaxation time after each pulse is 6 h. This pulse testing procedure is comparable to the method described in [41]. Values for SOC of 0% and 100% are linearly extrapolated. Results for tests at a climate chamber temperature of 25 °C are shown in Fig. 5b and indicate that values for charge and discharge are not identical and tend to higher value towards the end for both charge and discharge.

The pulse characterization over the SOC range is conducted at climate chamber temperatures from 10 °C to 60 °C in steps of 10 °C and additionally at 25 °C. Results for a SOC of 50% at various temperatures are shown in Fig. 5c. As expected for lithium-ion batteries, charge and discharge resistances increase with decreasing temperature due to the slow-down of electrochemical and physical processes.

Dedicated modeling of the voltage hysteresis, which is prominent in lithium iron phosphate electrodes [42–44], is necessary for accurate equivalent circuit modeling of the cell [45]. A time-independent hysteresis model for the voltage hysteresis U_{Hys} is implemented as a function of the state of charge based on the C/50 charge and discharge curves from open circuit voltage measurements. Results are shown in Fig. 5d.

Overvoltages ΔU, the difference between the cell terminal voltage U_T and the open circuit voltage, are thus calculated through the ohmic losses in the series resistance at current I and the hysteresis voltage:

$$\Delta U = U_T - U_{OCV} = I \cdot R_i(SOC,T) + \mathrm{sgn}(I) \cdot U_{Hys}(SOC) \quad (1)$$

As both the open circuit voltage of the cell and reversible heat production are a function of the full-cell entropy S [46–48], the entropy profile for the cell is measured. The SOC is changed from 0% to 100% in 10% steps using a C/20 current at 25 °C and the battery is subsequently allowed to relax for 13 h at the same temperature, following a thermal cycle: Temperature change to +60 °C; Relaxation for 3 h; Temperature change to −10 °C; Relaxation for 3 h. Entropy S is calculated as dU_{OCV}/dT from cell voltages after relaxation at +60 °C and −10 °C. The method is comparable to the procedure described in [49]. Results are shown in Fig. 5e.

The temperature-dependent open circuit voltage of the cell can then be approximated by first order expansion around the reference temperature of 25 °C:

$$U_{OCV}(T,SOC) = U_{OCV,Ref}(SOC) + (T - T_{Ref}) \cdot \left.\frac{dU_{OCV}}{dT}\right|_{T=T_{Ref}}(SOC) \quad (2)$$

Neglecting slow side reactions due to cell ageing or self-discharge and further the heat of mixing due to concentration gradients within the cell, which can generally be neglected for typical loads for lithium-ion cells [49,50], the heat source in the cell $\dot{Q}_{Cell}$ cell can be calculated as the sum of irreversible energy losses and the reversible heat production:

$$\dot{Q}_{Cell} = I \cdot \left(\Delta U + T \cdot \left.\frac{dU_{OCV}}{dT}\right|_{T=T_{Ref}}(SOC) \right) \quad (3)$$

Cell self-discharge s is measured via a separate experiment. Cells are fully discharged at 25 °C to a low cut-off rate of C/50, charged to 50% SOC, rested for one month and again fully discharged at 25 °C. The difference between charged capacity and discharged capacity after storage is taken as constant self-discharge as a function of temperature for the simulation. Storage temperatures are 10 °C, 15 °C, 25 °C, 35 °C, 45 °C and 55 °C. Results are shown in Fig. 5f, indicating a strong increase at higher temperatures.

As self-discharge is covered through this specific approach, the coulombic efficiency in the simulation is taken as 100%.

For thermal modeling, the single-cell is implemented as 0D lumped thermal capacity. Cell mass m_{Cell} is measured as 85 g. Cell specific heat capacity $c_{p,Cell}$ is taken from existing experimental data as 838 J/(kg K) from accelerating rate calorimeter measurements [51]. Cell heat capacity $C_{th,Cell}$ can then be calculated:

$$C_{th,Cell} = m_{Cell} \cdot c_{p,Cell} \quad (4)$$

For validation of energy loss calculation, full cycle tests at different current rates are conducted on a single cell placed in an isothermal battery calorimeter at 30 °C. Thus, energy losses can be calculated both from electrical measurement at the cell as well as from cell heat rate to ambient. The utilized calorimeter *IBC 284* is an in-house development of the National Renewable Energy Laboratory described in [52–55].

Both charge and discharge are conducted at the same constant-current following a constant-voltage phase with a low cut-off current of C/50. Thus, each cycle equals approximately a coulombic efficiency of 100% and different tests have a comparable depth of discharge of 100%. Constant-current rates vary from 0.1 C to 2 C. Between each current inversion and experiment variation, tests are paused for 6 h to allow full thermal equilibration. Energy losses from electrical measurements are calculated from the difference between charged and discharged energy of one cycle. Electrical energy is calculated from time integral of the cell current and four-pole measurement of the cell

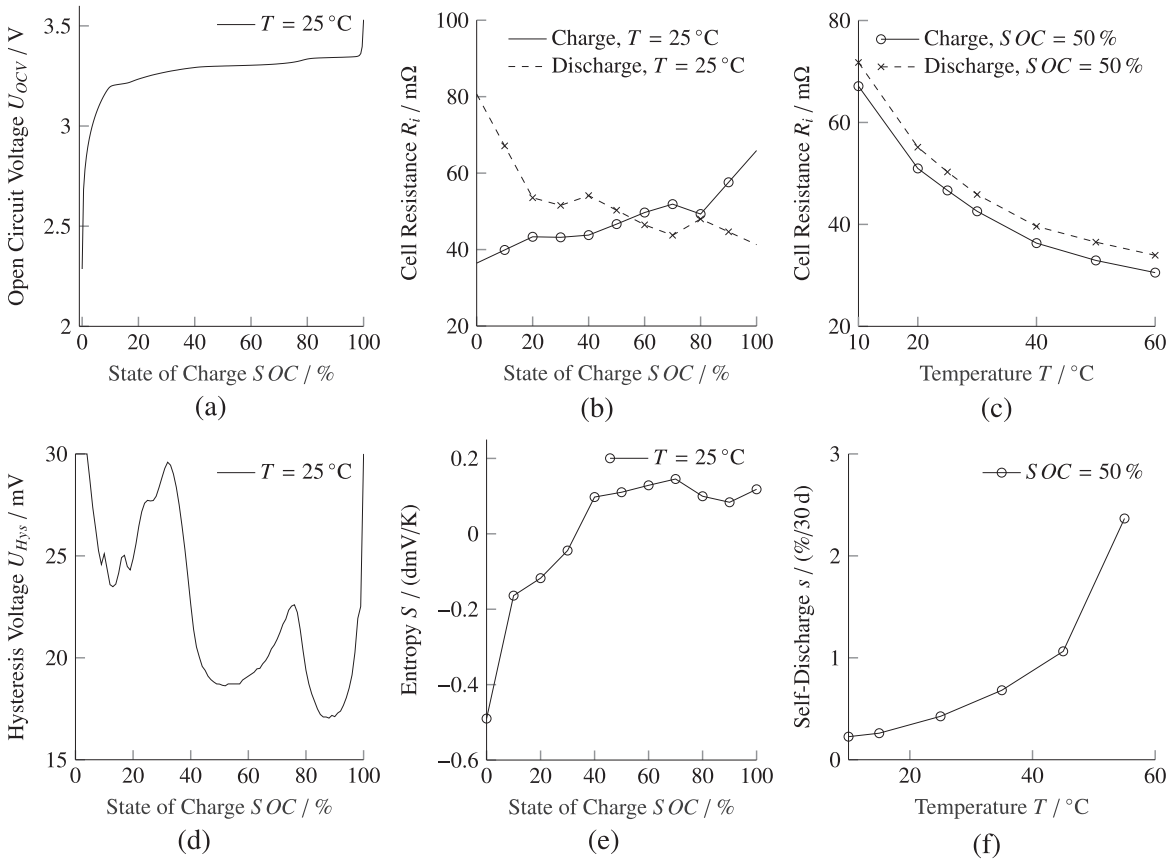

Fig. 5. Battery model parametrization for lithium iron phosphate cell: (a) Open circuit voltage over state of charge at 25 °C, (b) cell resistance (pulse 1 C, 6 min) over state of charge at 25 °C, (c) Cell resistance (Pulse 1 C, 6 min) over temperature at state of charge 50%, (d) cell hysteresis voltage over state of charge at 25 °C, (e) Full-cell entropy over SOC at 25 °C, and (f) self-discharge rate over temperature at state of charge 50%.

voltage.

For the calculation of the heat rate through isothermal calorimetry, the cell voltage is measured at both the cell poles and at the wiring entering the test chamber to factor for the off heat of the wiring and contact resistances from the power cables leading to the battery poles. The time integral of heat-flow measurements over a full cycle equals the irreversible heat production, as reversible heat production is canceled out [46]. Energy losses are thus calculated as the time integral of heat rate of each full cycle.

Fig. 6 shows the energy loss calculation of the single-cell full cycle tests from simulation, electrical measurements, and isothermal calorimetry measurements.

Energy losses in a round-trip cycle vary from 2.4% for 0.1 C, (electr. exp. data) equal to a 97.6% energy efficiency to 14.5% for 2 C (electr. exp. data), equating to a 85.5% energy efficiency. Model results for thermal and electrical values are plotted as a single line, as no difference derives from the model. Electrical and thermal experimental measurements show good agreement with each other as well as with the model, resulting in a model error of less than 10% for the energy loss calculation over the full considered range. An error of 10% in energy loss calculation for 1 C full cycle equates to an error of energy efficiency of 0.9%.

2.2.2. Rack model

The single-cell model is extended for application in the battery rack simulation. Capacity and resistance values for the cell blocks, modules, and the battery rack are calculated assuming no cell variations.

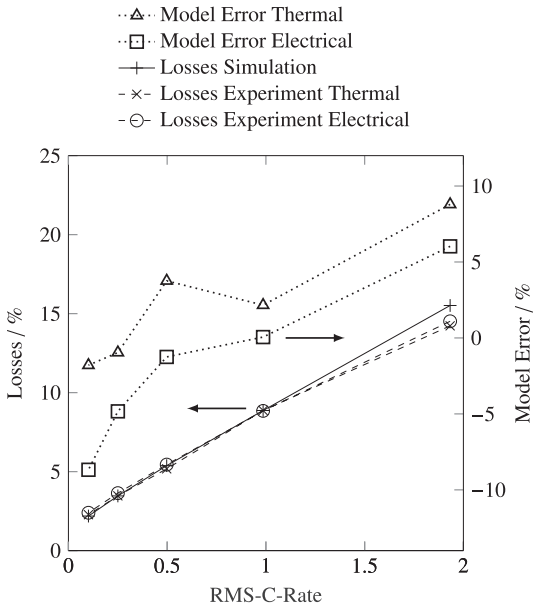

Fig. 6. Comparison of battery energy loss of full cycle tests from 0.1 C to 2 C at 30 °C for data from simulation, electrical measurements and isothermal calorimetry measurements.

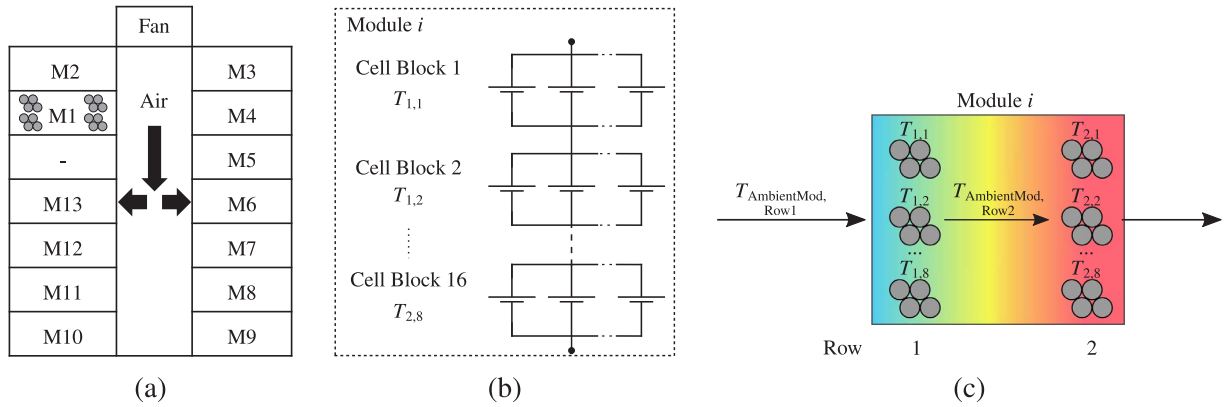

Fig. 7. Schematic illustration of battery rack and module: (a) Rack setup with air flow and module positioning, (b) electrical module layout with separate temperature nodes for each block of parallel connected cells, and (c) thermal module model with thermal gradient in cooling air.

The battery rack consists of 14 slots, of which 13 are equipped with identical battery modules and one slot with control electronics. All modules are cooled by a single radial fan which supplies a vertical air duct in the battery rack, as shown in Fig. 7a. In each module, the cell blocks are set up in two rows, with the first rows lying next to the air duct entry and the second further downstream, which is drawn schematically in *module position 1*.

Contact resistances for connecting cells in parallel, the connection of the cell blocks in series and also the connection of the modules are added to the electrical multi-cell model. For parametrization, 10 s charge pulse tests are conducted on the cell, cell block, module and battery rack levels at climate chamber temperature of 25 °C. All pulses are started from an SOC of 50%, where open circuit voltage can be assumed constant during the pulse due to its short duration and the flat voltage curve (see Fig. 5a). As cell temperature does not change significantly due to the short pulses, the resistance values from different setups can be compared. Cell resistance for a 10 s charge pulse $R_{DC10s,Exp}$ is calculated as:

$$R_{DC10s,Exp} = \frac{U_{t=10\,s} - U_{t=0\,s}}{I} \tag{5}$$

Pulse current rate for all setups is 1 C, respective to the setup's capacity. Before the pulse, tests are paused for 6 h to allow cell equilibration to open circuit voltage and climate chamber temperature. Contact resistances $R_{Contact}$ between two setups are calculated as the difference between the experimental value from the actual assembled setup $R_{DC10s,Exp}$ and the theoretical value calculated by scaling up the respective smaller setup $R_{DC10s,Scaled}$, i.e. for the module:

$$R_{Contact,\,Module} = R_{DC10s,Exp,Module} - R_{DC10s,Scaled} = R_{DC10s,Exp,Module} - n_{Blocks/Module} \cdot R_{DC10s,Exp,Block} \tag{6}$$

Contact resistances for the single-cell measurement are not measured separately and are thus included in the cell resistance value. Table 2 shows the results.

Comparing the 10 s puls rack resistance linearly scaled from the single cell contribution (619.67 mΩ) to the actual rack resistance (674.98 mΩ) gives a relative increase of 8.9%. It should be noted, that in experiments as well as in simulation, the contact resistances are to be considered additionally to cell resistances of longer pulse durations, which are higher than those of 10 s. The impact of contact resistance is, therefore, smaller than the relative values given here.

Table 2
Battery connector resistances for cell block, module and rack. Experimental data from 10 s charge pulses at 50% SOC and 25 °C.

	$R_{DC10s,Exp}$	$R_{DC10s,Scaled}$	$R_{Contact}$
Cell	35.75 mΩ	-	*included*
Block	3.08 mΩ	2.98 mΩ	0.10 mΩ (+3.5%)
Module	49.44 mΩ	49.31 mΩ	0.12 mΩ (+0.2%)
Rack	674.98 mΩ	642.72 mΩ	32.26 mΩ (+5.0%)

For the thermal model of the battery rack, each module is calculated as a separate unit. The thermal module model calculates each cell block as 0D lumped thermal capacity. A schematic drawing of the electrical module layout with separate temperature nodes for each block of parallel connected cells is shown in Fig. 7b. Heat rate from cell block connector losses is given as additional input to the heat source of the cell block $\dot{Q}_{Block}$ and thus to the thermal capacity of the cell block. Losses and their respective heat rate from contact resistances in the module and rack are directly given as heat input to the system air and not considered in the module model:

$$\dot{Q}_{Block} = I \cdot \left(\Delta U + T \cdot \frac{dU_{OCV}}{dT} \right) + I^2 \cdot R_{Contact,Block} \tag{7}$$

For the heat capacity of the cell block $C_{th,Block}$, the copper bar $m_{Connector,Block}$ connecting the cells in parallel and to the next neighboring cell block is added to the block thermal capacity [56]:

$$C_{th,Block} = n_{Cell/Block} \cdot C_{th,Cell} + m_{Connector,Block} \cdot c_{p,Cu} \tag{8}$$

The heat balance between a cell block and the ambient temperature in the row k, $T_{AmbientMod,Rowk}$, is based on the heat exchange rate $\dot{Q}_{Block\text{-}AmbMod}$ and the respective thermal resistance $R_{th,Block\text{-}AmbientMod}$:

$$C_{th,Block} \frac{dT_{Block}}{dt} = \dot{Q}_{Block} - \dot{Q}_{Block\text{-}AmbMod} = \dot{Q}_{Block} - \frac{T_{Block} - T_{AmbientMod,Rowk}}{R_{th,Block\text{-}AmbientMod}} \tag{9}$$

Fig. 7c shows the thermal module model structure. The first row receives air from the ventilation duct of the system, at the controlled temperature $T_{Air,Duct}$:

$$T_{AmbientMod,Row1} = T_{Air,Duct} \tag{10}$$

The second row is cooled with downstream air and on average receives warmer air. Based on the air mass flow rate of the module $\dot{m}_{Air,Module}$ and the specific heat capacity of air $c_{p,Air}$, the air temperature increase in the first row due to heat exchange with the cell blocks is calculated in the module model as an averaged temperature. The resulting air temperature is then applied as ambient temperature for the second row:

$$T_{AmbientMod,Row2} = T_{AmbientMod,Row1} + \frac{\sum \dot{Q}_{Block\text{-}AmbMod,Row1}}{\dot{m}_{Air,Module} \cdot c_{p,Air}} \tag{11}$$

Thermal model parameters for the heat transfer are collected through experimental characterization. A module equipped with

temperature sensors glued on the cell's surfaces is installed in the battery rack. Eight temperatures are monitored per cell block to calculate accurate average block temperatures. The battery rack is placed in a temperature controlled chamber set to 25 °C with the radial fan also receiving air at 25 °C.

Long-term pulses of 60 s alternating charge and discharge at an average SOC of 50% are applied until constant conditions for temperature are achieved. Thus, time-averaged heat production is in equilibrium with heat transfer to ambient air. Assuming no changes in battery cell entropy and resistance over the pulse duration, steady-state conditions can be used for the calculations of heat transfer. Reversible heat production is cancelled out through the alternating current pulses, as the reversible heat rate changes sign with current direction [46].

Energy loss and thus irreversible heat production $\overline{P}_{\mathrm{Loss,Block}}$ is calculated from the measured voltage for each cell block and battery rack current. Heat transfer coefficients can then be calculated for each of the eight cell blocks in the first row:

$$R_{\mathrm{th,Block\text{-}Ambient}} = \frac{\overline{T}_{\mathrm{Block}} - T_{\mathrm{AmbientMod,Row1}}}{\overline{P}_{\mathrm{Loss,Block}}} \tag{12}$$

Air mass flow and heat transfer coefficients for the second row are fitted numerically. The procedure is then repeated for each of the 13 module positions, resulting in 13 air mass flow values and 208 heat transfer coefficients. Tests for all 13 module positions are conducted at a fan power of 100% nominal power. A comparison of 208 block temperatures in the long term pulse test gives minimum/mean/maximum block temperature increases as +3 K/7 K/13 K. The strong thermal gradient confirms the necessity for detailed thermal modeling of the battery rack.

For validation of the battery rack model, full cycle tests with 1 C are applied for several hours with the sensor module in position No. 13. Time-averaged experimental min./mean/max. block temperature increases above 25 °C are 5 K, 9 K, and 12 K. In comparison, simulated values are 4 K, 9 K, and 15 K and thus in good agreement. Furthermore, this analysis provides insight into the safety of the battery rack at full nominal current, which is an important factor for deployment. The maximum experimentally observed temperature increase is 15 K above air inlet temperature. At the set-point air temperature of the system in operation of 15 °C, this equals to a maximum cell block temperature of 30 °C - which is below the maximum cell surface temperature of 60 °C specified by the cell manufacturer with a large safety margin.

To model different fan power settings, tests are extended for module position 13 for fan power settings of 12.5%, 25%, 50% and 75%, with a reduced current rate for safety. The relative change of heat coefficients and air mass flow rates from the fan power settings of 100% is then applied to the thermal parameters of the other 12 modules in the rack.

In summary, the electrical battery model allows the calculation of three loss mechanisms: overvoltages, self-discharge, and losses in the battery connector. The thermal model features a temperature calculation with respect to varying heat transfer conditions in both module and rack, air inlet temperature and fan power and serves as an input for the temperature dependency of the loss mechanisms in the electrical battery model.

2.3. Power electronics

Each of the eight battery racks in the system is connected to a dedicated power electronics unit. The power electronics components are installed in three-phase connection to the electrical grid on the low voltage level, which has a line-to-line voltage of 400 V. The power electronics units, which are manufactured by Siemens under brand name Sinamics S120, are comprised of a bidirectional inverter/rectifier unit and a grid interface module for filtering with an LCL-filter. This topology is known as a single-stage three-phase full bridge bidirectional converter [57]. Nominal power is 36 kW each. Fig. 8 shows the topology of a single rack power electronics unit connected to the battery.

The operating DC voltage range of the power electronics is specified as 600–750 V. The nominal battery rack discharge cut-off voltage of 416 V is below the minimum DC voltage of the power electronics and therefore no full discharge is possible. This results in a minimum cell voltage of 2.88 V. However, due to the flat open circuit voltage curve of the lithium iron phosphate chemistry over the battery state of charge, a still very low minimum SOC of 1.8% can be reached and thus results in only a small reduction of usable capacity.

The power electronics components are modeled in MATLAB Simulink. The power loss calculation for the power electronics units includes losses in both the inverter/rectifier unit and the grid interface module:

$$P_{\mathrm{Loss,PE}} = P_{\mathrm{Loss,Inv./Rect.}} + P_{\mathrm{Loss,Interface}} \tag{13}$$

The loss calculation in the inverter/rectifier units considers the losses due to conduction and switching in the IGBT and diodes:

$$P_{\mathrm{Loss,Inv./Rect.}} = P_{\mathrm{Loss,IGBT,Switch}} + P_{\mathrm{Loss,IGBT,Cond}} + P_{\mathrm{Loss,Diode,Switch}} + P_{\mathrm{Loss,Diode,Cond}} \tag{14}$$

The calculation approach for the switching and conduction losses of the semiconductor in the inverter/rectifier is based on the approach proposed by Drofenik and Kolar [58]. The losses are dependent on the switching frequency f_{Switch}, the junction temperature of the semiconductors T_{J}, the blocking voltage of the semiconductors, which corresponds to the DC voltage U_{DC}, the forward current i_{F} and the forward voltage U_{F} of the diodes and the collector current i_{C} and the collector-emitter-voltage U_{CE} of the IGBTs. This results in the respective equations for switching/conduction losses for the IGBTs and diodes:

$$P_{\mathrm{Loss,IGBT,Switch}} = (E_{\mathrm{On}}(U_{\mathrm{DC}},i_{\mathrm{C}}) + E_{\mathrm{Off}}(U_{\mathrm{DC}},i_{\mathrm{C}}))\cdot f_{\mathrm{Switch}} \tag{15}$$

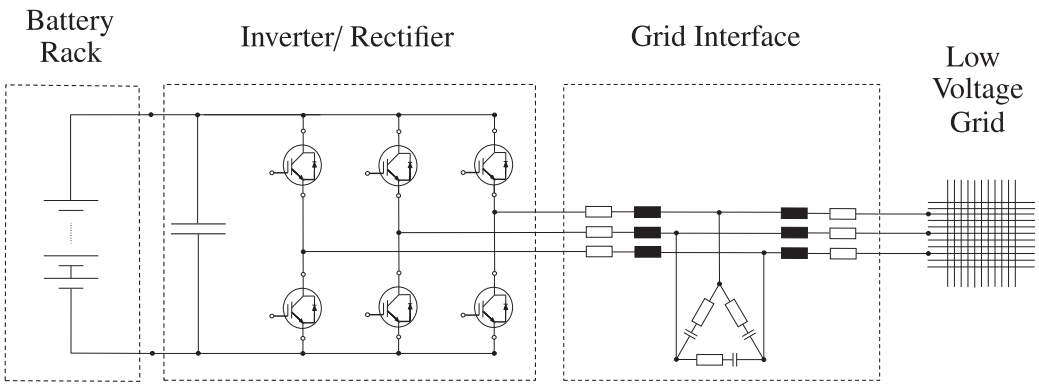

Fig. 8. Power electronics topology connecting a single battery rack to the low voltage grid.

$$P_{\text{Loss,Diode,Switch}} = E_{\text{Rec}}(U_{\text{DC}},i_{\text{F}})\cdot f_{\text{Switch}} \quad (16)$$

$$P_{\text{Loss,IGBT,Cond}} = U_{\text{CE}}(T_{\text{J}},i_{\text{C}})\cdot i_{\text{CE}} \quad (17)$$

$$P_{\text{Loss,Diode,Cond}} = U_{\text{F}}(T_{\text{J}},i_{\text{F}})\cdot i_{\text{F}} \quad (18)$$

For the simulation of the 36 kW inverter/rectifier unit, the 150 Ampere Infineon FS150R12KE3 IGBT module is implemented [59]. Further parametrization and model parameters are explained in detail in Appendix A.

The calculation approach for the LCL-filter takes the core and the conduction losses into account:

$$P_{\text{Loss,Interface}} = P_{\text{Loss,LCL,Core}} + P_{\text{Loss,LCL,Cond}} \quad (19)$$

The core losses of the LCL-filter are dependent of the grid voltage U_{Grid} and frequency f_{Grid} and thus implemented without load dependency:

$$P_{\text{Loss,LCL,Core}} \sim U_{\text{Grid}}^2 \cdot f_{\text{Grid}}^2 = \text{const.} \quad (20)$$

The conduction losses are calculated from Ohm's law losses through the total inductor resistances $R_{\text{LCL,total}}$ and the current i_{Grid}:

$$P_{\text{Loss,LCL,Cond}} = R_{\text{LCL,total}} \cdot i_{\text{Grid}}^2 \quad (21)$$

Simulations results for conversion of 400 V AC to 600 V DC and input power up to 100 % of nominal power are compared to experimental data by the manufacturer [60]. Experimental and simulated power loss values are shown with the relative model error in Fig. 9.

The model error for power loss is under 7% over the entire operating range. At nominal power, an error of 7% for the power loss calculation equals to a difference of 0.18% in efficiency from the experimental value of 97.41%. The Simulink model used here enables a calculation of power loss according to the input parameters DC voltage, load direction, operating point and system air temperature.

The power electronics simulation in Simulink offers a high temporal resolution in the order of *microseconds*. Thereby, the temporal responses of fast processes such as the power electronics switching can be modeled adequately. The time response of macroscopic observables of the system such as the temperature of the battery occurs in the *seconds* range. The power electronics model is thus simulated for varying system air temperatures, current directions, DC voltages and load conditions. Under each condition, simulation is run until a constant temperature and thus constant operating conditions are achieved. The then time-averaged results for each operating point are saved and integrated into the system simulation as a function of the four parameters.

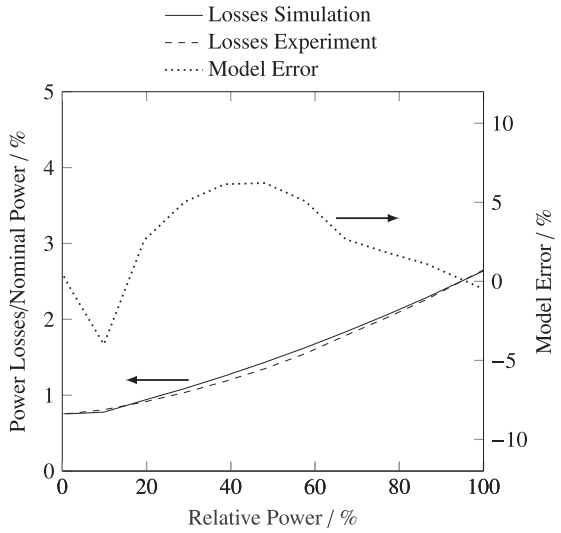

Fig. 9. Power electronics losses for AC to DC conversion over operation range at 600 V DC. Simulation data at 25 °C ambient air temperature, experimental data from [60].

In summary, the power electronics model enables a calculation of the conversion losses. The covered loss mechanisms in the grid interface module are conduction and core losses and in the inverter/rectifier unit the losses in IGBT and Diode with respective separation for switching and conduction losses.

2.4. Thermal management

The thermal management of the system can be separated into three parts: *System thermal management*, which covers the overall temperature control of the container; *Battery thermal management*, which covers the temperature control of the battery rack within in the system; *Power electronics thermal management*, which covers the temperature control of the inverter/rectifier unit and the grid interface unit. Each is explained separately in the following Sections 2.4.1–2.4.3.

2.4.1. System thermal management

The system thermal management of the storage container features a two-zone setup to separately manage the temperatures of the battery racks and the power electronics, as in general, lithium-ion batteries are more temperature sensitive e.g in terms of cell degradation. Further, the power electronics are the main heat source in the system. Battery racks, which require most of the volume of the system are placed in the main part of the container, the battery zone. The power electronics are placed in a metal cabinet inside of the container, the power electronics zone.

For calculation of the operating points and power consumption of the thermal management components, a thermal system model is necessary which allows the calculation of heat flows and air temperatures in the separate zones and the ventilation duct. A thermal resistance network is defined which connects air temperatures in the system with the models of the battery racks, the power electronics components and the ambient outdoor conditions. Fig. 10 shows an overview of the thermal system model.

Parameters for the thermal system model are given in Appendix B.

The container main ventilation duct is fed by ambient outdoor air and/or air from the battery zone. Inside the ventilation duct, the vaporizer of the air conditioning unit can actively control bidirectional heat exchange with the air flow. From the ventilation duct, air is supplied to the battery racks, to the battery zone and to the power electronics zone, each via a separate fan. Setpoint temperature in the ventilation duct is 15 °C, according to the desired ambient temperature for the lithium-ion cells.

The battery zone is fed from the outflow of the battery racks and further actively controlled with a single fan fed from the ventilation duct. Target temperature range is 10–20 °C. The power electronics zone is controlled to a wider range of 0–40 °C according to manufacturer specifications [60]. If the battery zone requires heat input, outflow air from the power electronics zone can be directed to it instead of releasing it to the ambient outdoors.

The split inverter, connected to the vaporizer in the ventilation duct, has a nominal cooling and heating power of 10.0 kW and 11.2 kW, respectively. The four fans supplying air from the ventilation duct to the power electronics zone as well as the single fan for the battery zone each have a nominal power consumption of 101 W from 24 V supply.

Convective heat flows in the thermal system model are calculated as follows:

$$\dot{Q}_{\text{Conv}} = \dot{V}\cdot c_{p,\text{Air}}\cdot\rho_{\text{Air}}\cdot T \quad (22)$$

Conductive heat flows between two objects are calculated with the interface area A, the temperature difference ΔT and the thermal resistance R_{th}:

$$\dot{Q}_{\text{Cond}} = A\cdot\frac{\Delta T}{R_{\text{th}}} \quad (23)$$

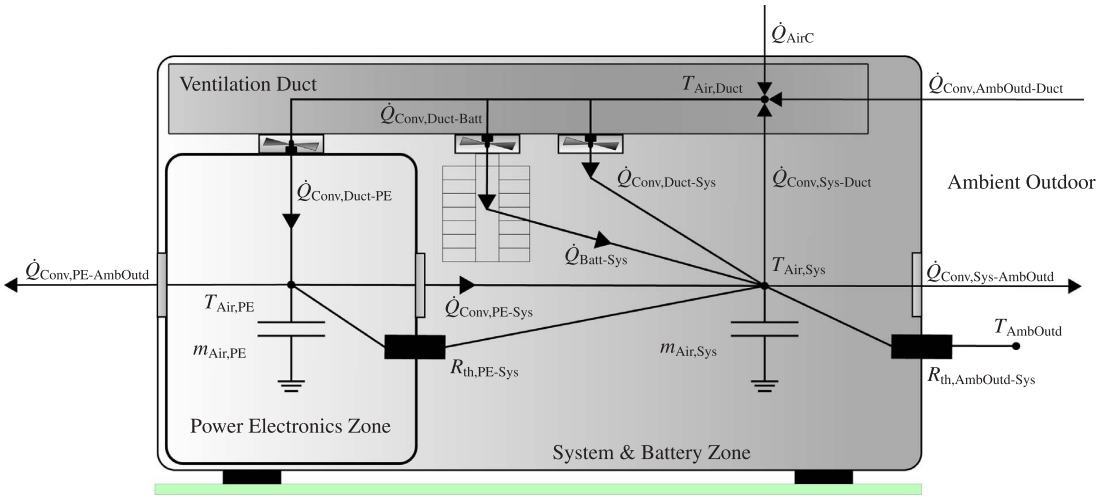

Fig. 10. System thermal management model overview: Thermal resistance network of the container system with two-climate zones, air conditioned by ambient outdoor air and active cooling/heating. Figure and approach based on [28,29].

Thermal resistances between the battery zone and ambient as well between the battery zone and the power electronics zone are calculated from the heat transfer coefficients on both sides and the containment material heat conductivity.

Coupling to the thermal battery model gives the heat transfer from the battery racks to the battery zone $\dot{Q}_{Batt\text{-}Sys}$, calculated from the convective heat input from the ventilation duct $\dot{Q}_{Conv,Duct\text{-}Batt}$ and from the heat exchange within the rack:

$$\dot{Q}_{Batt\text{-}Sys} = \dot{Q}_{Conv,Duct\text{-}Batt} + \sum \dot{Q}_{Block\text{-}AmbMod} \tag{24}$$

Heat balance for the battery zone is given as:

$$m_{air,Sys}\cdot c_{p,Air}\cdot\frac{dT_{air,Sys}}{dt} = P_{C\&M,Sys} + P_{C\&M,Batt} + \dot{Q}_{Batt\text{-}Sys} + \dot{Q}_{Conv,Duct\text{-}Sys} + \dot{Q}_{Conv,PE\text{-}Sys} + \dot{Q}_{Cond,PE\text{-}Sys} + \dot{Q}_{Cond,AmbOutd\text{-}Sys} - \dot{Q}_{Conv,Sys\text{-}Duct} - \dot{Q}_{Conv,Sys\text{-}AmbOutd} \tag{25}$$

Heat balance for the power electronics zone is given as:

$$m_{Air,PE}\cdot c_{p,Air}\cdot\frac{dT_{Air,PE}}{dt} = P_{Loss,PE} + P_{C\&M,PE} + \dot{Q}_{Conv,Duct\text{-}PE} - \dot{Q}_{Conv,PE\text{-}Sys} - \dot{Q}_{Conv,PE\text{-}AmbOutd} - \dot{Q}_{Cond,PE\text{-}Sys} \tag{26}$$

The heat balance for the ventilation duct considers no thermal mass or conductive heat exchange and is given as:

$$0 = \dot{Q}_{Conv,AmbOutd\text{-}Duct} + \dot{Q}_{Conv,Sys\text{-}Duct} + \dot{Q}_{AirC} - \dot{Q}_{Conv,Duct\text{-}PE} - \dot{Q}_{Conv,Duct\text{-}Batt} - \dot{Q}_{Conv,Duct\text{-}Sys} \tag{27}$$

Based on the affinity laws for a fan with nominal fan power $P_{Fan,Nom}$ and nominal volumetric flow rate $V_{Fan,Nom}$, the volumetric flow rate for a different power can be calculated [61]:

$$\dot{V}_{Fan} = \dot{V}_{Fan,Nom}\cdot\left(\frac{P_{Fan}}{P_{Fan,Nom}}\right)^3 \tag{28}$$

The pressure loss occurring in the ventilation is unknown and is neglected in the simulation. In reality this would decrease the flow rate, but as results show, the contribution of fan power consumption on the total system power consumption is low. This approach is used for all calculations of air flow rate in the thermal management model.

Power consumption of active cooling/heating with the split-inverter unit is calculated with the Coefficient of Performance *COP*, which is taken constant as 3.0 for cooling (corresponding to air-cooled compressor units with cooling power greater than 10 kW, coolant R410A and average vaporizing temperature 8 °C [62]) and 4.0 for heating, respectively:

$$P_{AirC} = COP_{Heating/Cooling}\cdot\dot{Q}_{AirC} \tag{29}$$

2.4.2. Battery thermal management

The battery racks are separately fan-cooled with a radial fan on top of the rack supplying air from the system ventilation duct. Battery rack fans are controlled as follows: 100% if maximum cell temperature in the rack is higher than inlet temperature by 5 K; 10% if maximum cell temperature in the rack is lower and the rack is in operation; 0% if maximum cell temperature in the rack is lower and the rack is not in operation. The nominal power consumption of each battery rack fan is 82 W from 24 V supply.

2.4.3. Power electronics thermal management

Both the power electronics units, inverter/rectifier module, and grid interface module use internal fan cooling which circulates air from the power electronics zone. Fan cooling of the power electronics units is not modulated except for turn-on/turn-off and thus has a constant power consumption during operation of 36 W for the inverter/rectifier module and 11.8 W for the grid interface module [60], both from 24 V supply.

In summary, the thermal system model enables a calculation of system temperatures in the ventilation duct, the battery zone, and the power electronics zone, as well as the power consumption of the thermal management. In the system thermal management model the loss mechanisms covered are the air conditioning by active cooling/heating and the fan ventilation of battery zone/power electronics zone. For component thermal management, the power consumptions of the fan cooling of the inverter/rectifier units, the grid interface units, and the battery racks are calculated.

2.5. Control and monitoring components

For an accurate evaluation of the system power consumption, the monitoring and control components are analyzed and grouped by their function. As the operation mode and thus power consumption changes for some components in the power electronics group (i.e. contactor), power consumption is evaluated for both the state of standby as well as when the system is in operation. For all components which consume power from the 24 V supply, a conversion efficiency of 91.5% is

Table 3
Power consumption of control and monitoring component groups in standby and operation-mode.

Group	Standby mode	Operation mode
Battery	287 W	287 W
Power Electronics	422 W	463 W
System	81 W	81 W
Total	789 W	830 W

implemented, based on the nominal efficiency of the installed 24 V supply.

Table 3 shows the consumption of the monitoring and control components, grouped by their affiliation and the total sum. The power consumption from 24 V is here already corrected by the power supply efficiency.

For the components related to the battery, the largest contributor is the battery management with the slave modules for each of the 104 battery modules. In the power electronics group, the modular setup of the system requires dedicated voltage sensing and control units for each battery rack, which leads to additional power consumption. Components for monitoring the overall system (i.e. remotely accessible computer) have low power consumption.

In summary, the model calculates power consumption for control and monitoring in both standby and operation mode of the system. The components are grouped by their related function into battery, power electronics, and overall system.

2.6. Performance indicators

For the evaluation of the system efficiency, two round-trip efficiencies are defined which give average values for a simulated operation duration.

The conversion round-trip efficiency $\eta_{\text{Conversion}}$ considers losses which occur on the conversion path from the energy charged, $E_{\text{Charge,AC}}$, and the energy discharged, $E_{\text{Discharge,AC}}$ from/to the grid. It includes only the conversion losses in the battery and power electronics, but not the system consumption:

$$\eta_{\text{Conversion}} = \frac{E_{\text{Discharge,AC}}}{E_{\text{Charge,AC}}} \tag{30}$$

The total round-trip efficiency η_{Total} further includes the energy consumed by the system for thermal management as well as for the control and monitoring components $E_{\text{System Consumption}}$:

$$\eta_{\text{Total}} = \frac{E_{\text{Discharge,AC}}}{E_{\text{Charge,AC}} + E_{\text{System Consumption}}} \tag{31}$$

The relative loss ϕ of mechanism i is calculated through the ratio of the energy loss to the total energy input:

$$\phi_i = \frac{E_{\text{Loss},i}}{E_{\text{Charge,AC}} + E_{\text{System Consumption}}} \tag{32}$$

To compare different load profiles, utilization ratios are defined. The temporal utilization τ_t is the ratio of the time in which the simulation is in operation $t_{\text{Operation}}$ (System Power ≠ 0) to the evaluated duration $t_{\text{Simulation}}$:

$$\tau_t = \frac{t_{\text{Operation}}}{t_{\text{Simulation}}} \tag{33}$$

The charge-based utilization τ_Q is the ratio of the charge-throughput of the battery $Q_{\text{Throughput}}$ to the theoretically possible maximum throughput during the simulation duration $Q_{\text{Throughput,theoretical max}}$. at cycling the system at the maximum battery current of 1 C:

$$\tau_Q = \frac{Q_{\text{Throughput}}}{Q_{\text{Throughput,theoretical max}}} \tag{34}$$

Based on the performance indices defined, the various simulation results are evaluated in the following.

3. Results and discussion

The system model now enables a system simulation of various applications. In Section 3.1 the general system performance is first analyzed through generic profiles. The model is then used in Section 3.2 to simulate several real-world grid application scenarios.

3.1. Evaluation of generic profiles

The generic profiles analyze the variation of three specific parameters: system power, time in operation and average state of charge, which are discussed in Sections 3.1.1–3.1.3 Ambient outdoor temperature is set to 20 °C for all generic profile simulations.

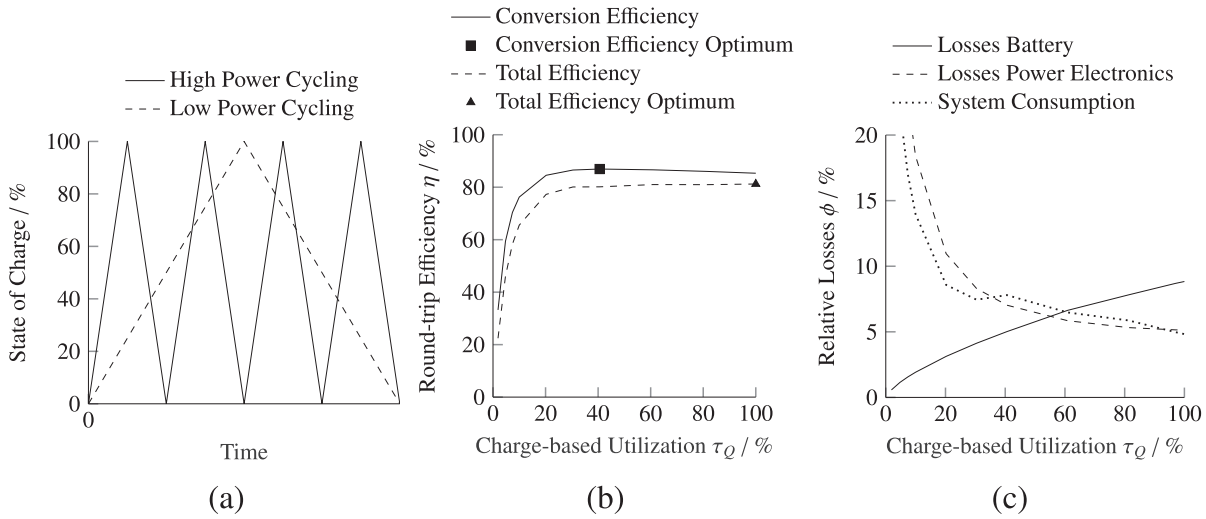

Fig. 11. Results of generic variable power full cycle profile: (a) Profile schematic, (b) energy efficiency, and (c) energy loss distribution.

3.1.1. Variable power

The *variable power* profile cycles the system with varying power settings without interruption, which leads to different charge utilizations. The schematic SOC profiles over time for two exemplary simulations, *high* and *low* power cycling, are shown in Fig. 11a. The temporal utilization is 100% for all simulations.

Results for the conversion efficiency over the charge-based utilization are shown in Fig. 11b. Conversion efficiency is low for the low utilization scenarios. For higher utilization, conversion efficiencies increase to a peak value of 87% at 41% charge-based utilization (marked as conversion efficiency optimum) and decreases slightly afterward. Total efficiency is slightly lower, peaking at 81% at full utilization (marked as total efficiency optimum). Towards full load, the difference between conversion and total efficiency decreases and at full utilization, conversion efficiency is 85%, and thus only 4 percentage points lower.

The relative losses, again over the charge-based utilization grouped into battery, power electronics, and system consumption, are shown in Fig. 11c. For the conversion efficiency, only battery and power electronics are relevant. Battery losses increase almost linearly with higher operating power, as expected from the results for the battery model (see Fig. 6). Power electronics conversion losses and total system consumption contribute significantly and together make up the majority of losses for low utilization. This is attributed to their loss behavior/power consumption even for no-load operation (see Fig. 9 and Table 3). In the low power simulations, the power electronics are the largest contributor to losses but are overtaken by the system consumption at high power operation when the thermal management power consumption rises. At high power operating points, the power electronics efficiency improves and system consumption increases due to increased load for the battery and system thermal management. On the other hand, for high utilization ranging between 50% and 100%, the battery is the largest contributor to the losses.

In summary, the results of the *variable power* profile show that low power operation results in significant losses due to the power electronics and the system consumption. The battery is the smallest contributor to the losses at low power operation and the inversely the strongest contributor at high power operation.

3.1.2. Variable system operation time

The *variable system operation time* profile cycles the system with full nominal power with varying pauses after each full cycle. The SOC profiles for two exemplary simulations, high and low operation time, are shown in Fig. 12a. The temporal utilization, not shown, scales linearly with the charge-based utilization.

The resulting efficiencies, shown in Fig. 12b, exhibit relatively constant conversion efficiencies for all utilization ratios of approximately 84–85%, as is expected due to the constant system power during operation. Peak conversion efficiency is 85% at full utilization (marked as conversion efficiency optimum), mainly explained with increased battery temperature due to the missing periods for temperature equilibration. This leads to decreasing cell resistances and thus higher battery efficiencies. At the lowest evaluated utilization, the battery self-discharge starts to have an increasing impact on the conversion efficiency due to the long rest periods between a cycle. For low utilization simulations, the total efficiency shows low values but converges to the conversion efficiency with increasing utilization. Peak total efficiency is at 81% (marked as total efficiency optimum), which is the identical peak value already identified in the generic profile for variable power (see Section 3.1.1).

The relative losses, shown in Fig 12c, for power electronics and battery remain constant for higher utilization, whereas the relative losses due system consumption are high for low utilization. The reason is that the energy for system consumption increases sublinearly with increasing utilization and thus is relatively lower at high utilization.

In summary, the results of the *variable system operation time* profile show that overall a higher charge throughput results in higher total system efficiency.

3.1.3. Variable average state of charge

The *variable average state of charge* profile cycles the system with full nominal power with varying averages for the SOC. The SOC is varied in each simulation for 5%, i.e. from 75% to 80% with an average SOC of 77.5%. Two SOC profiles for exemplary simulations, high and low average SOC, are shown in Fig. 13a. As power is throttled due to voltage limitations in battery and power electronics at very high and low SOCs, the profile is only evaluated for the middle region of SOC from 20% to 80%. The temporal and charge-based utilizations are then both 100% for all simulations.

Results for the efficiencies over the average SOC (Fig. 13b) show only a slight increase in the conversion efficiency to higher SOCs. Peak conversion efficiency (marked as conversion efficiency optimum) at an average SOC of 60% is 85% as previously already identified (see Section 3.1.1 and 3.1.2), but differences to lower and higher average state of

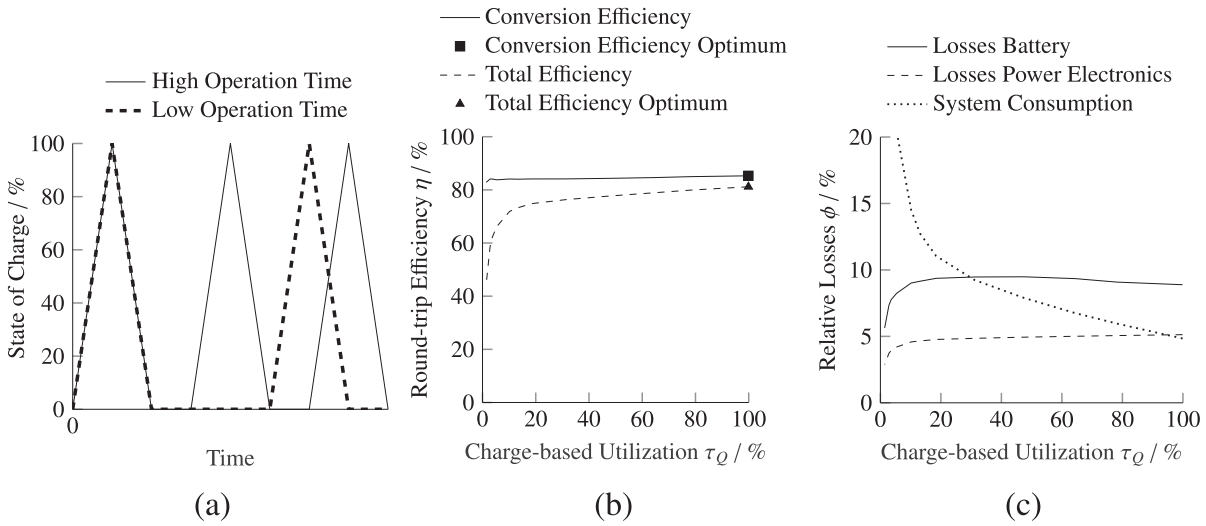

Fig. 12. Results of generic variable pause duration full cycle profile: (a) Profile schematic, (b) energy efficiency, and (c) energy loss distribution.

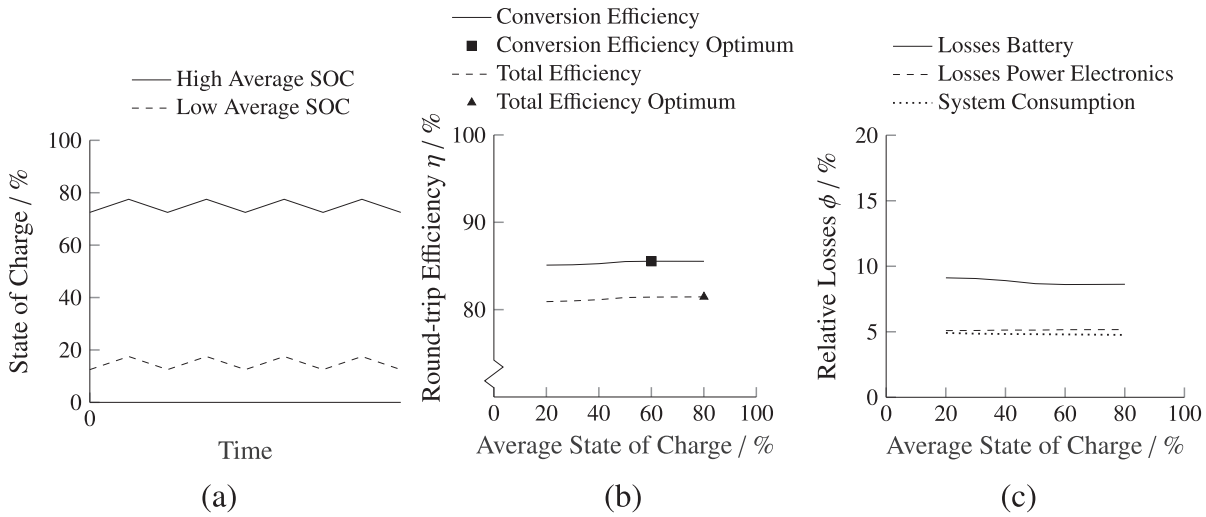

Fig. 13. Results of generic variable average state of charge profile: (a) Profile schematic, (b) energy efficiency, and (c) energy loss distribution.

charge are less than 1 percentage point. The total efficiency similar remains relatively constant as well at the previously identified peak value of 81%.

The relative losses, shown in Fig. 13c, indicate that this improvement originates from reduced battery losses which can be attributed to lower average resistance values in the cell. Even though power electronics losses increase at a higher battery rack voltage and thus with higher SOCs, this effect is noticeably smaller than for the battery.

Summarizing, the results for the *variable average state of charge* profile show that the energy efficiency is relatively stable over the middle SOC range, with a small trend towards higher efficiencies for higher SOC.

3.2. Evaluation of grid application scenarios

Three grid applications for Germany are evaluated for a prediction of real-world system performance, which will be briefly explained in the following.

Primary Control Reserve (PCR) is the support of the grid frequency by providing positive or negative power to the grid in case of frequency deviations from the nominal frequency in the European grid of 50 Hz [63]. The process is coordinated by the transmission system operators and activated through the grid frequency. The reserve power in the simulation is scaled to an offered power of 200 kW.

The load profile in this work is taken from existing work on control reserve [64]. Lately, the regulation for PCR has been subject to additions and clarifications due to new market participants such as battery systems [65]. The load profile in this work might not yet take into account recent regulations, however, it follows the explained specifications and covers the characteristics of frequency regulation with battery storage system.

Secondary Control Reserve (SCR), the second evaluated grid application is used to restore the availability of the power bandwidth of the primary control power in case of imbalances of power in the grid for a longer duration than 30 s. The control is centralized and fully automated through the local transmission operator. Positive and negative reserve power are tendered separately. SCR is tendered for periods of a full week and further separated into the base period (8 AM to 8 PM) and peak period (8 PM to 8 AM), resulting in four different types which can be offered. The requested power for a system offering SCR is further influenced by the energy price set by the system operator. The load profile for two units providing the same type of secondary control reserve power can therefore still vary. More information can be found at [66].

The load profile in this work is again taken from existing work [64]. Negative reserve power of 200 kW is provided for the base period and the battery is discharged during the peak period. The load profile in this work cannot be considered as a general secondary control reserve profile, but rather as an example with little storage utilization as is shown later.

PV-Battery (PV-B), the third evaluated grid application is storage of power from multiple residential households in a local low voltage grid. This grid application is not a remunerated grid service in Germany, but as the load profile has the characteristics of a residential photovoltaic battery system it is included in the study as a comparison.

The load profile is calculated from the residual load curve of multiple households with photovoltaic-battery systems. A number of 40 households with each a photovoltaic peak power 5 kW is considered, which results in approximately 5 kWh of nominal storage capacity per household. More details on the load profile are given in Appendix C.

Simulation duration for all grid applications is one year to include all seasonal variations.

Table 4 shows a comparison of the three grid application load profiles. Additionally to the previously defined charge-based and temporal utilizations, the number of full equivalent cycles per year is given. PCR is the highest utilized scenario. SCR here is a very low utilization scenario. PV-B is similar to PCR in terms of temporal utilization but the charge-throughput is lower.

For all grid applications, the ambient outdoor conditions are taken for the location Berlin, Germany in 1 h temporal resolution from the software Greenius 4.1.1 from the German Aerospace Center [67]. Year average temperature is 8.9 °C.

Table 5 shows the results for the conversion and total round-trip efficiency. PCR features both the highest conversion and total efficiency due to its higher charge-based utilization. For SCR, the total efficiency is very low due to the very low charge-based utilization. PV-B features a lower conversion efficiency than PCR due to the similar temporal

Table 4
Parameters of load profiles for grid application scenarios.

	PCR	SCR	PV-B
Full equivalent cycles/ a	409	18	223
Temporal utilization τ_t	61.5%	4.2%	59.7%
Charge-based utilization τ_Q	9.3%	0.4%	5.1%

Table 5
Conversion and total efficiency of grid application scenarios.

	PCR	SCR	PV-B
Conversion efficiency $\eta_{Conversion}$	80.2%	69.6%	72.0%
Total efficiency η_{Total}	71.6%	22.6%	59.5%

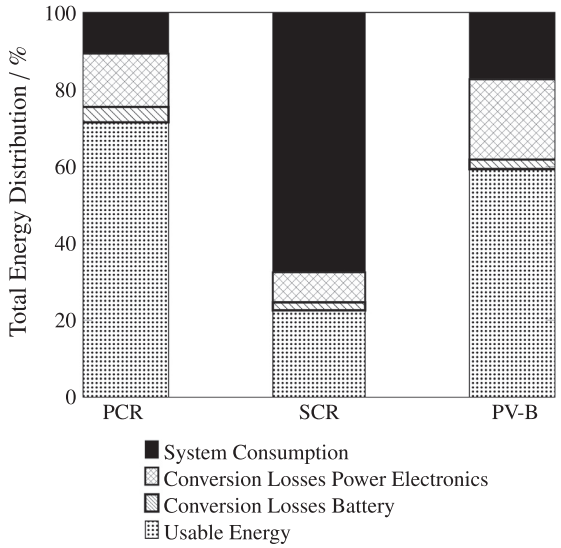

Fig. 14. Distribution of energy input in grid application scenarios primary control reserve, secondary control reserve and photovoltaic-battery.

utilization but with lower charge-based utilization, which results in low average power in operation.

Fig. 14 shows the distribution of total energy input into the system for the grid scenarios, separated into usable energy, conversion losses for battery and power electronics and the system consumption. Usable energy is the discharged energy during the simulation. Battery conversion losses are the smallest contribution in all scenarios due to the low average system power, which leads to an efficient operation in the battery (see Fig. 6). Power electronics losses are in comparison higher, again due to the low average system power which here leads to a less efficient operation (see Fig. 9). Relative energy for system consumption shows to be not negligible in all scenarios and is very large in the low utilization scenario SCR, in which the energy for system consumption is in total large compared to the low energy throughput.

Table 6
Energy loss breakdown in grid application scenarios.

	PCR	SCR	PV-B
Total losses (1-18)	28.5%	77.4%	40.7%
Conversion losses (1-9)	17.8%	9.9%	23.4%
Power electronics (1-6)	13.8%	7.8 %	20.9%
Inverter/Rectifier (1-4)	8.8%	4.9%	13.2%
IGBT (1-2)	7.5%	4.1%	11.4%
Switching (1)	6.8%	3.8%	10.5%
Conduction (2)	0.7%	0.3%	0.9%
Diode (3-4)	1.4%	0.7%	1.8%
Switching (3)	1.2%	0.7%	1.7%
Conduction (4)	0.1%	0.1%	0.1%
Grid interface (5-6)	5.0%	3.0%	7.7%
Core (5)	4.6%	2.7%	7.3%
Conduction (6)	0.4%	0.2%	0.4%
Battery (7-9)	4.0%	2.1%	2.5%
Overvoltage (7)	3.9%	1.9%	2.4%
Connector (8)	0.1%	0.1%	0.1%
Self discharge (9)	0.0%	0.0%	0.0%
System consumption (10-18)	10.7%	67.5%	17.3%
Thermal management (10-15)	3.7%	7.2%	5.8%
System (10-13)	1.0%	5.8%	1.8%
AirC Cooling (10)	0.8%	3.5%	1.5%
AirC heating (11)	0.0%	0.0%	0.0%
Fan battery zone (12)	0.2%	2.3%	0.3%
Fan PE zone (13)	0.0%	0.0%	0.0%
Power electronics (14)	2.2%	1.3%	3.5%
Fan power electronics (14)	2.2%	1.3%	3.5%
Battery (15)	0.5%	0.1%	0.4%
Fan battery (15)	0.5%	0.1%	0.4%
Monitoring (16-18)	7.1%	60.3%	11.5%
System (16)	0.7%	6.1%	1.1%
Power electronics (17)	3.9%	32.3%	6.3%
Battery (18)	2.5%	21.8%	4.1%

Fig. 15 shows the distribution of the conversion losses grouped by the relative system operating point. In all scenarios, the majority of conversion losses occurs at less than 10% of nominal power, which can mostly be attributed to the low efficiency of the power electronics. For PCR and PV-B, the losses at nominal power are very low in comparison, as the operating points are rarely requested by the load profile. Only SCR shows significant conversion losses at nominal power.

Table 6 shows the distribution of the previously defined 18 groups of energy loss mechanisms. The breakdown of conversion losses (1-9) explains the high losses in the low power operating regions. The loss mechanisms in the power electronics (1-6) which are relatively load-independent (switching of IGBTs and diodes (1,3), core losses in the interface module (5)) are the biggest contributors. In the battery rack (7-9), losses in the connector (8) and self-discharge (9) are relatively

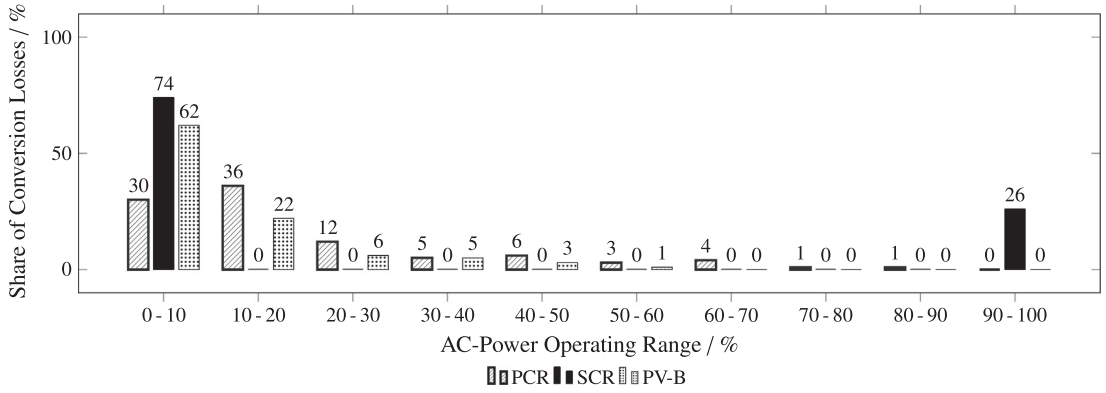

Fig. 15. Distribution of conversion losses (battery and power electronics) over system operating point in grid application scenarios primary control reserve, secondary control reserve and photovoltaic-battery.

small in comparison to the overvoltages (7).

Power consumption for the system thermal management (10-15) is relatively small as the annual average temperature of 8.9 °C at the system location is lower than the set-point temperatures in the system (15 °C in the battery zone) and thus air cooling with outdoor air can be utilized most of the time. For component thermal management, the share of power electronics (14) is much larger than that for the battery (15) due to the non-modulated fans.

Power consumption for control and monitoring (16-18) are dominated by the power electronics (17) due to the modular setup with a lot of control components. In general, the power consumption for control and monitoring is high due to the system being designed for research purposes with extensive monitoring.

In summary, the simulated grid applications confirm the results of the generic profiles. High charge throughput at high system powers improves efficiency in comparison to low utilized systems at low power. A higher temporal utilization does not increase system efficiency if the higher utilization time does not lead to higher charge throughput and thus lowers the average system power. For conversion losses, the battery losses are small compared to the power electronics losses, which are high in all cases due to a large share of low operating points in all scenarios. System power consumption overall is not negligible in typical grid applications and can outweigh the conversion losses if utilization is very low.

4. Conclusions

A system model of a stationary lithium-ion battery system is created for a use-case specific analysis of the system energy efficiency. The model offers a holistic approach by calculating conversion losses and auxiliary power consumption.

The simulation is parametrized based on a prototype container system with lithium iron phosphate cells (192 kWh). It features eight battery racks, which are each coupled to the low voltage grid with bi-directional inverters. For thermal management, the system has a two-zone climate system for separate and energy efficient temperature control of the battery racks and the power electronics, which are both air cooled.

Component models for the battery, power electronics, thermal management and the control and monitoring components are developed and coupled. The key loss mechanisms are identified and modeled. In total, 18 loss mechanisms are analyzed in detail. Both battery and power electronics loss calculation are validated against experimental data. The thermal management model features the calculation of the power consumption related to the battery, the power electronics, and the overall system. For the system model, a thermal resistance network is coupled with ambient data. All relevant control and monitoring components are included in the calculation of system power consumption.

The model is then evaluated using generic profiles which vary in terms of system power, operation time and average state of charge. Results show that low power operation (< 10% of system power) should be avoided due to relatively high losses in the power electronics. A high temporal utilization of the system is only beneficial if it leads to an increased charge throughput. The energy efficiency is shown to be relatively stable over the middle SOC range. Peak conversion energy efficiency is shown to be 87% under constant cycling with partial load at a charge-based system utilization of 41%. At full nominal power and constant cycling, conversion energy efficiency is 85%. Total system energy including auxiliary energy consumption reaches its peak value of 81% at full nominal power and constant cycling, as here the auxiliary energy consumption is the smallest relative to the here high energy throughput of the system.

The exemplary load profile derived from the grid applications Primary Control Reserve, Secondary Control Reserve and the storage of surplus photovoltaic power are evaluated with regards to the resulting performance. The simulation of grid applications confirm the results of the generic profiles. Conversion round-trip efficiency is in the range of 70–80% for all scenarios. Overall system efficiency, which also considers system power consumption, is 8–13 percentage points lower for Primary Control Reserve and the photovoltaic-battery application. However, for Secondary Control Reserve, the total round-trip efficiency is found to be extremely low at 23%, and thus 47 percentage points lower due to the low charge throughput.

5. Future work and outlook

Studies with a stronger focus on the thermal aspects could improve the accuracy of the battery model by introducing a more sophisticated approach, that calculates the surface as well as the core temperatures of the cells.

With real-world temperature measurements for the key system components, the thermal system model can be validated. For improved validation of the system thermal management model and its power consumption, real-world data of the system performance should be measured over a whole year to capture seasonal variations.

With the calculation of system losses enabled as a function of the system operating point through the model, energy optimized operation strategies can be developed, i.e. by avoiding low efficiency operating points. With a detailed prediction of conversion losses for both the power electronics and the battery, the total system power can be distributed to few power electronics/battery rack units, which promises significant reduction of the losses at partial load. This operation strategy, however, requires an active management of the battery rack state of charge levels across the separate battery racks. For the battery chemistry in this work, lithium iron phosphate, the flat open circuit voltage at the middle state of charge levels poses a strong challenge for the accurate state of charge estimation.

By coupling the simulation with an economic model, operation strategies can further be improved by including an accurate calculation of lost energy and thus costs. Optimized operational strategies could improve economic prospects for future system installations and enable new applications scenarios.

For the design of battery storage systems, the operation points of the load profile should be evaluated with a focus on the energy efficiency. Battery systems with multiple inverters in parallel operation could improve the part-load efficiency in the power electronics by variable activation. A sensitivity study evaluating different topologies and operations is planned.

As the system thermal management is shown to be a small part of the energy losses, simpler and less costly configurations compared to the system of this work should be further evaluated as possible options. However, the aging of the battery cells needs to be considered in this evaluation as well. The safety analysis of the battery system also needs to be included, studied and updated with prospective thermal management setups. The safety aspect should be studied in more detail and validated by experimental data, especially if higher system temperatures are expected to occur.

Regarding the monitoring and control components, it is shown that systems with high amounts of passive components should be reviewed for their standby power consumption as they are shown to be significant and should be included in future studies.

Acknowledgements

The authors thank Christian Huber and Korbinian Schmidt for the construction of the battery modules equipped with temperature sensors and Nick Becker for the work on the Simulink model of the power electronics unit. The research project IHEM is funded by the Federal Ministry for Economic Affairs and Energy within the “Funding initiative Electrical Storages” (Grant No. 03ET1205G) and cared by Project Management Juelich. The authors also thank the Bavarian Ministry of

Economic Affairs and Media, Energy and Technology for their support via the EEBatt project. Parts of this study were supported by the Vehicle Technologies Office, Office of Energy Efficiency and Renewable Energy, U.S. Department of Energy under contract number WBS1.1.2.406. The responsibility for the content of this publication lies with the author.

Appendix A. Power electronics model parameterization

In the prototype system under investigation, six power electronics units with a nominal power of 36 kW and two units with a nominal power of 16 kW are installed, resulting in a nominal system power of 248 kW. For the sake of simplification, we consider a system of eight 36 kW units in the following simulation resulting in a nominal power of 288 kW.

Parameters for the Simulink model are shown in Table A.7.

Table A.7
Power electronics model parameters for Simulink model based on Siemens S120 unit.

Simulation step width	0.5 µs	See text
Grid		
Line-to-line voltage	400 V	[60]
Frequency	50 Hz	[60]
Short circuit power	10 MVA	[60]
Inverter/Rectifier		
Control & DC Bus		
Switching frequency	8 kHz	[60]
Phase shift	0	see text
Max. modulation index	$2/\sqrt{3}$	See text
Proportional correction	0.5	See text
Integral correction	50	See text
DC bus capacity	1.410 mF	[68]
IGBT		
Conduction	$U_{CE}(I,T)$	[69]
Energy Switching Turn-on	$E_{On}(I, T = 125\,^{\circ}C)$	[69]
Energy Switching Turn-off	$E_{Off}(I, T = 125\,^{\circ}C)$	[69]
Thermal Impedance	Z_{th}	[69]
Diode		
Conduction	$U_F(I,T)$	[69]
Energy switching turn-off	$E_{Rec}(I, T = 125\,^{\circ}C)$	[69]
Thermal impedance	Z_{th}	[69]
Module casing		
Thermal impedance	9 mK/W	[69]
Thermal capacity	0.1 J/K	See text
Heat sink		
Thermal impedance	0.19 K/W	See text
Thermal capacity	1 J/K	See text
Grid interface module		
Core losses	108 W	[60]
Filter capacity	10 µF	[68]
Damping resistance	733 mΩ	[68]
Inductance to grid	1 µH	[68]
Inductance to inverter	48 µH	[68]
Inductor resistance to grid	13.6 mΩ	See text
Inductor resistance to inverter	13.6 mΩ	See text

Simulation step width is 0.5 µs resulting from convergence analysis for the model.

For the current control loop, proportional and integral correction are set to 0.5 and 50, respectively, to achieve load changes to full nominal power within one period of grid frequency (20 ms). The maximum modulation index for pulse width modulation is set to $2/\sqrt{3}$ in accordance with third-order harmonic pulse width modulation. Phase shift is set to zero as only active power is relevant for the grid services evaluated in this work.

Thermal modeling of the IGBT, the diode, module casing is based on the approached by [70]. The thermal capacity of the IGBT/Diode module casing and of the heat sink are reduced to low values to achieve fast convergence to thermal steady-state conditions, as the model is later reduced to steady-state evaluation. The thermal impedance for the heat sink to ambient is fitted to a value of 0.19 K/W from inverter overload tests on an inverter test bench. In these, the inverter turned off at the maximum junction temperature of 150 °C. As the fan cooling of power electronics unit is not modulated except turn-on/turn-off, the resulting thermal parameters can be used for all load simulations during operation. Also, power is limited in the simulation to not reach junction temperatures over 145 °C.

The core losses in the grid interface module are assumed to be independent of load and temperature and thus are taken as constant from manufacturer experimental data for the zero-load as 108 W [60]. For conduction losses, the resistances in the inductor to the grid and to the inverter/rectifier unit are calculated from the losses at nominal power again from manufacturer experimental data to 13.6 mΩ [68].

Appendix B. Thermal management model parameterization

Table B.8 shows the model parameters for the given thermal system model. For the share of the volume occupied by air, a value of 75% for both thermal zones is used, based on calculations considering the interior of the container.

Table B.8
System thermal management model parameters based on 20-foot container with two-zone thermal management.

Air thermal parameters		
Density ρ_{Air} (15 °C, Sea Lvl.)	1.225 kg/m^3	[71]
Specific heat $c_{p,Air}$ (15 °C, Sea lvl.)	1.005 kJ/kg/K	[71]
Container geometry		
Width	2.44 m	[72]
Height	2.90 m	[72]
Length	6.06 m	[72]
Vol. occupied by Air	75%	See text
Container thermal parameters		
Root heat conductivity	3.23 K m^2/W	[72]
Roof heat transfer (Inside)	0.10 K m^2/W	[73]
Roof heat transfer (Outside)	0.04 K ,m^2/W	[73]
Wall heat conductivity	3.23 K m^2/W	[72]
Wall heat transfer (Inside)	0.13 K m^2/W	[73]
Wall heat transfer (Outside)	0.04 K m^2/W	[73]
Floor heat conductivity	2.22 K m^2/W	[72]
Floor heat transfer (Inside)	0.17 K m^2/W	[73]
Floor heat transfer (Outside)	0.04 K m^2/W	[73]
PE zone geometry		
Width	2.44 m	[72]
Height	2.90 m	[72]
Length	0.50 m	[72]
Vol. occupied by Air	75%	See text
PE zone thermal parameters		
Containment heat conductivity	0.18 K m^2/W	[74]
Wall heat transfer (In-/Outside)	0.13 K m^2/W	[73]

Appendix C. Definition of grid application scenario PV-Battery

For photovoltaic power production a profile is generated in 15 min temporal resolution using the software Greenius 4.1.1 from the German Aerospace Center (DLR) [67]. Meterological data for photovoltaic power production is set to Berlin, Germany. The household load profile is taken as the Standard Load Profile H0 for residential German households in the temporal resolution of 1 h [75].

References

[1] International Energy Agency. Key world energy statistics; 2016 < https://www.iea.org/publications/freepublications/publication/key-world-energy-statistics.html > .
[2] European Commission. A roadmap for moving to a competitive low carbon economy in 2050; 2011 < http://eur-lex.europa.eu/legal-content/EN/ALL/?uri=CELEX:52011DC0112 > .
[3] Aneke M, Wang M. Energy storage technologies and real life applications – a state of the art review. Appl Energy 2016;179:350–77. http://dx.doi.org/10.1016/j.apenergy.2016.06.097.
[4] Weiß T, Schulz D. GERMANY: overview of the electricity supply system and an estimation of future energy storage needs; 2013.
[5] Fürstenwerth D, Waldmann L, et al. Study: electricity storage in the German energy transition; 2014.
[6] Nykvist B, Nilsson M. Rapidly falling costs of battery packs for electric vehicles. Nat Clim Change 2015;5(4):329–32. http://dx.doi.org/10.1038/nclimate2564.
[7] Technical University of Munich. Energy neighbor goes online; 2015 < https://www.tum.de/en/about-tum/news/press-releases/detail/article/32661/ > .
[8] Dunn B, Kamath H, Tarascon J-M. Electrical energy storage for the grid: a battery of choices. Science (New York, NY) 2011;334(6058):928–35, doi:http://dx.doi.org/10.1126/science.1212741.
[9] Younicos. Europe's first commercial battery power plant to triple its capacity; 2016 < https://www.younicos.com/europes-first-commercial-battery-power-plant-triple-capacity/ > .
[10] Munsell M. In shift to longer-duration applications. US energy storage installations grow 100% in 2016. Greentech Media < https://www.greentechmedia.com/articles/read/in-shift-to-longer-duration-applications-us-energy-storage-installations-gr > .
[11] Darcovich K, Kenney B, MacNeil DD, Armstrong MM. Control strategies and cycling demands for Li-ion storage batteries in residential micro-cogeneration systems. Appl Energy 2015;141:32–41. http://dx.doi.org/10.1016/j.apenergy.2014.11.079.
[12] Braun M, Büdenbender K, Magnor D, Jossen A. Photovoltaic self-consumption in Germany – using lithium-ion storage to increase self-consumed photovoltaic energy, doi:http://dx.doi.org/10.4229/24thEUPVSEC2009-4BO.11.2.
[13] Goebel C, Hesse H, Schimpe M, Jossen A, Jacobsen H-A. Model-based dispatch strategies for lithium-ion battery energy storage applied to pay-as-bid markets for secondary reserve. IEEE Trans Power Syst, doi:http://dx.doi.org/10.1109/TPWRS.2016.2626392.
[14] de Oliveira e Silva G, Hendrick P. Photovoltaic self-sufficiency of Belgian households using lithium-ion batteries, and its impact on the grid. Appl Energy 2017;195:786–99. http://dx.doi.org/10.1016/j.apenergy.2017.03.112.
[15] Nyholm E, Goop J, Odenberger M, Johnsson F. Solar photovoltaic-battery systems in Swedish households – self-consumption and self-sufficiency. Appl Energy 2016;183:148–59. http://dx.doi.org/10.1016/j.apenergy.2016.08.172.
[16] Mariaud A, Acha S, Ekins-Daukes N, Shah N, Markides CN. Integrated optimisation of photovoltaic and battery storage systems for UK commercial buildings. Appl Energy 2017;199:466–78. http://dx.doi.org/10.1016/j.apenergy.2017.04.067.
[17] Balcombe P, Rigby D, Azapagic A. Energy self-sufficiency, grid demand variability and consumer costs: Integrating solar PV, Stirling engine CHP and battery storage. Appl Energy 2015;155:393–408. http://dx.doi.org/10.1016/j.apenergy.2015.06.017.
[18] Truong CN, Naumann M, Karl RC, Müller M, Jossen A, Hesse HC. Economics of residential photovoltaic battery systems in Germany: the case of Teslas powerwall. Batteries 2016;2(2):14. http://dx.doi.org/10.3390/batteries2020014.
[19] Naumann M, Karl RC, Truong CN, Jossen A, Hesse HC. Lithium-ion battery cost analysis in PV-household application. Energy Proc 2015;73:37–47. http://dx.doi.org/10.1016/j.egypro.2015.07.555.
[20] Bennett CJ, Stewart RA, Lu JW. Development of a three-phase battery energy storage scheduling and operation system for low voltage distribution networks. Appl Energy 2015;146:122–34. http://dx.doi.org/10.1016/j.apenergy.2015.02.012.
[21] Castillo-Cagigal M, Caamaño-Martín E, Matallanas E, Masa-Bote D, Gutiérrez A, Monasterio-Huelin F, et al. PV self-consumption optimization with storage and active DSM for the residential sector. Solar Energy 2011;85(9):2338–48. http://dx.doi.org/10.1016/j.solener.2011.06.028.
[22] Schmiegel AU, Kleine A. Optimized operation strategies for PV storages systems

yield limitations, optimized battery configuration and the benefit of a perfect forecast. Energy Proc 2014;46:104–13. http://dx.doi.org/10.1016/j.egypro.2014.01.163.
[23] Purvins A, Papaioannou IT, Debarberis L. Application of battery-based storage systems in household-demand smoothening in electricity-distribution grids. Energy Convers Manage 2013;65:272–84. http://dx.doi.org/10.1016/j.enconman.2012.07.018.
[24] Zeh A, Witzmann R. Operational strategies for battery storage systems in low-voltage distribution grids to limit the feed-in power of roof-mounted solar power systems 2014;46:114–23.
[25] Zeh A, Mueller M, Hesse HC, Jossen A, Witzmann R. Operating a multitasking stationary battery storage system for providing secondary control reserve on low-voltage level. In: Speh R, editor. International ETG congress 2015, ETG-Fachberichte, VDE Verlag, Berlin [u.a.]; 2015 < http://ieeexplore.ieee.org/document/7388523/ > .
[26] Zeh A, Müller M, Naumann M, Hesse HC, Jossen A, Witzmann R. Fundamentals of using battery energy storage systems to provide primary control reserves in Germany. Batteries 2016;2(3):29. http://dx.doi.org/10.3390/batteries2030029.
[27] Patsios C, Wu B, Chatzinikolaou E, Rogers DJ, Wade N, Brandon NP, et al. An integrated approach for the analysis and control of grid connected energy storage systems. J Energy Storage 2016;5:48–61. http://dx.doi.org/10.1016/j.est.2015.11.011.
[28] Neubauer J, Pesaran A, Coleman D, Chen D, Analyzing the effects of climate and thermal configuration on community energy storage systems. In: Electrical energy storage applications and technologies (EESAT) conference; 2013 < http://www.nrel.gov/docs/fy14osti/60290.pdf > .
[29] Neubauer J. Battery lifetime analysis and simulation tool (BLAST) documentation; 2014 < http://www.nrel.gov/docs/fy15osti/63246.pdf > .
[30] Magnor D, Soltau N, Bragard M, Schmiegel A, de Doncker RW, Du Sauer. Analysis of the model dynamics for the battery and battery converter in a grid-connected 5kW photovoltaic system. In: 25th European photovoltaic solar energy conference, (PVSEC); 2010, doi:http://dx.doi.org/10.4229/25thEUPVSEC2010-4CO.1.4.
[31] Tjaden T, Weniger J, Messner C, Knoop M, Littwin M, Kairies K-P, et al. Open simulation model for grid-coupled PV battery systems. In: 32. Symposium photovoltaische solarenergie; 2017.
[32] Weniger J, Tjaden T. Performance-simulation model for AC-coupled PV battery systems (PerModAC): Documentation V1.0 (01.03.2017) < https://pvspeicher.htw-berlin.de/veroeffentlichungen/daten/permodac/ > .
[33] Tjaden T, Weniger J, Bergner J, Schnorr F, Quaschning V. Influence of the location and user behaviour on the energy evaluation of PV storage systems (German title: Einfluss des Standorts und des Nutzerverhaltens auf die energetische Bewertung von PV-Speichersystemen). In: 29. Symposium photovoltaische solarenergie; 2014.
[34] Weniger J, Tjaden T, Quaschning V. Comparison of various indicators for evaluation of the energy performance of PV battery systems (German title: Vergleich verschiedener Kennzahlen zur Bewertung der energetischen Performance von PV-Batteriesystemen). In: 32. Symposium photovoltaische solarenergie; 2017.
[35] Gatta FM, Geri A, Lauria S, Maccioni M, Palone F. Battery energy storage efficiency calculation including auxiliary losses: Technology comparison and operating strategies. In: PowerTech, 2015 IEEE Eindhoven; 2015. p. 1–6, doi:http://dx.doi.org/10.1109/PTC.2015.7232464.
[36] Gatta FM, Geri A, Lamedica R, Lauria S, Maccioni M, Palone F, et al. Application of a LiFePO4 battery energy storage system to primary frequency control: simulations and experimental results. Energies 2016;9(11):887. http://dx.doi.org/10.3390/en9110887.
[37] Rydh CJ, Sandén BA. Energy analysis of batteries in photovoltaic systems. Part I: performance and energy requirements. Energy Convers Manage 2005;46(11–12):1957–79. http://dx.doi.org/10.1016/j.enconman.2004.10.003.
[38] Rydh CJ, Sandén BA. Energy analysis of batteries in photovoltaic systems. Part II: energy return factors and overall battery efficiencies. Energy Convers Manage 2005;46(11–12):1980–2000. http://dx.doi.org/10.1016/j.enconman.2004.10.004.
[39] Technical University of Munich. Web portal of the Energy Neighbor < https://www.energyneighbor.de/en/home.html > .
[40] Technical University of Munich. EEBatt – Interdisciplinary Energy Storage Research Project < https://www.mse.tum.de/en/eebatt/ > .
[41] Lin X, Perez HE, Mohan S, Siegel JB, Stefanopoulou AG, Ding Y, et al. A lumped-parameter electro-thermal model for cylindrical batteries. J Power Sour 2014;257:1–11. http://dx.doi.org/10.1016/j.jpowsour.2014.01.097.
[42] Dreyer W, Jamnik J, Guhlke C, Huth R, Moskon J, Gaberscek M. The thermodynamic origin of hysteresis in insertion batteries. Nat Mater 2010;9(5):448–53. http://dx.doi.org/10.1038/NMAT2730.
[43] Kim J, Seo G-S, Chun C, Cho B-H, Lee S. OCV hysteresis effect-based SOC estimation in extended Kalman filter algorithm for a LiFePO4-C cell. In: IEEE international electric vehicle conference (IEVC); 2012. p. 1–5, doi:http://dx.doi.org/10.1109/IEVC.2012.6183174.
[44] Srinivasan V, Newman J. Existence of path-dependence in the LiFePO[sub 4] electrode. Electrochem Solid-State Lett 2006;9(3):A110. http://dx.doi.org/10.1149/1.2159299.
[45] Hu X, Li S, Peng H. A comparative study of equivalent circuit models for Li-ion batteries. J Power Sour 2012;198:359–67. http://dx.doi.org/10.1016/j.jpowsour.2011.10.013.
[46] Bernardi D. A general energy balance for battery systems. J Electrochem Soc 1985;132(1):5. http://dx.doi.org/10.1149/1.2113792.
[47] Rao L. Heat-generation rate and general energy balance for insertion battery systems. J Electrochem Soc 1997;144(8):2697. http://dx.doi.org/10.1149/1.1837884.
[48] Ye Y, Shi Y, Cai N, Lee J, He X. Electro-thermal modeling and experimental validation for lithium ion battery. J Power Sour 2012;199:227–38. http://dx.doi.org/10.1016/j.jpowsour.2011.10.027.
[49] Forgez C, Vinh Do D, Friedrich G, Morcrette M, Delacourt C. Thermal modeling of a cylindrical LiFePO4/graphite lithium-ion battery. J Power Sour 2010;195(9):2961–8. http://dx.doi.org/10.1016/j.jpowsour.2009.10.105.
[50] Thomas KE, Newman J. Thermal modeling of porous insertion electrodes. J Electrochem Soc 2003;150(2):A176. http://dx.doi.org/10.1149/1.1531194.
[51] Rumpf K, Moraleja K, Geder J, Jossen A. Comparing the specific heat capacity of lithium-ion cells using adiabatic calorimetry. In: Batterieforum Deutschland; 2016.
[52] Keyser MA, Pesaran A, Mihalic MA, Ireland J. Calorimeters for testing energy storage systems and power electronics methods of making the same and methods of use: US Patent; 2016 < https://worldwide.espacenet.com/publicationDetails/biblio?FT=D&date=20161025&DB=&locale=&CC=US&NR=9476780B2&KC=B2&ND=1 > .
[53] Keyser M, Saxon A, Powell M, Shi Y. Battery thermal characterization. In: Vehicle technologies office (VTO) annual merit review and peer evaluation; 2016 < http://www.nrel.gov/docs/fy16osti/66260.pdf > .
[54] National Renewable Energy Laboratory. Isothermal battery calorimeters; 2015 < http://www.nrel.gov/docs/fy15osti/63245.pdf > .
[55] Pesaran AA, Russell DJ, Crawford JW, Rehn R, Lewis EA. A unique calorimeter-cycler for evaluating high-power battery modules. In: Battery conference on applications and advances; 1998. pp. 127–31.
[56] Davis JR, et al. Copper and copper alloys. ASM International; 2001.
[57] Pires VF, Romero-Cadaval E, Vinnikov D, Roasto I, Martins JF. Power converter interfaces for electrochemical energy storage systems–a review. Energy Convers Manage 2014;86:453–75. http://dx.doi.org/10.1016/j.enconman.2014.05.003.
[58] Kolar JW, Drofenik U. A general scheme for calculating switching- and conduction-losses of power semiconductors in numerical circuit simulations of power electronic systems: Uwe Drofenik; Johann W. Kolar. In: I. o. E.E. o. Japan, editor. IPEC-Niigata 2005. Institute of Electrical Engineers of Japan (Tokyo); 2005.
[59] Hornkamp M, Tschirbs R. Current shunt resistors integrated in IGBT power modules for medium power drive application. In: PCIM Asia; 2004.
[60] Siemens AG. Sinamics S120 manual; 2016 < https://support.industry.siemens.com/cs/ww/de/view/109740020/en?dl=en > .
[61] Lobanoff VS, Ross RR. Centrifugal pumps: design and application: design and application, 2nd ed. Gulf Professional Publishing; 2013.
[62] German institute of standardization. DIN EN ISO 6946:2007 Building components and building elements – Thermal resistance and thermal transmittance - Calculation method < https://www.beuth.de/de/norm/din-en-iso-6946/100557483 > .
[63] European Network of Transmission System Operators for Flectricity. Operation handbook. Policy 1: load-frequency control and performance.
[64] Müller M, Zeh A, Rohr S, Schuster SF, Campestrini C, Hesse H, et al. Evaluation of the aging behaviour of stationary lithium-ion battery storage systems for different photovoltaic-driven applications in low voltage grids. In: 31st European photovoltaic solar energy conference and exhibition. p. 3092–8, doi:http://dx.doi.org/10.4229/EUPVSEC20152015-7DV.4.4.
[65] German Transmission System Operators. Key points and degrees of freedom for the provision of primary control reserve. Guidelines for providers of primary control reserve. (German title: Eckpunkte und Freiheitsgrade bei Erbringung von Primärregelleistung. Leitfaden für Anbieter von Primärregelleistung); 2014 < https://www.regelleistung.net/ext/download/eckpunktePRL > .
[66] German Transmission System Operators. REGELLEISTUNG.NET Internet platform for the allocation of control reserve < https://www.regelleistung.net/ext/?lang=en > .
[67] German Aerospace Center. Greenius < http://freegreenius.dlr.de/ > .
[68] Siemens AG. Unpublished data.
[69] Infineon. Technical Information IGBT-modules FS150R12KE3 (02.10.2013) < http://www.infineon.com/dgdl/Infineon-FS150R12KE3-DS-v03_01-en_de.pdf?fileId=db3a304412b407950112b4311d745388 > .
[70] Graovac Dusan, Pürschel Marco. Infineon application note - IGBT power losses calculation using the data-sheet parameters; 2009.
[71] International Civil Aviation Organization. ICAO standard atmosphere.
[72] Container manufacturer specifications.
[73] German institute of standardization. DIN V 18599-7:2016-10 Energy efficiency of buildings - Calculation of the net, final and primary energy demand for heating, cooling, ventilation, domestic hot water and lighting - Part 7: Final energy demand of air-handling and air-conditioning systems for non-residential buildings < https://www.beuth.de/de/vornorm/din-v-18599-7/259375956 > .
[74] Electrical cabinet manufacturer specifications.
[75] Federal Association of the German Energy and Water Industries. Standard Load Profile H0.

4 Energy efficiency evaluation of grid connection scenarios for stationary battery storage systems

This section introduces the paper *Energy efficiency evaluation of grid connection scenarios for stationary battery storage systems* and is based on the paper without further reference.

Chapter 3 showed that the PE in the grid connection can be a major source of energy losses in BESS. In this paper, different grid connection topologies for BESS are investigated towards their efficiency.

Utility-scale BESS typically comprise of several PE units. Various grid connection topologies result, depending on the conversion stages within each unit, the PFDS between the PE units and additionally the grid level (LV/MV) to which the system is connected. These grid connection scenarios vary with respect to the choice of the power conversion technology and how the different technologies are connected and how they distribute the power flow within the grid connection.
Detailed models are developed for the key components of the various topologies, the inverter/rectifier, the DC-DC converter and the transformer. The simulation model parameters are based on state-of-the-art industry components and compared against experimental data.
The component models are coupled to grid connection topology models. The representative system is again based on the *Energy Neighbor*, which was previously been introducted in Section 2.2.1 and analyzed for its overall system energy efficiency in Chapter 3. The conversion losses and resulting energy efficiency are compared between the various topologies.

The comparison of single-stage and two-stage topologies shows that conversion setups without the intermediate DC link conversion stage are more efficient than those with. Therefore, it is desirable to choose a battery rack topology that supports the required DC voltage of the used inverter/rectifier.
The incremental PFDS, which distributes the actual load to the minimum amount of necessary inverters/rectifiers is more efficient than operating more inverters/rectifiers than necessary as in the homogeneous PFDS, in particular at low loads. Hence, a setup should be realized that allows the shutdown of non-necessary PE.
From a technical perspective, to minimize dissipation losses, the connection to the LV grid is more efficient due to the absence of the transformer which introduces extra conversion losses and causes high amounts of no-load losses. Thus, if possible, considering grid limitations, system power capacity and aspects of the system application, a connection to the LV grid is preferable. It should be mentioned, that the results cover only the BESS. The evaluation is thus limited to the perspective of the BESS operator and does not include the losses occurring in the distribution grid itself.
Following these results, the single-stage LV topology with incremental PFDS achieves the best results concerning the efficiency of the grid connection for the system, while the two-stage MV topology with homogeneous PFDS causes the highest losses and leads to the lowest efficiency.
Finally, the topologies are evaluated in two real-world grid application scenarios, namely PCR and SCR, which both confirm the previous conclusions. Losses between the evaluated grid connection scenarios, as well as between the grid application scenarios vary significantly.

Author contribution The author of this thesis initiated, structured and lead the research from the idea along with industry collaboration towards the final results. The paper draft was written also by the author of this thesis. The model development and evaluation were conducted in collaboration with Nick Becker through his master's thesis. Parts of the results have also been presented at the conferences *International Renewable Energy Storage Conference (IRES) 2018* by the author of this thesis.

Energy efficiency evaluation of grid connection scenarios for stationary battery storage systems

Michael Schimpe, Nick Becker, Taha Lahlou, Holger C. Hesse, Hans-Georg Herzog, Andreas Jossen

Energy Procedia 155, pp. 77-101, 2018

Permanent weblink:
https://doi.org/10.1016/j.egypro.2018.11.065

Reproduced under the terms of the Creative Commons Attribution 4.0 License (CC BY-NC-ND 4.0, http://creativecommons.org/licenses/by-nc-nd/4.0/), which permits non-commercial non-derivative reuse of the work, provided the original work is properly cited.

Available online at www.sciencedirect.com

ScienceDirect

Energy Procedia 155 (2018) 77–101

Energy Procedia

www.elsevier.com/locate/procedia

12th International Renewable Energy Storage Conference, IRES 2018

Energy efficiency evaluation of grid connection scenarios for stationary battery energy storage systems

Michael Schimpe[a,*], Nick Becker[a], Taha Lahlou[a], Holger C. Hesse[a], Hans-Georg Herzog[a], Andreas Jossen[a]

[a]*Technical University of Munich (TUM), Department of Electrical and Computer Engineering, Arcisstr. 21, 80333 Munich, Germany*

Abstract

The connection to the electrical grid is a key component of stationary battery energy storage systems. Utility-scale systems comprise of several power electronics units. Various grid connection topologies may be used, depending on the conversion stages within each unit, the load distribution between the power electronics and additionally the grid level to which the system is connected. The energy efficiency, which is a key performance indicator for storage systems, is compared between various scenarios. Detailed models are developed for the key components: The inverter/rectifier, the DC-DC converter, and the transformer. The respective model parameterization is based on state-of-art industry components and compared against experimental data. Two grid application scenarios, namely Primary Control Reserve and Secondary Control Reserve, are simulated for a comparison in reference application scenarios often discussed for utility-scale battery energy storage systems. Results show that grid connection setups without an intermediate DC link conversion stage are more efficient than those with. The optimum number of inverters in dependence on the actual load is determined. The connection to the low-voltage grid is more efficient due to the absence of the transformer which introduces significant additional losses. The topology models developed herein can be integrated into system models that include the overall systems or used for the design of novel battery systems grid connection topologies with detailed evaluation down to the component level.

© 2018 The Authors. Published by Elsevier Ltd.
This is an open access article under the CC BY-NC-ND license (https://creativecommons.org/licenses/by-nc-nd/4.0/)
Selection and peer-review under responsibility of the scientific committee of the 12th International Renewable Energy Storage Conference.

Keywords: Stationary Battery Energy Storage; Power Electronics Topology; Grid-Connected Inverter; Energy Efficiency; Low-Voltage Grid; Medium-Voltage Grid

1. Introduction

In future electric grids with a high share of volatile renewable energy sources, energy storage systems can compensate for time shifts between electricity production and demand, as well as provide grid services [1–3]. Battery energy

*Corresponding author. Tel.: +49-(0)89-289-26967
E-mail address: michael.schimpe@tum.de

1876-6102 © 2018 The Authors. Published by Elsevier Ltd.
This is an open access article under the CC BY-NC-ND license (https://creativecommons.org/licenses/by-nc-nd/4.0/)
Selection and peer-review under responsibility of the scientific committee of the 12th International Renewable Energy Storage Conference.
10.1016/j.egypro.2018.11.065

storage systems (BESS), notably lithium-ion based systems, lately achieved significant technical and economic improvements [1, 4], which have lead to an increasing interest and growth in installations for grid ancillary services [5].

The grid connection of BESS enables batteries to charge and discharge from, respectively to, the electrical grid. To connect the direct current (DC) of batteries to the electrical grid, which is based on alternating current (AC), power electronics components (PE) are required for the conversion of electricity and the control of the power flow. If the grid voltage differs from the AC voltage range of the PE, a transformer is often used to convert the voltage to the non-matching and typically higher voltage levels of the electrical grid.

The energy efficiency is a key performance indicator for BESS. As the grid connection requires different conversion steps, a series of energy losses occur. Depending on the battery power and voltage, different types of power electronics, i.e. DC-DC converters and inverters/rectifiers, are required. As BESS are applicable to a wide array of applications, which can also require specific points of connection to the grid, furthermore the grid level to which the BESS is connected, can vary. A variety of technical possible grid connection topologies arises, which may differ in terms of their energy efficiency.

This work aims for a simulation-based review of the energy efficiency of grid connection topologies. Models are developed for an inverter/rectifier, a DC-DC converter, and a transformer. The models are parameterized based on available industry components, to focus on application-oriented results. The model results for the energy losses are compared against experimental data for validation. Based on these three component models, eight scenarios for the grid connection are proposed and evaluated.

The evaluation is based on an actual prototype system, a 192 kWh, 20-foot container battery system, named the *Energy Neighbor* [6]. The system features eight individual high-voltage battery racks.

The evaluation thus encompasses the simulation of the grid connection for the eight battery racks in various topologies. Finally, actual grid application scenarios are simulated for an application-oriented comparison of the different topologies, namely Primary Control Reserve and Secondary Control Reserve.

The remainder of this contribution is structured as follows: Section 1.1 introduces the examined grid connection topologies, followed by a review of the literature in Section 1.2. In Section 2 the topology simulation model, the component models, and their parameterization are described. Results of component models and the grid application simulations are discussed in Section 3. Section 4 concludes the key findings of the comparison, and Section 5 gives an outlook on the study's implications for the design and operation of the grid connection of BESS.

1.1. Grid connection topologies

Three parameters of application-ready industry-component-based grid connection topologies are analyzed: *Conversion stages* within the power electronics (single-stage/two-stage converters), *load distribution* within the power electronics (homogeneous operation/incremental operation) and finally the *grid level* (low-voltage/medium-voltage) to which the system is connected.

The study thus evaluates eight grid connection scenarios, which derive from the combined variation of the three parameters. The three parameters are each explained in the following Sections 1.1.1 to 1.1.3.

1.1.1. Power electronics conversion stages

Depending on the battery DC power and DC voltage and the AC voltage, different conversion stages are used for the bidirectional AC/DC conversion. BESS typically use DC pack voltages below 1000 V due to safety issues of the installation and maximum voltages of up to 1200 V of the commonly used IGBTs [7]. As BESS require charging and discharging power, the PE require bidirectional operation capability.

Pires et al. [8] described three technology types of power converters as interfaces between electrochemical energy storage systems and electrical AC grids. These are divided into standard, multilevel and multiport technology which are subdivided into single- and two-stage topologies. The standard technology is based on the voltage source inverter (VSI) and defines the simplest structure. The shortfalls of the traditional VSI, such as the limitation of the AC voltage by the DC link voltage can be overcome by the proposal of Z-source and quasi-Z-source inverters. Single-stage converters can be achieved with low device counts, costs, and losses [8]. Two-stage converters can provide suitable DC voltage levels so that the inverter stage can be directly interfaced into the electrical grid [8]. More sophisticated converter technologies, such as Multilevel and multiport technologies appear to have advantages for certain storage setups, however, come at the cost of additional switching devices and more complex control algorithms [8] and are,

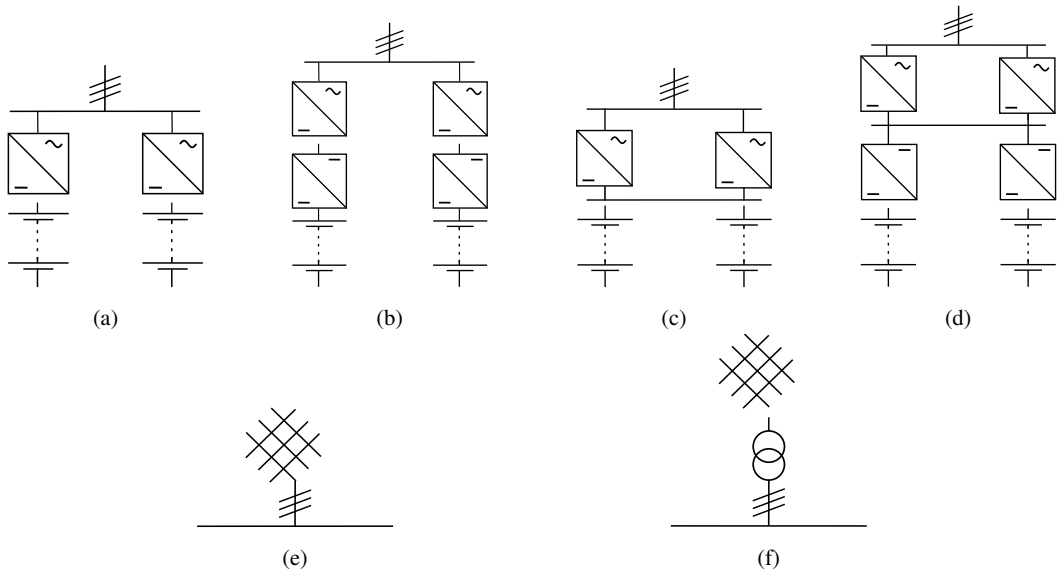

Fig. 1. Overview of evaluated grid connection topologies: a) Single-stage with dedicated power electronics per battery; b) Two-stage with dedicated power electronics per battery; c) Single-stage with common DC bus; d) Two-stage with common DC bus; e) Connection to the low-voltage grid; f) Connection to the medium-voltage grid via a transformer. All topologies are drawn for an exemplary system with two battery racks, simulation results of this study are based on a system with eight battery racks. Derivative of Figure by Hesse et al. ([1], used under CC-BY.)

as of today, not industrially available for BESS and thus excluded to focus the study on topologies based on available technologies.

Single-Stage Converters directly convert bidirectionally between AC and DC [8]. For voltage source inverters, the conversion is limited in terms of the maximum ratio between AC and DC voltage, depending on the pulse width modulation method: For a conversion using a VSI with third harmonic injected pulse width modulation between three-phase 400 V AC, which is used in the European low-voltage grid, and DC, a theoretical minimum voltage of 566 V DC is required. In practice, the minimum voltage of 600 V DC is typically specified, as this meets the above-mentioned criteria for the conversion to AC with a buffer for voltage variations in the grid and overvoltages in the filter components. Fig. 1a shows a single-stage converter setup connecting battery racks each dedicated and directly to the electrical low-voltage voltage. In this figure, all topologies are drawn for a system with only two battery racks for the sake of simplification. The evaluation is nonetheless based on the actual prototype system with eight battery racks.

Two-Stage Converters introduce an intermediate DC stage within the converter, to and from which lower or higher DC voltages are converted [8]. This enables a connection of a wider voltage range for BESS. The increased voltage range can be used to connect low voltage batteries or to fully utilize a battery with a wide voltage range over the state of charge. Typical DC link voltages are 600 V, as this meets the above-mentioned criteria for the conversion to AC via the VSI with the described buffer. Fig. 1b shows a two-stage converter setup connecting battery racks each dedicated to the electrical low-voltage grid.

1.1.2. Power electronics load distribution

If multiple battery racks are installed in one system, the question of load distribution between the power electronics units and the battery racks arises.

In this study, all modeled battery racks, and single-stage/two-stage units have identical specifications in terms of nominal power and capacity. The topologies are set up and controlled to result in equal loads on all battery racks in the system. Assuming no variation of power flow due to temperature imbalances or production variation between the battery racks [9], equal power flows and state of charge levels consequently result for all racks. The resulting current in all battery racks is thus equal and consequently the resulting battery losses in the different configurations as well. They are therefore excluded from the study, and the focus is put on the losses in the grid connection only.

As such, this leaves the investigation of load distribution between the PE units.

Based on the considered equal battery load across all battery racks in this work, a grid connection topology with dedicated PE units for each battery rack (see Fig. 1a and Fig. 1b) requires each unit to have equal loads. The total system power is divided equally among the PE units and thus battery racks. This operation mode is defined as *homogeneous operation*.

If several inverters/rectifiers connect in parallel to the electrical grid to a single DC source, a common DC bus is formed (see Fig. 1c-1d). In this configuration, all battery racks are connected in parallel and thus can be operated as one single, large battery that has one state-of-charge level. The distribution of the total system power between the inverter/rectifier units can now be varied without introducing different state-of-charge levels between the different racks.

The arising issue of circulating currents between the parallel connected units can be mitigated through various methods which are discussed in the later following literature review in Section 1.2.

In this work, only topologies and load distribution strategies that lead to an identical state-of-charge within the system are evaluated. Topologies with separate battery racks (see Fig. 1a) thus are only evaluated for homogeneous operation.

As the loss behavior of inverters has a non-linear dependence with the output power, largely due to the switching losses in the semiconductors and core losses in the filters, it is beneficial for the efficiency to turn on as few inverters/rectifiers as possible. Thus, only the necessary number of inverters/rectifiers is in operation. Between the inverters in operation, we assume that power is distributed equally. This operation mode is defined as *incremental operation*, as units are incrementally activated with increasing system power.

For clarification, Fig. 2a shows the exemplary load distribution between two inverter units, unit 1 and unit 2. The relative unit power (y-axis) gives the power for the separate units over the relative system power (x-axis) which is their combined power output. In the homogeneous operation, the relative unit power increases equally with the system power over the whole operating range and both units operate at identical power. In incremental operation, when the relative system power is below 50 %, only unit 1 is turned on and provides the complete system power alone. At total system power of 50 %, unit 2 turns on. As system power is now shared equally among both units, relative power for

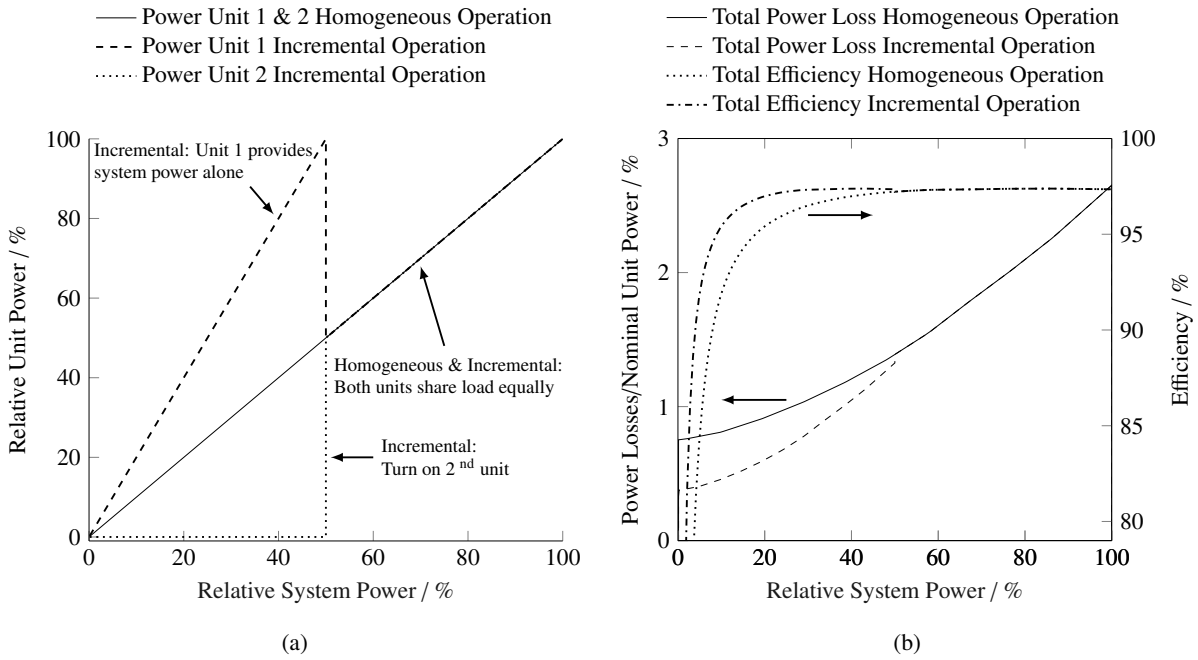

Fig. 2. Comparison of operation modes for two inverters in homogeneous and incremental operation mode: a) Load distribution, b) Power loss and energy efficiency. Simulation data for the power loss and efficiency per unit is taken of an inverter/rectifier Siemens Sinamics S120 36 kW unit, which is further studied in Section 2.2.

unit 1 drops to 50 % and relative power for unit 2 is also at 50 % after turn-on. In this state, where both units are in operation, there is no difference in load distribution between homogeneous and incremental operation.

Fig. 2b shows the corresponding results for the total power losses and the energy efficiency in each operation mode. The data for the power loss and efficiency per unit is taken for an inverter/rectifier Siemens Sinamics S120 36 kW unit, which is studied in detail and explained in Section 2.2.

At the turn-on of the system (relative system power ≠ 0 %), the total power loss for homogeneous operation is twice as high as for incremental operation. For homogeneous operation, the load-independent losses occur in two units, whereas in incremental operation only one unit contributes to the losses. The results for the energy efficiency show the efficiency gain in the incremental operation mode at system loads between 0 % to 50 % as well as the identical efficiency for both operation modes when all units are in operation and at equal load.

For single-stage or two-stage converter systems and homogeneous operation (see Fig. 1a and Fig. 1b) this power distribution requires no common DC bus.

In single-stage converter systems for incremental operation (see Fig. 1c), a common DC bus for all battery racks is set up. For the two-stage converter systems in incremental operation (see Fig. 1d), the common DC bus couples the DC-DC converters. It is noted, that a common DC bus could also be introduced at the battery level, enabling incremental operation for both DC-DC converters as well as the inverter/rectifier units. This scenario is not included in this study but could be evaluated with the method proposed by coupling the models of the inverter/rectifier and the DC-DC converter together.

It is also noted, that this study is a power-flow-based energy efficiency evaluation. In practice, product-specific requirements or regulations might prohibit the installation of units in a specific configuration or require additional safety equipment, such as isolating transformers. This study does not cover these aspects and should be interpreted as a simulation study for efficiency calculations only.

1.1.3. Grid level

Through the coupling via transformers, BESS can technically be connected to all grid levels. Grid levels in the exemplary German-Austrian-Switzerland grid are as follows: Extra-high voltage in the transmission system (220 kV AC or 380 kV AC), high voltage in the supra-regional distribution system (36 to 150 kV AC), medium voltage in the regional distribution system (1 to 36 kV AC) and low-voltage in the local distribution system (0.4 kV AC) [1, 10].

Today the majority of BESS are installed in the low-voltage (LV) and medium-voltage (MV) grid level [1, 11, 12]. Behind-the-meter applications, e.g. using the BESS to increase the self-consumption of energy produced by a photovoltaic system [13] or to reduce the demand charge rate by reducing peak loads, require the connection to the grid level of the meter [1, 14]. This is typically the LV level for residential and small industrial customers. Large industrial customers, which operate their own transformers, may also have access to the MV level behind their meter [1]. Local grid applications, e.g. BESS voltage control [15] or BESS transformer relief [16], may require the BESS at the specific grid level, typically again the LV and MV level [1]. Systems providing grid ancillary services, e.g. control reserve power [17], can feature system power of several Megawatt and are due to practical power limitations often installed at the MV level [1, 18]. However, pooling of multiple smaller units is another option and thus also smaller systems in the LV level can participate for some ancillary services [19, 20]. The focus on LV and MV is also in accordance with the grid feed-in of a large share of variable renewable energy sources. E.g. in Germany, 98 % of all photovoltaic installations feed into the LV or MV grid level and 50 % onshore wind turbine feed into the MV grid level [12].

This work evaluates the grid connection without a transformer to the LV grid (see Fig. 1e) as well as the grid connection to the MV grid through a transformer (see Fig 1f). The method can, however, be applied to a grid connection through a transformer to any grid level. Using multiple transformers can increase the reliability of the grid connection, but is in general less energy efficient and not discussed further.

1.2. Literature and state of the art review

Few studies compared the energy efficiency of the typical grid connection topologies: The energy efficiency is evaluated for single units of inverters/rectifiers in [21–24] and specific grid connection topologies in broader system model approaches in [16, 25]. Design challenges of parallel operated inverters with a common DC and AC bus, as necessary for incremental operation modes, are discussed in [26–28]. Existing reports by power electronics manufac-

turers confirm the availability of components capable of parallel operation [29, 30]. The given literature is discussed in the following.

According to King et al. [21], the relationship between the AC and DC power out- and input of a VSI appears to be nearly linear. However, the losses within the inverter and the electrical characteristics of the inverter circuit show nonlinear coherences at different voltage and power levels. To achieve an adequate representation of the relationship between the input and output power, a model fitting process is suggested that considers different performance parameters of the semiconductor switches. The suggested model equations show a linear and a square power coherence. The model equation is fitted to measurements considering various power and voltage levels.

Notten et al. [22] proposed a method for the modeling of the loss behavior of a VSI, which is based on the constant load-independent part and a second part which includes all the load-dependent losses and show a square-power correlation to the load. The parameters of the suggested equation are based on measurements at different power states. Therefore, the method can be based on measurements representing the relationship between the input and output power.

Ponnaluri et al. [23] introduced a method for the calculation of the power losses occurring during the conversion from DC to AC and vice versa. The method uses the switching and conduction behavior of the power electronic switches. The conduction behavior is hereby reduced to a voltage offset and the equivalent internal resistance, which corresponds to the current flow. The switching behavior is based on the switching energies during the turn-on and -off process. Resulting dependencies are thus the DC voltage, the switching frequency, and the power flow. They further stated that for the correct power loss calculation, the average current values cannot be used and the actual current during the entire AC cycle must be considered.

Casanellas [24] described a more detailed approach for the calculation of power losses in VSIs considering bidirectional IGBTs with anti-parallel diodes. The power losses are split up into conduction and switching losses for the IGBTs and diodes and have to correspond to the alternating current and voltage of the VSI's AC side. Therefore, the modulation function and the modulation index during the power conversion is required. Furthermore, Casanellas approximated the conduction and switching behavior with linear equations considering current and temperature variation. Simulation results for the power losses are reported accurate with 10 % deviation to experimental measurements.

Patsios et al. [16] developed a BESS system model coupled with a grid model. For the power electronics, a discrete time model based on a single IGBT was implemented, and for the transformer load-free losses were included. They attributed most of the losses to the power electronics, which motivates a more detailed study on the subject.

Chatzinikolaou and Rogers [25] presented a method for the evaluation of grid-connected BESS designs. They calculated the steady-state power losses of the power electronics, the battery pack and the balancing circuits. Three topologies connected to the 11 kV grid level were compared: a LV battery with single-stage three-phase bridge inverter and a step-up transformer, an intelligent high-voltage battery featuring module level MOSFETs for module balancing and a single-stage two-level converter interface without a transformer, and a battery using a cascaded H-bridge multilevel converter. The losses in the power electronics were calculated as the switching and conduction losses in the IGBTs respectively the MOSFETs and the turn-off losses of the diodes, whereas the turn-on losses of the diodes were considered as not significant. The transformer was implemented with a constant efficiency. The power electronics were evaluated for a nominal size and load of 1 MW. Overall efficiency was found to be the highest for the LV battery with a step-up transformer and lowest for the multilevel converter. Transformer, semiconductor conduction and switching losses were separately calculated and showed strong deviations between the different system setups.

Khadem et al. [26] presented a review of the issues occurring during parallel VSIs with a common AC and DC bus and mitigation approaches. Differences in the amplitude of voltage and phase angle of parallel operation inverters result in active and/or reactive power circulations. For parallel operation, the output voltage of all inverters must be kept strictly in phase in order to guarantee equal active power output for the corresponding inverters. Reactive currents can still circulate between inverters, if their output voltage magnitudes differ from each other, leading to unnecessary inverter load and losses. This problem can be overcome with control strategies, which can be classified as active load sharing/current distribution and droop control. Active load sharing generates reference currents for each parallel-connected inverter and tries to achieve an equal current distribution. The drawback is the essential communication between all inverters and the resulting reduction of reliability in case of interconnection mismatches. Droop control works without communication between the inverters. The inverters are controlled in such a way that the amplitude

and frequency of the reference voltage signal will follow a droop as the load current increases and these droops are used to allow independent inverters to share the load in proportion to their capacities.

Zhang et al. [27] showed that circulating currents occur in parallel VSIs with a common AC and DC bus if the carrier signals are unsynchronized. A possible solution is to use line-frequency transformers with the same number of inverters on the AC side, but this adds additional mass, cost, and volume. Therefore, the effects of different pulse width modulation (PWM) methods on the circulation currents are analyzed. While unipolar PWM causes circulation currents and high leakage currents, it is shown that a bipolar PWM in a conventional full bridge inverter leads to the cancellation of circulating currents and the lowest amount of leakage currents.

Wei et al. [28] developed a control scheme for parallel VSIs with a common AC and DC bus that reduces circulating-current by adding a circulating-current control loop to a frequency and voltage droop plus virtual impedance control method. The scheme leads to fewer switching states that allow cross and zero-sequence currents and achieves proper current separation between multiple inverters/rectifiers. Due to the reduction of the circulation current, the inverters/rectifiers act as if they were independently operating in the energy grid.

Based on the existing studies on parallel VSIs with a common AC and DC bus, it is shown that the possibly introduced circulating currents can be avoided using various control schemes. This work thus does not include such detrimental effects of the parallel operation. Finally, a review of the available industrial inverter systems confirms the availability of inverter units capable of parallel operation: E.g. Bonfiglioli and Siemens offer inverter systems specified for parallel operation with a common DC input [29, 30].

In summary, the literature shows the variation of grid connection topologies under research. To our knowledge, no study compares the typical grid connection scenarios with respect to their energy efficiency. Further, this study encompasses industry components which follow all required grid standards and thus gives application-oriented results. By using three separate component models, which can be variably parameterized, the method can be applied to a wide array of components and topologies. Finally, this study adds to the existing work by evaluating performance indicators for grid connection scenarios as well as by simulating grid application scenarios which are in line with grid regulation codes.

2. Methodology

Section 2.1 defines the topology model which is used to evaluate the various grid connection scenarios. The sub-component models including their parameterization for the inverter/rectifier, the DC-DC converter, and the transformer are each given in the Sections 2.2 to 2.4. Section 2.5 introduces and compares the grid application scenarios which are then evaluated with the topology model.

2.1. Grid connection model

In the grid connection simulation, the total power loss $P_{\mathrm{Loss,Sys}}$ is calculated through the sum of the power losses of each component type:

$$P_{\mathrm{Loss,Sys}} = \sum P_{\mathrm{Loss,DC\text{-}DC}} + \sum P_{\mathrm{Loss,\ Inv./Rect.\ Unit}} + P_{\mathrm{Loss,Transformer}} \tag{1}$$

The sub-component models are simulated in MATLAB and Simulink. The step-widths in the component models are in the range of microseconds. The simulation of the year-long grid application scenarios uses reduced component models. These are created by simulating the component models until steady-state conditions are achieved. Then, time-averaged values are calculated for varying parameters, i.e. voltage and input power. These are later used as input parameters for the reduced models. The topologies are finally simulated by combining the steady-state time-averaged component models.

In the simulation, the power electronics components, namely the inverter/rectifier and the DC-DC converter, can be turned off according to the operation strategy chosen. When the system is providing power in the homogeneous load distribution, all eight power electronics units are in operation and the power is shared equally among the in-

verter/rectifier units. In the incremental operation, additional inverter/rectifier units are activated every 25 kW of system power.

The transformer, when present in a topology, is kept constantly connected to the grid and thus contribute loss even in the case of no load.

The grid connection model is simulated by applying the load profile as the input parameter to the grid-side of the setup. The component losses are calculated with power settings compensating also for conversion losses occurring in the other components, i.e. for discharging the system in a two-stage topology, the DC-DC converter will draw more power from the battery side to account for the DC-DC converter losses and the following inverter/rectifier to follow the load profile on the AC side of the inverter/rectifier.

For the battery, the battery racks of the *Energy Neighbor* are used as a reference, each with a nominal energy of 24 kWh. The cell chemistry is lithium iron phosphate/graphite (LFP-C). Due to the flat open circuit potential of the LFP-C chemistry, battery voltage variations due to the changing state of charge are not included in this simulation for the sake of simplification. As the battery racks are under similar load in all topologies with only small differences caused by different conversion losses in the grid connection, the overvoltages in the battery racks are similar between the different topologies and thus do not affect the comparison of the topologies. The nominal voltage of the battery packs is consequently used as a constant value for the battery-side voltage.

A detailed study of the overall system energy efficiency based on the single-stage power electronics topology in the homogeneous load distribution and further including battery losses was conducted in [31].

The battery racks in the reference system *Energy Neighbor* have a nominal DC voltage of 665 V, which is subsequently used in the single-stage topology simulations. The two-stage topologies are introduced to evaluate grid connections with a DC voltage lower than the minimum 563 V required for the inverter. Thus, here a nominal voltage of 500 V for the battery is used. The selection for 500 V is based on a voltage that requires a DC-DC converter and a voltage that is not significantly lower than 600 V to not affect the comparison between different topologies due to a very large voltage difference as with i.e. a low voltage 48 V battery. Other battery voltages can be evaluated with the proposed model but will not be included in this study.

The DC link voltage in the two-stage topologies uses 600 V, as this is the nominal DC voltage of the inverter/rectifier and slightly above the minimum voltage criteria.

The grid voltage on the AC side of the inverters is taken as 400 V, according to the connection to a European LV grid. For the medium-voltage grid connections, 400 V is also taken as the voltage for the AC link between the inverter and the transformer secondary side. On the primary (grid) side of the transformer, the voltage 10 kV is taken to emulate the connection to a European medium-voltage grid.

2.2. Inverter/rectifier model

The inverter/rectifier model is based on the *Sinamics S120* units manufactured by Siemens. Any information for this and other Siemens components here and following is based on the author's interpretation of manufacturer information/manuals and is not to be interpreted as official manufacturer's statements.

The units are comprised of a bidirectional inverter/rectifier unit and an LCL-filter module, as the inverter/rectifier unit requires this for the operation. Fig. 3 shows the detailed topology of a single unit. The manufacturer specifies the unit's operating DC voltage range as 600-750 V. The nominal power of each unit is 36 kW. The model used for the inverter/rectifier has previously been presented in [31], but will be summarized here again. The power loss calculation for the complete unit includes losses in the inverter/rectifier part, $P_{\text{Loss,Inv./Rect.}}$, and in the LCL-filter module, $P_{\text{Loss,LCL}}$ [31]:

$$P_{\text{Loss,Inv./Rect. Unit}} = P_{\text{Loss,Inv./Rect.}} + P_{\text{Loss,LCL}} \tag{2}$$

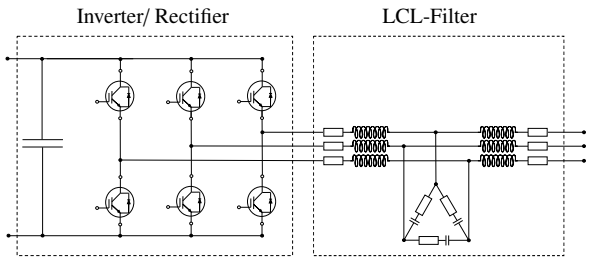

Fig. 3. Structure of inverter/rectifier mode, based on Siemens Sinamics S120 36 kW unit [8, 32, 33]. Figure serves as a schematic representation of the model only and is not an official manufacturer's drawing. Figure is modified with credit to [34].

The loss calculation in the inverter/rectifier unit calculates the conduction losses and switching losses in both the IGBT and the freewheeling diodes:

$$P_{\text{Loss,Inv./Rect.}} = P_{\text{Loss,IGBT,Switch}} + P_{\text{Loss,IGBT,Cond}} + P_{\text{Loss,Diode,Switch}} + P_{\text{Loss,Diode,Cond}} \tag{3}$$

The equations implemented in Simulink through the *Half-bridge IGBT With Loss Calculation Block* for calculation of the switching and the conduction losses in the semiconductors, namely the IGBTs and diodes have previously been presented in [31]. Parameters for the switching loss calculation are turn-on/-off switching energy of the IGBTs, $E_{\text{On}}/E_{\text{Off}}$, the turn-off switching energy of the diodes, E_{Rec}, and the respective actual switching frequency, f_{Switch}.

IGBT switching energy is calculated as a function of the blocking voltage of the semiconductors which corresponds to the respective DC voltage U_{DC} and the collector current i_{C}:

$$P_{\text{Loss,IGBT,Switch}} = \left(E_{\text{On}}(U_{\text{DC}}, i_{\text{C}}) + E_{\text{Off}}(U_{\text{DC}}, i_{\text{C}})\right) \cdot f_{\text{Switch}} \tag{4}$$

The switching energy in the freewheeling diode is calculated as a function of the forward current i_{F} and as well the respective voltage:

$$P_{\text{Loss,Diode,Switch}} = E_{\text{Rec}}(U_{\text{DC}}, i_{\text{F}}) \cdot f_{\text{Switch}} \tag{5}$$

The implemented IGBT module, which includes the freewheeling diode, is a 150 A Infineon FS150R12KE3 module [35], according to [36]. As the parameters for the turn-on/-off switching energy of the IGBTs and the turn-off switching energy of diodes are only available for 125 °C, they are both implemented without a temperature dependence [31].

The conduction losses are calculated depending on the saturation voltage U_{CE} of the IGBTs, the forward voltage U_{F} of the freewheeling diodes, and collector-emitter current i_{C}, and forward current i_{F}. U_{CE} of the IGBTs is implemented as function of the junction temperature of the semiconductors T_{J}, and the collector current. The forward voltage of the freewheeling diode is implemented as function of the forward current and also of the junction temperature.

$$P_{\text{Loss,IGBT,Cond}} = U_{\text{CE}}(T_{\text{J}}, i_{\text{C}}) \cdot I_{\text{C}} \tag{6}$$

$$P_{\text{Loss,Diode,Cond}} = U_{\text{F}}(T_{\text{J}}, i_{\text{F}}) \cdot I_{\text{F}} \tag{7}$$

The losses in the LCL-filter are calculated separately as core losses, $P_{\text{Loss,LCL,Core}}$ and conduction losses $P_{\text{Loss,LCL,Cond}}$:

$$P_{\text{Loss,LCL}} = P_{\text{Loss,LCL,Core}} + P_{\text{Loss,LCL,Cond}} \tag{8}$$

The core losses are implemented without dependence of the load or temperature with constant losses during operation of 108 W, taken from manufacturer experimental data for the operation at zero-load [31, 33]. Measurements data used here, and subsequently is taken from [33] and is corrected for auxiliary power consumption for cooling and control of the units.

$$P_{\text{Loss,LCL,Core}} = \text{const} \tag{9}$$

The conduction losses depend on the inductor resistances $R_{\text{LCL,in}}$ and are calculated following Ohm's law:

$$P_{\text{Loss,LCL,Cond}} = R_{\text{LCL,in}} \cdot I_{\text{Grid}}^2 \tag{10}$$

The values for the resistance are calculated from the losses at nominal power, again taken from manufacturer experimental data [33], to 13.6 mΩ [31].

For the simulation step width, a value of 0.5 µs showed converged values for the power losses [31]. Ambient temperature is set constant to 25 °C. For the DC Bus capacity resistance, no parameter is available and thus a low value with negligible influence on the results is implemented. Parameters for the complete inverter/rectifier unit model are shown in Appendix A. For further explanation of control and thermal parameters, we refer to the previous study in [31].

For a validation of the inverter/rectifier model, the simulation results for conversion of 400 V AC to 600 V DC and input power from 0 to 100 % of nominal power are compared to experimental data provided by the manufacturer [31, 33]. Experimental data and the model results for the power loss values are shown together with the relative model error in Fig. 4. The validation of the inverter/rectifier unit was previously presented in [31] and is shown here again for the completeness of the model presentation. The comparison shows, that the relative model error is below 7 % over the entire operating range. In terms of the energy efficiency, an error of 7 % for the power loss calculation at nominal power equals to a low deviation of 0.18 % for the energy efficiency from the experimental value of 97.41 % [31, 33].

The reduced inverter/rectifier model thus enables a calculation of power loss according to the input parameters DC voltage, load direction, and operating point.

2.3. DC-DC converter model

The DC-DC converter modeled is based on a component by Siemens and distributed under the brand name *Sinamics DCP*. The topology of the considered converter is a double-interleaved cascaded boost/buck converter [37] and is capable of bidirectional power flow. Fig. 5 shows the schematics of the converter model. The boost functionality, as well as the buck functionality, is possible in both power flow directions. The DC voltage range of the unit is specified to a maximum range of 30 to 800 V. Nominal specifications throttle the current to maximum rates of 50 A. Nominal power of each unit is 30 kW. At the considered battery voltage for the two-stage scenarios of 500 V, this results in a

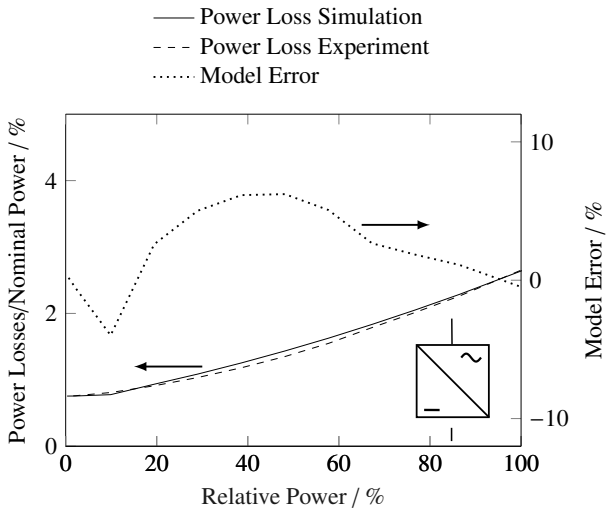

Fig. 4. Inverter/rectifier: Comparison of simulated and experimentally measured power loss for AC to DC conversion at 600 V DC. Ambient temperature 25 °C. Experimental data from [33]. Figure credit [34].

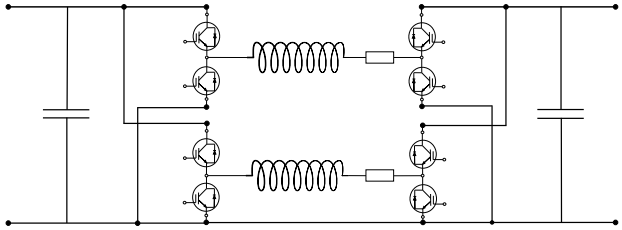

Fig. 5. Structure of DC-DC converter model, based on Siemens Sinamics DCP 30 kW unit [37, 38]. Figure serves as a schematic representation of the model only and is not an official manufacturer's drawing.

maximum continuous power of 25 kW [37]. Both parts of the double-interleaved cascaded converter share the load equally in the simulation.

The Ohmic losses in the storage chokes are calculated as the conduction losses $P_{\text{Loss,L,cond}}$. The power losses in IGBTs and diodes are simulated with respective separation for switching losses $P_{\text{Loss,IGBT/Diode,switch}}$ and conduction losses $P_{\text{Loss,IGBT/Diode,cond}}$. The converter power losses are the sum of all the respected losses and are calculated in the same fashion as in equations 4 to 7 of the inverter/rectifier model.

$$P_{\text{Loss,DC-DC}} = P_{\text{Loss,L,Cond}} + P_{\text{Loss,IGBT,Switch}} + P_{\text{Loss,IGBT,Cond}} + P_{\text{Loss,Diode,Switch}} + P_{\text{Loss,Diode,Cond}} \tag{11}$$

For the simulation of conduction and switching behavior of the IGBTs and diodes, an IGBT module with a nominal current of 80 A is implemented. Datasheet parameters for the IGBT/diode switching energy at low currents are missing and approximated through iteration to achieve valid simulation results for the power losses. For the DC Bus no parameters are available and thus the values from the inverter/rectifier unit are implemented. The resistance parameter for the storage chokes is selected based on a comparable DC-DC converter.

Due to the high switching frequency, a high temporal resolution is required to obtain converging simulation results. Compared to the inverter/rectifier unit model, the temporal resolution is increased to 0.2 µs.

As the fan cooling of the DCP units is modulated with unit load and no information on the modulation method is available, the IGBT module case temperature is implemented as a constant value of 125 °C.

Further simulation parameters are summarized in Appendix B.

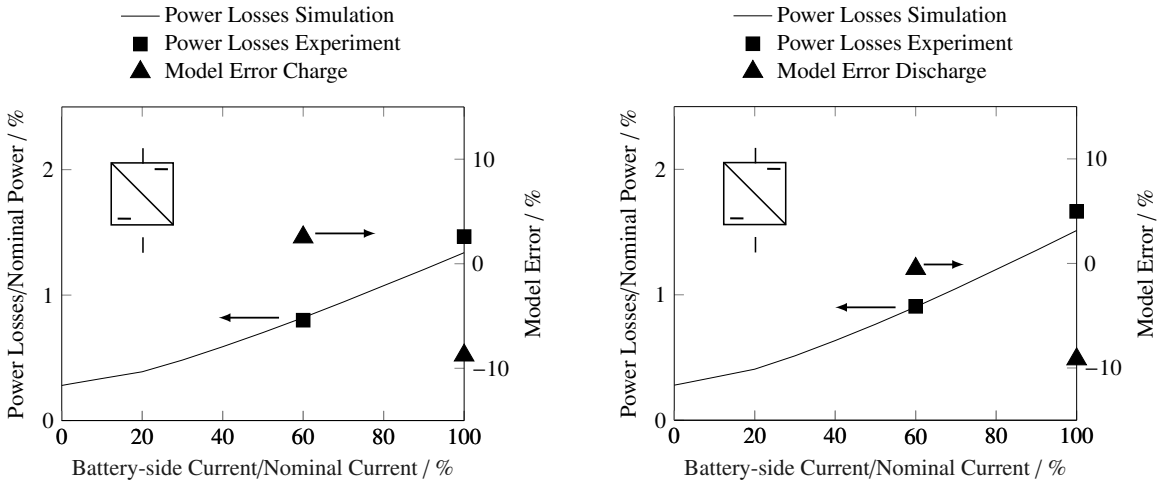

Fig. 6. DC-DC Converter: Comparison of simulated and experimentally measured power loss conversion between 500 V DC (Battery Side) and 600 V DC: a) Charge, b) Discharge. Experimental data for Siemens Sinamics DCP 30 kW unit from [39].

Simulation results for bidirectional conversion between 500 V DC (battery side) to 600 V DC (system DC link) and input power up to 100% of nominal current are compared to experimental data by the manufacturer in Fig. 6a (charge) and Fig. 6b (discharge). The nominal current operating point in the discharge direction represents the highest model error at 9.2 %. However, the error of the power loss calculation equals to a deviation of only 0.14 % in efficiency from the experimental value of 98.0 %. Unfortunately no experimental data for low-load operation is available from the manufacturer, however, the validation at 60 % load with a deviation of less than 2.5 % indicates that the model is in good agreement with the simulation at operating power lower than nominal power.

The DC-DC converter model is simulated with a fixed voltage of 600 V on the DC link side, and 500 V on the battery side at varying current directions and loads. The results over the operating points are simulated, saved and integrated into the system simulation as a function of the varied parameters.

In summary, the reduced DC-DC converter model enables a calculation of power loss according to the input parameters load direction and operating point.

2.4. Transformer Model

The considered transformer is based on a component by Siemens, which is distributed under the brand name GEAFOL Basic [40]. It is a cast resin dry-type transformer. The 50 Hz transformer is specified for the nominal power of 250 kVA and transforms 400 V to 10 kV and vice versa in a three-phase setup. In the simulation, the primary side is configured as delta wiring configuration and the secondary side in star wiring configuration respectively.

The simulation is based on a three-phase transformer model in Simulink. The required model parameters represent the components of the simplified equivalent circuit diagram of a transformer.

The transformer power losses are the sum of the load-independent core losses due to hysteresis and eddy current losses $P_{\mathrm{Loss,TR,Core}}$, and of the load-dependent conduction losses occurring in the transformer windings $P_{\mathrm{Loss,TR,Cond}}$:

$$P_{\mathrm{Loss,Transformer}} = P_{\mathrm{Loss,TR,Core}} + P_{\mathrm{Loss,TR,Cond}} \tag{12}$$

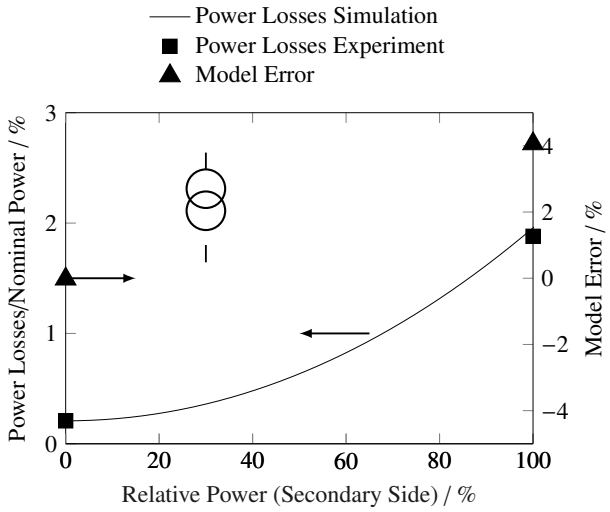

Fig. 7. Transformer: Comparison of simulated and experimentally measured power loss for transformer between 400 V AC and 10 kV AC. Experimental data from [40].

The core losses depend on the grid voltage U_{Grid} and frequency f_{Grid} and are calculated with the equivalent core resistance $R_{\text{TR,Core}}$:

$$P_{\text{Loss,TR,Core}} \sim U_{\text{Grid}}^2 \cdot f_{\text{Grid}}^2 \sim 1/R_{\text{TR,Core}} \tag{13}$$

The conduction losses are dependent on the resistances of the primary $R_{\text{TR,Prim}}$ and secondary $R_{\text{TR,Sec}}$ winding and follow Ohm's law:

$$P_{\text{Loss,TR,Cond}} = R_{\text{TR,Prim}} \cdot I_{\text{TR,Prim}}^2 + R_{\text{TR,Sec}} \cdot I_{\text{TR,Sec}}^2 \tag{14}$$

As the manufacturer recommends to adjust the given measured load losses at nominal power from laboratory conditions with a factor of +10 %, due to the higher average core temperature in application conditions, the factor was included in the calculations and following validation [41]. Further details on the calculation of the equivalent circuit parameters are described in Appendix C.

Simulation results for conversion of 400 V AC to 10 kV AC and input power up to 100% of nominal power are compared to the experimental data given by the manufacturer in Fig. 7. The power loss curve of the simulation corresponds to the typical curve of transformer power losses with increasing load. The model error for the core losses is almost negligible (0.02 %). At nominal power, the deviation increases to 4.06 % compared to the to the manufacturer's specification, which is equal to an efficiency deviation of only 0.08 %.

The transformer simulation results are converted to a reduced model that enables the calculation of power losses according to the operating point, following the same procedure as for the inverter/rectifier model and the DC-DC converter model.

2.5. Grid application scenarios

Two exemplary grid applications are evaluated for a comparison of the topologies in actual application scenarios. Both scenarios are scaled to an offered reserve power of 200 kW and taken from existing work on control reserve [42] and have been used in previous studies in [31], where they have also been discussed in more detail.

The first application, *Primary Control Reserve (PCR)*, is also known as frequency control. The system provides positive or negative power to the grid in case of frequency deviations from the nominal frequency in the European grid of 50 Hz [43]. More details are given in [31].

In contrast, the second application, *Secondary Control Reserve (SCR)*, is also a grid application in the German grid. SCR is used to restore the availability of the power bandwidth of the PCR in case of longer imbalances in the grid. Positive or negative reserve power can be provided, however not both simultaneously. The provision is tendered for a full week and further separated into the base period (8 PM to 8 AM) and peak period (8 AM to 8 PM on weekdays), which gives four different SCR types. As the request for control power is remunerated, the actual requested power also depends on the set energy price for the specific system. More information can be found at [44]. In [42] and subsequently this work, negative reserve power is provided for the base period and the battery is discharged during the peak period. More details are given in [31].

Both applications are evaluated for a full year of operation.

Fig. 8 shows the annual load duration curve of both scenarios from [42], normalized to 200 kW system power. PCR shows a relatively symmetrical power in both charge and discharge direction. Full system power is almost never activated. SCR shows a high peak in charge (positive) direction, which occurs when the reserve power is requested. As the system is discharged slowly during the peak period, the discharge power is lower. Both scenarios show long rest periods, where no power is requested, although less pronounced for PCR. To compare the load profiles quantitatively, two utilization ratios are defined. The temporal utilization τ_t is the ratio of the time in which the simulation is in operation $t_{\text{Operation}}$ (System Power $\neq 0$) to the evaluated duration $t_{\text{Simulation}}$ (1 year) [31]:

$$\tau_t = \frac{t_{\text{Operation}}}{t_{\text{Simulation}}} \tag{15}$$

The energy-based utilization τ_E is the ratio of the energy-throughput of the system $E_{\text{Throughput}}$ to the theoretically possible maximum throughput during the simulation duration $E_{\text{Throughput,theoretical max.}}$ at cycling the system at the nominal system power of 200 kW:

$$\tau_Q = \frac{E_{\text{Throughput}}}{E_{\text{Throughput,theoretical max.}}} \tag{16}$$

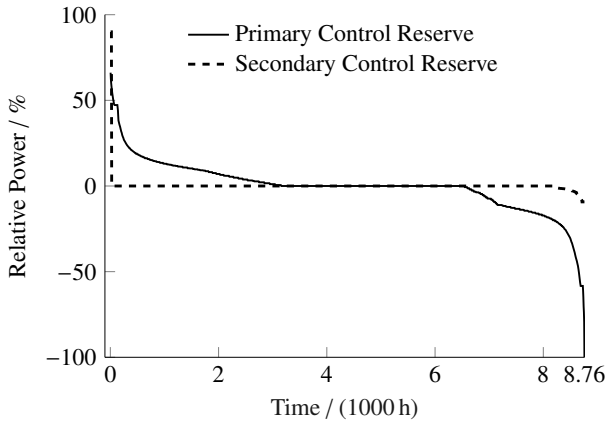

Fig. 8. Normalized load duration curve of grid application profiles for *Primary Control Reserve* and *Secondary Control Reserve*. Profile data from [42].

Table 1. Parameters of grid application scenarios *Primary Control Reserve* and *Secondary Control Reserve*.

	PCR	SCR
Rel. Avg. Power in Operation	14.2 %	6.4 %
Full Equivalent Cycles / a	397.0	19.0
Temporal Utilization τ_t	61.2 %	6.6 %
Energy-based Utilization τ_E	8.7 %	0.4 %

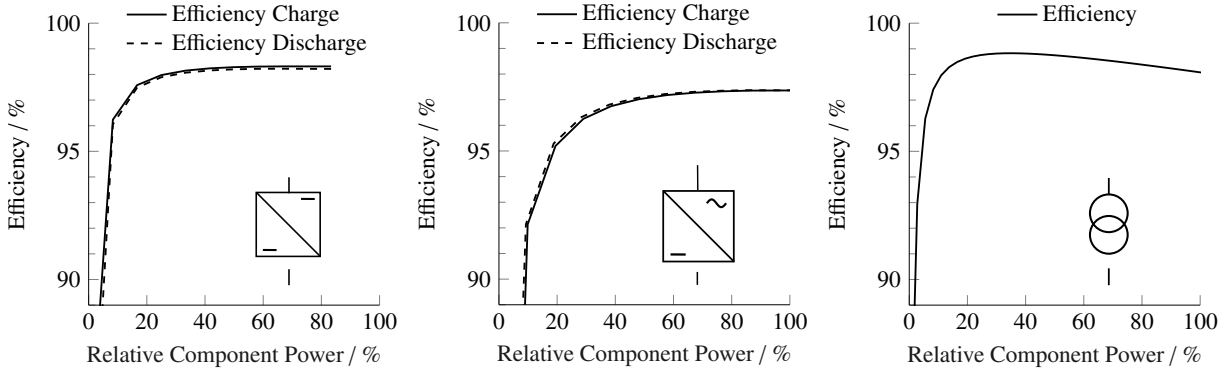

Fig. 9. Comparison of conversion efficiency: a) DC-DC conversion between 500 V DC (Battery Side) and 600 V DC (DC link), b): AC-DC / DC-AC conversion between 600 V DC and 400 V AC, c) voltage conversion between 400 V AC and 10 kV AC. All data: Simulation results.

Table 1 shows the results for the utilization ratios, the full equivalent cycle count of a full years operation, and the average power in operation relative to a system power of 200 kW. The calculations are based on the load profile which is given as input to the model and are thus independent of the grid connection topologies under investigation. As the results confirm, PCR is a high utilization scenario compared to SCR, both in terms of full equivalent cycles per year as well for temporal and energy-based utilization.

3. Results and Discussion

The results of the separate sub-component models are compared in terms of their energy efficiency in Section 3.1. The comparison of power loss during operation for different load distribution modes and the grid connection topologies are given in Section 3.2. Finally, in Section 3.3, the results for the performance of the investigated grid connection scenarios in the two grid application scenarios are compared.

3.1. Component model results

The three components of the grid interconnection possibilities are characterized by their power efficiency $\eta_{\text{Conversion}}$ which is based on the relationship between the output power P_{Out} and the input power P_{In}:

$$\eta_{\text{Conversion}} = \frac{P_{\text{Out}}}{P_{\text{In}}} = \frac{P_{\text{In}} - P_{\text{Loss}}}{P_{\text{In}}} \tag{17}$$

Results for the three sub-component models are shown in Fig. 9. The DC-DC converter (see Fig. 9a) shows no-load losses of 0.27 % of its nominal power at the conversion ratio from 500 V to 600 V if the unit is in operation. The maximum relative output power is limited to 83.3 %, due to the maximum current of 50 A, which results in a maximum continuous power of 25 kW at 500 V on the lower voltage side. The peak efficiency of 98.3 % is reached at nominal power during charging.

The inverter/rectifier unit (see Fig. 9b) presents the lowest efficiency characteristics of the three components. The no-load losses per unit are 0.76 % of its nominal power if the unit is in operation. The peak efficiency of 97.41 % is also reached at nominal power.

The transformer's (see Fig. 9c) no-load losses 0.21 % relative to the rated power of 250 kVa. Efficiency increases to it's maximum of 98.83 % at 35.34 % of the transformers rated power, where no-load and load losses are equal. Further increasing power reduces the efficiency due to the increase of the conduction losses.

3.2. Topology evaluation

The topology evaluation is based on the respective power loss behavior.

To analyze the effect of the load distribution, the loss behavior of the single-stage low-voltage topology (see Fig. 1a) is analyzed in detail in Fig. 10. To show the influence of the power losses of PE units in operation at zero-load, here the difference whether units are turned off at zero-load (shutdown mode) or not is made.

The homogeneous load distribution power loss curve with and without shutdown mode differ only for zero-load of the entire system (System Power = 0 kW).

The incremental load distribution shows to be very distinguishable from the homogeneous load distribution and is sensitive to the setting of a possible shutdown mode the entire operating range of the system.

The incremental load distribution with shutdown mode completely turns off at zero system load and thus no losses occur. Across the entire operating range, it shows the least power losses due to the optimized of units in operation. With increasing system power, the activation of an additional unit leads to an instant increase in power losses. This confirms that keeping as few as possible units in operation is beneficiary for the reduction of power losses.

In contrary, the incremental load distribution without shutdown mode shows the highest power losses for the majority of system powers, due to the permanent load independent losses of all power electronics units. Comparing the power loss curves of the incremental load distribution and homogeneous operation, both without shutdown mode, confirms that distributing the system power evenly across all units in operation reduces the power losses, as the losses increase nonlinearly with the power in a single unit (see Fig. 4).

Finally, the power losses of all distribution methods align in the last one-eighth of the system power spectrum as here all units are in operation and feature equal loads.

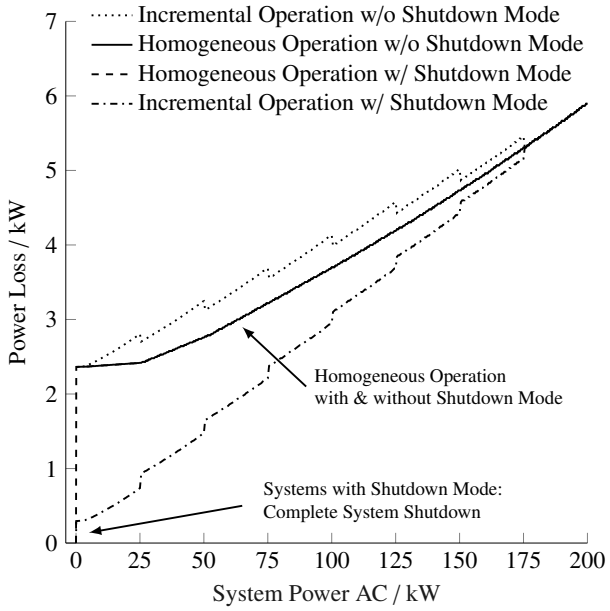

Fig. 10. Power loss of single-stage low-voltage topology simulation for homogeneous/incremental load distribution and with/without shutdown mode. For the ease of representation only charge direction is shown.

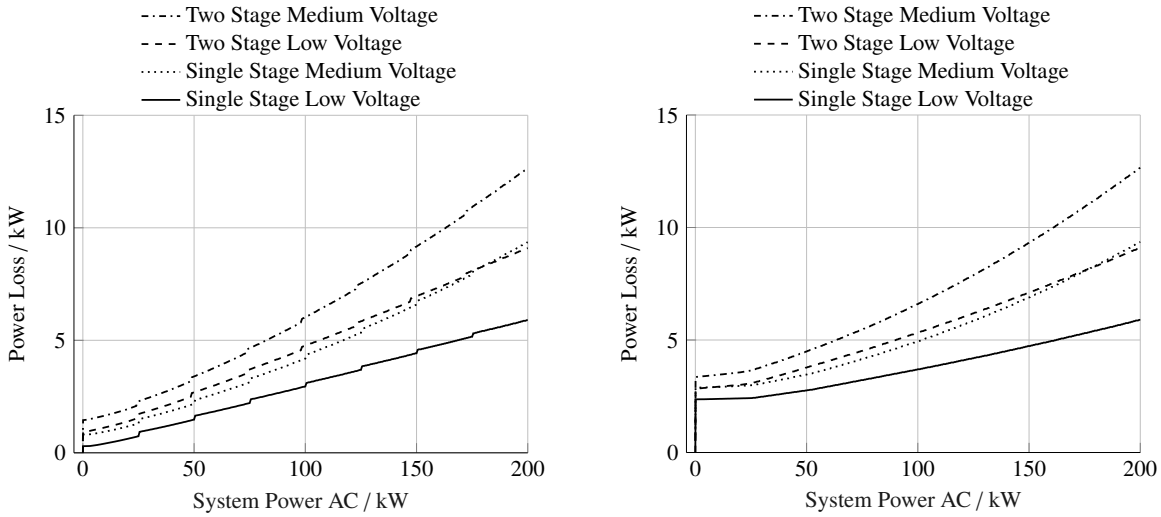

Fig. 11. Power loss simulation of grid connection topologies over operating range: a) incremental operation, b) homogeneous operation. For the ease of representation only charge direction is shown.

Because of the described high no-load losses and the technical possibility of a complete shutdown of power electronics unit, only the operation with shutdown mode is further considered in this study.

The loss behavior of the four grid connection technologies with incremental load distribution is represented in Fig. 11a and with homogeneous load distribution in Fig. 11b. The additional losses of the transformer and the DC-DC converter are similar in the incremental and homogeneous operation. They only vary very little due to the higher base load of the inverters/rectifiers in the homogeneous load distribution. Therefore, the loss curve of the DC-DC converter can be considered as an addition to the inverter/rectifier loss curve for the two-stage applications, and the transformer losses increase the total power losses with its square gradient and throughout occurring no-load losses in medium-voltage grid interconnections.

The power losses of all interconnection possibilities are significantly lower for the incremental load distribution at system powers levels at lower loads. With higher loads, the difference is reduced.

Finally, it is again mentioned that the power losses due to the power electronics are zero at zero-load due to the shutdown mode, but the transformer is not turned off and has constant no-load losses.

3.3. Grid application evaluation

For the comparison of the energy losses in the various grid connection scenarios in the applications PCR and SCR, the relative round-trip energy losses ϕ are defined. The relative round-trip loss of a component i, i.e. the inverter/rectifier, the DC-DC converter or the transformer, is calculated through the ratio of the respective total energy loss during both charging and discharge $E_{\mathrm{Loss,i}}$ to the total energy input to the system, derived from sum of the discharged energy and the energy lost in the system:

$$\phi_i = \frac{E_{\mathrm{Loss},i}}{E_{\mathrm{Discharge,AC}} + E_{\mathrm{Loss,System}}} \tag{18}$$

The results for the relative amount of losses and their origin in the application PCR are shown in Fig. 12a and Fig. 12b. Comparing the load distribution modes, the incremental operation in Fig. 12a is beneficial compared to the

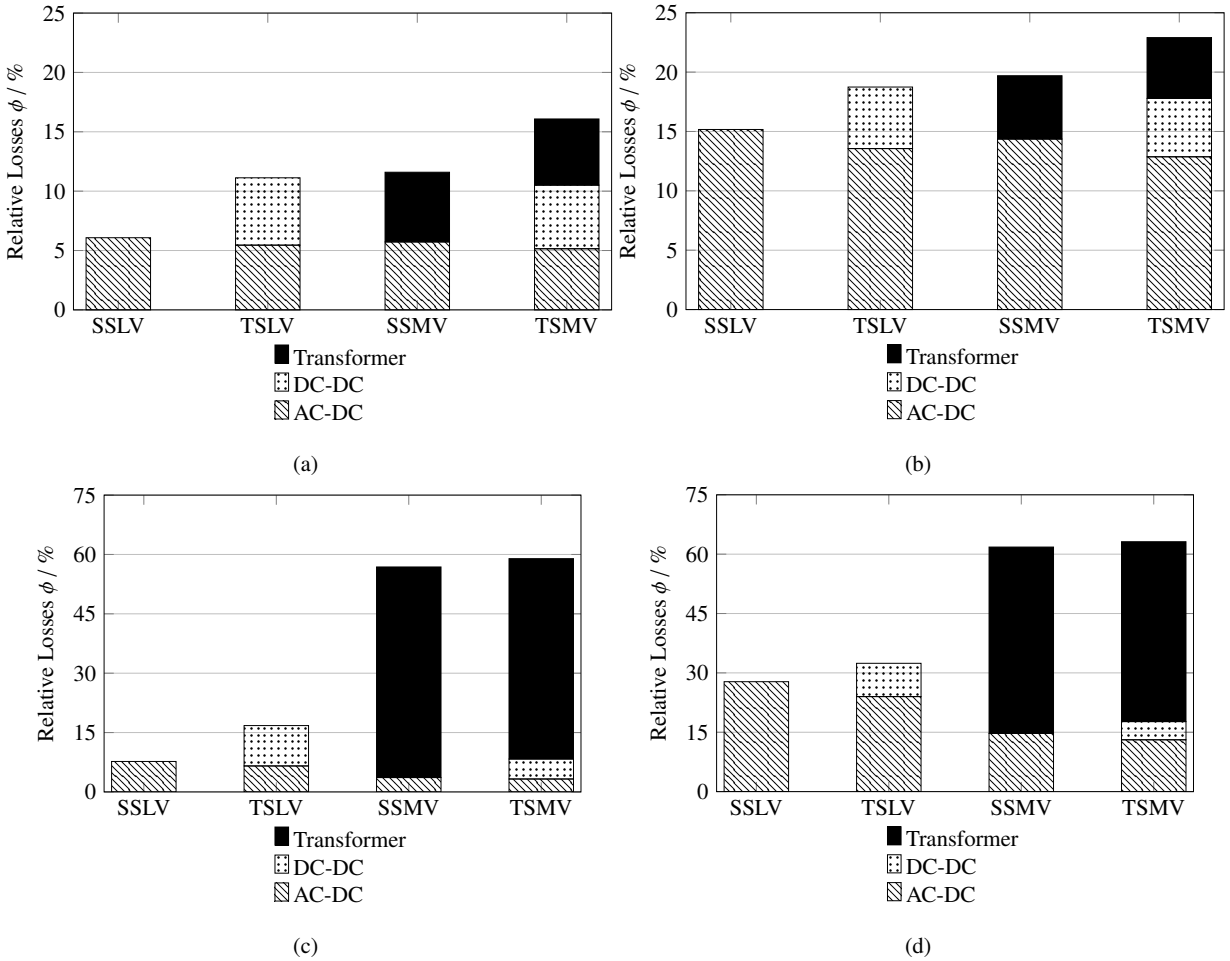

Fig. 12. Energy loss comparison of grid connection scenarios for grid applications Primary Control Reserve and Secondary Control Reserve: a) PCR incremental operation, b) PCR homogeneous operation, c) SCR incremental operation, d) SCR homogeneous operation. Topology abbreviations: Single Stage (SS), Two Stage (TS), Low-Voltage Grid (LV), Medium-Voltage Grid (MV).

homogeneous operation in Fig. 12b. This is explained due to the higher losses at low loads which are highly prominent in the scenario PCR (see Section 2.5).

Comparing the single-stage and two-stage topology, the additional conversion step can up to double the relative losses in the worst case. The increase of the relative losses due to the additional losses of the DC-DC converter is similar for the incremental and the homogeneous operation, however, the impact on the homogeneous operation is relatively speaking lower than in the incremental operation. This behavior matches the loss behavior shown in Fig 11a and Fig 11b.

The comparison of the LV and MV grid connection topologies shows that the additional losses of the transformer impact the relative losses for incremental operation (Fig 11a) and homogeneous operation (Fig 11b) also similarily. In summary, the high no-load losses of the inverter/rectifier have the largest impact on the overall relative losses and the efficiency of the interconnection technology. The best case solution for PCR in terms of energy efficiency is the single-stage low-voltage incremental operation at relative losses of 6.1 %. The worst case is represented by the two-stage medium-voltage homogeneous operation which nearly quadruples the relative losses to 22.9 %.

The results for the scenario SCR are shown in Fig. 12c and Fig 12d. Here, the incremental operation (see Fig. 12c) again shows the reduced loss behavior compared to the homogeneous operation (see Fig. 12d). Due to the very low temporal utilization in the scenario SCR, the losses in the transformer are high compared to the losses in the power

electronics, as the transformer cannot be turned off and thus no-load losses occur constantly. The relative losses thus increase to values higher than 60 %. The relative share of the power electronics losses here visibly drops slightly, as the high additional losses introduced by the transformer add to the total energy input of the system and thus making the power electronics losses relatively smaller.

The comparison of single-stage and two-stage topologies shows the same behavior as in the PCR application with overall higher relative losses, due to the lower average load demands during discharge and the consequently lower efficiencies of the respected technologies.

The best case is again achieved with the single-stage low-voltage incremental operation, here at relative losses of 7.7 %. The worst case for the relative losses is also again represented by the two-stage medium-voltage homogeneous operation at 63.1 %.

In summary, the grid application scenarios confirm the results of the previously compared power losses calculation for the various grid connection scenarios.

4. Conclusion

The connection of the battery to the electrical grid is a key component of stationary BESS. Utility-scale systems typically comprise of several power electronics units. Various grid connection topologies result; depending on the conversion stages within each unit, the load distribution between the power electronics units and additionally the grid level to which the system is connected. These grid connection scenarios vary with respect to the choice of the power conversion technology and how the different technologies are connected and how they distribute the power flow within the grid connection.

Detailed components models are developed for the key components of the various topologies, the inverter/rectifier, the DC-DC converter, and the transformer. The simulation model parameters are based on the state-of-the-art industry components and compared against experimental data.

The component models are coupled to grid connection topology models for a container storage system featuring eight battery racks. The conversion losses and resulting energy efficiency, as key performance indicators for BESS, are compared between the various topologies.

The comparison of single-stage and two-stage topologies shows that conversion setups without the intermediate DC link conversion stage are more efficient than those with. Therefore, it is desirable to choose a battery rack topology that supports the required DC Voltage of the used inverter/rectifier.

Distributing the actual load a minimum amount of necessary inverters/rectifiers is more efficient than operating more inverters/rectifiers at lower loads. Hence, a setup should be realized that allows the shutdown of non-necessary power electronics.

From a technical perspective, to minimize dissipation losses the connection to the LV grid is more efficient due to the absence of the transformer which introduces extra conversion losses and causes high amounts of no-load losses. Thus, if possible, considering grid limitations, system power and aspects of the storage application, a connection to the LV grid is preferable.

Following these results, the single-stage low-voltage topology with incremental load distribution achieves the best results concerning the efficiency of the grid connection for the system, while the two-stage medium-voltage topology with homogeneous load distribution causes the highest losses and leads to the lowest efficiency. It should be mentioned, that the results cover only the BESS. The evaluation is thus limited to the perspective of the BESS operator and does not include the losses occurring in the distribution grid itself.

Finally, the topologies are evaluated in two real-world grid application scenarios, namely Primary Control Reserve and Secondary Control Reserve, which both confirm the previous conclusions. Losses between the evaluated grid connection scenarios, as well as between the grid application scenarios vary significantly.

5. Outlook

The results of this study can serve as design guidelines for the grid connection of utility-scale BESS. The developed simulation methods can be used for the design of the grid connection from the component level upwards. The possible

improvements of the system in terms of energy efficiency, e.g. by using different IGBTs or in terms of component sizing, can be evaluated for the desired grid application scenario of the BESS.

Further work should be conducted on non-equal load distribution between separate battery racks with dedicated power electronics. This would thus include separate battery models for each rack and a more sophisticated control strategy, which controls the State of Charge.

The reduced component models, as well as the reduced grid connection model, can also be implemented in energy management systems allowing improved operating strategies, i.e. by avoiding low-efficiency operation through minimum power thresholds.

Acknowledgements

The research project Intelligent Home Energy Management (IHEM) is funded by the Federal Ministry for Economic Affairs and Energy within the “Funding initiative Electrical Storages” (grant number 03ET1205G) and cared by Project Management Juelich. The authors also thank the Bavarian Ministry of Economic Affairs and Media, Energy and Technology for their support via the EEBatt project. The authors kindly thank the component manufacturer for the provision of production information. Any manufacturer data cited/presented in this work was provided for scientific uses or approximations such as simulation models only. Any data presented in this work does not declare/contain official statements for any company’s products of any kind and is to be interpreted as a simulation study only. The responsibility for the content of this publication lies with the author.

Appendix A. Inverter/rectifier model parameters

Table A.2. Inverter/rectifier model parameters based on Siemens Sinamics S120 36 kW unit. Model parameters are selected by the authors and do not represent official manufacturer information. Table reproduced with modifications from [34].

Simulation Step Width	0.5 µs	Text
Grid		
Line-to-line Voltage	400 V	[33]
Frequency	50 Hz	[33]
Short Circuit Power	10 MVA	[33]
Inverter/Rectifier		
Control & DC Bus		
Switching Frequency	8 kHz	[33]
Phase Shift	0	[31]
Max. Modulation Index	$2/\sqrt{3}$	[31]
Proportional Correction	0.5	[31]
Integral Correction	50	[31]
DC Bus Capacity	1.410 mF	[45]
DC Bus Resistance	1 mΩ	Text
IGBT		
Conduction	$U_{\mathrm{CE}}(I,T)$	[35]
Energy Switching Turn-on	$E_{\mathrm{On}}(I, T = 125\,^{\circ}\mathrm{C})$	[35]
Energy Switching Turn-off	$E_{\mathrm{Off}}(I, T = 125\,^{\circ}\mathrm{C})$	[35]
Thermal Impedance	Z_{th}	[35]
Diode		
Conduction	$U_{\mathrm{F}}(I,T)$	[35]
Energy Switching Turn-Off	$E_{\mathrm{Rec}}(I, T = 125\,^{\circ}\mathrm{C})$	[35]
Thermal Impedance	Z_{th}	[35]
Module Casing		
Thermal Impedance	9 mK/W	[35]
Thermal Capacity	0.1 J/K	[31]
Heat Sink		
Thermal Impedance	0.19 K/W	[31]
Thermal Capacity	1 J/K	[31]
LCL-filter		
Core Losses	108 W	[33]
Filter Capacity	10 µF	[45]
Damping Resistance	733 mΩ	[45]
Inductance Grid-side	1 µH	[45]
Inductance Inverter-side	48 µH	[45]
Inductor Resistance Grid-side	13.6 mΩ	Text
Inductor Resistance Inverter-side	13.6 mΩ	Text

Appendix B. DC-DC converter model parameters

Table B.3. DC-DC converter model parameters, based on Siemens Sinamics DCP 30 kW Unit. Model parameters are selected by the authors and do not represent official manufacturer information.

Simulation Step Width	0.2 µs	Text
DC-DC Converter		
Switching Frequency	20 kHz	[37]
Proportional Current Gain	0.2	[38]
Integral Current Correction	200	[38]
Precontrol Multiplier	0.98	[38]
DC Bus Capacity	1.410 mF	Text
DC Bus Resistance	1 mΩ	Text
Storage Choke Inductance	0.7 mH	[39]
Storage Choke Resistance	14.5 mΩ	Text
IGBT		
Conduction	$U_{CE}(I, T = 125\,°C)$	[46]
Energy Switching Turn-on	$E_{on}(U, I, T = 125\,°C)$	[46]
Energy Switching Turn-off	$E_{off}(U, I, T = 125\,°C)$	[46]
Thermal Impedance	Z_{th}	[46]
Diode		
Conduction	$U_F(I, T = 125\,°C)$	[46]
Energy Switching turn-off	$E_{rec}(U, I, T = 125\,°C)$	Text
Thermal Impedance	Z_{th}	[46]
Module Casing		
Case Temperature	125 °C	Text

Appendix C. Transformer model parameterization

Core resistance $R_{TR,Core}$ and inductance $L_{TR,Core}$ are calculated from the no-load losses P_0 (Value: 520 W [40]):

$$\begin{aligned} R_{TR,Core} &= 3 \cdot \frac{U_{Prim}^2}{P_0} \\ L_{TR,Core} &= \frac{U_{Prim}}{I_\mu \cdot (2\pi \cdot f_{Grid})} = \frac{R_{TR,Core}}{2\pi \cdot f_{Grid}} \end{aligned} \tag{C.1}$$

Due to the lack of information concerning the reactive current I_μ, the absolute value of the complex resistance of the inductance is assumed to be as high as the core resistance.

Winding resistances ($R_{TR,Prim}$, $R_{TR,Sec}$) and inductances ($L_{TR,Prim}$, $L_{TR,Sec}$) are calculated from the load losses at nominal power P_k (Value: (1 + 10 %) · 3800 W [40]), the impedance voltage u_Z (Value: 4 % [40]) and the apparent power per phase S_n, each at nominal current flow on the primary transformer side, with the assumption of equal loss distribution between primary and secondary side:

$$\begin{aligned} I_n &= \frac{S_n}{3 \cdot U_{Prim}} \\ R_{TR,Prim} &= \frac{1}{2} \frac{P_k}{3 \cdot I_n^2} \end{aligned} \tag{C.2}$$

Because of the delta wiring configuration on the primary side and the star wiring configuration on the secondary transformer side, the secondary winding resistance $R_{\mathrm{TR,Sec}}$ is adjusted with the factor $1/3$ and the voltage ratio: $U_{\mathrm{TR,Prim}}/U_{\mathrm{TR,Sec}}$.

$$R_{\mathrm{TR,Sec}} = \frac{1}{2}\frac{P_k}{3 \cdot I_n^2}\frac{1}{3 \cdot (U_{\mathrm{Prim}}/U_{\mathrm{Sec}})^2} \tag{C.3}$$

The inductances are calculated with the complex short circuit impedance Z_T and winding resistance R_{T}, which is assumed equally split up for both transformer sides. Therefore, the real part of the complex impedance is assumed as $R_{\mathrm{T}} = 2 \cdot R_{\mathrm{TR,Prim}}$.

$$\begin{aligned} Z_{\mathrm{T}} &= \frac{u_{\mathrm{Z}} \cdot U_{\mathrm{Prim}}}{I_n \cdot \sqrt{3}} \\ X_{\mathrm{T}} &= \sqrt{Z_{\mathrm{T}}^2 - R_{\mathrm{T}}^2} \\ L_{\mathrm{TR,Prim}} &= \frac{1}{2}\frac{X_{\mathrm{T}}}{2\pi \cdot f_{\mathrm{Grid}}} \\ L_{\mathrm{TR,Sec}} &= \frac{1}{2}\frac{X_{\mathrm{T}}}{2\pi \cdot f_{\mathrm{Grid}}}\frac{1}{(U_{\mathrm{TR,Prim}}/U_{\mathrm{TR,Sec}})^2} \end{aligned} \tag{C.4}$$

Table C.4. Transformer model parameters, calculated for Siemens Geafol Basic 250 kVA unit [40]. Model parameters are selected by the authors and do not represent official manufacturer information.

Simulation Step Width	0.1 ms	Text
Equivalent Circuit Parameters		
Core Resistance	576.92 kΩ	Text
Core Inductance	1.836 kH	Text
Primary Winding Resistance	10.032 Ω	Text
Secondary Winding Resistance	5.3 mΩ	Text
Primary Stray Inductance	30.4 mH	Text
Secondary Stray Inductance	48.284 µH	Text

The simulation step width is increased in comparison to the power electronics model to 0.1 ms since there are no switching conditions occurring during the power transformation.

References

[1] H. Hesse, M. Schimpe, D. Kucevic, A. Jossen, Lithium-Ion Battery Storage for the Grid—A Review of Stationary Battery Storage System Design Tailored for Applications in Modern Power Grids, Energies 10 (12) (2017) 2107. doi:10.3390/en10122107.

[2] M. Aneke, M. Wang, Energy storage technologies and real life applications – A state of the art review, Applied Energy 179 (2016) 350–377. doi:10.1016/j.apenergy.2016.06.097.

[3] D. Fürstenwerth, L. Waldmann, et al., Report: Electricity Storage in the German Energy Transition (2014).

[4] B. Nykvist, M. Nilsson, Rapidly falling costs of battery packs for electric vehicles, Nature Climate Change 5 (4) (2015) 329–332. doi:10.1038/nclimate2564.

[5] B. Dunn, H. Kamath, J.-M. Tarascon, Electrical energy storage for the grid: a battery of choices, Science (New York, N.Y.) 334 (6058) (2011) 928–935. doi:10.1126/science.1212741.

[6] Technical University of Munich, Energy Neighbor goes online (2015).
URL https://www.tum.de/en/about-tum/news/press-releases/detail/article/32661/

[7] Infineon, IGBT Selection Guide (2016).
URL https://www.infineon.com/dgdl/Infineon-IGBT_Discretes_Selection_Guide-SG-v00_00-EN.pdf?fileId=db3a3043324cae8c01326cea43bc17bc

[8] V. F. Pires, E. Romero-Cadaval, D. Vinnikov, I. Roasto, J. F. Martins, Power converter interfaces for electrochemical energy storage systems–A review, Energy conversion and management 86 (2014) 453–475. doi:10.1016/j.enconman.2014.05.003.
[9] K. Rumpf, M. Naumann, A. Jossen, Experimental investigation of parametric cell-to-cell variation and correlation based on 1100 commercial lithium-ion cells, Journal of Energy Storage 14 (2017) 224–243. doi:10.1016/j.est.2017.09.010.
[10] Swissgrid Ltd., Grid - Transmission system - Grid levels: Various grid levels transport electricity.
URL https://www.swissgrid.ch/swissgrid/en/home/grid/transmission_system/grid_levels.html
[11] A. Becker, H. Loges, S. Kippelt, A. Gitis, G. Merei, D. Echternacht, M. Müller, A. Zeh, M. Kleimaier, M. Leuthold, et al., Electricity Storage Systems in Medium-and Low-Voltage Networks, in: International ETG Congress 2015; Die Energiewende-Blueprints for the new energy age; Proceedings of, 2015, pp. 1–8.
[12] T. Aundrup, H.-P. Beck, A. Becker, A. Berthold, Battery storage systems in the low voltage and mid voltage grid level - applications and economics as well as impact on electric grids (German title: Batteriespeicher in der Nieder-und Mittelspannungsebene-Anwendungen und Wirtschaftlichkeit sowie Auswirkungen auf die elektrischen Netze) (2015).
[13] C. N. Truong, M. Naumann, R. C. Karl, M. Müller, A. Jossen, H. C. Hesse, Economics of Residential Photovoltaic Battery Systems in Germany: The Case of Teslas Powerwall, Batteries 2 (2) (2016) 14. doi:10.3390/batteries2020014.
[14] J. Neubauer, M. Simpson, Deployment of behind-the-meter energy storage for demand charge reduction, National Renewable Energy Laboratory, Tech. Rep. NREL/TP-5400-63162.
[15] E. Reihani, S. Sepasi, L. R. Roose, M. Matsuura, Energy management at the distribution grid using a Battery Energy Storage System (BESS), International Journal of Electrical Power & Energy Systems 77 (2016) 337–344. doi:10.1016/j.ijepes.2015.11.035.
[16] C. Patsios, B. Wu, E. Chatzinikolaou, D. J. Rogers, N. Wade, N. P. Brandon, P. Taylor, An integrated approach for the analysis and control of grid connected energy storage systems, Journal of Energy Storage 5 (2016) 48–61. doi:10.1016/j.est.2015.11.011.
[17] A. Zeh, M. Müller, M. Naumann, H. C. Hesse, A. Jossen, R. Witzmann, Fundamentals of using battery energy storage systems to provide primary control reserves in Germany, Batteries 2 (3) (2016) 29. doi:10.3390/batteries2030029.
[18] Younicos, Europe's first commercial battery power plant to triple its capacity (2016).
URL https://www.younicos.com/europes-first-commercial-battery-power-plant-triple-capacity/
[19] Swissgrid Ltd., Control pooling.
URL https://www.swissgrid.ch/swissgrid/en/home/reliability/power_market/control_pooling.html
[20] M. Müller, L. Viernstein, C. N. Truong, A. Eiting, H. C. Hesse, R. Witzmann, A. Jossen, Evaluation of grid-level adaptability for stationary battery energy storage system applications in Europe, Journal of Energy Storage 9 (2017) 1–11. doi:10.1016/j.est.2016.11.005.
[21] D. L. King, S. Gonzalez, G. M. Galbraith, W. E. Boyson, Report: Performance Model for Grid-Connected Photovoltaic Inverters (2007).
URL http://citeseerx.ist.psu.edu/viewdoc/download?doi=10.1.1.464.6452&rep=rep1&type=pdf
[22] G. Notton, V. Lazarov, L. Stoyanov, Optimal sizing of a grid-connected PV system for various PV module technologies and inclinations, inverter efficiency characteristics and locations, Renewable Energy 35 (2) (2010) 541–554. doi:10.1016/j.renene.2009.07.013.
[23] S. Ponnaluri, G. O. Linhofer, J. K. Steinke, P. K. Steimer, Comparison of single and two stage topologies for interface of BESS or fuel cell system using the ABB standard power electronics building blocks, in: Power Electronics and Applications, 2005 European Conference on, 2005, pp. 9–pp. doi:10.1109/EPE.2005.219502.
[24] F. Casanellas, Losses in PWM inverters using IGBTs, IEE Proceedings - Electric Power Applications 141 (5) (1994) 235. doi:10.1049/ip-epa:19941349.
[25] E. Chatzinikolaou, D. J. Rogers, A Comparison of Grid-Connected Battery Energy Storage System Designs, IEEE Transactions on Power Electronics 32 (9) (2017) 6913–6923. doi:10.1109/TPEL.2016.2629020.
[26] S. K. Khadem, M. Basu, M. F. Conlon, Parallel operation of inverters and active power filters in distributed generation system—A review, Renewable and Sustainable Energy Reviews 15 (9) (2011) 5155–5168. doi:10.1016/j.rser.2011.06.011.
[27] L. Zhang, K. Sun, Y. Xing, J. Zhao, Parallel Operation of Modular Single-Phase Transformerless Grid-Tied PV Inverters With Common DC Bus and AC Bus, IEEE Journal of Emerging and Selected Topics in Power Electronics 3 (4) (2015) 858–869. doi:10.1109/JESTPE.2015.2417196.
[28] B. Wei, J. M. Guerrero, X. Guo, J. C. Vasquez, A Circulating-Current Suppression Method for Parallel Connected Voltage Source Inverters (VSI) with Common DC and AC Buses, IEEE Transactions on Industry Applications (2017) 1doi:10.1109/TIA.2017.2681620.
[29] Bonfiglioli, Product description RPS.
URL https://www.bonfiglioli.com/media/products/attachments/VE_CAT_RTL_STD_ENG-DEU_R00_1.pdf
[30] Siemens AG, Sinamics S120 Grid Infeed Manual (2015).
URL https://support.industry.siemens.com/cs/ww/en/view/109476635
[31] M. Schimpe, M. Naumann, N. Truong, H. C. Hesse, S. Santhanagopalan, A. Saxon, A. Jossen, Energy efficiency evaluation of a stationary lithium-ion battery container storage system via electro-thermal modeling and detailed component analysis, Applied Energy 210 (2018) 211–229. doi:10.1016/j.apenergy.2017.10.129.
[32] Siemens AG, Sinamics S120 List Manual (2016).
[33] Siemens AG, Sinamics S120 Function Manual Drive Functions (2016).
URL https://support.industry.siemens.com/cs/ww/de/view/109740020/en?dl=en
[34] Reprinted from Applied Energy, Vol 10, M. Schimpe, M. Naumann, N. Truong, H.C. Hesse, S. Santhanagopalan, A. Saxon, A. Jossen, Energy efficiency evaluation of a stationary lithium-ion battery container storage system via electro-thermal modeling and detailed component analysis, Pages 211-229, Copyright Elsevier.
[35] Infineon, Technical Information IGBT-modules FS150R12KE3 (02.10.2013).
URL http://www.infineon.com/dgdl/Infineon-FS150R12KE3-DS-v03_01-en_de.pdf?fileId=db3a304412b407950112b4311d745388

[36] M. Hornkamp, R. Tschirbs, Current shunt resistors integrated in IGBT power modules for medium power drive application, in: PCIM Asia, 2004.
[37] Siemens AG, Sinamics DCP Operating Instructions/Manual (2016).
URL https://support.industry.siemens.com/cs/ww/en/view/109480223
[38] Siemens AG, Sinamics DCP List Manual (2016).
URL https://support.industry.siemens.com/cs/af/en/view/99007204
[39] Siemens AG, Unpublished data.
[40] Siemens AG, Geafol Basic Transformer Brochure (2015).
URL https://www.siemens.com/global/en/home/products/energy/high-voltage/transformers/geafol-transformers.html
[41] Siemens AG, GEAFOL Transformer Planning Guidelines (2015).
URL https://www.siemens.com/content/dam/internet/siemens-com/global/products-services/energy/high-voltage/transformers/geafol/geafol-pdf-english/siemens-brochure-transformers-geafol-planning-guidelines-en.pdf
[42] M. Müller, A. Zeh, S. Rohr, S. F. Schuster, C. Campestrini, H. Hesse, R. Witzmann, M. Lienkamp, A. Jossen, Evaluation of the Aging Behaviour of Stationary Lithium-Ion Battery Storage Systems for Different Photovoltaic-Driven Applications in Low Voltage Grids, in: 31st European Photovoltaic Solar Energy Conference and Exhibition (EU PVSEC 2015), 2015. doi:10.4229/EUPVSEC20152015-7DV.4.4.
[43] European Network of Transmission System Operators for Electricity, Operation Handbook. Policy 1: Load-Frequency Control and Performance (2009).
URL https://erranet.org/wp-content/uploads/2017/02/Policy_1_final.pdf
[44] German Transmission System Operators, REGELLEISTUNG.NET Internet platform for the allocation of control reserve.
URL https://www.regelleistung.net/ext/?lang=en
[45] Siemens AG, Control Software Starter (2017).
[46] IGBT Module Manufacturer, Datasheet.

5 Power flow distribution strategy for improved power electronics energy efficiency in battery storage systems: Development and implementation in a utility-scale system

This section introduces the paper *Power Flow Distribution Strategy for Improved Power Electronics Energy Efficiency in Battery Storage Systems: Development and Implementation in a Utility-Scale System* and is based on the paper without further reference.

Chapter 3 revealed that the PE can be a major source of energy losses in BESS. Chapter 4 then showed that different grid connection topologies have a strong influence on the energy efficiency.

In this chapter, a second approach for reducing PE losses, a software-based PFDS is proposed, developed and tested in an industrial utility-scale BESS. The system, operated by *The Mobility House*, has been described in Section 2.2.2. Section 2.3.5 introduced measurement methods for the evaluation of field-deployed systems in operation, which are used in this paper.

Before summarizing the paper, a brief introduction to PFDS is given. Considering a single battery rack, consisting of a battery and a PE unit, Figure 5.1 shows the relative losses ϕ of battery, PE and total conversion over relative power $P_{\mathrm{AC,R}}/P_{\mathrm{AC,N,R}}$ for charging and discharging at steady-state conditions. Here the difference between the battery efficiency, which is highest at low power, to the PE efficiency, which is lowest at low power operation, is clearly visible. An optimum operating point can be achieved around 30 % to 40 % of nominal power for the specific configuration.

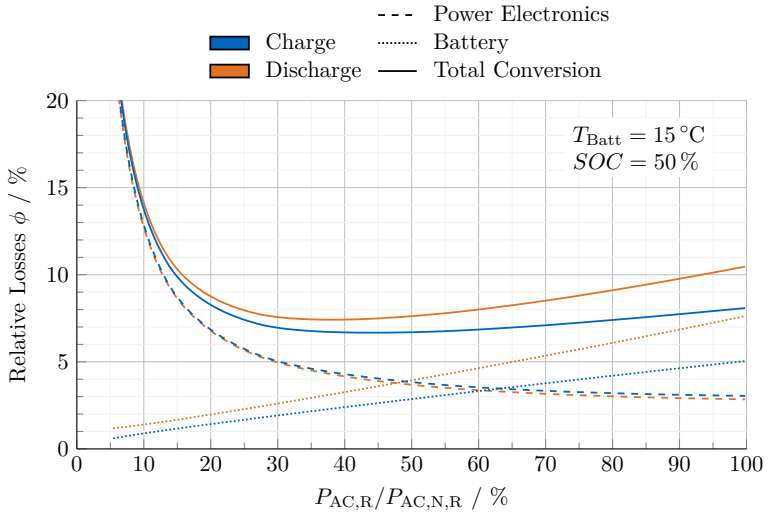

Figure 5.1: Relative losses of battery, PE and total conversion over relative rack load for charging and discharging at steady-state conditions. Figure adapted from [71].

Moving from the single battery rack towards a complete system, Figure 5.2 shows three BESS system architectures and PFDS. Figure 5.2a shows a system with separate racks and *uniform* PFDS. This PFDS is sometimes also defined as *homogenous* or *equal* PFDS and was also analyzed in the previous Chapters 3 and Chapter 4.
Figure 5.2b shows again a system with separate racks but with *efficiency-optimized* PFDS. Here, to avoid low efficiency at low power operating points, an *efficiency-optimized* PFDS is used which optimizes the power distribution among the racks - towards the optimum operating point around 30 % to 40 % of nominal power. The SOC between the different racks has to be managed, as the rack load will differ in operation, which leads to diverging SOC.
Figure 5.2c shows a system with DC-coupled racks and coupled PE, with the also efficiency-optimized *incremental* PFDS. The arrangement allows to use only the necessary number and the SOC does need not to be managed actively between the racks.

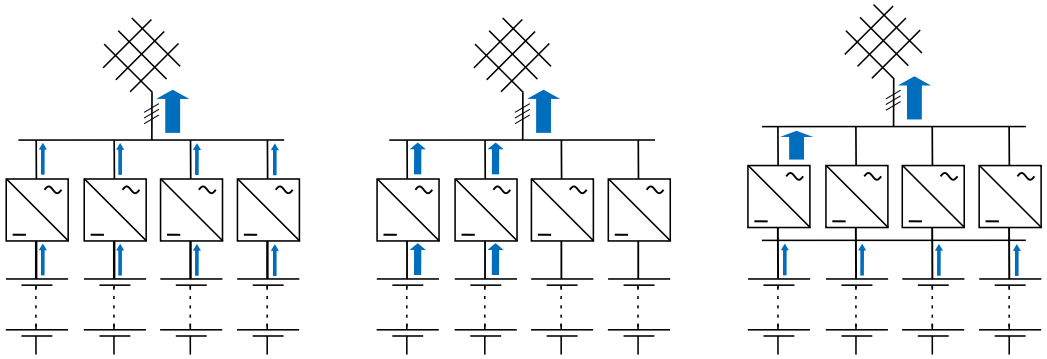

Figure 5.2: BESS system architectures and power flow distribution strategies: a) separate racks with *uniform* PFDS. b) separate racks with *efficiency-optimized* PFDS. c) DC-coupled racks with efficiency-optimized *incremental* PFDS. Figure adapted from [71].

Figure 5.3 shows the steady-state system a) discharge, b) charge and c) round-trip conversion efficiency $\eta_{\mathrm{Conv,Sys}}$ over relative system power $P_{\mathrm{AC,Sys}}/P_{\mathrm{AC,N,Sys}}$ for the three PFDS: *Uniform/homogenous* PFDS, *efficiency-optimized* PFDS on both separate racks, and efficiency-optimized *incremental* PFDS on DC-coupled racks.
The highest energy efficiency is achieved with the incremental PFDS on DC-coupled racks, as here the PE units are optimally operated and the battery power flow is evenly distributed among all racks. The second highest efficiency is achieved with the efficiency-optimized PFDS on separate racks. In comparison to the uniform PFDS, the issue of low efficiency at low power operating points is reduced strongly. The small “bumps” in both efficiency-optimized PFDS curves result from the switching when the number of active PE is changed.

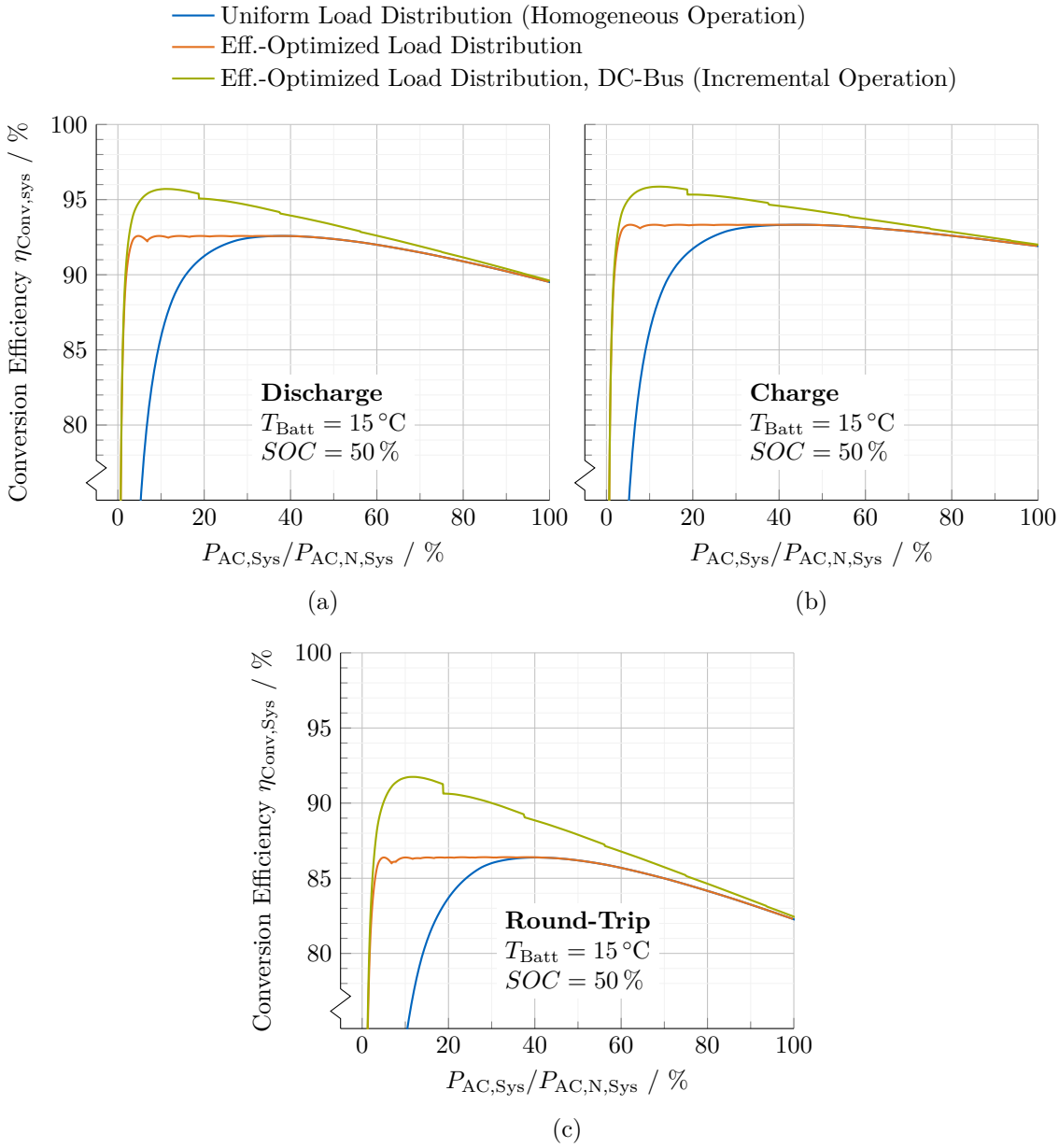

Figure 5.3: Steady-state system a) discharge, b) charge and c) round-trip conversion efficiency over relative system load for three power flow distribution strategies: *uniform* PFDS, *efficiency-optimized* PFDS on both separate racks, and efficiency-optimized *incremental* PFDS on DC-coupled racks. Figure adapted from [71].

In the paper referenced in this chapter, a utility-scale Second-Life system providing PCR is analyzed regarding its energy efficiency. The system consisting of separate racks operates on uniform PFDS and is then changed to operate on an efficiency-optimized PFDS.

A detailed system analysis is conducted, revealing the overall system energy efficiency at 56 %. The system is set up of several TU, which consist of the PE and the battery. The majority of losses occur in the TU. The energy efficiencies of the TU providing PCR are between 73 % and 77 %.
Simulation of the system reveals, that the main loss mechanism of the TU as well as of the overall system is identified as the no-load loss of the PE. The no-load losses have significant importance, as dynamic losses of the PE and those of the battery are small for the application PCR, which features a low average load. The PE units are however in constant operation, leading to the high amount of energy losses.
A temporal distribution analysis of the load profile shows that the PCR load is for 99.95 % of the time, and thus almost entirely, under 50 % of the nominal power of the TU.

Some TU in the system consist of two identical power strings. Based on this, an optimized PFDS for the power flow of the TU onto the two power strings is proposed. The goal is to reduce the no-load and partial-load losses by providing PCR with a single power string when possible. This consequently reduces the no-load losses of the second power string through its deactivation. The optimized PFDS thus controls the power flow for each power string independently. As this requires a dedicated management of the battery SOC in each power string, a battery SOC management strategy is also developed.
The optimized PFDS is implemented in a TU of the system and put into operation for PCR. The comparison of the analysis based on measured data shows that the TU energy efficiency is improved by 9 percentage points, which equates to a reduction of the energy losses by 24 %. The reduction also leads to a reduced energy balance for the intraday trading by 34 %. The overall energy throughput of the TU is reduced by 7 %. The optimized PFDS also successfully manages the battery SOC of the individual battery packs.

In summary, the proposed optimized PFDS can improve energy efficiency in BESS consisting of multiple units.

Author contribution The author of this thesis developed the system model for energy efficiency evaluations, initiated as well as coordinated the study, and wrote the paper draft. Through his master's thesis, Christian Piesch adapted the system model, parameterized and evaluated the data from simulation and the field test, and developed the optimized PFDS. Julian Paß provided model parameters and field-test data, and coordinated the implementation of the new control strategies in the system. Parts of the results have also been presented at the conference *International Renewable Energy Storage Conference (IRES) 2018* by the author of this thesis.

Power Flow Distribution Strategy for Improved Power Electronics Energy Efficiency in Battery Storage Systems: Development and Implementation in a Utility-Scale System

Michael Schimpe, Christian Piesch, Holger C. Hesse, Julian Paß, Stefan Ritter, Andreas Jossen

Energies 11(3), 533, 2018

Permanent weblink:
https://doi.org/10.3390/en11030533

Reproduced under the terms of the Creative Commons Attribution 4.0 License (CC BY 4.0, http://creativecommons.org/licenses/by/4.0/), which permits unrestricted reuse of the work in any medium, provided the original work is properly cited.

energies

MDPI

Article

Power Flow Distribution Strategy for Improved Power Electronics Energy Efficiency in Battery Storage Systems: Development and Implementation in a Utility-Scale System

Michael Schimpe [1,*], Christian Piesch [1], Holger C. Hesse [1], Julian Paß [2], Stefan Ritter [2] and Andreas Jossen [1]

[1] Department of Electrical and Computer Engineering, Institute for Electrical Energy Storage Technology, Technical University of Munich, Arcisstr. 21, 80333 Munich, Germany; C.Piesch@gmx.net (C.P.); holger.hesse@tum.de (H.C.H.); andreas.jossen@tum.de (A.J.)

[2] The Mobility House GmbH, St.-Cajetan-Str. 43, 81669 Munich, Germany; Julian.Pass@mobilityhouse.com (J.P.); Stefan.Ritter@mobilityhouse.com (S.R.)

* Correspondence: michael.schimpe@tum.de; Tel.: +49-89-289-26973

Received: 21 January 2018; Accepted: 27 February 2018; Published: 1 March 2018

Abstract: Utility-scale battery storage systems typically consist of multiple smaller units contributing to the overall power dispatch of the system. Herein, the power distribution among these units is analyzed and optimized to operate the system with increased energy efficiency. To improve the real-life storage operation, a holistic system model for battery storage systems has been developed that enables a calculation of the energy efficiency. A utility-scale Second-Life battery storage system with a capacity of 3.3 MWh/3 MW is operated and evaluated in this work. The system is in operation for the provision of primary control reserve in combination with intraday trading for controlling the battery state of charge. The simulation model is parameterized with the system data. Results show that losses in power electronics dominate. An operational strategy improving the energy efficiency through an optimized power flow distribution within the storage system is developed. The power flow distribution strategy is based on the reduction of the power electronics losses at no-load/partial-load by minimizing their in-operation time. The simulation derived power flow distribution strategy is implemented in the real-life storage system. Field-test measurements and analysis prove the functionality of the power flow distribution strategy and reveal the reduction of the energy throughput of the units by 7%, as well as a significant reduction of energy losses in the units by 24%. The cost savings for electricity over the system's lifetime are approximated to 4.4% of its investment cost.

Keywords: battery storage system; energy efficiency; power flow distribution; system simulation; primary control reserve; field-test

1. Introduction

Energy storage systems are a promising option to provide flexibility and grid services in future electric grids [1,2]. Today, lithium-ion battery systems are being built in increasing number of installations as well as increasing power and energy capacities [3]. Such utility-scale battery systems typically consist of multiple units which together comprise the total nominal system power and energy [4].

In this work, we focus on systems consisting of multiple units, which each feature a battery and a dedicated power electronics (PE) and can thus be operated independently. In contrast, topologies that connect battery packs of multiple units in parallel may lead to heterogeneous current flows between

parallel-connected battery packs due to variances for the battery impedance and capacity, which cannot be controlled [5,6]. This is of particular importance for systems which feature battery packs of varying State of Health or different battery chemistries, such as the battery packs in the Second-Life battery systems of this work. Dedicated PE for each battery pack is thus widely used, as in the battery storage system of this work.

The actual power for each unit is calculated based on the power flow distribution strategy (PFDS) of the system. The total system power is the sum of the power of all units. Typically, battery systems distribute the system power flow equally among the units comprising the system (Equal PFDS). The Equal PFDS is a technically stable and simple approach, as it ideally leads to identical levels of the battery state of charge (SOC) in all units. Between units of varying nominal energy, e.g., a unit of 50 kWh and a unit of 100 kWh, the total system power is scaled for the units according to their nominal energy to 1/3 for the 50 kWh unit and 2/3 for the 100 kWh unit. It is noted that the power capacity of the units has also to be taken into consideration.

However, the equal division of the total system power among all units also leads to low-power operating points for the units. PE show low efficiencies at partial load, and consequently relatively high conversion losses occur. Figure 1a shows the typical power loss curve of a bidirectional inverter applicable to battery storage systems. Losses at no-load/partial load are relatively high, and at no load, the losses amount to approximately 0.75% of the nominal unit power or 28.40% of the unit losses at nominal power. Figure 1b shows the resulting conversion energy efficiency, which is consequently low at partial load.

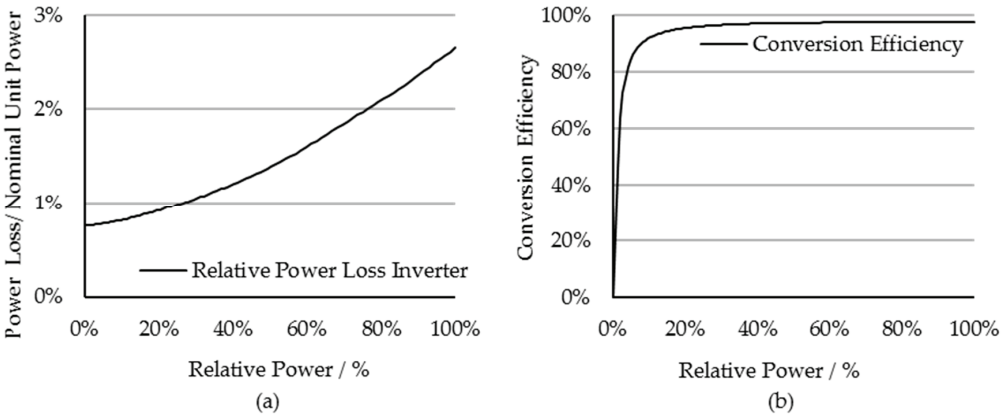

Figure 1. Power losses in a bidirectional inverter: (**a**) power losses over relative power; and (**b**) conversion energy efficiency over relative power. Data from [7].

As the energy efficiency is a key performance indicator for battery storage systems and recent investigations showed that overall system efficiencies for real-world grid applications are indeed lower than typical literature values, especially due to the PE, options on how to reduce these losses require investigation [7].

The studied system is a Second-Life battery storage system, operated by *The Mobility House* in Lünen, Germany [8]. The system is set up from used battery packs from electric cars and has a nominal capacity/power of 3.3 MWh/3 MW. It should be noted that the system is part of a larger system with a total capacity of 13 MWh, but this study focusses on the 3.3 MWh sub-system only. The system is in operation for the provision of Primary Control Reserve (PCR) in combination with intraday trading (ID) for controlling the battery SOC. Further details on the system and its application follow in the subsequent Section (Section 2).

Thus far, only a few studies investigated power flow distribution strategies for battery systems. A PFDS for improving energy efficiency was proposed by Choi et al. in [9]. The focus was put on the

system availability in their proposed method. Lee et al. discussed and tested the provision of frequency control through multiple energy storage systems based on hierarchical cluster structures, but with a focus on system availability and reliability and no consideration of energy efficiency [10]. Cho and Yun proposed an optimized PFDS for improved energy efficiency based on genetic algorithms which aim for the optimal operating point of the power electronics as well as balanced energy throughput [4]. In contrast to the reviewed studies, this work features an analysis of a utility-scale Second-Life battery system in detail for its energy efficiency and consequently the development of an optimized PFDS and its implementation. Field-test measurements are evaluated and show the feasibility of the PFDS as well as the successfully improved operation metrics.

A holistic system model for battery storage systems that enables a realistic calculation of the energy efficiency is parameterized with the system structure, the component data, and the application load profiles. The system so far operates on equal PFDS. After validating the system model with the measurement data from the system, a detailed energy loss analysis is conducted. Results confirm the high conversion losses in the PE at the low operating point of the system.

Consequently, an optimized PFDS is proposed. The optimized PFDS is based on the reduction of the operation time of the PE. Only the currently required inverters are in operation. The mechanism for the improvement of the overall system efficiency is thus the reduction of the PE losses occurring at low load and at no load. Simulation results suggest significant potential for the improvement of energy efficiency. The optimized PFDS is implemented in the battery system. Measurements show the functionality of the operational strategy, the reduction of the energy throughput as well as the significant reduction of energy losses.

The paper is structured as follows. Section 2 introduces the Second-Life battery system and its grid application in detail. Section 3 describes the system model used for the energy loss analysis and presents the results. Section 4 presents the optimized PFDS and the results of the implementation in the storage system. Section 5 concludes the study and their results. Finally, future work is suggested in Section 6.

2. Second-Life Battery System

The system in this work is a Second-Life battery storage system. Second-Life here refers to the *second* application of automotive batteries that were *first* used in battery electric vehicles. The stationary application for the battery packs extends their usage beyond their initial mobile application. The concept is a promising approach to reduce the high costs associated with the battery packs for a battery system [11,12], and thus improve the economic viability of battery storage systems and their applications [13–15]. As Second-Life is still a relatively new concept, economic and battery lifetime evaluations are still under investigation today [16–18]. As one of the first systems and at time of the installation the largest Second-Life system in the world, the system in this work also shows the technical feasibility of Second-Life concepts.

The system in this work is based on battery packs of electric vehicles sold under brand name *Smart electric drive* by Daimler and is operated by *The Mobility House* in cooperation with *GETEC* and *REMONDIS* in Lünen, Germany [8]. The system setup and measurements, as well as the system model and its parameters, are provided by *The Mobility House* and are unpublished and company-internal data. The model parameters cited [19] and system measurements used/presented in the following are thus not available for publication as raw data.

The system is in operation for the provision of PCR, a grid ancillary service for frequency control. PCR is the stabilization of the grid frequency by providing positive or negative power to the grid in case of frequency deviations from the nominal frequency. For systems providing PCR, the actually required power to be provided is determined by the measured frequency deviation [20]. The ancillary service is remunerated and coordinated by the Transmission System Operators (TSO) [21]. As battery systems have limited storage capacity, they need to charge/discharge power additionally to the frequency control power to maintain their SOC. This additional power can be flexibly bought/sold through

power contracts, such as intraday trading. Specific protocols and regulations have been set by the TSO for the PCR operation and market participation of battery systems [22]. Model-based studies on battery systems providing PCR already evaluated battery lifetime [23,24], sensitivity studies on the energy management strategies and regulations [25], as well as economic implications for the battery system operation [24].

Figure 2 shows a schematic overview of the system under investigation. The system consists of six Technical Units (TU), the auxiliary system components, and the grid connection.

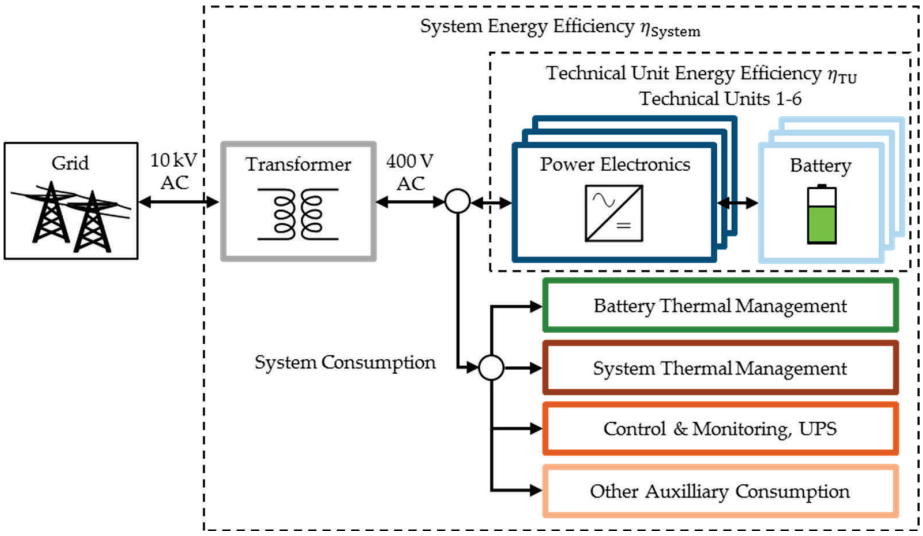

Figure 2. Storage system overview with grid connection and auxiliary components.

The TU each consist of batteries with dedicated PE. The auxiliary components are required for the operation of the overall system (Battery Thermal Management, System Thermal Management, and Control and Monitoring). A transformer connects the system-internal 400 V AC low-voltage to the 10 kV medium-voltage grid [26]. The TU, as well as the auxiliary components, are connected to the low voltage level within the system.

The calculation boundaries of the round-trip technical unit energy efficiency η_{TU}, which includes the battery and the power electronics, as well as for the overall round-trip system energy efficiency η_{System}, which further includes the transformer and the auxiliary system consumption, are also indicated in Figure 2.

Figure 3 shows a detailed overview of the TU with their varying specifications and setups. TU 2–5 each consist of two identical power strings. Both power strings each provide half of the nominal power/energy of the TU. TU 3–5 are identical and shown only once.

TU 1 serves as a backup unit for the other units and is used rarely for system-internal load balancing. It is therefore typically not providing PCR. TU 2–6 provide PCR to the electrical grid. Each TU providing PCR is acting as an independent unit. The PFDS is thus only considered within the specific TU. For the units featuring only a single power string (TU 1, TU 6) no PFDS is relevant. Within the units that consist of two power strings (TU 2–5), the equal PFDS distributes the power equally to both power strings that have identical nominal power for the ideal case, in which no SOC difference between the batteries of the two power strings is measured. If a SOC difference arises, a correction factor is applied to achieve an equal SOC between the power strings again.

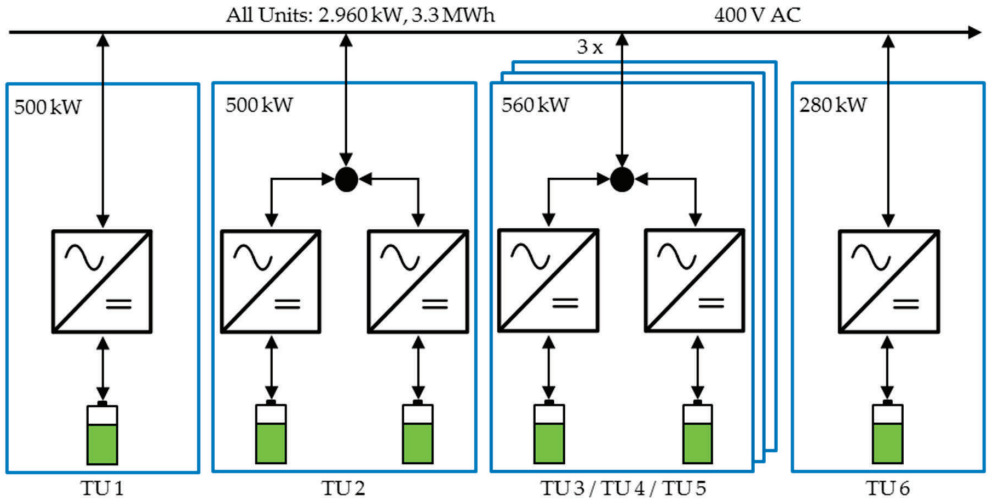

Figure 3. Overview of all Technical Units.

3. System Simulation

Section 3.1 introduces the system model structure, the component models, and parameterization. Section 3.2 then presents the model validation against measured data as well as the results and implications of the energy loss analysis of the system.

3.1. Model Development

The model developed for the system analysis is based on an existing system model by Schimpe et al. [7]. The model is developed for holistic energy efficiency evaluations of container-size to utility-scale battery storage systems. Separate component models are implemented and coupled to an overall system model.

The existing model is adapted to the specific system structure and parameters for all components of the specific system are implemented.

Table 1 shows the grouped components of the system, their respective component model type as well as the main parameters used for the model parameterization.

The battery-pack, part of the TU, is modeled based on a single-cell model. The cell is simulated through an equivalent circuit model featuring an open circuit voltage $U_{\mathrm{Cell,OCV}}$ as well as a resistance R_{Cell}, which accounts for the overvoltages within the cell. The resistance parameters are derived from pulse parameterization for both directions of current I, charge (positive) and discharge (negative). The battery packs are water-cooled and stored at approximately 20 °C ambient temperature, and operate at a low average load as will be discussed in Section 3.2. The cell temperatures are thus expected to not increase in temperature strongly. As thermal parameters of the cell and pack are not available, the cell parameters, open circuit voltage and resistance values, are taken and implemented at a temperature of 25 °C versus the State of Charge *SOC*. Mismatching losses in the series-connection and increases in battery cell resistances due to cell degradation are not implemented, as no information is available, but in general, are both expected to increase losses.

The second component model of the TU, the PE model, is implemented through look-up data of the power losses $P_{\mathrm{PE,Loss}}$ as function of the power, P_{PE}. The data, which is provided for each PE type by the PE manufacturer, is implemented with separate data for both power flow directions, charge, as well as discharge. Power factor is set to 1 for both system operation providing PCR as well as in the measurements of the power loss curves.

The transformer connecting the overall system to the grid is modeled based on measured data for the power loss at both no-load and full-load, which is provided by the transformer manufacturer.

The transformer losses $P_{\mathrm{TF,Loss}}$ are then calculated with a square-power function for the load-dependent losses, which feature Ohmic loss behavior, as function of the secondary-side power $P_{\mathrm{TF,Sec}}$.

Table 1. Component model overview.

Component Group	Component	Type	Parameter Overview (All: Data from [19])
Technical Unit	Battery	Equivalent Circuit Model	$U_{\mathrm{Cell,OCV}}(SOC, T = 25\,^{\circ}\mathrm{C})$, $R_{\mathrm{Cell}}(SOC, \mathrm{sgn}(I), T = 25\,^{\circ}\mathrm{C})$
	Power Electronics	Loss-Curve Look-Up Data	$P_{\mathrm{PE,Loss}}(\mathrm{sgn}(P_{\mathrm{PE}}), P_{\mathrm{PE}})$
Grid Connection	Transformer	Loss-Curve Look-Up Data	$P_{\mathrm{TF,Loss}}(P_{\mathrm{TF,Sec}})$
Auxiliary Components	Battery Thermal Management System (B-TMS)	Measured Data over Time (No Model)	$P_{\mathrm{Aux,B\text{-}TMS}}(t)$
	System Thermal Management System (S-TMS)		$P_{\mathrm{Aux,S\text{-}TMS}}(t)$
	Control & Monitoring incl. Uninterruptible Power Supply (C&M)		$P_{\mathrm{Aux,C\&M}}(t)$
	Other		$P_{\mathrm{Aux,Other}}(t)$
System Control	Load Profile	Measured Data over Time (Model Input)	$P_{\mathrm{TU,AC}}(t)$
	Initial/End State of Charge		$SOC_{\mathrm{TU}}(t)$

The auxiliary components are not modeled but implemented through measured data for their power consumption. Four groups are defined: (I) Battery Thermal Management System (B-TMS); (II) System Thermal Management System (S-TMS); (III) Control and Monitoring components that include the Uninterruptible Power Supply (C&M); and (IV) the remaining consumption for various components. Detailed measurements of the remaining various components are not available; however, a large share of consumption is assumed to be attributed to ambient air filter components. For each auxiliary component group, the measured power consumption P_{Aux} is implemented as function of time t.

The power control of the system is implemented as the load profile for each TU, based on the measured data over time, $P_{\mathrm{TU,AC}}$. The SOC measured in each TU (average SOC for a TU with two power strings), SOC_{TU}, is set as initial value for the simulation after every 24 h to remove SOC drift between the model and the system due to small deviations for the battery current, which add up over long simulation durations. The changes in SOC through the reset are included in the loss calculation.

3.2. Simulation Results

Before analyzing the energy losses of the complete system, the TU model is validated against measured data. The measured efficiency values here and in the following include the differences of stored energy through the changed battery SOC between the beginning and the end of the considered period.

Table 2 shows the charged/discharged energy of the TU, and the simulated/measured round-trip energy efficiency and their deviation for the month of March 2017.

Table 2. Charged/discharged energy and simulated/measured round-trip energy efficiency for Technical Units 1–6 for March 2017.

TU	Application	Charged Energy in MWh	Discharged Energy in MWh	Simulation Efficiency $\eta_{\mathrm{TU,Sim}}$	Measured Efficiency $\eta_{\mathrm{TU,Meas}}$	Simulation Deviation $\eta_{\mathrm{TU,Sim}} - \eta_{\mathrm{TU,Meas}}$
TU 1	Back-Up + ID	7.75	5.04	64.79%	64.95%	−0.16%
TU 2	PCR + ID	18.79	14.38	76.01%	76.65%	−0.64%
TU 3	PCR + ID	19.01	13.88	71.11%	73.14%	−2.03%
TU 4	PCR + ID	19.34	14.08	71.36%	72.88%	−1.52%
TU 5	PCR + ID	19.38	14.19	71.52%	73.34%	−1.82%
TU 6	PCR + ID	9.69	7.18	71.74%	74.11%	−2.37%
All TU	various	93.96	68.76	71.77%	73.25%	−1.48%

Energy throughput for TU 2–6 varies with the respective unit power. TU 1, the backup unit, is rarely active for inter-system balancing operation. TU 2–6 providing PCR show similarly measured

efficiencies between 72.88% and 76.65%. The different efficiencies are caused by technical setup variations, such as varying battery types, which are each implemented with specific parameters, and different inverter sizes (see Figure 3). TU 1, the backup unit, is active at only low relative power and thus has a relatively low efficiency.

The simulation results for the energy efficiency of the various TU are between 0.16% and 2.37% higher than the measured values. This trend in the deviation results possibly from the battery model. In the implemented type of equivalent circuit model, all battery overvoltages under load are calculated based on the single resistor in the model. Battery overvoltages are, however, dynamic, increasing with longer durations of load [27]. A battery operating under fluctuating load thus operates with decreased overvoltages compared to a battery model using a non-dynamic resistor only. Finally, the accuracy of the power electronics parameters for the power loss curve can significantly influence the model result.

All units in total have a measured efficiency of 73.25% for which the simulation predicts an efficiency of 71.77%, equating to a deviation of −1.48%. Summarized, the model is in good agreement with the measured data for the system.

When considering the complete system, the round-trip energy efficiency η_{System} is found significantly lower at 56.06%, again for March 2017. The reduction is due to the additional energy losses in the transformer (1.79 MWh) as well as due to the auxiliary energy consumption (B-TMS 1.47 MWh, S-TMS 2.57 MWh, C&M 7.88 MWh, Other 1.18 MWh).

To identify the exact mechanism, the loss distribution analysis for the complete system is conducted and shown in Figure 4 for the operation presented in Table 2. The left side shows the distribution grouped by transformer losses, auxiliary consumption and the losses occurring in the TU.

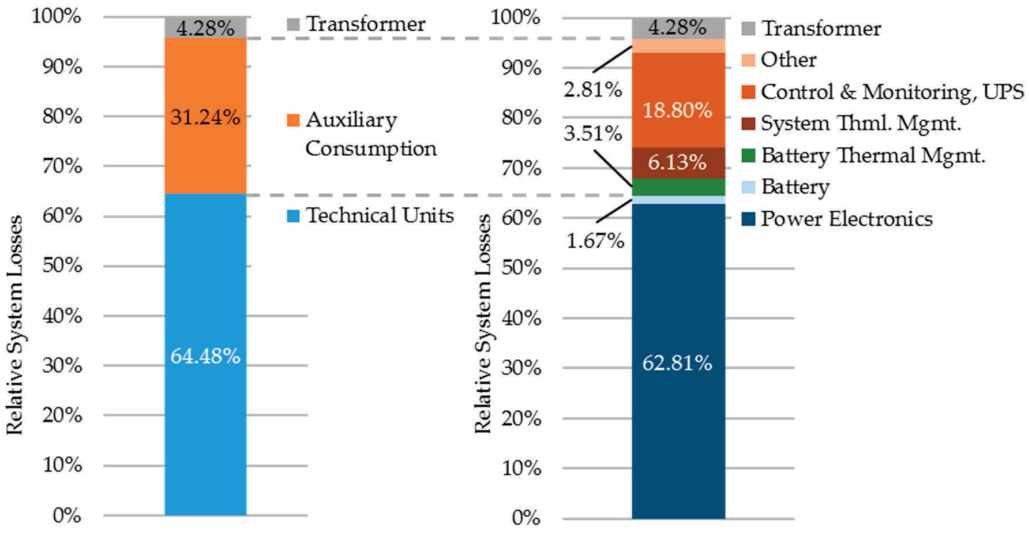

Figure 4. Overall system energy loss analysis based on model data for March 2017 for all units in operation for Primary Control Reserve/Intraday trading/Back-Up power.

With 64.48% of the overall losses, the TU are responsible for most losses. Second is the auxiliary consumption, which leads to 31.24% of all losses. The transformer's share of losses at 4.28% is here the smallest contributor.

The right side shows the analysis with a more detailed breakdown. Within the TU, the PE is identified as the largest contributor, whereas the batteries are the smallest contributor of all loss mechanisms. The breakdown of the auxiliary consumption shows that all components are relevant contributors. The Control and Monitoring of the overall system, which also includes the power consumption of the uninterruptible power supply, is the biggest contributor to the auxiliary

consumption and the second-largest in overall. It is noted that the energy consumption of the thermal management is subject to changes with varying outdoor temperatures and that this analysis specifically covers March 2017 only.

As the model represents the auxiliary consumption only as measured data, no improvement strategies for the auxiliary consumption of the given system through improved operation can be evaluated. The transformer is a passive component and thus also offers no improvement potential through operational strategies. Consequently, an improved operational strategy derived from the analysis in this work will focus on the TU operation, which is the largest contributor to the system losses as the previous analysis has shown.

Figure 5 shows the loss distribution for all TU. Here the differentiation between *no-load* losses and *dynamic* losses for the PE is made. Losses within the PE are the sum of switching and conduction losses within the semiconductors, magnetic losses in filter components, and Ohmic losses in general. As no detailed PE model is available, the losses are grouped into no-load losses and dynamic losses. No-load losses are defined as the power losses occurring at no output power, but with the PE unit in operation, fully connected to its AC and DC sources, and with the switching control active. Dynamic losses are defined as the losses that occur additionally to the no-load loss value when the unit increases its output power.

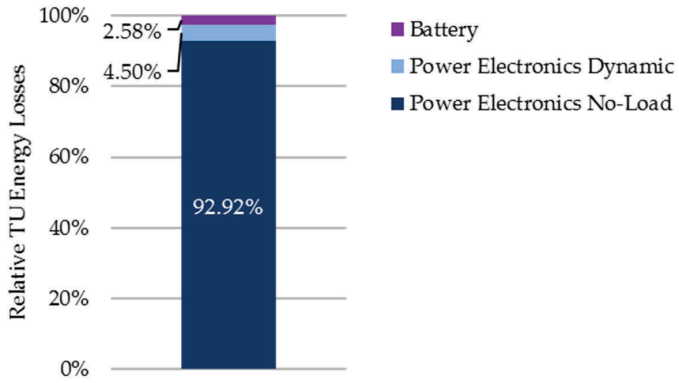

Figure 5. Technical Unit energy loss analysis based on model data for March 2017.

The analysis shows that in total the no-load losses lead to 92.92% of the overall losses of the TU. The battery losses and the dynamic PE losses are in comparison much smaller.

For further evaluation of the origin of losses in the TU, the profile of the application is analyzed. Figure 6a shows the measured AC-side power of TU 6 ($P > 0$: Charge, $P < 0$: Discharge) over time. Within the representative duration of six arbitrary hours, the maximum absolute power is 78.92 kW, and the average of the absolute power is only 16.52 kW. Both values are relatively small in comparison to the nominal PE power of 280 kW. The selected duration is representative of the available data in terms of two aspects: (I) grid frequency fluctuations constantly require the operation of the TU; and (II) TU power is on average low.

The resulting power losses (simulated data) are shown in Figure 6b. The PE losses here constantly show a high offset value as the PE is in operation at all times. The offset value is also high in comparison to additional dynamic losses or to the battery losses, which confirms the previous findings of the TU loss analysis (see Figure 5).

The conclusion from the loss analysis is that the PE no-load losses are the largest contributor to the system losses. As the losses can only be avoided when the PE unit is turned off, an analysis of the actual power demand is conducted to evaluate if this is an option considering the load profile. Figure 7 shows the temporal distribution of the relative power of TU 5 in March 2017.

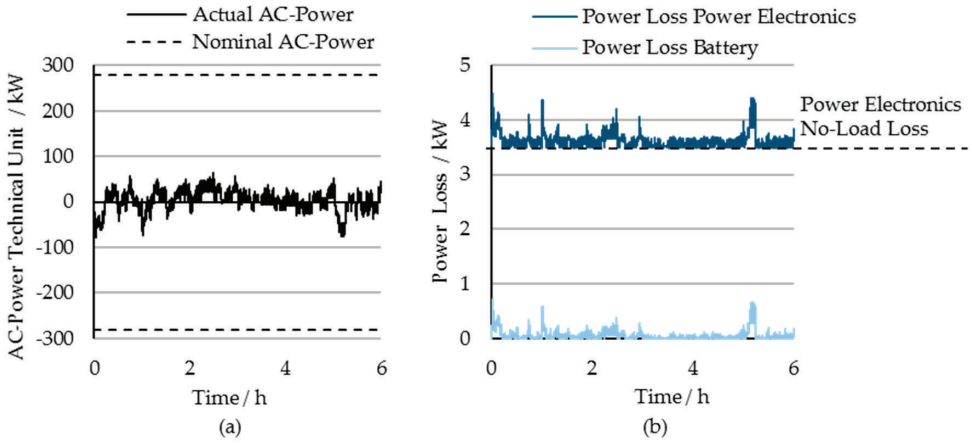

Figure 6. Time series analysis for load profile and power loss for a single Technical Unit (TU 6) during an arbitrary six-hour timeframe: (**a**) measured AC-power ($P > 0$: Charge, $P < 0$: Discharge); and (**b**) simulated power losses in power electronics and battery.

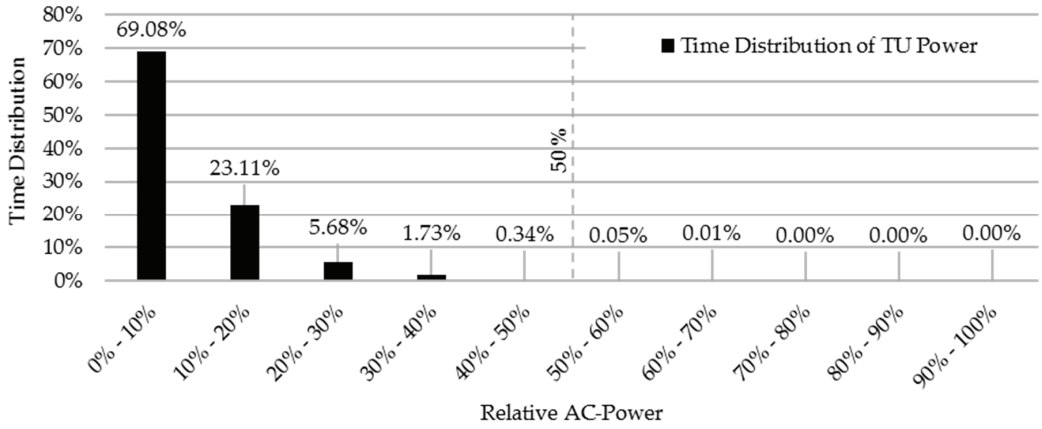

Figure 7. Temporal distribution of the relative power of a single Technical Unit (TU 5) in March 2017.

Most of the time, the power is low: 99.95% of the time, the relative power is under 50%. As TU 3–5 consist of two power strings of identical setup, during this time, theoretically, only a single power string would be sufficient for providing the output power. This result motivates the development of an optimized PFDS that uses this optimization potential.

4. Optimized Power Flow Distribution Strategy

Section 4.1 describes the proposed optimized PFDS based on the previously discussed results. The procedure and results of the implementation in the storage system are presented in Section 4.2.

4.1. Proposal and Development

The energy loss analysis showed that the biggest contributor to the system losses are the no-load PE losses and that they are responsible for 92.92% of the losses occurring in the TU. The profile analysis showed that most of the time, less than 50% of the TU power is required in the PCR application.

As the no-load losses can be reduced through deactivation of PE units, a PFDS that uses only the minimum number of required power strings within the TU is expected to have significant potential to improve the energy efficiency. The PFDS is applicable for the TU consisting of two power strings.

This proposed optimized PFDS is a non-equal PFDS that consequently leads to a variation of the SOC between the batteries in the power strings. The total TU power for both charge and discharge has to be kept available at all times. E.g., if one string is at the maximum SOC due to insufficient SOC management, the string cannot provide power for the charge direction, which results in a reduction of the TU charge power availability by 50%. The SOC difference between the two strings should thus be as small as possible so the TU power availability does not differ from an equal PFDS. The PFDS thus also has to respect the varying SOC values in terms of the energy management for the provision of PCR.

Figure 8 shows the schematic overview for a TU with two power strings. The unit power P_{TU} is distributed to the power strings $P_{TU,1}$ and $P_{TU,2}$:

$$P_{TU} = P_{TU,1} + P_{TU,2} \tag{1}$$

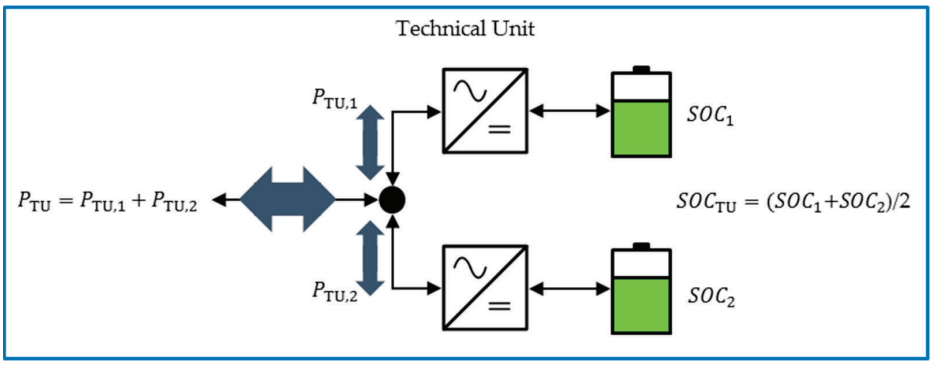

Figure 8. Schematic overview of a Technical Unit consisting of two power strings.

The two battery SOC values, SOC_1 and SOC_2, and the corresponding average SOC for the unit SOC_{TU}, are also shown.

For the provision of PCR, the average SOC of the TU SOC_{TU} is aimed to be held around the goal value SOC_{Goal} of approximately 50% with approximately 10% allowed variation resulting in the minimum/maximum SOC limits SOC_{min} and SOC_{max}. The intraday power $P_{TU,Intraday}$ for the TU is accordingly controlled to maintain the average SOC of the TU. The total unit power P_{TU} ($P_{TU} > 0$: Charge, $P_{TU} < 0$: Discharge) is therefore defined as the sum of the required power for PCR, $P_{TU,PCR}$, and the Intraday power $P_{TU,Intraday}$:

$$P_{TU} = P_{TU,PCR} + P_{TU,Intraday} \tag{2}$$

Both individual power string SOC values are additionally required to be maintained within the range of SOC_{min} to SOC_{max}. The distribution of the unit power P_{TU} to the power of both strings $P_{TU,1}$ and $P_{TU,2}$ therefore has to fulfill the SOC management as well as the reduction of the no-load/low-load losses in the PE through a distribution of the unit power to a single string when possible. Equation (3) defines the SOC difference within a TU ΔSOC_{TU}.

$$\Delta SOC_{TU} = SOC_2 - SOC_1 \tag{3}$$

The conditions and PFDS settings shown in Table 3 define the operation when both power strings are active. The SOC imbalance between both power strings is minimized with a droop control based on the SOC difference ΔSOC_{TU}. At a SOC difference of 10%, a value chosen based on practical results, the droop control is fully activated.

Table 3. State of Charge droop control for operation with both power strings active.

Power	Condition ΔSOC_{TU}	Set-Point for $P_{TU,1}/P_{TU}$	Set-Point for $P_{TU,2}/P_{TU}$
$P_{TU} \geq 0$	$\Delta SOC_{TU} \leq -10\%$	0%	100%
	$-10\% < \Delta SOC_{TU} \leq +10\%$	$50\% + 1/20\% \times \Delta SOC_{TU}$	$50\% - 1/20\% \times \Delta SOC_{TU}$
	$\Delta SOC_{TU} \geq +10\%$	100%	0%
$P_{TU} < 0$	$\Delta SOC_{TU} \leq -10\%$	100%	0%
	$-10\% < \Delta SOC_{TU} \leq +10\%$	$50\% - 1/20\% \times \Delta SOC_{TU}$	$50\% + 1/20\% \times \Delta SOC_{TU}$
	$\Delta SOC_{TU} \geq +10\%$	0%	100%

The set-point values can be overridden when the set-point value for a power string would exceed its current maximum power. This can be the case, e.g., when both power strings are required for the provision of the power, such as at a TU power of 75% at the same time as an absolute SOC deviation ΔSOC_{TU} higher than 10%. The power is then provided by the power strings as much as technically possible. The power, which then cannot be provided by a power string, is distributed to the other power string—overriding the set-point value here.

The conditions and PFDS settings shown in Table 4 define the operation for operating points that can theoretically be provided with a single power string: $|P_{TU}| \leq P_{TU,String,max}$.

Table 4. Operation modes for optimized Power Flow Distribution Strategy for operating points theoretically requiring only a single power string ($|P_{TU}| \leq P_{TU,String,max}$).

Mode	Condition SOC_1	Condition SOC_2	Charge $P_{TU} \geq 0$		Discharge $P_{TU} < 0$	
			$P_{TU,1}/P_{TU}$	$P_{TU,2}/P_{TU}$	$P_{TU,1}/P_{TU}$	$P_{TU,2}/P_{TU}$
Mode 1	$SOC_{min} < SOC_1 < SOC_{max}$	$SOC_{min} < SOC_2 < SOC_{max}$	100% switching every 6 h of in-operation time to 0%	0% switching every 6 h of in-operation time to 100%	100% switching every 6 h of in-operation time to 0%	0% switching every 6 h of in-operation time to 100%
Mode 2	$SOC_1 \leq SOC_{min}$	$SOC_{min} < SOC_2 < SOC_{max}$	100%	0%	0%	100%
Mode 3	$SOC_{min} < SOC_1 < SOC_{max}$	$SOC_2 \leq SOC_{min}$	0%	100%	0%	100%
Mode 4	$SOC_1 \geq SOC_{max}$	$SOC_{min} < SOC_2 < SOC_{max}$	0%	100%	0%	100%
Mode 5	$SOC_{min} < SOC_1 < SOC_{max}$	$SOC_2 \geq SOC_{max}$	100%	0%	0%	100%
Mode 6	$SOC_1 \leq SOC_{min}$	$SOC_2 \leq SOC_{min}$	Both power strings active, see Table 3			
Mode 7	$SOC_1 \geq SOC_{max}$	$SOC_2 \geq SOC_{max}$	Both power strings active, see Table 3			
Mode 8	$SOC_1 \leq SOC_{min}$	$SOC_2 \geq SOC_{max}$	100%	0%	0%	100%
Mode 9	$SOC_1 \geq SOC_{max}$	$SOC_2 \leq SOC_{min}$	0%	100%	100%	0%

The standard operation is *Mode 1* when both power string SOC levels are within the limits. Every full six hours of in-operation time of a power string, the operation is switched to the other power string to balance operation time equally. In *Modes 2–3*, one power string is at or below the lower SOC limit and thus deactivated for discharge operation. Similarly, in *Modes 4–5*, a power string is at or above the upper SOC limit and consequently deactivated for charge operation. For *Modes 6–7*, both power strings are activated as the SOC is violating the same lower or upper SOC limit. The operation of the two strings consequently follows the distribution according to Table 3. Finally, *Modes 8–9* are specified for the unlikely case that a power string violates the upper limit at the same time when the other power string violates the lower limit. In the case one of the *Modes 2–9* is activated, *Mode 1* is only reactivated when the value of SOC_1 and/or SOC_2 has/have reached SOC_{Goal} again.

It is here noted that the PE in the system have a time-limit for their start-up process, meaning that five minutes have to be passed between two start-up procedures. Thus, if a unit is turned on, it is not deactivated for five minutes to ensure it is still available for turn-on even right after its turn-off.

4.2. Field-Test Results

The proposed optimized PFDS is implemented on TU 4. TU 3 and TU 5, which feature the identical technical setup as TU 4 and operate unmodified on equal PFDS, are used as a reference. The three units are put in operation for the provision of PCR. Values for TU 3 and TU 5 are averaged for relative comparisons to TU 4.

Table 5 shows the results of the evaluated period. Energy efficiency is evaluated for 12 full days, 3–14 August 2017. The in-operation time of the power electronics is evaluated for a slightly increased duration of ≈14 days. The evaluation timeframe varies due to the procedure of data collection in the different components. As the operation of the TU, in general, does not change significantly and the timeframe of the 12 days is included in the 14 days, the data can be compared with the note that the timeframes differ slightly.

Table 5. Field-test results for Technical Unit (TU) energy efficiency and in-operation time of Power Electronics (PE) with equal Power Flow Distribution Strategy (PFDS) (TU 3, TU 5) and optimized PFDS (TU 4). Data for energy efficiency are for 3–14 August 2017. Data for PE in-operation time are for the extended testing timeframe of 14 days in August 2017.

Parameter	TU 3	TU 4	TU 5
Power Flow Distribution Strategy	Equal	Optimized	Equal
Measured TU Energy Efficiency	62.81%	71.72%	63.22%
Measured PE In-Operation Time	100.00%	62.52%	100.00%

TU 4 with the optimized PFDS shows an energy efficiency of 71.72%, which is significantly increased from 62.81% in TU 3, respectively 63.22% in TU 3. This increase in the energy efficiency by 8.71 percentage points shows the success in the reduction of losses in the TU. The averaged in-operation time of the PE units in each TU, which is the optimization approach for the optimized PFDS, is reduced from 100% for TU 3 and TU 5 to 62.52% for TU 4.

The analysis of the charge/discharge energy throughput is shown in Figure 9 for TU 3–5 for the period 3–14 August 2017. The overall discharged energy is identical across all units. However, the charged energy shows a reduction from 5.50/5.51 MWh (TU 3/TU 5) to 4.88 MWh, concluding that the increased energy efficiency is a consequence of a reduced energy input. The reduction of the total energy throughput from 8.95/8.98 MWh (TU 3/TU 5) by 6.72% to 8.36 MWh (TU 4) consequently also leads to a reduced charge throughput for the battery pack in TU 4, resulting in fewer battery cycles.

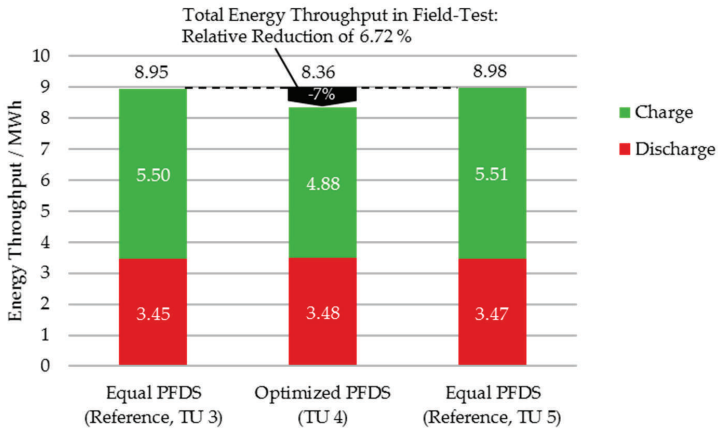

Figure 9. Field-test results for energy throughput (AC-measurement, charge/discharge) of Technical Units (TUs) 3–5 for 3–14 August 2017. TU 3 and TU 5 operate on equal Power Flow Distribution Strategy (PFDS); TU 4 operates on optimized PFDS.

The optimized PFDS also influences the intraday trading. Figure 10 shows the intraday charge/discharge energy as well as their sum for TU 3–5 for the period 3–14 August 2017.

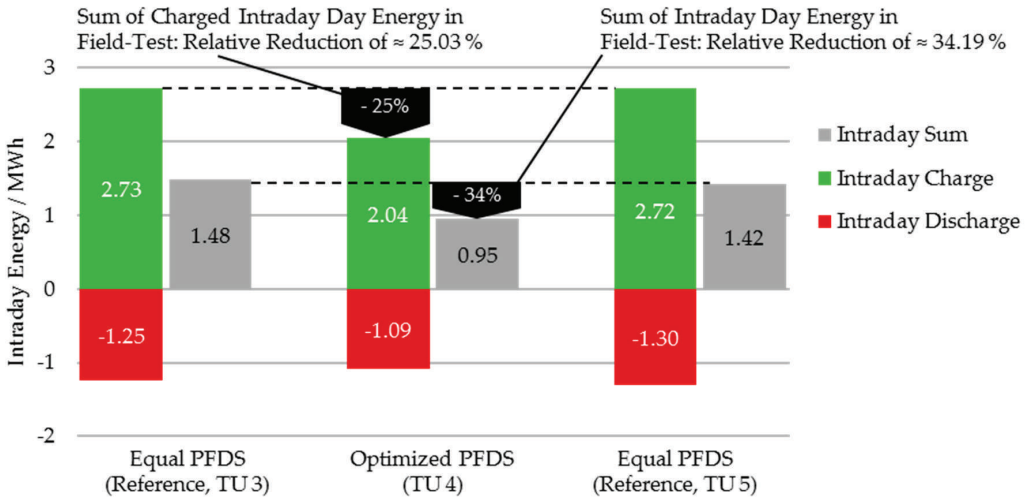

Figure 10. Field-test results for intraday energy charge/discharge/sum of TUs 3–5 for 3–14 August 2017. TU 3 and TU 5 operate on equal Power Flow Distribution Strategy (PFDS); TU 4 operates on optimized PFDS.

The energy charged through intraday trading is reduced in TU 4 from 2.73/2.72 MWh (TU 3/TU 5) by 25.03% to 2.04 MWh (TU 4). The energy discharged through intraday is slightly less reduced from 1.25/1.30 MWh (TU 3/TU 5) by 14.56% to 1.09 MWh. The sum of intraday energy is consequently significantly reduced from 1.48/1.42 MWh by 34.19% to 0.95 MWh. This large reduction for the sum of intraday energy exchange indicates a strong reduction of the energy lost during operation.

To put the improvement of the optimized PFDS into an economic context through a rough estimate: Scaling the reduction of the sum of intraday energy for the single TU to a full year gives the potential for electricity savings in a single TU of approximately 15.21 MWh per year and 304.17 MWh over an assumed operation time of 20 years. As no aging model is available, the battery lifetime cannot be accurately predicted. Scaling the energy throughput of the TU to 20 years of operation results in the relatively high number of approximately 5250 equivalent cycles. It is noted that the lifetime of 20 years, therefore, is not guaranteed and requires further evaluation.

Using an energy price of 29.13 €/MWh (Intraday 15-min call auction base period average price in Germany in 2016 [28]), these savings of bought energy equate to a cost reduction over the full operation time of 8860 €.

The saving can be put into comparison with the investment costs of a battery system. Based on the nominal energy of ≈600 kWh of the TU and literature-based specific system costs of 340 €/kWh (398 $/kWh for Tesla Powerpack 2 in 2016 [29]), the system costs can be approximated to ≈200,000 €. The cost reduction through the optimized PFDS of 8860 € over the assumed operation time of 20 years, therefore, equates to ≈4.43% of the battery system investment cost. If the operation time is less, the improvement is reduced linearly, i.e., for 10 years of operation time accordingly to 2.21%.

Figure 11 continues the technical analysis through an evaluation of the reduction of energy losses through the optimized PFDS.

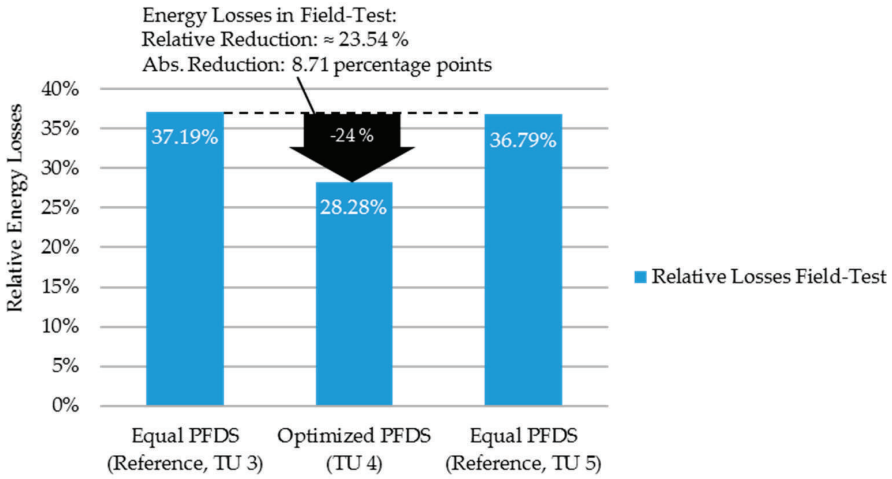

Figure 11. Field-test results for energy losses in TUs 3–5 for 3–14 August 2017. TU 3 and TU 5 operate on equal Power Flow Distribution Strategy (PFDS); TU 4 operates on optimized PFDS.

The relative reduction of the energy losses by 23.54% equates to a reduction of 8.71 percentage points, which can also be expressed as an increased round-trip energy efficiency by 8.71 percentage points.

The temporal distribution of the SOC control modes of the optimized PFDS (see Table 4) in TU 4 is shown in Table 6.

Table 6. Field-test results for the State of Charge control mode in optimized Power Flow Distribution Strategy (Technical Unit 4) from the extended testing timeframe of 14 days in August 2017.

Mode	1	2	3	4	5	6	7	8	9
Temporal Share	68.93%	10.00%	10.79%	3.26%	4.00%	2.99%	0.03%	0.00%	0.00%

The analysis reveals that mostly *Mode 1*, in which both power string SOC levels are in the desired range, is in operation, i.e., 68.93% of the time. *Modes 2–3*, in which one of the power string is at the lower SOC limit, are in total active for 20.78% of the time. In comparison, *Modes 4–5*, in which a power string is at the upper limit, are in total active for only 7.26%. This is expected, as the TU tend to lower SOC values due to the conversion losses. *Modes 6–7*, in which both power strings are in conflict with the same SOC limit, are rarely active, only 3.02% of the time. *Modes 8–9* are not in operation, as their activation is expected only for erroneous operation or start-up of the system.

Finally, the evaluation of the measured SOC in the TU in the field-test, given as the average value between the two power strings in each TU, is shown in Table 7 for TU 3–5. The minimum, time-average and maximum SOC in the evaluated timeframe are given.

Table 7. Field-test results for the State of Charge (SOC) in the Technical Unit (TU) with equal Power Flow Distribution Strategy (PFDS) (TU 3 and TU 5) and optimized PFDS (TU 4) for the extended testing timeframe of 14 days in August 2017.

Parameter	TU 3	TU 4	TU 5
Power Flow Distribution Strategy	Equal	Optimized	Equal
Minimum SOC of TU	40.09%	39.56%	39.73%
Time-Average SOC of TU	49.34%	50.39%	49.52%
Maximum SOC of TU	60.62%	60.99%	60.41%

The values for the min/time-average/max. SOC levels are similar for all TU, operating on either equal PFDS or optimized PFDS. The TU operate in general between 40% and 60% with a time-average SOC of 50%. This confirms the stable operation for both PFDS in accordance with the desired SOC limits.

5. Conclusions

A utility-scale second-life system providing PCR is analyzed and optimized regarding its energy efficiency. First, a detailed system analysis is conducted, revealing the overall system energy efficiency at 56%. The majority of losses occur in the TU, which consist of the PE and the battery: The energy efficiencies of the five TUs providing PCR are between 73% and 77%. Simulation of the system reveals, that the main loss mechanism of the TU as well as of the overall system is identified as the no-load losses of the PE. The no-load losses have significant importance as dynamic losses of the PE and those of the battery are small for the application PCR, which features a low average load. The PE are however in constant operation, leading to the high amount of energy losses.

A temporal distribution analysis of the load profile shows that the PCR load is for 99.95% of the time, and thus almost entirely, under 50% of the nominal power of the TU. As some TU in the system consist of two identical power strings, an optimized PFDS for the power flow of the TU onto the two power strings is proposed. The goal is to reduce the no-load and partial-load losses by providing PCR with a single power string when possible. This consequently reduces the no-load losses of the second power string. The optimized PFDS thus controls the power flow for each power string independently. As this requires a dedicated management of the battery SOC in each power string, a new battery SOC management strategy is also developed.

The optimized PFDS is implemented in a TU of the system and put into operation for PCR. The comparison of the analysis based on measured data shows that the energy efficiency is improved by 9 percentage points, which equates to a reduction of the energy losses by 24%. The reduction also leads to a reduced energy balance for the intraday trading by 34%. The overall energy throughput of the TU is reduced by 7%. The optimized PFDS also successfully manages the battery SOC of the individual batteries.

In summary, the proposed optimized PFDS can improve energy efficiency in battery systems consisting of multiple units. A rough approximation of the economic value of the optimized PFDS in terms of the reduction of intraday energy trading balance shows that the improvement equates to 4.4% of the battery system investment costs.

6. Outlook

For an accurate evaluation of the PFDS, a full year of operation data can be collected.

The optimized PFDS so far only includes optimization through rule-based reduction of the operation time of a second power string. Future optimized PFDS can include dynamic PE losses, as well as battery losses, to optimize system operation for an overall optimal operating point. As the distribution of the power to a single power string leads to higher currents in the battery, a battery-degradation model can be used to predict the impact on the battery lifetime. Combining the energy losses calculation with a battery-degradation model can provide a holistically optimized PFDS.

The here proposed PFDS controls the power flow in a single TU between two identical power strings. The PFDS can be developed to operate for non-identical power strings in a TU, as well as to optimize PFDS between several TUs and between several complete storage systems. Future simulations could reveal the technical potential of such topologies in detail. However, regulations for the fail-safe provision of PCR have to be considered, which may require n-1 redundancy that could contradict a single large aggregated unit.

Acknowledgments: This work was supported by the German Research Foundation (DFG) and the Technical University of Munich (TUM) in the framework of the Open Access Publishing Program. The research project IHEM is funded by the Federal Ministry for Economic Affairs and Energy within the "Funding initiative Electrical

Storages" (grant number 03ET1205G) and managed by Project Management Jülich. The responsibility for the content of this publication lies with the author.

Author Contributions: Michael Schimpe developed the battery system model for energy efficiency evaluations, initiated as well as coordinated the study, and wrote the paper draft. Christian Piesch adapted the system model, parameterized and evaluated the data from simulation and the field test, and developed the optimized distribution strategy. Julian Paß provided model parameters and field-test data, and coordinated the implementation of the new control strategies in the system. Holger C. Hesse, Stefan Ritter and Andreas Jossen provided overall guidance for the study and contributed to many fruitful discussions on the methodology. All authors have read and approved the final manuscript. Julian Paß and Stefan Ritter are employees of the company *The Mobility House*, which operates the analyzed system commercially.

Conflicts of Interest: The authors declare no further conflict of interest.

References

1. Hesse, H.; Schimpe, M.; Kucevic, D.; Jossen, A. Lithium-Ion Battery Storage for the Grid—A Review of Stationary Battery Storage System Design Tailored for Applications in Modern Power Grids. *Energies* **2017**, *10*, 2107. [CrossRef]
2. Aneke, M.; Wang, M. Energy storage technologies and real life applications—A state of the art review. *Appl. Energy* **2016**, *179*, 350–377. [CrossRef]
3. Munsell, M. In Shift to Longer-Duration Applications, US Energy Storage Installations Grow 100% in 2016. Greentech Media [Online], 7 March 2017. Available online: https://www.greentechmedia.com/articles/read/in-shift-to-longer-duration-applications-us-energy-storage-installations-gr (accessed on 2 November 2017).
4. Cho, S.-M.; Yun, S.-Y. Optimal Power Assignment of Energy Storage Systems to Improve the Energy Storage Efficiency for Frequency Regulation. *Energies* **2017**, *10*, 2092. [CrossRef]
5. Brand, M.J.; Hofmann, M.H.; Steinhardt, M.; Schuster, S.F.; Jossen, A. Current distribution within parallel-connected battery cells. *J. Power Sources* **2016**, *334*, 202–212. [CrossRef]
6. Klein, M.P.; Park, J.W. Current Distribution Measurements in Parallel-Connected Lithium-Ion Cylindrical Cells under Non-Uniform Temperature Conditions. *J. Electrochem. Soc.* **2017**, *164*, A1893–A1906. [CrossRef]
7. Schimpe, M.; Naumann, M.; Truong, N.; Hesse, H.C.; Santhanagopalan, S.; Saxon, A.; Jossen, A. Energy efficiency evaluation of a stationary lithium-ion battery container storage system via electro-thermal modeling and detailed component analysis. *Appl. Energy* **2018**, *210*, 211–229. [CrossRef]
8. The Mobility House GmbH. World's Largest 2nd-Use Battery Storage Is Starting Up. Available online: http://www.mobilityhouse.com/en/worlds-largest-2nd-use-battery-storage-is-starting-up/ (accessed on 2 November 2017).
9. Choi, J.; Choi, I.; An, G.; Won, D.J. Advanced Power Sharing Method for Energy Efficiency Improvement of Multiple Battery Energy Storages System. *IEEE Trans. Smart Grid* **2016**, *1*, 1292–1300. [CrossRef]
10. Lee, S.-J.; Choi, J.-Y.; Won, D.-J.; Choi, I.-S.; An, G.-H.; Choi, Y.-J. Frequency control of energy storage system based on hierarchical cluster structure. In Proceedings of the 2015 IEEE Eindhoven PowerTech, Eindhoven, The Netherlands, 29 June–2 July 2015; IEEE: Eindhoven, the Netherlands, 2015; pp. 1–5.
11. Truong, C.N.; Naumann, M.; Karl, R.C.; Müller, M.; Jossen, A.; Hesse, H.C. Economics of Residential Photovoltaic Battery Systems in Germany: The Case of Teslas Powerwall. *Batteries* **2016**, *2*, 14. [CrossRef]
12. Naumann, M.; Karl, R.C.; Truong, C.N.; Jossen, A.; Hesse, H.C. Lithium-ion Battery Cost Analysis in PV-household Application. *Energy Procedia* **2015**, *73*, 37–47. [CrossRef]
13. Neubauer, J.; Pesaran, A. The ability of battery second use strategies to impact plug-in electric vehicle prices and serve utility energy storage applications. *J. Power Sources* **2011**, *196*, 10351–10358. [CrossRef]
14. Neubauer, J.S.; Pesaran, A.; Williams, B.; Ferry, M.; Eyer, J. A Techno-Economic Analysis of PEV Battery Second Use: Repurposed-Battery Selling Price and Commercial and Industrial End-User Value. In *Proceedings of the 2012 SAE World Congress & Exhibition, Detroit, MI, USA, 24–26 April 2012*; SAE International400 Commonwealth Drive: Warrendale, PA, USA, 2012.
15. Neubauer, J.S.; Wood, E.; Pesaran, A. A Second Life for Electric Vehicle Batteries: Answering Questions on Battery Degradation and Value. *SAE Int. J. Mater. Manf.* **2015**, *8*, 544–553. [CrossRef]
16. Heymans, C.; Walker, S.B.; Young, S.B.; Fowler, M. Economic analysis of second use electric vehicle batteries for residential energy storage and load-levelling. *Energy Policy* **2014**, *71*, 22–30. [CrossRef]

17. Gladwin, D.T.; Gould, C.R.; Stone, D.A.; Foster, M.P. Viability of "second-life" use of electric and hybridelectric vehicle battery packs. In Proceedings of the IECON 2013-39th Annual Conference of the IEEE Industrial Electronics Society, Vienna, Austria, 10–13 November 2013; IEEE: Vienna, Austria, 2013; pp. 1922–1927.
18. Viswanathan, V.V.; Kintner-Meyer, M. Second Use of Transportation Batteries: Maximizing the Value of Batteries for Transportation and Grid Services. *IEEE Trans. Veh. Technol.* **2011**, *60*, 2963–2970. [CrossRef]
19. The Mobility House GmbH. Unpublished Company-Internal Measurement Data/Model Parameters. 2017, not available for publishing.
20. European Network of Transmission System Operators for Electricity (ENTSOE). Operation Handbook. Policy 1: Load-Frequency Control and Performance. 2009. Available online: https://www.entsoe.eu/publications/system-operations-reports/operation-handbook/Pages/default.aspx (accessed on 2 November 2017).
21. German Transmission System Operators. REGELLEISTUNG.NET Internet Platform for the Allocation of Control Reserve. Available online: https://www.regelleistung.net/ext/?lang=en (accessed on 1 December 2017).
22. German Transmission System Operators. Key Points and Degrees of Freedom for the Provision of Primary Control Reserve. Guidelines for Providers of Primary Control Reserve. (German Title: Eckpunkte und Freiheitsgrade bei Erbringung von Primärregelleistung. Leitfaden für Anbieter von Primärregelleistung). 2014. Available online: https://www.regelleistung.net/ext/download/eckpunktePRL (accessed on 1 December 2017).
23. Gatta, F.; Geri, A.; Lamedica, R.; Lauria, S.; Maccioni, M.; Palone, F.; Rebolini, M.; Ruvio, A. Application of a LiFePO4 Battery Energy Storage System to Primary Frequency Control: Simulations and Experimental Results. *Energies* **2016**, *9*, 887. [CrossRef]
24. Zeh, A.; Müller, M.; Naumann, M.; Hesse, H.; Jossen, A.; Witzmann, R. Fundamentals of Using Battery Energy Storage Systems to Provide Primary Control Reserves in Germany. *Batteries* **2016**, *2*, 29. [CrossRef]
25. Thien, T.; Schweer, D.; Vom Stein, D.; Moser, A.; Sauer, D.U. Real-world operating strategy and sensitivity analysis of frequency containment reserve provision with battery energy storage systems in the german market. *J. Energy Storage* **2017**, *13*, 143–163. [CrossRef]
26. Swissgrid Ltd. Grid-Transmission System-Grid Levels: Various Grid Levels Transport Electricity. Available online: https://www.swissgrid.ch/swissgrid/en/home/grid/transmission_system/grid_levels.html (accessed on 1 December 2017).
27. Jossen, A. Fundamentals of battery dynamics. *J. Power Sources* **2006**, *154*, 530–538. [CrossRef]
28. European Power Exchange. EPEX SPOT INTRADAY MARKETS REACH ALL-TIME HIGH IN 2016. Available online: https://www.epexspot.com/de/presse/press-archive/details/press/EPEX_SPOT_Intraday_markets_reach_all-time_high_in_2016 (accessed on 2 November 2017).
29. Lambert, F. Tesla Slashes Price of the Powerpack System by Another 10% with New Generation. Available online: https://electrek.co/2016/11/14/tesla-powerpack-2-price/ (accessed on 2 November 2017).

© 2018 by the authors. Licensee MDPI, Basel, Switzerland. This article is an open access article distributed under the terms and conditions of the Creative Commons Attribution (CC BY) license (http://creativecommons.org/licenses/by/4.0/).

6 Comprehensive modeling of temperature-dependent degradation mechanisms in lithium iron phosphate batteries

This section introduces the paper *Comprehensive Modeling of Temperature-Dependent Degradation Mechanisms in Lithium Iron Phosphate Batteries* and is based on the paper without further reference.

In Section 2.3.6 the methods for aging experiments and the development of semi-empirical battery degradation models were introduced. In Chapter 3 a thermal model for BESS covering the cell, module, rack, and the system level was presented. Temperature level significantly influences the degradation behavior of battery cells and therefore requires detailed modeling.

In this paper, a comprehensive semi-empirical model approach for the capacity loss of lithium-ion batteries is presented. Emphasis is put on the temperature-dependence of the cycle-aging mechanisms. The approach is based on a reduced set of internal cell parameters and physically supported degradation functions. For parameterization, a lifetime test study with LFP-C cells is conducted, including storage and cycle tests.

SOC dependence of the calendar aging is implemented through coupling the anode open circuit potential in a Tafel equation based approach. Temperature dependence of calendar aging is calculated with the Arrhenius equation.
For the cycle aging, the emphasis is placed on the varying degradation at different temperatures. Three cycle aging correlations are identified and correlated to two physical cell internal degradation effects: Lithium loss due to transport limitations, possibly lithium plating, during charging at low temperature and increased SEI layer growth due to cycling at high temperature. Degradation is separated under different conditions: High temperature, low temperature, and low temperature at a high SOC. Current rate dependence and SOC dependence is implemented where observed. Cycle aging is correlated with the charge throughput. No direct correlation with the cycle depth is implemented, but cycle operation at high SOC leads to an increased capacity loss in the cycle model.
For model validation, a comparison of the simulation results to the experimental aging data is conducted. The model application in a stationary storage real-world scenario based on the application in a residential PV-BESS is tested via additional profiles, which have not been used for model parameterization and feature varying cycle depth. Tests are continued for up to 114 days beyond the longest parametrization tests to a total duration of 348 days.

Both the parameterization tests, as well as dynamic current tests exclusively used for validation, are in good agreement with the model results. At the end of the dynamic current profile validation tests between 10 °C and 45 °C, after 348 days, the model error is below 1 % of the original cell capacity and the maximum relative error for the capacity loss is below 21 %. The optimum temperature for a minimum of capacity loss is also shown to be accurately predicted.

Author contribution The experimental setups, methods, and procedures as well as the hypothesis for the degradation model were developed by the author this thesis. The paper draft was written also by the author this thesis. The experiments, data analysis, and model development were conducted in collaboration with Markus Kuepach through his master's thesis. Kandler Smith from the National Renewable Energy Laboratory (Colorado, USA), which the author of this thesis visited through a research exchange, supported the research through discussions and reviewing of the paper.
The results have also been presented at the conference *232nd ECS Meeting* by the author of this thesis.

Comprehensive Modeling of Temperature-Dependent Degradation Mechanisms in Lithium Iron Phosphate Batteries

Michael Schimpe, Markus Edler von Kuepach, Maik Naumann, Holger C. Hesse, Kandler Smith, Andreas Jossen

Journal of The Electrochemical Society 165 (2) A181–A193, 2018

Permanent weblink:
https://doi.org/10.1149/2.1181714jes

Reproduced under the terms of the Creative Commons Attribution 4.0 License (CC BY, http://creativecommons.org/licenses/by/4.0/), which permits unrestricted reuse of the work in any medium, provided the original work is properly cited.

Comprehensive Modeling of Temperature-Dependent Degradation Mechanisms in Lithium Iron Phosphate Batteries

M. Schimpe,[1,*,z] M. E. von Kuepach,[1] M. Naumann,[1] H. C. Hesse,[1] K. Smith,[2,] and A. Jossen[1]**

[1]*Technical University of Munich (TUM), Institute for Electrical Energy Storage Technology (EES), 80333 Munich, Germany*
[2]*National Renewable Energy Laboratory, Transportation and Hydrogen Systems Center, Golden, Colorado 80401, USA*

For reliable lifetime predictions of lithium-ion batteries, models for cell degradation are required. A comprehensive semi-empirical model based on a reduced set of internal cell parameters and physically justified degradation functions for the capacity loss is developed and presented for a commercial lithium iron phosphate/graphite cell. One calendar and several cycle aging effects are modeled separately. Emphasis is placed on the varying degradation at different temperatures. Degradation mechanisms for cycle aging at high and low temperatures as well as the increased cycling degradation at high state of charge are calculated separately. For parameterization, a lifetime test study is conducted including storage and cycle tests. Additionally, the model is validated through a dynamic current profile based on real-world application in a stationary energy storage system revealing the accuracy. Tests for validation are continued for up to 114 days after the longest parametrization tests. The model error for the cell capacity loss in the application-based tests is at the end of testing below 1% of the original cell capacity and the maximum relative model error is below 21%.
© The Author(s) 2018. Published by ECS. This is an open access article distributed under the terms of the Creative Commons Attribution 4.0 License (CC BY, http://creativecommons.org/licenses/by/4.0/), which permits unrestricted reuse of the work in any medium, provided the original work is properly cited. [DOI: 10.1149/2.1181714jes]

Manuscript submitted October 11, 2017; revised manuscript received November 7, 2017. Published January 12, 2018. This was Paper 179 presented at the National Harbor, Maryland Meeting of the Society, October 1–5, 2017.

Today, stationary energy storage systems utilizing lithium-ion batteries account for the majority of new storage capacity installed.[1] In order to meet technical and economic requirements, the specified system lifetime has to be ensured.

For reliable lifetime predictions, cell degradation models are necessary. Physicochemical models that include aging mechanisms are based on a detailed set of parameters which are often not readily available, computationally costly and require experimental parameterization of degradation rates.[2–4] Instead, purely empirical models can be parameterized without knowledge of internal cell setup through extensive testing. Several purely empirical studies capture calendar aging[5,6] or cycle aging[7,8] without evaluating interdependencies. Through superposition, some empirical model approaches combine calendar and cycle aging[9–12] but tend to neglect the temperature dependence of the cycle aging mechanisms and are prone to extrapolation errors due to the utilized mathematical functions.

Due to the limited knowledge about degradation mechanisms, empirically based models conventionally lump multiple degradation effects into single functions. This leads to the aforementioned prediction errors when deviating from the parameterization test conditions. E.g. for cycle aging, Waldmann et al. reported a transition of dominating aging mechanisms at 25°C.[13] The aging for temperatures above 25°C was attributed to the solid-electrolyte interface (SEI) growth and cathode degradation, while below 25°C the aging was attributed to lithium plating. In fact, for an improved understanding of cell internal degradation, model development should aim for a separation of the degradation mechanisms wherever possible. The respective mechanisms can then be modeled through functions that are suitable for the degradation driving factors.

In this work, a comprehensive semi-empirical capacity loss model for lithium-ion cells is introduced. A novelty of the approach is that a reduced set of internal cell data, i.e. electrode half-cell potential curves, is integrated into the model development. Further, various capacity loss mechanisms for calendar and cycle aging are captured separately in an empirical, yet physically supported approach.

For parameterization through experimental data, a lifetime test study is conducted. Cell type and experimental parameters are in accordance with an application in stationary systems. Stationary systems require a long lifetime in terms of cycles (e.g. thousands of cycles) and years of operation (e.g. 10–20 years) for economic viability.[14–16]

Lithium iron phosphate ($LiFePO_4$) cell have shown capacity retention for more than 5,000 full cycles before usable capacities fall below 80%, a benchmark number rendering them suitable for stationary applications.[17]

Consequently, the study and parameterization are based on a commercial $LiFePO_4$ cell. The lifetime study is separated into parameterization and validation tests. Validation tests, derived from the application in a residential photovoltaic-battery system, are conducted subsequent to and distinguished from model parameterization and thus show the model performance in application-oriented conditions.

This paper is organized as follows. First, an overview of the experimental setup is given. The experimental results are then presented followed by the respective aging model. The calendar aging is discussed first, followed by the cycle aging. After summarizing the proposed model, the results are presented alongside with experimental data of parameterization test points and compared to points for model validation.

Experimental

For parameterization and evaluation of the proposed model, a lifetime test study is conducted. The experimental tests and procedures are briefly described.

The parameterization is based on a commercial 26650-format lithium iron phosphate cell (Sony US26650FTC1) designed for stationary applications.[18] Datasheet parameters with notes for the respected voltage and current limits for this study are given in Table I.

The lifetime study is separated into parameterization and validation cycle tests. Validation tests are however excluded from model parameterization, to show the model performance in a dynamic real-world application scenario. Table II gives an overview of the experimental tests at various conditions. Storage tests capture parameterization and validation of calendar aging. The cycle tests conditions at various temperatures and different parameters for the current evaluate the cycle aging. The superscript numbers indicate the number of cells per test point, for statistical evaluation. The majority of test points only features a single cell, as a low variation ($< 1\%$ of original cell capacity for the capacity loss) for different cells at identical test points was observed in previous studies and is again confirmed in the results of this study. Therefore, the variable current profile tests featuring

*Electrochemical Society Student Member.
**Electrochemical Society Member.
[z]E-mail: michael.schimpe@tum.de

Downloaded on 2018-01-13 to IP 185.17.207.4 address. Redistribution subject to ECS terms of use (see ecsdl.org/site/terms_use) unless CC License in place (see abstract).

Table I. Cell Sony US26650FTC1 datasheet parameters.[18]

Parameter	Value	Notes
Nominal Voltage	3.2 V	
Nominal Capacity	3000 mAh	Rated Capacity is 2850 mAh. Capacity 3000 mAh is denoted as nominal in this study, as all tested cells have this capacity at begin-of-life.
Charge Voltage	3.60 V ± 0.05 V	3.60 V is used in this study.
Discharge Voltage	2.00 V	
Continuous Max. Charge Current	2.85 A	Continuous max. charge current of 1C – 3.00 A is used in the study, based on the begin-of-life capacity of 3000 mAh.
Continuous Max. Discharge Current	20 A	
Temperature Range Charge	0 to +45°C	Max. surface temperature is +60°C.
Temperature Range Discharge	−20 to +60°C	Max. surface temperature +80°C

three cells for a single temperature were reduced after approximately 180 days of testing to two cells for the respective temperature. Test durations vary in the study – the longest test duration for parametrization is 234 days. Tests for validation are continued for up to 114 days beyond the longest parametrization tests to a total duration of 348 days.

Temperatures in the tests are 0°C, 10°C, 15°C, 25°C, 35°C, 45°C and 55°C, to probe for varying degradation mechanisms. The storage tests are conducted at varying State of Charge (SOC) in steps of 12.5% from 0% to 100%. The SOC is set through charging the cell with an amount of charge calculated with respective SOC and the current cell capacity, starting from a SOC of 0%. Storage tests are performed at all temperatures except 0°C, where the calendar aging is expected to be negligible.

Cycle aging parameterization is based on constant current (CC) full cycle tests at C-rates of 0.25C, 0.5C, and 1C, with and without Constant Voltage (CV)-phases at the end of charging. The chosen current rates cover the current range of the validation current profile, which is discussed below.

The cut-off current rate for the CC-CV tests is C/10. Constant Current C-rates are identical for both charge and discharge. Both CC and CC-CV tests operate over the full manufacturer-specified voltage range of 2.0 V to 3.6 V.

For the model validation in application-oriented settings, a dynamic profile for application in a residential photovoltaic-battery system in Germany is tested. Test points are indicated in column *Val* of Table II. The profile data was provided by the Fraunhofer Institute for Solar Energy Systems from Project *ESPEN - Potentials of electrochemical storages in power grids in competition to further technologies and system solutions*[19] and scaled to the nominal cell capacity. Figure 1 shows the resulting current profile.

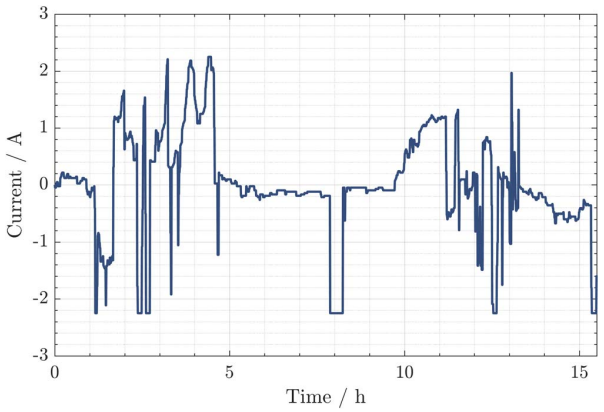

Figure 1. Current profile for validation tests representing a PV-residential application usage of the cell. Current direction for charging is positive. Profile data is based on[19] and repetitively applied to the batteries tested with test condition *Val*.

Table III. Parameters of validation PV-residential current profile *Val*. Data from Ref. 19.

Parameter	Value	Parameter	Value
Profile Duration	15.5 h	Time Resolution	60 s
Charge Throughput per Cycle relative to Nominal Cell Capacity (Charge)	1.56	Charge Throughput per Cycle relative to Nominal Cell Capacity (Discharge)	1.56
Time-averaged C-Rate (Charge)	+ 0.24C	Time-averaged C-Rate (Discharge)	−0.17C
Max. C-Rate (Charge)	+0.75C	Max. C-Rate (Discharge)	−0.75C
Start SOC of Profile	28%	Average SOC	51.4%
Min. SOC	5.4%	Max. SOC	80%

The profile is representative of a summer and a winter day. Rest durations are excluded for acceleration of the test results, leading to a profile duration of 15.5 h. As the profile defines the battery current and features a coulombic efficiency of 100%, the profile can be repeated permanently. The current profile features several current inversions, leading to varying cycle depths. It, therefore, supports the model validation in terms of the influence of the cycle depth on the capacity loss. Table III gives further parameters of the profile. All parameters relative to the cell capacity (Charge throughput, average/max. C-Rate, SOC values) are calculated with the nominal capacity of the cells (3 Ah).

Table II. Experimental test points of the lifetime study. Superscripts indicate the number of cells per test point. Column *Val* indicates validation test points based on dynamic-current application profiles.

	Storage									Cycle						
	SOC									CCC-Rate			CC-CVC-Rate			
T/°C	0	12.5	25	37.5	50	62.5	75	87.5	100	0.25	0.5	1	0.25	0.5	1	Val
0										X^1	X^1	X^2	X^1	X^1	X^1	
10	X^1	X^1	X^1	X^1	X^1	X^1	X^1	X^1	X^1	X^1	X^1	X^3	X^1	X^1	X^1	X^3
15	X^1	X^1	X^1	X^1	X^1	X^1	X^1	X^1	X^1			X^3			X^1	X^3
25	X^1	X^1	X^1	X^1	X^1	X^1	X^1	X^1	X^1	X^1	X^1	X^3	X^1	X^1	X^1	X^3
35	X^1	X^1	X^1	X^1	X^1	X^1	X^1	X^1	X^1			X^3			X^1	X^3
45	X^1	X^1	X^1	X^1	X^1	X^1	X^1	X^1	X^1			X^3			X^1	X^3
55	X^1	X^1	X^1	X^1	X^1	X^1	X^1	X^1	X^1	X^1	X^1	X^1	X^1	X^1	X^1	X^1

Downloaded on 2018-01-13 to IP 185.17.207.4 address. Redistribution subject to ECS terms of use (see ecsdl.org/site/terms_use) unless CC License in place (see abstract).

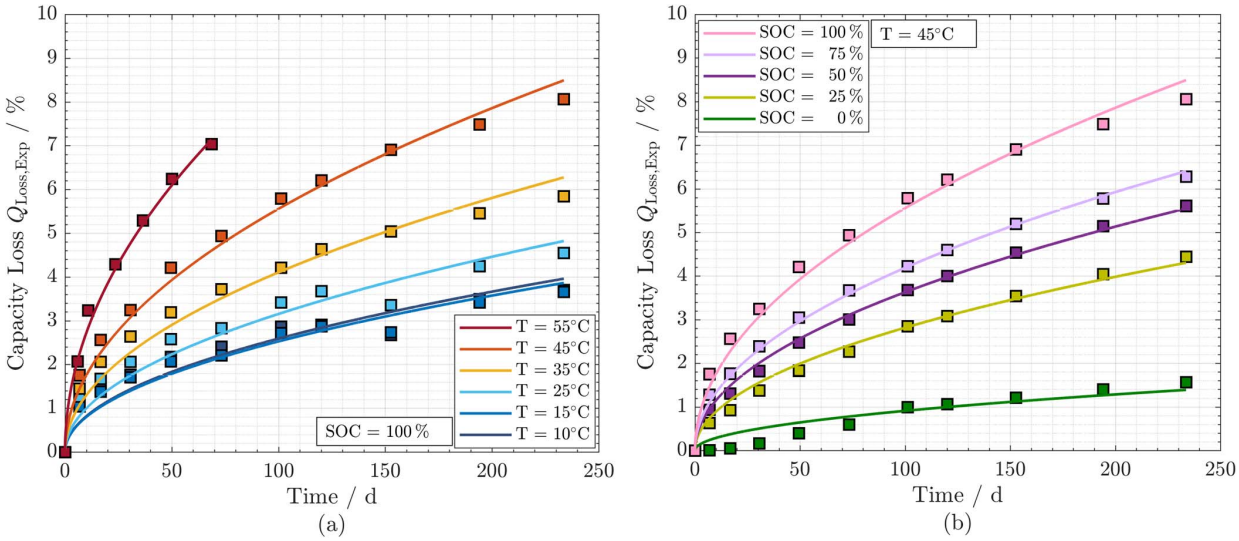

Figure 2. Capacity loss evaluation during storage: a) Influence of storage temperature at $SOC = 100\%$, b) Influence of State of Charge at $T = 45°C$. Trend lines are fitted for each test condition for visualization.

Regular Reference Performance Tests (RPT) are performed at 25°C to allow for comparison between different test conditions. The first RPT is performed after one week of testing. The RPT frequency is increased with increased duration of the testing for cells, which did show only small changes between RPTs, to up to 6 weeks. As the cells show a high cycle stability at 25°C, with less than 9% of capacity loss after 2800 full cycles at 1C, the RPTs are expected to not significantly affect the results.

To accurately determine cell capacity regardless of impedance increases, two full charge-discharge CC-CV cycles are conducted for measuring the cell capacity (CC rate 1C, current cut-off rate C/50), after an initial CC-CV discharge. For cell impedance, $R_{DC,10\ s}$ pulses and electrochemical impedance spectroscopy (EIS) tests are conducted, both at $SOC = 50\%$, after a relaxation time of 1 h and 12 h respectively.

In literature, typical limits for cell end of life (EOL) are a remaining capacity of 80% to the nominal value, corresponding to 20% of capacity loss,[9,20] or an increase in cell impedance of +50% to +100%.[9,21] Under such limits for EOL, the experiments reveal capacity loss to be the primary EOL criterion for all cells under test. E.g.: the test point CC cycling at ambient temperature of 45°C with 1C showed a capacity loss of 12% but only a moderate increase in the resistance $R_{DC,10\ s}$ of 4% after 2800 full equivalent cycles. Similarly, cells reaching 80% of remaining capacity also did not reach the EOL limit for impedance. Therefore, the capacity loss is the focus of this work.

For better visualization, the capacity loss in this work is not given through the value for the actual capacity (Unit: Ah), but normalized to the original cell capacity in the first RPT before the tests, $Q_{Disch,0}$. The capacity loss of the cell, $Q_{Loss,Exp,i}$ in the RPT numbered i is then calculated by averaging over two subsequent cycles in the RPT: $Q_{Disch,i,1}$ and $Q_{Disch,i,2}$. As a reference, the first RPT of the cell before the tests, $Q_{Disch,0}$ is used.

$$Q_{Loss,Exp,i} = Q_{Disch,0} - \left(Q_{Disch,i,1} + Q_{Disch,i,2}\right)/2 \quad [1]$$

Tests are stopped when cell capacity drops below 80% of original capacity in the RPT.[20,21] As the experimental results did not show a sudden increase in the rate of degradation, which is often described as non-linear aging that tends to appear below a cell capacity of 80%,[20] the proposed model does not include such changes in the degradation behavior and is not able to predict them either. The following model development, parameterization, and validation are thus limited to a cell capacity above 80% and do not include any mechanism for an increase in the rate of degradation.

Calendar Aging

The results of the storage experiments and their impact on the model are briefly discussed, followed by the definition of the calendar aging model.

Results of storage experiments.—Example results of the capacity loss during the storage experiments are shown in Figure 2. Data points represent the measurements taken in the RPT. A trend line is fitted according to Equation 2 and shown for each test condition for visualization purposes.

Figure 2a shows the influence of temperature through a comparison of test points for temperatures ranging from 10°C to 55°C, with a constant $SOC = 100\%$. Higher temperature leads to a higher rate of capacity loss. The rate of capacity loss also decreases with time. Tests at $T = 55°C$ were started later and the experiment is still in progress. Figure 2b shows the influence of the SOC during storage through a comparison of test points for SOC from 0% to 100%, with constant temperature $T = 45°C$. Higher SOC is also accompanied by a higher rate of capacity loss.

The three described trends, decreasing rate of capacity loss over time (I), the influence of temperature (II) and SOC (III) are in good accordance with literature and have been previously described in more detail.[5,6,21] The mentioned trends all show a strong influence on the rate of capacity loss and are thus included in the calendar aging model.

Calendar aging model.—Calendar aging is described with the loss of cyclable lithium to the growth of the SEI at the anode over the life of the battery, which can trap lithium permanently.[4,22–24] With increasing thickness and thus capacity loss, the growth decreases due to self-inhibited slow-down of the reaction. This decrease over time can be described with square-root dependence on time t, as used in existing models.[25,26] The temperature and SOC dependence of the calendar aging mechanism is defined through the stress factor k_{Cal}, which gives:

$$Q_{L,Cal}(t) = k_{Cal}(T, SOC) \cdot \sqrt{t} \quad [2]$$

This equation for the calendar aging capacity loss is fitted to experimental data for a test with constant temperature and SOC,

Downloaded on 2018-01-13 to IP 185.17.207.4 address. Redistribution subject to ECS terms of use (see ecsdl.org/site/terms_use) unless CC License in place (see abstract).

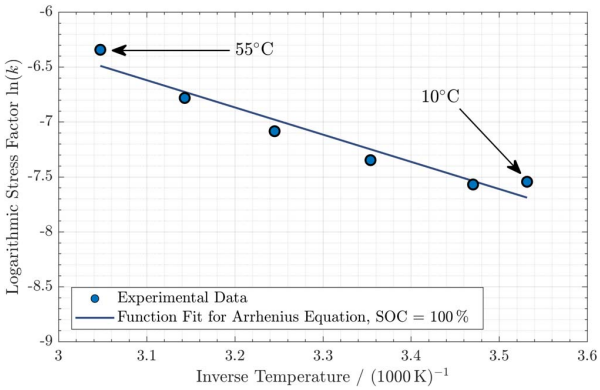

Figure 3. Arrhenius equation fit for temperature dependence of calendar stress factor. Data fitted for $SOC = 100\%$.

resulting in a condition-specific degradation stress factor. The trend lines in Figure 2 are fitted using this equation.

Assuming no correlation between the dependencies of capacity loss on temperature and SOC as commonly used,[6,9,11,25] the stress factor is calculated with:

$$k_{\text{Cal}}(T, SOC) = k_{\text{Cal,Ref}} \cdot f(T) \cdot f(SOC) \quad [3]$$

The calendar reference stress factor $k_{\text{Cal,Ref}}$ is defined and fitted for reference conditions at $T = 25°\text{C} = 298.15$ K and $SOC = 50\%$ to a value of $k_{\text{Cal,Ref}} = k_{\text{Cal}}(T = 298.15\text{ K},\ SOC = 50\%) = 3.694 \cdot 10^{-4}\ \text{h}^{-0.5}$.

Temperature dependence.—The temperature dependence of the calendar aging is modeled through the Arrhenius equation, as proposed by various authors:[5,9,11,26]

$$k_{\text{Cal}}(T, SOC = 50\%) = k_{\text{Cal,Ref}} \cdot \exp\left[\frac{-E_{\text{a,Cal}}}{R_g}\left(\frac{1}{T} - \frac{1}{T_{\text{Ref}}}\right)\right] \quad [4]$$

The parameter activation energy $E_{\text{a,Cal}}$, is determined by fitting the equation to the stress factors at $SOC = 100\%$, resulting in a value of 20592 J/mol. Constant parameters for the equation are the universal gas constant $R_g = 8.314$ J/(mol K) and $T_{\text{Ref}} = 298.15$ K. Figure 3 shows the comparison of model and experimental data, which indicates reasonable agreement for the fitting approach.

State of charge dependence.—The SOC dependence of the calendar aging mechanism is often fitted through polynomial[6] or exponential functions[5] using the SOC as an input variable. Other approaches include a function fit with the full-cell open circuit voltage as an input variable.[9,21] Although fitting such model equations can provide good correlations, the models do not consider underlying physical mechanisms. Evaluating the stress factors over the state of charge, as shown in Figure 4a, leads to plateau regions for SOCs between 37.5% and 62.5%, as well as between 87.5% and 100%. No clear polynomial nor exponential trend can be identified, motivating a more sophisticated model formulation. Keil et al. attributed the plateau effects to the graphite electrode (anode) with a link to anode potentials.[27]

As the growth of SEI on the anode is driven by a potential difference, a model, which is based on a reformulated Tafel equation, is proposed.

The Tafel equation is:

$$\Delta U = \frac{R_g \cdot T}{\alpha \cdot z \cdot F} \ln \frac{i}{i_0} \quad [5]$$

Rearranging, setting $z = 1$ for lithium-ions, and introducing reference values for current density i and temperature T gives:

$$i = i_{\text{Ref}} \cdot \exp\left[\frac{\alpha \cdot F \cdot \Delta U}{R_g \cdot T_{\text{Ref}}}\right] \quad [6]$$

The voltage difference ΔU is calculated from the anode open circuit potential U_{a}, which is SOC dependent, and a reference potential $U_{\text{a,Ref}}$:

$$i = i_{\text{Ref}} \cdot \left(\exp\left[\frac{\alpha \cdot F}{R_g}\left(\frac{U_{\text{a,Ref}} - U_{\text{a}}(SOC)}{T_{\text{Ref}}}\right)\right]\right) \quad [7]$$

The current density is converted to the stress factor approach with an additional constant offset k_0:

$$k_{\text{Cal}}(T = 25\ °\text{C},\ SOC) = k_{\text{Cal,Ref}} \cdot \left(\exp\left[\frac{\alpha \cdot \text{F}}{R_g}\left(\frac{U_{\text{a,Ref}} - U_{\text{a}}(SOC)}{T_{\text{Ref}}}\right)\right] + k_0\right) \quad [8]$$

This constant offset is required for proper fitting results and demands further investigations, as it is not included in the original Tafel equation.

Values for U_{a} are taken from Safari et al.[28] Reformulation of the anode stoichiometry dependent data from Safari et al. to a function of the full-cell SOC is presented in the Appendix. Reference potential $U_{\text{a,Ref}}$ is set to $U_{\text{a}}(SOC = 50\%) = 0.123$ V. Fitting the equation parameters at $T_{\text{Ref}} = 298.15$ K gives $\alpha = 0.384$, $k_0 = 0.142$. The

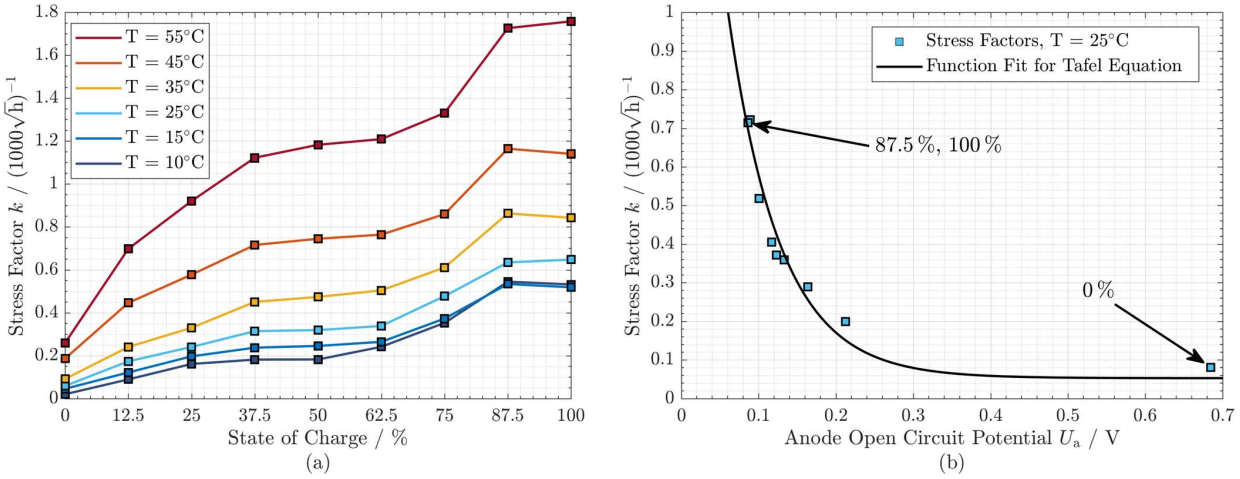

Figure 4. Modeling of State of Charge/anode open circuit potential dependence of calendar stress factor: a) Influence of SOC on stress factors, b) Tafel equation function fit for anode open circuit potential dependence of calendar stress factor. Data fitted for $T = 25°\text{C}$.

Downloaded on 2018-01-13 to IP 185.17.207.4 address. Redistribution subject to ECS terms of use (see ecsdl.org/site/terms_use) unless CC License in place (see abstract).

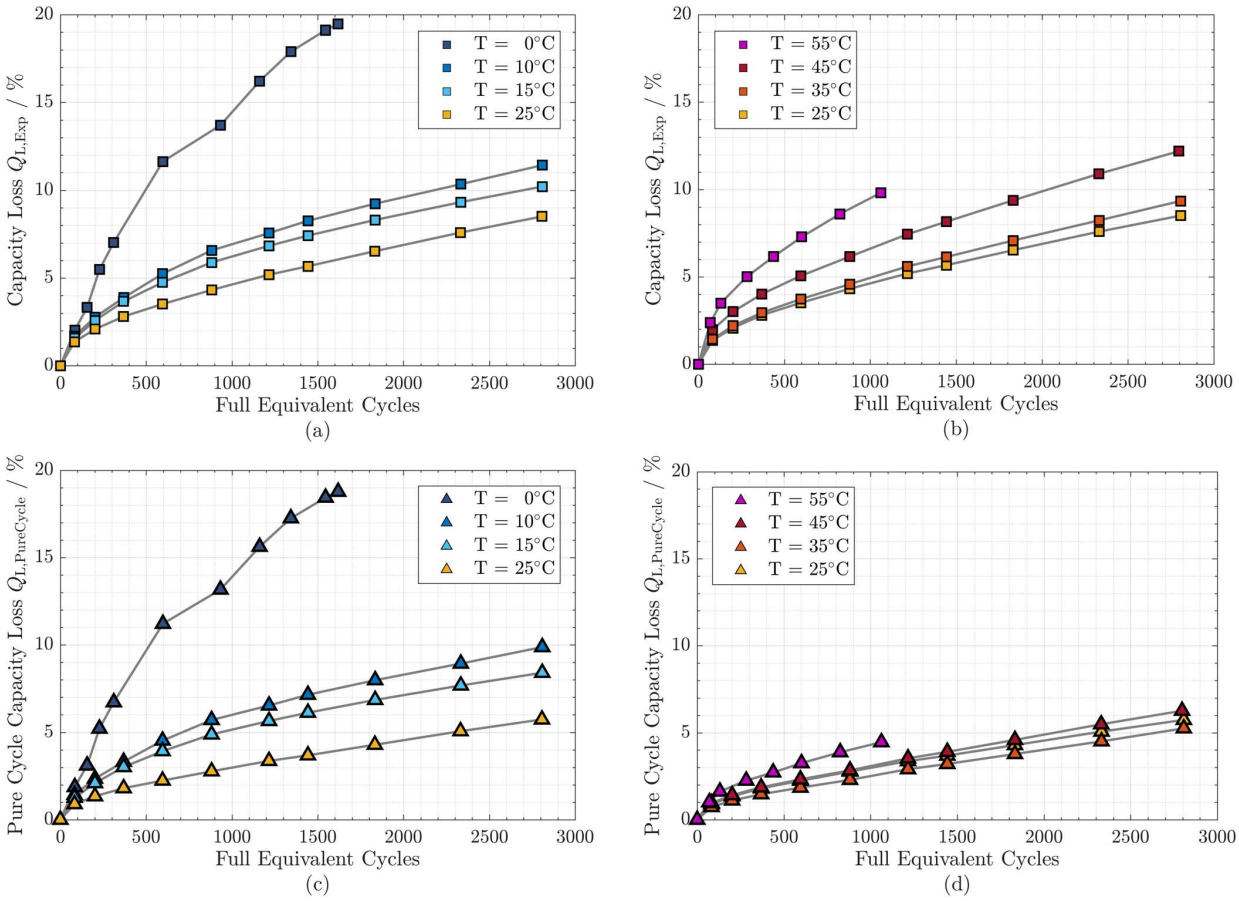

Figure 5. Temperature effect of capacity loss evaluation during CC cycle tests at 1C: a) Experimental capacity loss measurements at low temperatures (0°C to 25°C), b) Experimental capacity loss measurements at high temperatures (25°C to 55°C), c) Pure cycle capacity loss at low temperatures (0°C to 25°C), d) Pure cycle capacity loss at high temperatures (25°C to 55°C).

Faraday constant is given with $F = 96485$ C/mol. Stress factors and the Tafel equation fit are shown over the anode open circuit potential in Figure 4b for $T = 25°C$. The coupling of the stress factor with the anode potential shows good agreement and reflects with high precision similar values for the stress factors at high SOC values, i.e. at the SOC of 87.5% and 100%.

In summary, the stress factor due to calendar aging effects, as a function of temperature and storage SOC is obtained as follows:

$$k_{\text{Cal}}(T, SOC) = k_{\text{Cal,Ref}} \cdot \exp\left[\frac{-E_{\text{a,Cal}}}{R_g}\left(\frac{1}{T} - \frac{1}{T_{\text{Ref}}}\right)\right] \cdot \left(\exp\left[\frac{\alpha \cdot \text{F}}{R_g}\left(\frac{U_{\text{a,Ref}} - U_{\text{a}}(SOC)}{T_{\text{Ref}}}\right)\right] + k_0\right) \quad [9]$$

Cycle Aging

The results of the cycling experiments and their implications for the model, separated for their dependence on the temperature, the current rate as well as on the state of charge, are briefly discussed - followed by the cycle model definition.

Results of cycling experiments.—The measured capacity loss in the cycling experiments also reflects a capacity loss due to calendar aging, which occurs simultaneously.

Assuming that the calendar aging contributions to the cell aging follow the same mechanism for cells tested both under storage and cycling conditions, capacity loss from cycle-induced aging can be calculated as a superposition term to the calendar aging model outlined in the previous section.

After subtracting the model-based calendar aging, calculated with the average temperature measured in the experimental cycle tests – which is higher than ambient temperature due to the heat produced by the cells - and at an average $SOC = 50\%$, from the measured capacity loss, the *Pure Cycle* capacity loss is obtained:

$$Q_{\text{L,Pure Cycle}} = Q_{\text{L,Exp}} - Q_{\text{L,Cal}}\left(T = \overline{T_{Exp}}, SOC = 50\%, t = t_{\text{Exp}}\right) \quad [10]$$

This calculation neglects that the calendar aging is correlated non-linear with temperature and SOC, as well as that the time-averaged SOC is not exactly 50%. Calculations including the influence of the varying SOC and temperature in the cycle tests, however, show negligible influence on the model results and increase the efforts for parametrization significantly. Thus, the simplification based on the given average conditions is consequently used.

Temperature dependence.—Figure 5 shows the results for the CC cycle tests at 1C for various ambient temperatures over full equivalent cycles (FEC) of cycling (1 FEC = 6 Ah throughput). Top figures show the experimental capacity loss, bottom figures the calculated pure cycle capacity loss. Low temperatures (25°C and lower) are shown on the left side, high temperatures (25°C and higher) on the right side.

The experimental capacity loss is lowest for $T = 25°C$. Lower as well as higher temperatures lead to a rise of the capacity loss. The

Downloaded on 2018-01-13 to IP 185.17.207.4 address. Redistribution subject to ECS terms of use (see ecsdl.org/site/terms_use) unless CC License in place (see abstract).

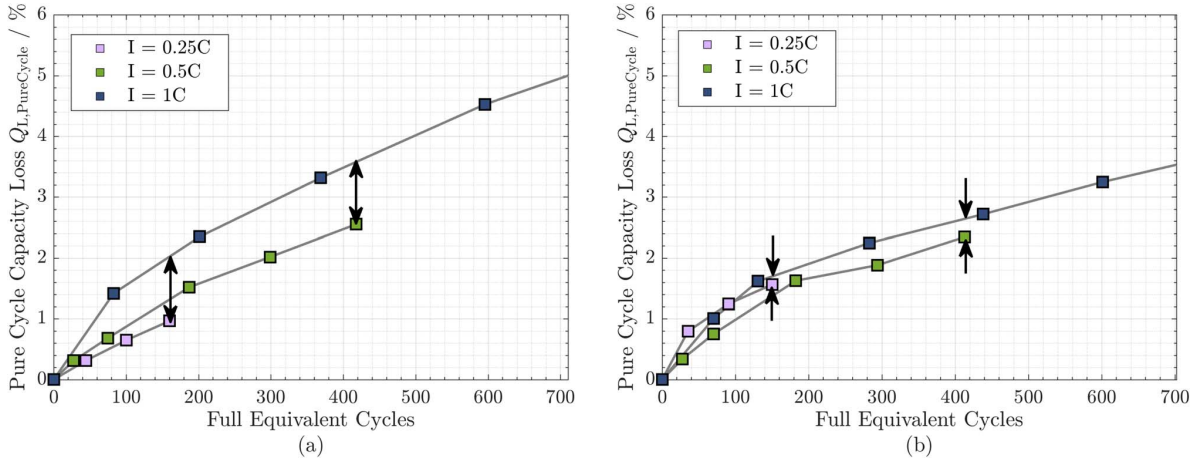

Figure 6. Current rate dependence of temperature effects: a) $T = 10°C$, b) $T = 55°C$. Arrows are added for visualization of strong/weak variation at low/high temperatures.

comparison between the experimental capacity loss and the pure cycle losses shows that the calendar aging factor that was subtracted has an increasing impact with increasing temperature. The pure cycle capacity loss has the minimum at $T = 35°C$ and increases strongly at lower temperatures and slightly with higher temperatures. The data underlines the dominance of storage effects at high temperatures and that of pure cycling effects at lower temperatures. A strong temperature dependence of the pure cycle capacity loss is also identified.

The capacity loss at low-temperature cycling is often described in the literature as dominated by transport limitations, possibly lithium plating.[29] Although we here and later in the text refer to transport limitations and lithium plating as possible mechanisms, no degradation analysis was conducted which could confirm or rebut this theory.

Cycling generally also mechanically disturbs the SEI, leading to fresh electrode surface area where new SEI can be formed.[25] This cycling-induced SEI growth increases with higher temperature – which may explain the increasing pure cycle capacity loss with higher temperatures. Both mechanisms, as well as the SEI growth during storage, reduce the capacity through the consumption of cyclable lithium. Assuming that these mechanisms both reduce the cyclable lithium in the battery cell are the dominating mechanisms under the respective operating conditions, the capacity loss can be modeled as a superposition of these factors. Further aging mechanisms, e.g., electrode material degradation, cannot be excluded but are difficult to deduce from full-cell test results.

Current rate dependence.—Figure 6 shows the pure cycle capacity loss for the CC cycle tests at current rates of 0.25C, 0.5C, and 1C for a low-temperature $T = 10°C$ (a) and a high temperature $T = 55°C$ (b). At the low temperature, the pure cycle capacity loss increases with the current rate, whereas at the high temperature the pure cycle capacity loss is similar for all current rates tested. This indicates a strong correlation with current rate for the cycle aging mechanism at low temperatures only and none with mechanisms present at high temperatures.

This correlation supports the assumptions for the low-temperature aging mechanism: Capacity losses due to transport limitations, possibly lithium plating, are correlated with a high charge current rate. The high-temperature aging mechanism, however, shows no correlation with the current rate.

State of charge dependence.—Figure 7 shows the pure cycle capacity loss for the CC-CV cycle tests at constant current rates of 0.5C and 1C, for a low temperature $T = 0°C$ (a) and a high temperature

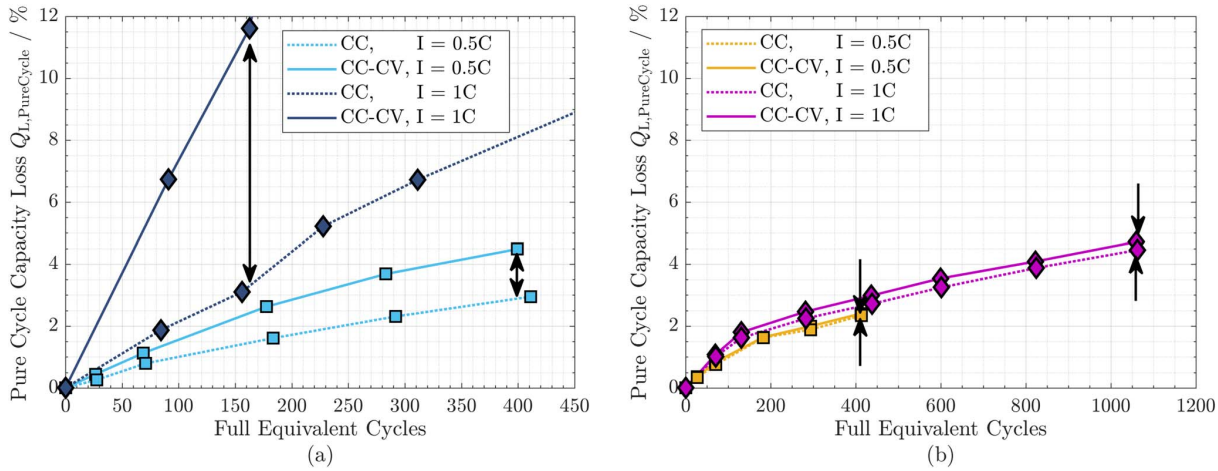

Figure 7. Influence of high SOC operation through CV-Phase at end of charge: a) $T = 0°C$, b) $T = 55°C$. Arrows are added for visualization of strong/weak variation at low/high temperatures.

Downloaded on 2018-01-13 to IP 185.17.207.4 address. Redistribution subject to ECS terms of use (see ecsdl.org/site/terms_use) unless CC License in place (see abstract).

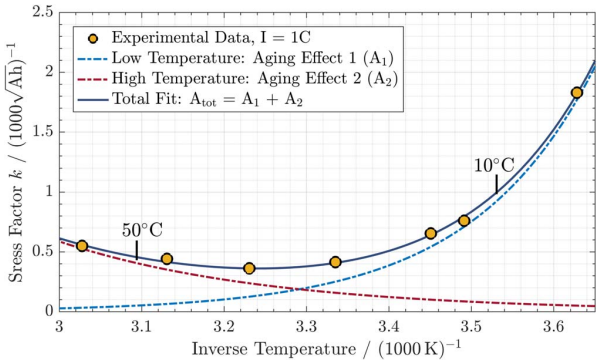

Figure 8. Superposition of two independent temperature dependent cycle aging capacity loss mechanisms for low temperature (A_1) and high temperature (A_2).

$T = 55°C$ (b). Similar to the CC tests at low temperature, the pure cycle capacity loss increases with the current rate, but not for the high temperature tests. Comparing the CC and CC-CV tests at low temperatures, the additional CV charging to a higher SOC leads to a strong increase of capacity loss, which is even more pronounced at the higher current rate. At high temperature, no difference between CC and CC-CV tests is visible due to the kinetics enhancements due to the Arrhenius-type dependence of reaction rates on temperature.

This again supports the assumptions for the aging mechanisms due to transport limitations, mentionable the possibility of lithium plating, which occurs during charging with current rates at increasing/high state of charge.[29] Finally, the aging mechanisms cannot be deduced definitely from the results and remain to be studied in future work.

Cycle aging model.—Based on the dependencies identified from the cells subjected to cycle aging, the cycle aging model is proposed. Three dominant mechanisms are defined:

- High Temperature $Q_{\mathrm{L,Cyc,High\ T}}$
- Low Temperature $Q_{\mathrm{L,Cyc,Low\ T}}$
- Low Temperature, High SOC $Q_{\mathrm{L,Cyc,Low\ T\ High\ SOC}}$

Following the previous assumption that all these aging mechanisms can be evaluated through superposition, the combined calendar and cycle aging model is proposed:

$$Q_{\mathrm{Loss}} = Q_{\mathrm{L,Cal}} + Q_{\mathrm{L,Cyc}} \quad [11]$$

$$Q_{\mathrm{Loss}} = Q_{\mathrm{L,Cal}} + Q_{\mathrm{L,Cyc,High\ T}} + Q_{\mathrm{L,Cyc,Low\ T}} + Q_{\mathrm{L,Cyc,Low\ T\ High\ SOC}} \quad [12]$$

The cycle model does not include Depth of Discharge as an input variable, which is typically used with cycle counting algorithms and S-N curves (also known as *Wöhler curve*) for characterization of the higher stress of deep discharge cycles, e.g. reported for NMC-C cells by Schmalstieg et al.[9] In fact, for lithium iron phosphate cells, the correlation of cyclic stress (S) against the cycles to end of life (N) was reported to be non-logarithmic previously.[11]

As such, the model proposed herein does not directly relate deeper cycles to increased capacity fade but calculates additional capacity loss for cells operating in high SOC regions due to the term attributed to lithium loss. Higher degradation during deeper cycles observed in our modeling approach is therefore attributed to the operation at higher SOC.

Temperature dependence.—The trend for the pure cycle capacity loss for high and low-temperature effects indicates a square root dependence on the charge throughput (see Figures 5c–5d) and is subsequently discussed. Figure 8 shows the experimental stress factors and mechanisms for low temperature (A_1), high temperature (A_2), and their sum ($A_{\mathrm{tot}} = A_1 + A_2$), all fitted to the stress factors calculated from experimental data.

An increased SEI growth due to mechanical disturbance of the SEI, which is the assumed, although not proven, high-temperature cycling capacity loss mechanism, is not known to be specific to the current direction but with the cycling of the battery in general. It is correlated in the model with the total charge throughput, during both charging and discharging, Q_{Tot}. The corresponding stress factor $k_{\mathrm{Cyc,High\ T}}$ is implemented as a temperature dependent term:

$$Q_{\mathrm{L,Cyc,High\ T}} = k_{\mathrm{Cyc,High\ T}}(T) \cdot \sqrt{Q_{\mathrm{Tot}}} \quad [13]$$

The low-temperature mechanism is implemented similarly, but with an additional current rate dependence. As the assumed mechanism for lithium loss occurs during charging; so the charge throughput in charge direction Q_{Ch} is chosen as input. The current rate dependence is also reflected in the model through the charge current I_{Ch} for the stress factor $k_{\mathrm{Cyc,Low\ T}}$:

$$Q_{\mathrm{L,Cyc,Low\ T}} = k_{\mathrm{Cyc,Low\ T}}(T, I_{\mathrm{Ch}}) \cdot \sqrt{Q_{\mathrm{Ch}}} \quad [14]$$

Fitting the stress factors to reference conditions at $T_{\mathrm{Ref}} = 298.15$ K at 1C cycling gives $k_{\mathrm{Cyc,High\ T,Ref}} = 1.456 \cdot 10^{-4} \cdot \mathrm{Ah}^{-0.5}$ and $k_{\mathrm{Cyc,Low\ T,Ref}} = 4.009 \cdot 10^{-4} \cdot \mathrm{Ah}^{-0.5}$. Temperature dependence is implemented through Arrhenius equation, with $E_{\mathrm{a,Cyc,\ High\ T}} = 32699$ J/mol, $E_{\mathrm{a,Cyc,Low\ T}} = 55546$ J/mol:

$$k_{\mathrm{Cyc,High\ T}}(T) = k_{\mathrm{Cyc,High\ T,Ref}} \cdot \exp\left[\frac{-E_{\mathrm{a,Cyc,High\ T}}}{R_g}\left(\frac{1}{T} - \frac{1}{T_{\mathrm{Ref}}}\right)\right] \quad [15]$$

$$k_{\mathrm{Cyc,Low\ T}}(T, I_{\mathrm{Ch}} = 1\mathrm{C}) = k_{\mathrm{Cyc,Low\ T,Ref}} \cdot \exp\left[\frac{E_{\mathrm{a,Cyc,Low\ T}}}{R_g}\left(\frac{1}{T} - \frac{1}{T_{\mathrm{Ref}}}\right)\right] \quad [16]$$

Current rate dependence.—Current rate dependence for the low-temperature mechanism is modeled via an exponential correlation with charge current, nominal cell capacity, and nominal current:

$$k_{\mathrm{Cyc,Low\ T}}(T = 25°C, I_{\mathrm{Ch}}) = k_{\mathrm{Cyc,Low\ T,Ref}} \cdot \exp\left[\beta_{\mathrm{Low\ T}} \cdot \frac{I_{\mathrm{Ch}} - I_{\mathrm{Ch,Ref}}}{C_0}\right] \quad [17]$$

With nominal cell capacity $C_0 = 3$ Ah, reference current $I_{\mathrm{Ch,Ref}} = 3$ A, fitting gives $\beta_{\mathrm{Low\ T}} = 2.64$ h. In summary, the low temperature stress factor is calculated as follows:

$$k_{\mathrm{Cyc,Low\ T}}(T, I_{\mathrm{Ch}}) = k_{\mathrm{Cyc,Low\ T,Ref}} \cdot \exp\left[\frac{E_{\mathrm{a,Cyc,Low\ T}}}{R_g}\left(\frac{1}{T} - \frac{1}{T_{\mathrm{Ref}}}\right)\right] \cdot \exp\left[\beta_{\mathrm{Low\ T}} \cdot \frac{I_{\mathrm{Ch}} - I_{\mathrm{Ch,Ref}}}{C_0}\right] \quad [18]$$

Figure 9a shows both stress factors correlations over temperature, with various current rates for the low-temperature mechanism. Figure 9b shows the exponential correlation of current for the low-temperature stress factor.

State of charge dependence.—The capacity loss attributed to the additional term for the mechanism at low temperatures at a high state of charge is calculated from experimental data of the CC-CV tests by subtraction of the previously developed terms of the calendar model and the cycle model for low and high temperature:

$$\begin{aligned} Q_{\mathrm{L,Exp,Cycle,High\ SOC}} &= Q_{\mathrm{L,Exp}} - Q_{\mathrm{L,Cal}}\left(T = \overline{T_{\mathrm{Exp}}}, SOC = 50\%, t = t_{\mathrm{Exp}}\right) \\ &\quad - Q_{\mathrm{L,cyc,Low\ T}}\left(T = \overline{T_{\mathrm{Ch,Exp}}}, I_{\mathrm{Ch}} = \overline{I_{\mathrm{Ch,Exp}}}, Q_{\mathrm{Ch}} = Q_{\mathrm{Ch,Exp}}\right) \\ &\quad - Q_{\mathrm{L,cyc,High\ T}}\left(T = \overline{T_{\mathrm{Exp}}}, Q_{\mathrm{Tot}} = Q_{\mathrm{Tot,Exp}}\right) \end{aligned} \quad [19]$$

Charge throughput is factored in linearly, after reviewing the correlation of $Q_{\mathrm{L,Exp,Cycle,\ High\ SOC}}$. For the stress factor, additionally to the

Downloaded on 2018-01-13 to IP 185.17.207.4 address. Redistribution subject to ECS terms of use (see ecsdl.org/site/terms_use) unless CC License in place (see abstract).

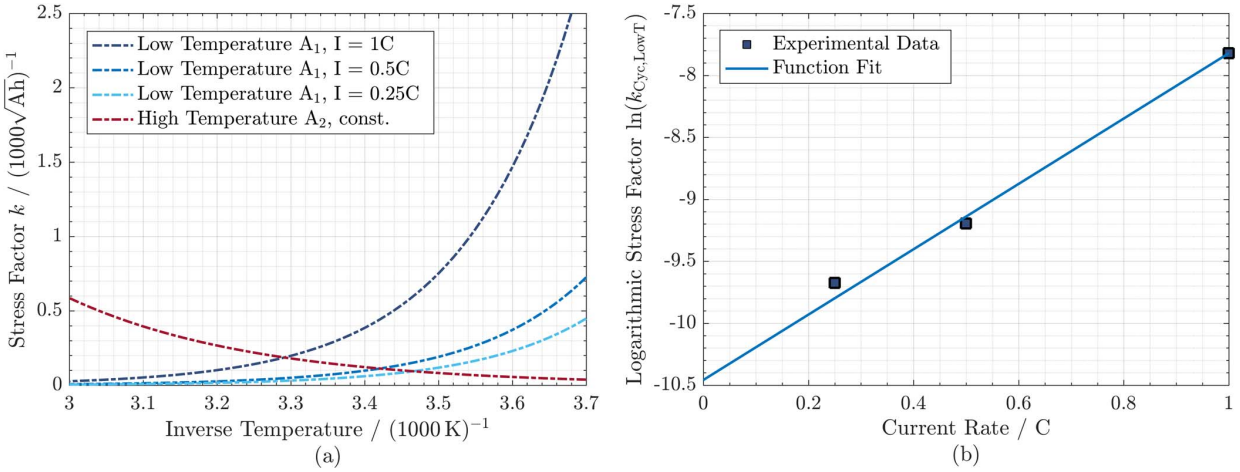

Figure 9. Current rate dependence of cold temperature effects in CC-Tests: a) Stress factor over temperature, b) Exponential correlation of low-temperature mechanism to charge current at $T = 25°C$.

temperature and charge current dependence, a dependence for the SOC is implemented. The stress factor is only applied if the SOC lies above a fixed SOC limit SOC_{Ref}, otherwise it set to zero:

$$Q_{\text{L,cyc,Low T High SOC}} = k_{\text{Cyc,Low T High SOC}}\,(T, I_{\text{Ch}}, SOC) \cdot Q_{\text{Ch}} \quad [20]$$

$$\begin{aligned} &k_{\text{Cyc,Low T High SOC}}\,(T, I_{\text{Ch}}, SOC) \\ &= k_{\text{Cyc,Low T High SOC,Ref}} \cdot \exp\left[\frac{E_{\text{a,Cyc,Low T High SOC}}}{R_g}\left(\frac{1}{T} - \frac{1}{T_{\text{Ref}}}\right)\right] \\ &\cdot \exp\left[\beta_{\text{Low T High SOC}} \cdot \frac{I_{\text{Ch}} - I_{\text{Ch,Ref}}}{C_0}\right] \\ &\cdot \left(\frac{\text{sgn}\,(SOC - SOC_{\text{Ref}}) + 1}{2}\right) \end{aligned} \quad [21]$$

Following this condition, only the charge throughput from experimental data which occurs in the tests above the SOC limit is considered for the fitting. Several cycles at the begin of the cycle tests were analyzed herefore: After disregarding cycles 1 to 3 at beginning of the cycling experiments due to changing conditions, cycles 4 to 10 were analyzed. Cell conditions after cycle 10 are similar to the analysis of these six cycles and are thus excluded from model parameterization to significantly reduce the efforts for parametrization. Temperature above the SOC limit is time averaged. The current value is averaged over the whole CC-CV charge cycle and thus still dominated by the CC phase. As the current is variable during the CV phase, a charge throughput weighted-average current was calculated and used for fitting:

$$\begin{aligned} \bar{\bar{I}}_{\text{Ch,Exp},SOC\geq 82\%} &= \sum\nolimits_i I_{\text{Ch,Exp}}\,(t = t_i) \\ &\cdot \frac{Q_{\text{Ch,Exp}}\,(t = t_i) - Q_{\text{Ch,Exp}}\,(t = t_i - 1)}{Q_{\text{Ch,Exp}}} \end{aligned} \quad [22]$$

Results for the conditions (Charge throughput, current, and temperature) are then implemented during fitting the long-term tests featuring hundreds of cycles. With the reference stress factor $k_{\text{Cyc,Low T High SOC,Ref}} = 2.031 \cdot 10^{-6}$ Ah^{-1} (at $T = 25°C$, $I_{\text{Ch}} = 3$ A) fitting Equation 21 with the results from Equation 19 and 22 based on the CC-CV tests gives $E_{\text{a,Cyc,Low T High SOC}} = 2.3 \cdot 10^5$ J/mol, $\beta_{\text{Low T High SOC}} = 7.8$ h with $SOC_{\text{Ref}} = 82\%$. Figure 10a shows the low temperature, high SOC stress factor correlation to temperature and current. Figure 10b shows the exponential correlation. Current rate values are slightly below their respective constant current test values due to the lowered rate in the CV phase.

Model Summary

The proposed model for the calculation of cell capacity loss Q_{Loss} through addition of the four capacity loss mechanisms is summarized as follows:

$$\begin{aligned} &Q_{\text{Loss}}\,(T, SOC, I_{\text{Ch}}, Q_{\text{Tot}}, Q_{\text{Ch}}) \\ &= Q_{\text{L,Cal}}\,(T, SOC, t) + Q_{\text{L,Cyc,High T}}\,(T, Q_{\text{Tot}}) \\ &\quad + Q_{\text{L,Cyc,Low T}}\,(T, I_{\text{Ch}}, Q_{\text{Ch}}) \\ &\quad + Q_{\text{L,Cyc,Low T High SOC}}\,(T, I_{\text{Ch}}, SOC, Q_{\text{Ch}}) \\ &= k_{\text{Cal}}\,(T, SOC) \cdot \sqrt{t} + k_{\text{Cyc,High T}}\,(T) \cdot \sqrt{Q_{\text{Tot}}} \\ &\quad + k_{\text{Cyc,Low T}}\,(T, I_{\text{Ch}}) \cdot \sqrt{Q_{\text{Ch}}} \\ &\quad + k_{\text{Cyc,Low T High SOC}}\,(T, I_{Ch}, SOC) \cdot Q_{\text{Ch}} \end{aligned} \quad [23]$$

For the fitting process of the stress factors, averaged experimental conditions, e.g. temperature, are calculated to constant values for the respective test conditions. However, in prospected model applications, cell conditions are instead variable, e.g. for cell temperature due to variable heat generation and ambient temperature. Thus, a rate-based integral approach is used, as proposed by Thomas et al.[30] The capacity loss for every time step with variable conditions is calculated. The integration variables τ and φ are defined, replacing time t and charge throughput Q respectively:

$$\begin{aligned} Q_{\text{Loss}} &= \int k_{\text{Cal}}\,(T, SOC) \cdot \left(2\tau^{0.5}\right)^{-1} d\tau \\ &\quad + \int k_{\text{Cyc,High T}}\,(T) \cdot \left(2\varphi^{0.5}\right)^{-1} d\varphi_{\text{Tot}} \\ &\quad + \int k_{\text{Cyc,Low T}}\,(T, I_{\text{Ch}}) \cdot \left(2\varphi^{0.5}\right)^{-1} d\varphi_{\text{Ch}} \\ &\quad + \int k_{\text{Cyc,Low T High SOC}}\,(T, I_{\text{Ch}}, SOC)\, d\varphi_{\text{Ch}} \end{aligned} \quad [24]$$

In conclusion, Table IV summarizes the model parameters and Figure 11 gives an overview of the stress factor correlations to cell conditions.

Downloaded on 2018-01-13 to IP 185.17.207.4 address. Redistribution subject to ECS terms of use (see ecsdl.org/site/terms_use) unless CC License in place (see abstract).

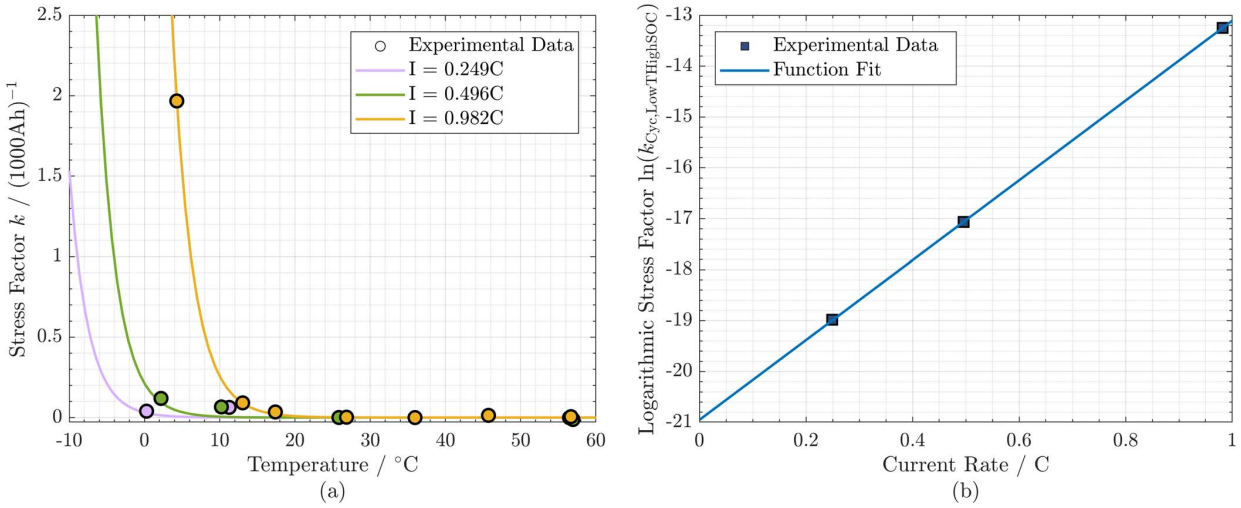

Figure 10. Current Rate Dependence of High State of Charge Temperature Effects in CC-CV tests: a) Stress factor over temperature, b) Exponential Dependence of stress factor on charge current at $T = 25°\text{C}$.

Model Validation

Validation storage tests.—Figure 12 shows the validation of the storage tests at sample temperatures of 15°C (top) and 45°C (bottom). Of these data points, only the test points at $SOC = 100\%$ are previously included in the model parametrization, the remaining data points can be considered as new to the model.

Model results (lines) and experimental data (marker) are shown on the left side. For comparison between the model results and the experimental data, the model error is shown on the right side. The

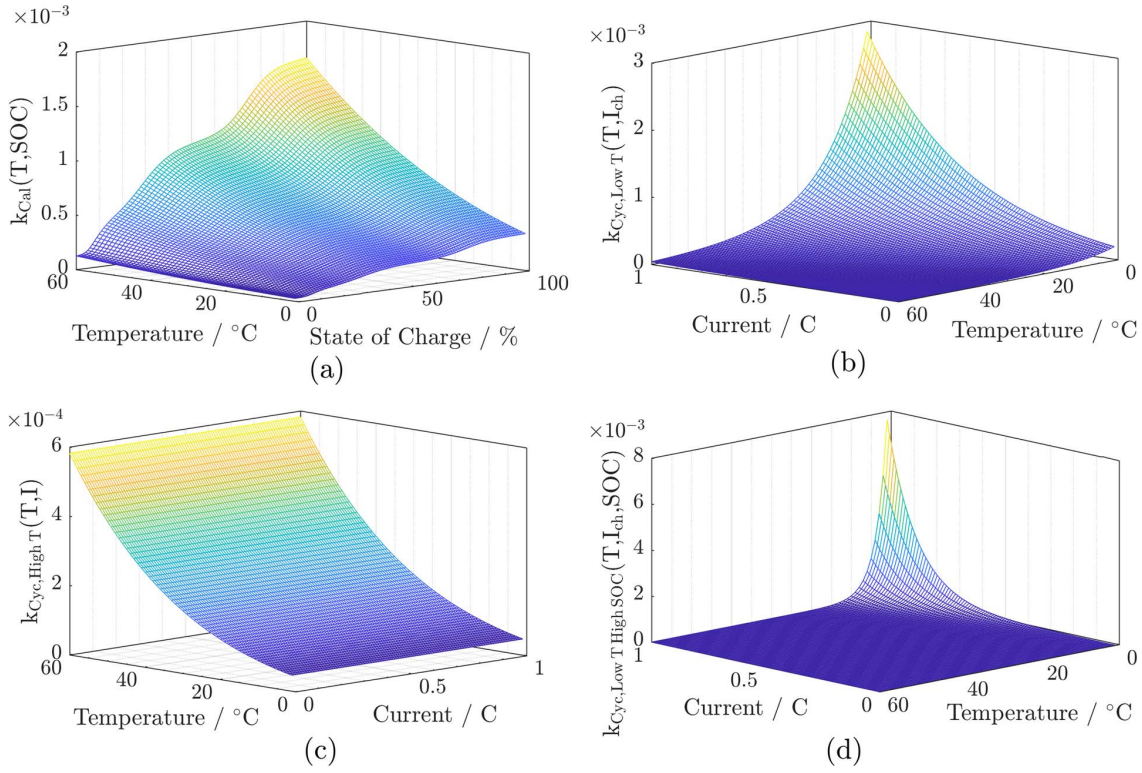

Figure 11. Overview of model stress factors: a) Calendar stress factor with temperature and State of Charge dependence (Unit: $\text{h}^{-0.5}$), b) Cycle stress factor for low-temperature effects with charge current and temperature dependence (Unit: $\text{Ah}^{-0.5}$), c) Cycle stress factor for high-temperature effects with temperature dependence (Unit: $\text{Ah}^{-0.5}$), d) Cycle stress factor for low temperature/high state of charge effects with charge current rate and temperature dependence (Unit: Ah^{-1}). Units for stress factors are not included in z-axis legend but shown in the figure caption for clarity.

Downloaded on 2018-01-13 to IP 185.17.207.4 address. Redistribution subject to ECS terms of use (see ecsdl.org/site/terms_use) unless CC License in place (see abstract).

Table IV. Summary of model parameters.

Model Parameter	Value	Note
$k_{\text{Cal,Ref}}$	$3.69 \cdot 10^{-4} \cdot \text{h}^{-0.5}$	$T = 25°\text{C}$, $SOC = 50\%$
$k_{\text{Cyc, High T, Ref}}$	$1.46 \cdot 10^{-4} \cdot \text{Ah}^{-0.5}$	$T = 25°\text{C}$, $I = 1\text{C}$
$k_{\text{Cyc, Low T, Ref}}$	$4.01 \cdot 10^{-4} \cdot \text{Ah}^{-0.5}$	$T = 25°\text{C}$, $I_{\text{Ch}} = 1\text{C}$
$k_{\text{Cyc,Low T High SOC,Ref}}$	$2.03 \cdot 10^{-6}\ \text{Ah}^{-1}$	$T = 25°\text{C}$, $I_{\text{Ch}} = 1\text{C}$
$E_{\text{a,Cal}}$	$2.06 \cdot 10^{4}$ J/mol	$SOC = 100\%$
$E_{\text{a,Cyc, High T}}$	$3.27 \cdot 10^{4}$ J/mol	$I = 1\text{C}$
$E_{\text{a,Cyc,Low T}}$	$5.55 \cdot 10^{4}$ J/mol	$I_{\text{Ch}} = 1\text{C}$
$E_{\text{a,Cyc,Low T High SOC}}$	$2.33 \cdot 10^{5}$ J/mol	$I_{\text{Ch}} = 1\text{C}$
α	$3.84 \cdot 10^{-1}$	
$\beta_{\text{Low T}}$	2.64 h	
$\beta_{\text{Low T High SOC}}$	7.84 h	
T_{Ref}	298.15 K	
$I_{\text{Ch,Ref}}$	3 A	
$U_{\text{a,Ref}}$	$1.23 \cdot 10^{-1}$ V	$SOC = 50\%$
k_0	$1.42 \cdot 10^{-1}$	
U_{a}	$U_{\text{a}}(SOC)$	See Appendix.

model error is calculated as:

$$\text{Model Error}_{\text{i}} = \text{Q}_{\text{Loss,i}} - \text{Q}_{\text{Loss,Exp,i}} \quad [25]$$

This model error should not be confused with the relative model error, which is here not shown.

For the lower temperature, the lower capacity loss leads to smaller errors. At the higher temperatures, approximately twice the capacity loss occurs during the test period, leading to higher errors. Nonetheless, throughout the test period, the model error remains below 2%.

Validation CC cycle tests.—Figure 13 shows the validation of the CC cycle tests through the calendar and the cycle aging mechanisms for high and low temperature, based on various averaged temperatures and current rates. Six test conditions are shown: Three different current rates at an ambient temperature of 0°C to show the model performance over the full current range, and three different ambient temperatures with a current rate of 1C to show the model performance over the full temperature range. Due to slightly varying cell conditions in the tests, multiple lines and experimental points are shown for some test points. For the model error (right), the value is averaged between the cells. For all cells except 0°C cycled at 1C, the model error is below 2%. The test point at 0°C cycled at 1C shows the highest aging gradient and peaks with a model error of 2.5% for two RPTs. At subsequent RPTs however, the model error decreases back to less than 1%.

Validation CC-CV cycle tests.—Figure 14 shows the validation of the CC-CV cycle tests through all aging mechanisms, based on the analyzed six cycles at various temperatures and current rates. Again, several test points at the lowest temperature, 0°C, show the model performance for the considered current range. As the test point at 1C exhibits an increased model error of 2.8% at end of life, an additional test point with a current rate of 1.7C is tested and evaluated. The test point at 1.7C, which even exceeds manufacturer specifications for the charge current, results in a model error of 0.8% at end of life, showing that the model can give good agreement with experimental data for high current rates. The two test points for higher temperatures are also in good agreement at the end of the tests.

Validation application-based dynamic current profile.—Figure 15 shows experimental data and model results for the dynamic current profile based on an application in a PV-residential battery system, as

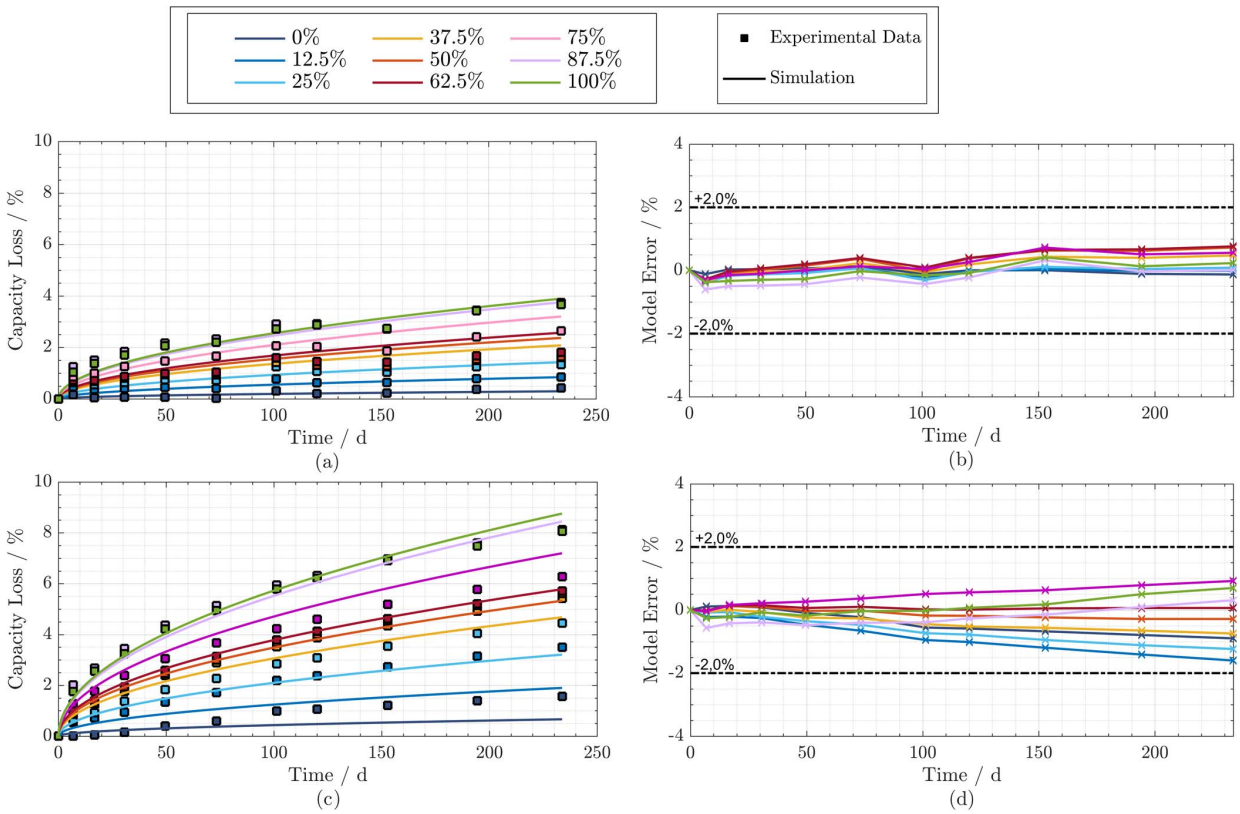

Figure 12. Comparison of model and experimental data for storage tests: a) Capacity loss at $T = 15°\text{C}$, b) Model error at $T = 15°\text{C}$, c) Capacity loss at $T = 45°\text{C}$, d) Model error at $T = 45°\text{C}$.

Downloaded on 2018-01-13 to IP 185.17.207.4 address. Redistribution subject to ECS terms of use (see ecsdl.org/site/terms_use) unless CC License in place (see abstract).

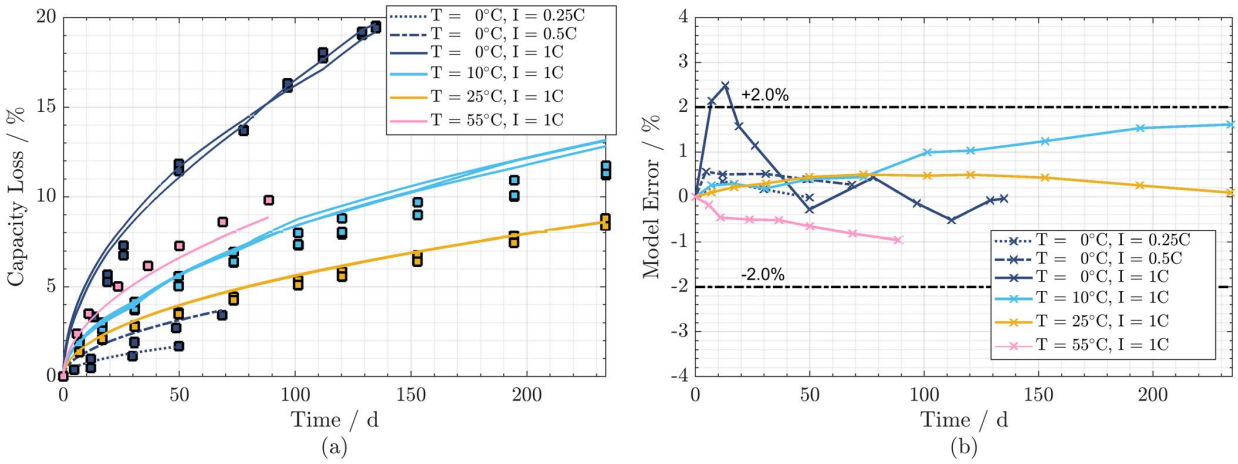

Figure 13. Comparison of model and experimental data for CC cycle tests: a) Capacity loss, b) Model error.

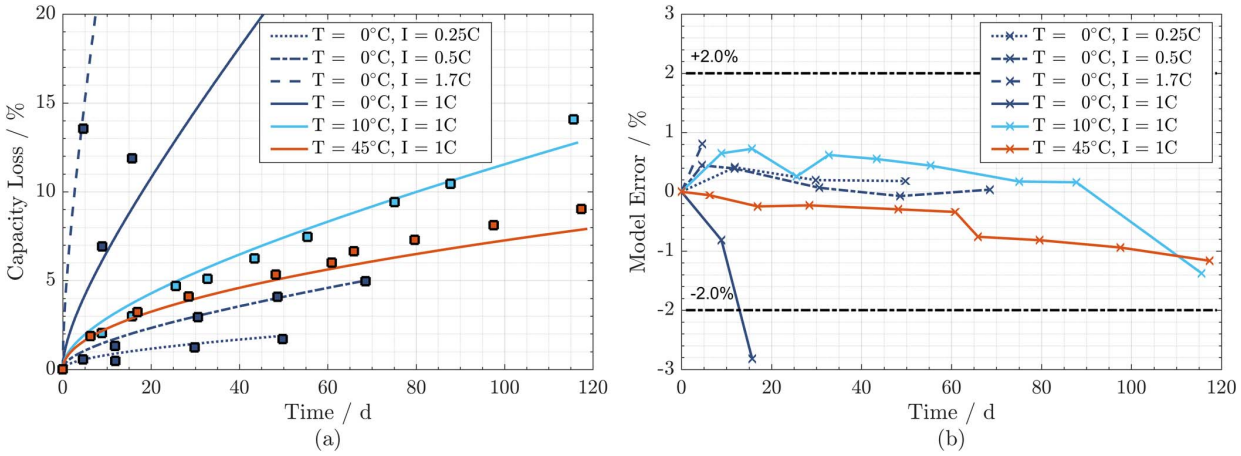

Figure 14. Comparison of model and experimental data for CC-CV cycle tests: a) Capacity loss, b) Model error.

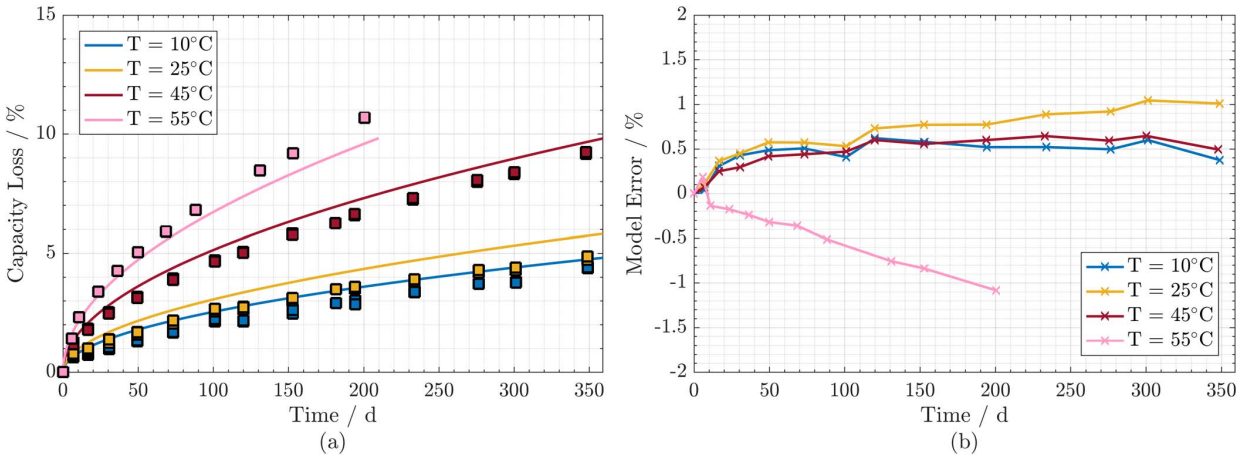

Figure 15. Comparison of model and experimental data for validation tests with PV-residential battery application profile: a) Capacity loss, b) Model error.

Downloaded on 2018-01-13 to IP 185.17.207.4 address. Redistribution subject to ECS terms of use (see ecsdl.org/site/terms_use) unless CC License in place (see abstract).

was presented previously (see Figure 1). Test data for validation is continued for up to 114 days after the longest parametrization tests to a total of 348 days.

For $T = 10°C, 25°C, 45°C$ the model shows a slight overprediction of capacity loss, whereas at $T = 55°C$ the model shows a trend towards underprediction. The trend for the overprediction at $T = 10°C, 25°C, 45°C$ is apparent along the whole test period, but levels off in the last RPT. The underprediction trend at $T = 55°C$ shows no leveling off. It should be noted though, that at $T = 55°C$ only a single cell is tested. For $T = 10°C, 25°C, 45°C$, the model errors are below 1% of the original cell capacity at the end of the test period. At $T = 55°C$ the model error is at ≈1% after ≈200 days. For the validation tests after 348 days, the relative model error, defined as $(Q_{\mathrm{Loss,i}} - Q_{\mathrm{Loss,Exp,i}})/Q_{\mathrm{Loss,Exp,i}}$, is at the highest value of +21% at $T = 25°C$.

The validation tests with a test duration of 348 days reached approximately 539 profile repetitions. As one profile repetition is an accelerated representation of a winter and a summer day (see Section Experimental Methods), this gives accelerated test results for 1078 days or approximately 3 years of operation of the representative system.

Summarized, the model results are in good agreement with the tests and validate the model performance in variable current applications, which have not been used for the model parameterization. Furthermore, the model shows good performance in the additional timeframe beyond parametrization, as well as at current loads with varying cycle depths.

Previous constant current cycle tests at 1C showed a minimum for the capacity loss for a temperature of 25°C (see Figure 5). The experimental and model results for the dynamic current profile instead show a minimum for the capacity loss at 10°C for the investigated conditions and increasing capacity loss with higher temperatures. The model results give insight that here the calendar aging-induced capacity loss is the dominant mechanism. The overall cycle induced capacity loss is comparably less due to the low average/maximum C-rates (see Table III). The model, therefore, predicts the trend for the influence of the operating temperature here accurately.

Conclusions

This article presents a comprehensive semi-empirical model approach for the capacity loss of lithium-ion batteries. The approach is based on a reduced set of internal cell parameters and physically supported degradation functions. For parameterization, a lifetime test study with lithium iron phosphate cells is conducted, including storage and cycle tests.

State of Charge dependence of the calendar aging is implemented through coupling the anode open circuit potential in a Tafel equation based approach. Temperature dependence of calendar aging is calculated with Arrhenius equation.

For the cycle aging, the emphasis is placed on the varying degradation at different temperatures. Three cycle aging correlations are identified and correlated to two physical cell internal degradation effects: Lithium loss due to transport limitations, possibly lithium plating, during charging at low temperature and increased SEI growth due to cycling at high temperature. Degradation is separated under different conditions: High temperature, low temperature, and low temperature at a high state of charge. Current rate dependence and State of Charge dependence is implemented where observed. Cycle aging is correlated with the charge throughput. No direct correlation with the cycle depth is implemented, but cycle operation at high SOC leads to an increased capacity loss in the cycle model.

For model validation, a comparison of the simulation results with the aging model to the experimental data is evaluated. The model application in a stationary storage real-world scenario based on the application in a PV-residential battery system is tested via additional profiles, which have not been used for model parameterization and feature varying cycle depth. Tests are continued for up to 114 days beyond the longest parametrization tests to a total duration of 348 days.

Both the parameterization tests, as well as dynamic current tests exclusively used for validation, are in good agreement with the model results. At the end of the dynamic current profile validation tests between 10°C and 45°C, after 348 days, the model error is below 1% of the original cell capacity and the maximum relative error for the capacity loss is below 21%. The optimum temperature for a minimum of capacity loss is also shown to be accurately predicted.

Outlook

Additional validation tests covering more application scenarios and/or stronger variation of test conditions, such as a dynamic ambient temperature or a non-repeating current profile can further support the assessment of the model performance for real-world applications.

Future work involves the model application in system simulations of stationary battery storage systems. Here, the model can be used for lifetime evaluation of various applications.

Through coupling with thermal pack and system models, the thermal management can be evaluated. I.e. the impact of thermal pack gradients and cooling setups over the system lifetime can be calculated. On the system level, the system temperature or thermal control strategies can be analyzed and subsequently optimized.

The model can also serve to develop operational strategies for the energy management system, in order to reduce cell degradation by avoiding high-stress factor conditions, i.e. high SOC for long storage durations and high current rates at a high state of charge.

Although the cell impedance was not identified as critical for the cell end-of-life criteria, the increase can be evaluated towards how it affects the thermal management and system energy efficiency over the lifetime.

Acknowledgments

The research project Intelligent Home Energy Management (IHEM) is funded by the Federal Ministry for Economic Affairs and Energy within the *Funding initiative Electrical Storages* (grant number 03ET1205G) and cared by Project Management Jülich. The authors also thank the Bavarian Ministry of Economic Affairs and Media, Energy and Technology for their support via the EEBatt project. K. Smith wishes to acknowledge support by the Vehicle Technologies Office, Office of Energy Efficiency and Renewable Energy, U. S. Department of Energy (DOE) under DOE Contract No. DE-AC36-08GO28308 with the National Renewable Energy Laboratory. The authors thank S. Santhanagopalan for the highly helpful discussions. The responsibility for the content of this publication lies with the author.

Appendix

Data for the open circuit potential of the lithium graphite anode U_a as a function of the degree of lithiation x_a is taken from Safari et al.:[28]

$$U_a(x_a) = 0.6379 + 0.5416 \cdot \exp(-305.5309 \cdot x_a) + 0.044 \tanh\left(-\frac{x_a - 0.1958}{0.1088}\right) - 0.1978 \tanh\left(\frac{x_a - 1.0571}{0.0854}\right) - 0.6875 \tanh\left(\frac{x_a + 0.0117}{0.0529}\right) - 0.0175 \tanh\left(\frac{x_a - 0.5692}{0.0875}\right) \quad [A1]$$

Anode stoichiometry x_a is calculated as function of the SOC of the full-cell by linearly interpolating between $SOC = 0\%$ and $SOC = 100\%$:

$$x_a(SOC) = x_a(SOC = 0\%) + SOC \cdot [x_a(SOC = 100\%) - x_a(SOC = 0\%)] \quad [A2]$$

The degree of lithiation at $SOC = 0\%$, respectively $SOC = 100\%$, is derived from fitting the half-cell open circuit potentials of both electrodes in combination with cell parameters to measured full-cell open circuit potential data.

Downloaded on 2018-01-13 to IP 185.17.207.4 address. Redistribution subject to ECS terms of use (see ecsdl.org/site/terms_use) unless CC License in place (see abstract).

Table AI. Cell parameters used for fitting half-cell open circuit potentials to full-cell open circuit potential from experimental data. Experimental data values refer to existing cell dissection experiments.

Parameter	Anode Li-C Value	Reference	Cathode $LiFePO_4$ Value	Reference
Stoichiometry $x(SOC = 0\%)$	$8.5 \cdot 10^{-3}$	*Fit*	$9.16 \cdot 10^{-1}$	*Fit*
Stoichiometry $x(SOC = 100\%)$	$7.8 \cdot 10^{-1}$	*Fit*	$4.5 \cdot 10^{-2}$	*Fit*
Max. Concentration Lithium	$3.14 \cdot 10^{4}\mathrm{mol/m^3}$	28	$2.28 \cdot 10^{4}\mathrm{mol/m^3}$	28
Surface Area Electrodes	$1.57 \cdot 10^{-1}\mathrm{m^2}$	*Exp.*	$1.57 \cdot 10^{-1}\mathrm{m^2}$	*Exp.*
Thickness Active Material	$6.01 \cdot 10^{-5}$ m	*Exp.*	$7.90 \cdot 10^{-5}$ m	*Exp.*
Volume Share Active Material	$4.86 \cdot 10^{-1}$	*Fit*	$4.55 \cdot 10^{-1}$	*Fit*

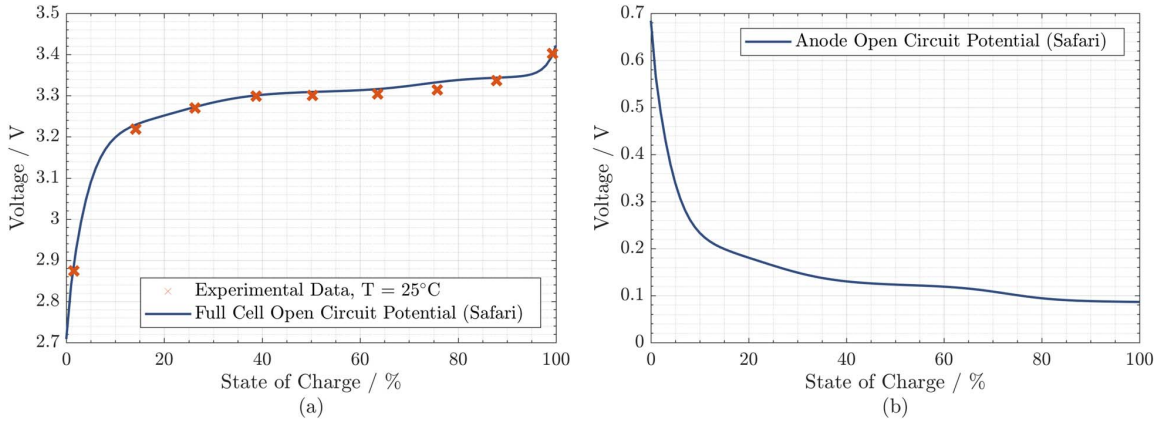

Figure A1. Open Circuit Potentials: a) Comparison of full-cell open circuit potential reconstructed from half-cell potentials against experimental data, b) Anode open circuit potential over the full-cell operating range.

Open circuit potential data for the lithium iron phosphate cathode ($LiFePO_4$) $U_c(x_c)$ is also taken from Safari et al.:[28]

$$\begin{aligned} U_c(x_c) = {} & 3.4323 - 0.8428 \cdot \exp\left[-80.2493 \cdot (1 - x_c)^{1.3198}\right] \\ & - 3.2474 \cdot 10^{-6} \cdot \exp\left[20.2645 \cdot (1 - x_c)^{3.8003}\right] \\ & + 3.2482 \cdot 10^{-6} \cdot \exp\left[20.2646 \cdot (1 - x_c)^{3.7995}\right] \end{aligned} \quad [A3]$$

The chosen parameters for fitting the half-cell open circuit potential to experimental full-cell data - measured, fitted or taken from literature - are given in Table AI.

Electrode surface area and active material thickness are chosen from existing experiments based on cell dissection. Stoichiometry and active material volume share values are fitted to the experimental full-cell open circuit potential, shown in Figure A1a. Figure A1b shows the corresponding anode open circuit potential over the full-cell state of charge, calculated with Equations A1 and A2.

ORCID

M. Schimpe https://orcid.org/0000-0001-5000-2045

References

1. M. Munsell, *Greentech Media* (07.03.2017).
2. C. Patsios, B. Wu, E. Chatzinikolaou, D. J. Rogers, N. Wade, N. P. Brandon, and P. Taylor, *Journal of Energy Storage*, **5**, 48 (2016).
3. X. Jin, A. Vora, V. Hoshing, T. Saha, G. Shaver, R. E. García, O. Wasynczuk, and S. Varigonda, *Journal of Power Sources*, **342**, 750 (2017).
4. C. Delacourt and M. Safari, *Journal of the Electrochemical Society*, **159**(8), A1283 (2012).
5. E. Sarasketa-Zabala, I. Gandiaga, L. M. Rodriguez-Martinez, and I. Villarreal, *Journal of Power Sources*, **272**, 45 (2014).
6. S. Grolleau, A. Delaille, H. Gualous, P. Gyan, R. Revel, J. Bernard, E. Redondo-Iglesias, and J. Peter, *Journal of Power Sources*, **255**, 450 (2014).
7. E. Sarasketa-Zabala, I. Gandiaga, E. Martinez-Laserna, L. M. Rodriguez-Martinez, and I. Villarreal, *Journal of Power Sources*, **275**, 573 (2015).
8. J. Wang, P. Liu, J. Hicks-Garner, E. Sherman, S. Soukiazian, M. Verbrugge, H. Tataria, J. Musser, and P. Finamore, *Journal of Power Sources*, **196**(8), 3942 (2011).
9. J. Schmalstieg, S. Käbitz, M. Ecker, and D. U. Sauer, *Journal of Power Sources*, **257**, 325 (2014).
10. M. Swierczynski, D.-I. Stroe, A.-I. Stan, R. Teodorescu, and S. K. Kaer, *IEEE Trans. on Ind. Applicat.*, **51**(4), 3453 (2015).
11. E. Sarasketa-Zabala, E. Martinez-Laserna, M. Berecibar, I. Gandiaga, L. M. Rodriguez-Martinez, and I. Villarreal, *Applied Energy*, **162**, 839 (2016).
12. M. Ecker, J. B. Gerschler, J. Vogel, S. Käbitz, F. Hust, P. Dechent, and D. U. Sauer, *Journal of Power Sources*, **215**, 248 (2012).
13. T. Waldmann, M. Wilka, M. Kasper, M. Fleischhammer, and M. Wohlfahrt-Mehrens, *Journal of Power Sources*, **262**, 129 (2014).
14. M. Naumann, R. C. Karl, C. N. Truong, A. Jossen, and H. C. Hesse, *Energy Procedia*, **73**, 37 (2015).
15. C. N. Truong, M. Naumann, R. C. Karl, M. Müller, A. Jossen, and H. C. Hesse, *Batteries*, **2**(2), 14 (2016).
16. A. Zeh, M. Müller, M. Naumann, H. C. Hesse, A. Jossen, and R. Witzmann, *Batteries*, **2**(3), 29 (2016).
17. Masayuki Yasuda, in *OREBA 1.0 - International Conference on Olivines for Rechargeable Batteries*, (2014).
18. M.-k. Konan, *SONY US26650FTC1 Product Specification*, (2010).
19. H.-P. Beck, *Project Report ESPEN - Potentials of electrochemical storages in power grids in competition to further technologies and system solutions*.
20. S. F. Schuster, T. Bach, E. Fleder, J. Müller, M. Brand, G. Sextl, and A. Jossen, *Journal of Energy Storage*, **1**, 44 (2015).
21. M. Ecker, N. Nieto, S. Käbitz, J. Schmalstieg, H. Blanke, A. Warnecke, and D. U. Sauer, *Journal of Power Sources*, **248**, 839 (2014).
22. J. Vetter, P. Novák, M. R. Wagner, C. Veit, K.-C. Möller, J. O. Besenhard, M. Winter, M. Wohlfahrt-Mehrens, C. Vogler, and A. Hammouche, *Journal of Power Sources*, **147**(1-2), 269 (2005).
23. A. Barré, B. Deguilhem, S. Grolleau, M. Gérard, F. Suard, and D. Riu, *Journal of Power Sources*, **241**, 680 (2013).
24. M. Broussely, P. Biensan, F. Bonhomme, P. Blanchard, S. Herreyre, K. Nechev, and R. J. Staniewicz, *Journal of Power Sources*, **146**(1-2), 90 (2005).
25. K. Smith, A. Saxon, M. Keyser, B. Lundstrom, Z. Cao, and A. Roc, in 2017 *American Control Conference (ACC)*, p. 4062, IEEE (2017).
26. S. Santhanagopalan, K. Smith, J. Neubauer, G.-H. Kim, A. Pesaran, and M. Keyser, *Design and analysis of large lithium-ion battery systems*, Artech House (2014).
27. P. Keil, S. F. Schuster, J. Wilhelm, J. Travi, A. Hauser, R. C. Karl, and A. Jossen, *J. Electrochem. Soc.*, **163**(9), A1872-A1880 (2016).
28. M. Safari and C. Delacourt, *Journal of the Electrochemical Society*, **158**(5), A562 (2011).
29. M. Petzl, M. Kasper, and M. A. Danzer, *Journal of Power Sources*, **275**, 799 (2015).
30. E. V. Thomas, I. Bloom, J. P. Christophersen, and V. S. Battaglia, *Journal of Power Sources*, **206**, 378 (2012).

Downloaded on 2018-01-13 to IP 185.17.207.4 address. Redistribution subject to ECS terms of use (see ecsdl.org/site/terms_use) unless CC License in place (see abstract).

7 Marginal costs of battery system operation in energy arbitrage based on energy losses and cell degradation

This section introduces the paper *Marginal Costs of Battery System Operation in Energy Arbitrage based on Energy Losses and Cell Degradation* and is based on the paper without further reference.

Chapter 2.1 previously introduced the definition of the marginal costs of operation, consisting of costs for energy losses, as well as of costs for the battery degradation. Regarding energy losses, Chapter 3 presented the required methods for the calculation, and Chapter 6 introduced a battery degradation model.

In this paper, a cost function considering both energy losses and cycle-induced capacity losses is defined to calculate the marginal costs of BESS operation. The electricity price scenario is in accordance with typical constellation at the German Day-Ahead energy trading market. The results reveal high costs due to energy losses at low power operation and high costs due to capacity losses at high power charge operation.
The cost function is evaluated for an optimal control in an energy trading scenario with variable electricity prices, showing large potential for an increased profit. For low price variation, the optimized power control aims for minimized marginal costs. At high price variation, which strongly exceeds marginal costs, the optimum operation according to the best prices is the most profitable control.
The subsequent discussion of the results presents various perspectives on which marginal costs should be included in an optimization. Costs for energy losses directly influence the revenue/cost of arbitrage operation. In contrast, costs for cycle-induced capacity losses can be evaluated through different perspectives – which might complicate including them in an operation optimization.

Author contribution The marginal cost model was initiated and developed by the author this thesis. The paper draft was written also by the author this thesis. The model evaluation was conducted in close collaboration with Jorn Reniers at the University of Oxford, which the author visited through a research exchange. The results have also been presented at the conference *2018 IEEE International Conference on Environment and Electrical Engineering and 2018 IEEE Industrial and Commercial Power Systems Europe* by the author of this thesis.

Marginal Costs of Battery System Operation in Energy Arbitrage based on Energy Losses and Cell Degradation

Michael Schimpe, Cong Nam Truong, Maik Naumann, Andreas Jossen, Holger C. Hesse, Jorn M. Reniers, David A. Howey

Proceedings of 2018 IEEE International Conference on Environment and Electrical Engineering and 2018 IEEE Industrial and Commercial Power Systems Europe, IEEE, 2018

Permanent weblink:
https://doi.org/10.1109/EEEIC.2018.8493717

©2018 IEEE. Reprinted, with permission, from
Michael Schimpe, Cong Nam Truong, Maik Naumann, Andreas Jossen, Holger C. Hesse, Jorn M. Reniers, and David A. Howey
Marginal Costs of Battery System Operation in Energy Arbitrage based on Energy Losses and Cell Degradation,
Proceedings of 2018 IEEE International Conference on Environment and Electrical Engineering and 2018 IEEE Industrial and Commercial Power Systems Europe, IEEE, 2018

Marginal Costs of Battery System Operation in Energy Arbitrage based on Energy Losses and Cell Degradation

Michael Schimpe, Cong Nam Truong, Maik Naumann, Andreas Jossen, Holger C. Hesse
Institute for Electrical Energy Storage Technology
Technical University of Munich
Munich, Germany
michael.schimpe@tum.de

Jorn M. Reniers, David A. Howey
Department of Engineering Science
University of Oxford
Oxford, United Kingdom

***Abstract*—Optimal control of a battery energy storage system for energy arbitrage strongly depends on the marginal costs of operation. A cost function considering energy conversion losses and cycle-induced capacity losses is defined to calculate the marginal costs as a function of system power and power flow direction. The results are evaluated and reveal increased costs due to energy losses at low power operation, as well as increased costs due to capacity loss costs during charge operation at high power. The marginal cost function is evaluated for an optimal system control in an energy arbitrage scenario with variable electricity prices. Here, results show that for low price variation the optimized power control aims for minimized marginal costs. At high price variation, that strongly exceeds marginal costs, the optimum operation according to the best prices is the most profitable control. Finally, a discussion on the inclusion of the cycle-induced capacity losses is presented.**

Keywords— energy efficiency; energy storage; batteries

I. Introduction

Battery Energy Storage Systems (BESS) are increasingly used for grid applications. Major applications today are grid ancillary services, which often feature capacity prices (Euro/MW) [1]. The operation of BESS in energy arbitrage, where revenue is created through charging/discharging at variable electricity prices, however, strongly depends on the electricity price (Euro/MWh). The economic viability of an arbitrage operation consequently relates to the electricity price difference as well as on the marginal cost of the system operation.

The marginal costs can be defined as additional costs occurring specifically through the battery operation for charging and discharging. Possible considered costs are energy losses during the operation and cycle-induced battery degradation. Energy consumption for auxiliary components of the BESS and calendar-aging effects of the battery can be considered as non-marginal, fixed costs – assuming they are negligibly dependent on the actual system operation – and are consequently excluded from the analysis.

The calculation of the marginal costs of system operation is, therefore, an important factor to calculate and optimize the economic viability of an arbitrage operation.

A. Literature Review

Koller et al. considered battery degradation by an explicit piecewise affine cost function for optimal control of BESS [2]. Xu et al. proposed a piecewise-linear cost function for implementation in market dispatch algorithms [3]. Goebel et al. investigated cost-minimized dispatch strategies for the provision of auction-based secondary control reserve, which reduced calendar and cycle battery degradation [4]. For energy arbitrage application, Reniers et al. compared battery models for power capability and degradation of increasing complexity [5]. Regarding energy losses, Schimpe et al. evaluated the energy efficiency of BESS [6-9], however, no evaluation of the economic significance of the energy losses was conducted.

Based on the reviewed literature, degradation cost functions based on simple as well as more sophisticated battery degradation models have been developed and used in various optimized control strategies. Separately, the energy efficiency has been evaluated for reference BESS in technical system simulations. To the knowledge of the authors, no combined techno-economic evaluation of marginal costs for energy losses and cycle-induced battery degradation has been presented so far.

This work presents an evaluation of the total marginal costs of BESS operation based on a system with lithium iron phosphate/graphite cells (LFP-C). The parameters for the models of both the energy losses and the battery degradation are based on the same battery cell designed for stationary applications for a realistic comparison. A case study on the profit-optimized operation in energy arbitrage is conducted to reveal the potential for optimization considering the detailed marginal cost calculation. A discussion on the inclusion of the cycle-induced capacity losses is presented to give different perspectives on the cost-optimized operation of BESS.

B. Structure of this work

Section II defines the calculation of the marginal cost of operation including the model-based calculation of energy conversion losses and the battery degradation. Section III evaluates the marginal cost of a full cycle of operation in detail to identify the characteristics and their sources. Section IV presents a case study of a simplified energy arbitrage scenario with variable electricity prices, in which the marginal cost model

978-1-5386-5186-5/18/$31.00 ©2018 IEEE

is used for an optimal control of the system to achieve the highest profit. Section V presents a critical discussion of the methodology used herein and of the calculation methods for the marginal costs. Section VI summarizes the main conclusions.

II. Calculation of Marginal Operation Cost

The marginal costs of operating the battery c_{Marginal} are defined for the general evaluation in Section III as costs in Euro (EUR, EURct) for a full cycle per installed kWh of nominal energy capacity. They comprise costs for energy conversion losses and for battery degradation. The considered energy losses are conversion losses of the battery and of the power electronics. The costs for the battery degradation are based on the cycle-induced capacity losses of the cells.

Both costs for the energy losses $c_{\text{Energy Loss}}$, as well as costs for capacity losses $c_{\text{Capacity Loss}}$, are calculated separately for charge (subscript *Ch*) and discharge (subscript *Disch*) as functions of the grid-side system power, P_{AC}:

$$c_{\text{Marginal}}(P_{\text{AC}}) = c_{\text{Energy Loss,Ch}}(P_{\text{AC}}) + c_{\text{Capacity Loss,Ch}}(P_{\text{AC}}) + c_{\text{Energy Loss,Disch}}(P_{\text{AC}}) + c_{\text{Capacity Loss,Disch}}(P_{\text{AC}}) \quad (1)$$

A. Costs for Energy Conversion Losses

The costs for energy losses are calculated based on a specific electricity price c_{Energy} (EUR/kWh) and the energy conversion losses occurring during the operation e_{Loss}:

$$c_{\text{Energy Loss}}(P_{\text{AC}}) = e_{\text{Loss}}(P_{\text{AC}}) \cdot c_{\text{Energy}} \quad (2)$$

The energy conversion losses in the power electronics are based on power loss measurements of a bidirectional Siemens Sinamics S120 36 kW inverter, which connects to the low voltage 400 VAC grid. Measurements are taken at 600 VDC, 675 VDC, and 750 VDC from 0% to 100% of nominal power for both charge and discharge, and then implemented through lookup tables as a function of voltage and relative power.

The energy conversion losses in the battery are calculated using an equivalent circuit model featuring an open circuit voltage and a single resistance. Parameters are implemented for a commercial cell (Sony US26650FTC1, LFP-C, Nominal Parameter: 3.2 V, 3 Ah [10]) designed for stationary applications [11]. As the system in this work is evaluated for a full cycle, and to allow comparable calculations independent of an increase in cell temperature, a constant State of Charge *SOC* of 50% and a constant cell temperature *T* of 25°C are used. This results in constant parameters for the open circuit voltage and the cell resistances.

Values for the resistance in charge/discharge direction and for the open circuit voltage are taken from [6]: $R_{\text{Ch}} = 46.66$ mΩ, $R_{\text{Disch}} = 50.29$ mΩ, U_{OCV}=3.30 V. The power loss in the battery is calculated based on Ohm's Law,

$$P_{\text{Loss,Battery}}(P_{\text{AC}}) = R_{\text{Ch/Disch}} \cdot (I_{\text{Battery}}(P_{\text{AC}}))^2, \quad (3)$$

with I_{Battery} being the battery current. Battery pack dimensioning is selected according to the voltage range of the inverter and an Energy-to-Power ratio of 1:1 resulting in the nominal energy of 36 kWh, a battery configuration of 208 cell blocks in series, and nominal pack voltage of 665.6 VDC.

Results for the calculated energy efficiencies are shown in Fig. 1. The power electronics show decreased efficiency (< 90%) at low power (< 10%) and steadily increasing efficiency with higher relative power. Instead, the battery shows the highest efficiency at low power and a linear decrease in efficiency with increasing power. Efficiency for charge and discharge is similar for the power electronics, whereas the battery shows a slightly higher efficiency for charge operation. Evaluating the combined efficiency of battery and power electronics shows for both charge and discharge a peak efficiency at approximately 36% of nominal power. The combined round-trip efficiency results in a peak round-trip efficiency of 91.1% at 36% of nominal power and a round-trip efficiency of 87.0% at 100% nominal power.

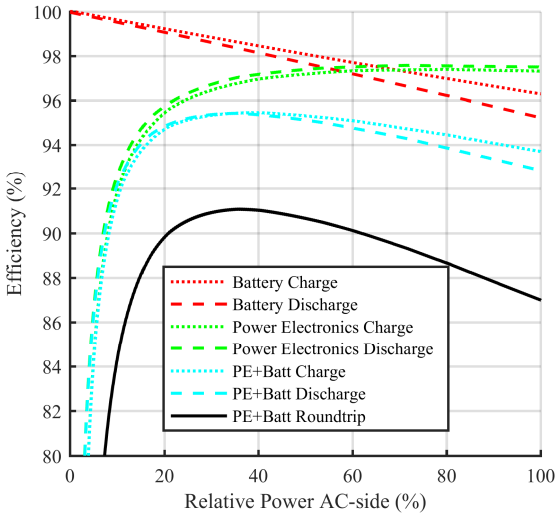

Fig. 1. Energy efficiency over relative system power for battery (Batt), power electronics (PE) for both charge/discharge separately and for the total round-trip.

For the evaluation of the costs for energy losses of a full cycle at various power operating points, given in detail following in Section III, a constant electricity price for c_{Energy} is used. In accordance with the application being energy arbitrage, an electricity price of 3.197 EURct/kWh, based on the calculated average of the base-/peak-period prices in the German Day-Ahead market for 2016, is selected (Year-average for Base period: 2.898 EURct/kWh; Peak period: 3.496 EURct/kWh [12]).

For the subsequent application of the model in the variable price scenario (see Section IV), the electricity cost was instead equated to the actual electricity price during the time of charging/discharging the system.

B. Costs for Battery Degradation

For the calculation of battery degradation costs $c_{\text{Capacity Loss}}$, the cycle-induced capacity losses are calculated. Calendar aging effects are not included, as they are assumed here to be independent of operation and thus not part of the marginal costs. The costs are calculated based on a price for the battery capacity c_{Capacity} and the cycle-induced capacity loss q_{Loss}:

$$c_{\text{Capacity Loss,Ch/Disch}}(P_{\text{AC}}) = c_{\text{Capacity}} \cdot q_{\text{Loss,Ch/Disch}}(P_{\text{AC}}) \quad (4)$$

The actual capacity loss q_{Loss} is calculated using the model presented in [13], which is parametrized for the same LFP-C cell used for the energy loss calculation (see Section II.A). The model is implemented in reduced form according to the constant conditions of the cell temperature T and the State of Charge SOC defined in Section II.A.

The cycle-induced capacity loss is calculated as the sum of two degradation mechanisms. The first mechanism (*High T*) is driven by the total charge throughput Q_{tot}, and is consequently active in both current directions, and features no current dependence. The second mechanism (*Low T*) is driven by the charge throughput in the charging direction Q_{Ch} and also features a charging current dependence. Charge and discharge are thus calculated separately:

$$Q_{\text{Loss,Ch}}(P_{\text{AC}}) = k_{\text{cyc,High T,Ref}} \cdot Q_{\text{tot}}^{0.5} + k_{\text{cyc,Low T}}(I_{\text{Battery,Ch}}(P_{\text{AC}})) \cdot Q_{\text{Ch}}^{0.5} \quad (5)$$

$$Q_{\text{Loss,Disch}}(P_{\text{AC}}) = k_{\text{cyc,High T,Ref}} \cdot Q_{\text{tot}}^{0.5} \quad (6)$$

The charging-induced capacity loss is calculated with an exponential correlation for the dependence of the charge current $I_{\text{Battery,Ch}}$:

$$k_{\text{cyc,Low T}}(I_{\text{Battery}}(P_{\text{AC}})) = k_{\text{cyc,Low T,Ref}} \cdot \exp[\beta_{\text{Low T}} \cdot (I_{\text{Battery,Ch}} - I_{\text{Battery,Ch,Ref}})/C_0] \quad (7)$$

Parameters are $\beta_{\text{Low T}} = 2.64$ h, $C_0 = 3$ Ah, $I_{\text{Battery,Ch,Ref}} = 3$ A, $k_{\text{cyc,Low T,Ref}} = 4.01 \cdot 10^{-4}$ Ah$^{-0.5}$ and $k_{\text{cyc,High T,Ref}} = 1.46 \cdot 10^{-4}$ Ah$^{-0.5}$. Parameters given are scaled for a single cell. Further information on the model can be found in [13].

The full equivalent cycles of the battery corresponding to a relative capacity loss q_{Loss} of 0.20 of the nominal capacity, according to an End-of-Life (EOL) criterion of a State of Health of 80% [13], are calculated for both charge and discharge separately as a function of P_{AC}. To linearize the square-root-dependent results, the averaged capacity loss per cycle is calculated from the cycle count until EOL. Results per cycle are then implemented in the cost calculation as $q_{\text{Loss,Ch/Disch}}(P_{\text{AC}})$. It is critically noted that the model in [13] is not parametrized until EOL at 25°C, so data are extrapolated. Longer tests are expected to show an earlier EOL and thus higher costs. Additionally, the calculation of cycle-induced degradation costs based on the EOL criterion is also more theoretical, as the EOL value of 80% mostly used is based on the full capacity loss and not only on the cycle-induced capacity loss only.

The implemented price for the battery c_{Capacity} is based on the battery price of 730 EUR/kWh of nominal energy (current Sony US26650FTC1-based module price excluding VAT [14]).

III. Results of Marginal Cost Model

The marginal cost model is calculated for a full cycle at various power operating points to evaluate the influence of power flow direction and operating point.

A. Costs for Energy Conversion Losses

Fig. 2 shows the marginal costs for energy conversion losses over relative system power. As a reference value, the electricity price difference between peak and base period (see Section II.A) of 0.60 EURct/kWh is indicated. As the value for the base period is calculated as year average of all hours, the peak to trough price difference, which is more relevant for energy arbitrage, would be 1.20 EURct/kWh, assuming a symmetric distribution of price around the average.

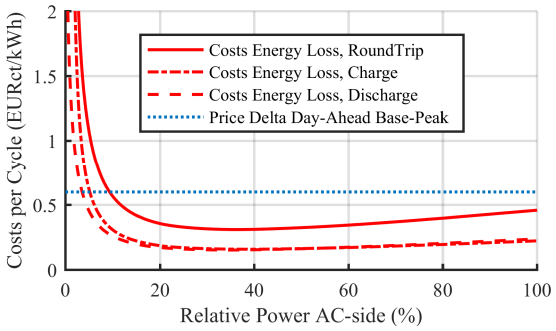

Fig. 2. Costs for energy conversion losses over relative system power.

Both charge and discharge efficiency result in high costs at low power due to the low efficiency of the power electronics (see Fig. 1). The round-trip costs for energy losses reach high values at low power, exceeding the reference price difference. For a relative power above 9%, the costs fall below the reference value. Towards higher power, exceeding 36% of nominal power, the costs increase again - although less steeply. At full nominal power, the round-trip energy loss costs are 0.46 EURct/kWh.

B. Costs for Cycle-Induced Capacity Losses

Fig. 3 shows the marginal costs for the cycle-induced capacity losses over relative system power.

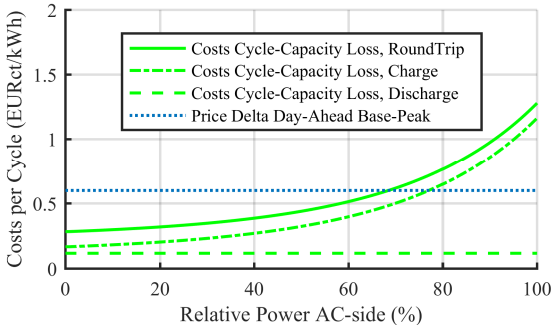

Fig. 3. Costs for capacity loss over relative system power.

While at low power both charge and discharge are similar in the related costs, at higher power the charge operation increases in costs. This deviation is attributed to the applied degradation model that calculates additional degradation for the charge direction with an exponential current dependence (see Section II.B). Under these assumptions, round-trip costs for the capacity losses exceed the average price difference at 69% of nominal power and reach 1.28 EURct/kWh at full nominal power.

C. *Total Marginal Costs of Operation*

Fig. 4 shows the total marginal costs, calculated as the sum of energy loss and capacity loss, over the relative system power.

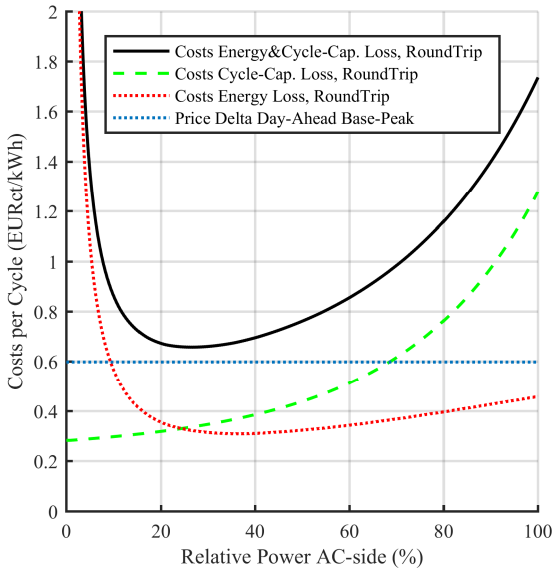

Fig. 4. Costs for the sum of energy loss and capacity loss over relative system power.

At low power, energy losses represent the largest share of costs. Instead, at high power, the costs for cycle-induced capacity loss exceed the costs for energy losses. The total marginal costs reach a minimum of 0.66 EURct/kWh at 27% of nominal power, exceeding the reference average price difference slightly. Here, costs for energy and capacity losses both similarly amount to approximately 0.3 EURct/kWh. At full nominal power, the energy loss costs increase to 0.46 EURct/kWh, the capacity loss costs to 1.28 EURct/kWh resulting in a total marginal cost of 1.74 EURct/kWh.

The total marginal costs exceed the reference price difference over the entire operating range, indicating that energy arbitrage is not profitable in the assumptions of this scenario. However, the reference price difference is based on the annual-average prices for specific periods and not on an optimized operation based on price forecasts – which could significantly improve the economics. It should also be noted that the reference price difference calculated for other EPEX Spot Day-Ahead markets in 2016 was higher (France: 0.87 EURct/kWh, Belgium 1.01 EURct/kWh [12]) – indicating possibly higher profitability.

A critical discussion on the marginal cost calculation and their inclusion into operation optimization schemes follows later in Section V.

To analyze optimization potential for the power flow directions individually, Fig. 5 shows the total marginal costs separated by charge and discharge over the relative system power. At low power operation, the energy losses, which are similar for charge and discharge, dominate and thus the total marginal costs are similar for both power flow directions. With increasing power, however, the capacity loss for the charge operation increases significantly.

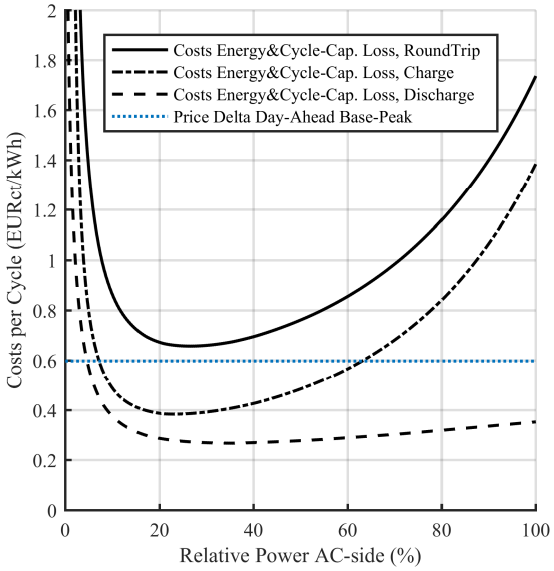

Fig. 5. Costs for the sum of energy loss and capacity loss, separated for charge and discharge, over relative system power.

IV. Case Study on Optimized Operation in Energy Arbitrage Application

The cost function is evaluated for an optimized system control in an energy arbitrage scenario with variable electricity prices to explore in more depth how the BESS profitability can be improved. For the sake of simplicity, in this case study, we assume prices were known a priori. Furthermore, for simplification, a period of four hours of operation is chosen.

Parameters are set to enable a single full cycle of arbitrage application as well as to enable charging in *hour 1* to *hour 2* and discharging in *hour 3* and *hour 4*. State of Charge at beginning is 0%. This results in an ease of optimization through brute force parameter-sweeping, while still allowing for optimization potential, e.g. by charging the BESS at full power in *hour 1* or possibly charging at approximately 50% of nominal power in *hour 1* and *hour 2*.

Price values are based on an arbitrary variation of the base period price (2.898 EURct/kWh [12]) by -50% (*hour 1*), -20% (*hour 2*), +25% (*hour 3*) and +30% (*hour 4*).

Fig. 6 shows the variable price scenario case study. The y-axis to the left shows the variable electricity price while the

y-axis to the right indicates absolute system power (*hour 1-2*: Charging only, *hour 3-4* Discharging only). Power is optimized for (a) profit considering electricity costs/revenue Π_{Electr}, which includes the variable electricity prices as well as the energy loss costs through increased charging energy/decreased discharging energy,

$$\Pi_{\text{Electr.}} = \int c_{\text{Energy}}(t) \cdot P_{\text{AC}}(t)\, dt \tag{7}$$

and (b) the total profit $\Pi_{\text{Electr\&Capacity Loss}}$, which additionally includes the cycle-induced capacity loss costs:

$$\Pi_{\text{Electr\&Capacity Loss}} = \int [c_{\text{Energy}}(t) P_{\text{AC}}(t) + C_{\text{Capacity Loss}}(P_{\text{AC}})] dt \tag{8}$$

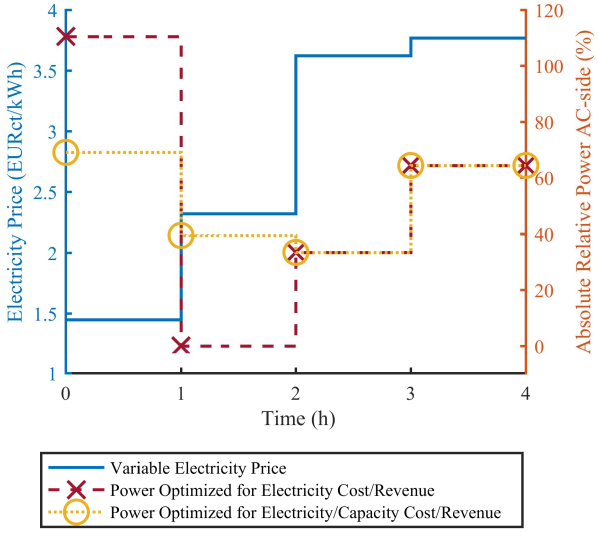

Fig. 6. Variable price scenario with optimized power for (a) profit based on electricity costs incl. var. prices & energy loss costs and (b) total profit incl. var. prices, energy loss costs & cycle-induced capacity loss costs.

The relative AC-side power exceeds 100% during charging slightly to account for losses in the conversion. During discharge, the maximum output power cannot be fully reached due to the losses in the conversion and limited battery capacity.

Optimization for electricity-only (a) shifts the operation to the best price during charging due to the high price difference. During discharging the price difference is lower and thus enables a shift towards operating points with higher efficiency.

Optimization for the total profit (b) shifts the power during charging to lower operating points to reduce the more significant costs for cycle-induced capacity losses. During discharge, the operation is identical to the result for electricity-optimized operation.

The results for the profit of the arbitrage operation under both profit considerations Π_{Electr} respectively $\Pi_{\text{Electr\&Capacity Loss}}$ are shown in Fig. 7. The operation mode "Full Power at Best Price" (FPBP) is added as a reference to evaluate the improvement through the optimization. In FPBP operation, the system is controlled with no consideration of marginal costs but only based on electricity prices. This results for the variable price (see Fig. 6) for charging in *hour 1* and discharging in *hour 4*, both at full power. Additionally, the theoretical profit based on the maximum price difference with no considered marginal costs at all is shown as a reference. The theoretical profit with no considered losses results in a profit of 2.39 EURct/kWh. As no costs are considered, the FPBP operation and the optimized operation result in identical profit.

Considering the energy loss costs, the profit is reduced by approximately 15% to 2.04 EURct/kWh for the optimized operation and 2.01 EURct/kWh for the FPBP operation. The cost optimization through improved energy efficiency is relatively small here in comparison to the price difference, resulting in an increase of the profit by only 1.1%.

Additionally considering the cycle-induced capacity loss costs further reduces the profit. The profit resulting from FPBP operation is strongly reduced by 89% from the theoretical profit to 0.26 EURct/kWh. Cycle-induced capacity losses are highest at the full power operation. The optimized operation reduces the capacity loss costs through a reduced charging power and consequently shows a profit of 1.20 EURct/kWh, which is an increase of 357% from the FPBP operation at 0.26 EURct/kWh.

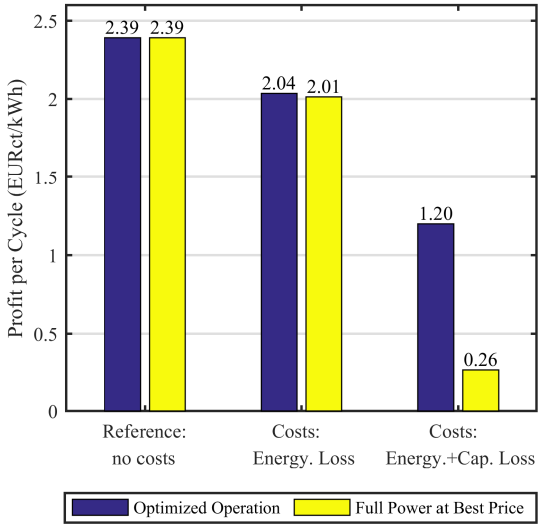

Fig. 7. Profit evaluation for a) profit based on electricity costs incl. var. prices & energy loss costs and b) total profit incl. var. prices, energy loss costs & cycle-induced capacity loss costs.

V. Discussion

The results of the cost model (see Section III) showed that the total marginal costs exceed the average price difference in the German Day-Ahead market – indicating that arbitrage based on average price signals is not economically viable. However, successfully trading price differences on an e.g. hourly base can indeed result in profitable operation (see Section IV). The price scenario as well as the ability to forecast prices thus clearly define the economic potential of energy arbitrage.

The concept of calculating marginal costs based on the sum of energy losses and capacity losses should be critically

evaluated. Energy losses directly influence the profit through costs for additionally charged energy/reduced discharged energy. Capacity loss costs occur based on the more theoretical calculation of using and depreciating the asset of the battery through cycle-induced capacity losses until End-of-Life. However, calendar aging should not be neglected, as although marginal cycle-induced capacity loss costs might be high, the battery should be used to create revenue - as calendar aging renders the battery degraded at some point anyway.

From a technical point of view, the End-of-Life criterion of 80% used in this study should also be critically evaluated. It is used in reference to the cycle-induced aging, but in reality, the mechanisms for calendar and cycle aging are not separated. Additionally, if no rapid increase in degradation occurs after the somewhat arbitrary 80% point, the battery could operate for a longer period until much lower State of Health values – thus dramatically decreasing capacity loss costs.

Another perspective is that the price of the battery as initial investment matters less to the system operator, as it can also be considered as a 'sunk cost'. Possibly a replacement cost of the battery, which might be theoretical but more up to date with market conditions, could also be used for calculating battery degradation costs. A revenue-oriented perspective could approximate the cycle-induced costs by calculating the cycle-induced reduction of battery lifetime and the thus reduced time available for revenue-generation.

Finally, the approach to optimize profit considering the degradation of the battery is based on the assumption that the BESS can create revenue in the future. BESS operators, however, might consider that future revenues are not guaranteed due to changing conditions in regulation or markets. Financing costs for BESS also motivate an operation scheme, which creates revenue as early as possible and may neglect cycle-induced degradation costs. Inflation further creates an incentive to create revenue as early as possible.

In summary, the decision whether costs for cycle-induced capacity losses are included in an optimized BESS control depends on the perspective and the timeframe of the evaluation. Energy loss costs, however, should be strictly included as they influence the profit at present conditions.

VI. Conclusions and Future Work

A cost function considering both energy losses and cycle-induced capacity losses is defined to calculate the marginal costs of BESS operation. The electricity price scenario is in accordance with the application in the German Day-Ahead market. The results reveal high costs due to energy losses at low power operation and high costs due to capacity losses at high power charge operation. The cost function is evaluated for an optimal control in an arbitrage scenario with variable electricity prices. For low price variation, the optimized power control aims for minimized marginal costs. At high price variation, that strongly exceeds marginal costs, the optimum operation according to the best prices is the most profitable control.

The subsequent discussion of the results presents various perspectives on which marginal costs should be included in an optimization. Costs for energy losses directly influence the revenue/cost of arbitrage operation. In contrast, costs for cycle-induced capacity losses can be evaluated through different perspectives – which might complicate including them in an operation optimization. The different perspectives on the calculation of the cycle-induced capacity loss costs should be quantified and compared in future work. Finally, the impact of the cost model based on real-world prices should be evaluated in an optimization. Here, the quality of the price forecast should be included realistically. To correctly assess the economic viability of a BESS investment, the total costs including the complete BESS, financing, and market participation have to be considered.

References

[1] H. Hesse, M. Schimpe, D. Kucevic, and A. Jossen, "Lithium-Ion Battery Storage for the Grid—A Review of Stationary Battery Storage System Design Tailored for Applications in Modern Power Grids," Energies, vol. 10, no. 12, p. 2107, 2017.

[2] M. Koller, T. Borsche, A. Ulbig, and G. Andersson, "Defining a degradation cost function for optimal control of a battery energy storage system," 2013 IEEE Grenoble Conference, Grenoble, 2013, pp. 1-6.

[3] B. Xu, J. Zhao, T. Zheng, E. Litvinov, and D. S. Kirschen, "Factoring the Cycle Aging Cost of Batteries Participating in Electricity Markets," IEEE Transactions on Power Systems, vol. 33, no. 2, pp. 2248-2259, 2018.

[4] C. Goebel, H. Hesse, M. Schimpe, A. Jossen, and H. A. Jacobsen, "Model-Based Dispatch Strategies for Lithium-Ion Battery Energy Storage Applied to Pay-as-Bid Markets for Secondary Reserve," IEEE Transactions on Power Systems, vol. 32, no. 4, pp. 2724-2734, 2017.

[5] J. Reniers, G. Mulder, S. Ober-Blöbaum, and D. Howey, "Improving optimal control of grid-connected lithium-ion batteries through more accurate battery and degradation modelling," Journal of Power Sources, vol. 379, pp. 91-102, 2018.

[6] M. Schimpe et al., "Energy efficiency evaluation of a stationary lithium-ion battery container storage system via electro-thermal modeling and detailed component analysis," Applied Energy, vol. 210, pp. 211-229, 2018.

[7] M. Schimpe et al., "Power Flow Distribution Strategy for Improved Power Electronics Energy Efficiency in Battery Storage Systems: Development and Implementation in a Utility-Scale System," Energies 11(3), 533, 2018.

[8] M. Schimpe et al., "Energy efficiency evaluation of grid connection scenarios for stationary battery storage systems," unpublished, 2018.

[9] K. Smith, M. Baggu, A. Friedl, T. Bialek, and M. R. Schimpe, "Performance and health test procedure for grid energy storage systems," 2017 IEEE Power & Energy Society General Meeting, Chicago, IL, 2017, pp. 1-5.

[10] M.-K. Konan, "SONY US26650FTC1 Product Specification," 2010.

[11] M. Yasuda, "Sony energy storage system using olivine type battery," OREBA 1.0 - International Conference on Olivines for Rechargeable Batteries, Montreal, 2014.

[12] [Online]. Available: https://www.epexspot.com/document/36851/2017-01-11_EPEX%20SPOT_2016_Annual%20Press%20Release.pdf. [Accessed: 28- Feb- 2018].

[13] M. Schimpe et al., "Comprehensive Modeling of Temperature-Dependent Degradation Mechanisms in Lithium Iron Phosphate Batteries," Journal of the Electrochemical Society, vol. 165, no. 2, pp. 181-193, 2018.

[14] [Online]. Available: https://www.mg-solar-shop.de/pv-battery-offgrid-systems/Sony-fORTELION-LiFE-PO4-Energy-Storage-Module-1-2-kW.html. [Accessed: 28- Feb- 2018].

8 Conclusion and outlook

This chapter summarizes the dissertation results, followed by an outlook towards future work. Section 8.1 collects the main conclusions of this work and Section 8.2 presents possible future research tasks.

8.1 Conclusions from the investigations

A holistic system model for the evaluation of the energy efficiency of BESS was presented in Chapter 3. The energy efficiency of BESS was analyzed in detail for a reference prototype system, the *Energy Neighbor*. Results revealed strongly varying energy efficiency values for different system applications, whereby the PE connecting the battery to the electrical grid were identified as a major source of energy losses in most cases.

Consequently, grid connection topologies consisting of different PE topologies and grid levels were compared regarding their energy efficiency in Chapter 4. Here, results showed that the choice of topology can strongly affect the energy efficiency and has to be considered specifically for each grid application.

As a second approach to reduce PE losses, a software-based PFDS was proposed in Chapter 5. The developed PFDS was tested in an industrial utility-scale BESS and shows stable operation as well as a strong reduction of energy losses.

Regarding battery lifetime, a comprehensive storage and cycle test experiment with a focus on the effect of battery temperature on the cycle-induced battery degradation was conducted with LFP-C cells and presented in Chapter 6. Based on experimental data, a semi-empirical model that captures separate degradation mechanisms was developed and successfully validated against application-oriented experiments. The experiments as well as the model correctly predict the optimum operating temperature for battery cells regarding degradation.

To evaluate and compare the impact of the energy losses and battery degradation on the economics of BESS operation, specifically their marginal costs of operation, a combined approach was presented in Chapter 7. Costs for lost energy and battery capacity losses are calculated and evaluated, revealing optimum operating points. The results were evaluated in a profit-optimized control strategy for BESS in energy arbitrage, showing large potential for an increased profit.

In summary, both energy efficiency and battery degradation are key BESS parameters requiring detailed consideration during system design. Operational control strategies offer opportunities for noticeable improvement.

8.2 Possible future research tasks

Regarding holistic system simulation model and system energy efficiciency, several aspects can be further investigated. For improved validation of the system thermal management model and its power consumption, real-world data of the system performance and key system components temperatures should be measured over a whole year to capture seasonal variations.

As the system thermal management is shown to be a small part of the energy losses, simpler and less costly configurations could be evaluated as a possible option. However, the aging of the battery cells needs to be considered in this evaluation as well.

Regarding future PE topologies, the efficiency at partial load can be further improved through incremental operation of parallel-connected semiconductions within single PE units.

Regarding battery degradation, the model could be further validated through additional validation tests covering more application scenarios or stronger variation of test conditions, such as a dynamic ambient temperature or a non-repeating battery current profile. Based on the further validated model, aging-optimized control strategies for battery temperature and battery current can be developed and again validated experimentally. The battery-model can be further detailed to include changes of the OCV and the cell impedance.
For the marginal cost calculation method, the evaluation showed different perspectives on the calculation of the cycle-induced capacity loss costs which should be quantified and compared in future work. The impact of the cost model based on time-resolved real-world prices should be evaluated in an optimization. Here, a price forecast calculation should be implemented to achieve more realistic results.

Regarding PFDS, the results for energy-efficiency optimized PFDS showed the stable operation as well as a strong reduction of energy losses in BESS. However, the PFDS was only considered between two power strings of identical nominal power/capacity. Utility-scale BESS consist of many more and also non-identical units. The software implementation of the PFDS can be extended to operate for non-identical and more than two power strings, as well as to optimize the PFDS between several BESS. Future simulations could reveal the technical potential of such topologies in detail and enable the development of the necessary complex SOC-management strategy. The more flexible PFDS could be applied to utility-scale BESS, distributed BESS, as well as to Vehicle-to-Grid applications.
A second important point for PFDS is that the efficiency-optimized PFDS concentrates the system power on single battery units and consequently lead to increased battery currents. The efficiency-optimized PFDS with higher battery currents can consequently lead to reduced battery lifetime and thus possibly be detrimental to the economics of the system application. A marginal-cost optimized PFDS, which respects battery degradation as well as energy loss could provide a holistically optimized PFDS.

Several of these aspects are going to be investigated with a focus on Second-Life batteries in the upcoming research project *EffSkalBatt*.

References

[1] International Energy Agency: *Key World Energy Statistics*, ed. by International Energy Agency, 2017

[2] European Commission: *A Roadmap for moving to a competitive low carbon economy in 2050*, 2011, URL: http://eur-lex.europa.eu/legal-content/EN/ALL/?uri=CELEX:52011DC0112

[3] Aneke, M.; Wang, M.: *Energy storage technologies and real life applications – A state of the art review*, in: *Applied Energy 179*, pp. 350–377, 2016

[4] Fürstenwerth, D.; Waldmann, L., et al.: *Report: Electricity Storage in the German Energy Transition*, 2014

[5] Hesse, H.; Schimpe, M.; Kucevic, D.; Jossen, A.: *Lithium-Ion Battery Storage for the Grid—A Review of Stationary Battery Storage System Design Tailored for Applications in Modern Power Grids*, in: *Energies 10 (12)*, p. 2107, 2017

[6] Nykvist, B.; Nilsson, M.: *Rapidly falling costs of battery packs for electric vehicles*, in: *Nature Climate Change 5 (4)*, pp. 329–332, 2015

[7] Technical University of Munich: *Energy Neighbor goes online*, 2015, URL: https://www.tum.de/en/about-tum/news/press-releases/detail/article/32661/

[8] Dunn, B.; Kamath, H.; Tarascon, J.-M.: *Electrical energy storage for the grid: a battery of choices*, in: *Science (New York, N.Y.) 334 (6058)*, pp. 928–935, 2011

[9] Younicos: *Europe's first commercial battery power plant to triple its capacity*, 2016, URL: https://www.younicos.com/europes-first-commercial-battery-power-plant-triple-capacity/

[10] Munsell, M.: *In Shift to Longer-Duration Applications, US Energy Storage Installations Grow 100% in 2016*, in: *Greentech Media 2017*, URL: https://www.greentechmedia.com/articles/read/in-shift-to-longer-duration-applications-us-energy-storage-installations-gr

[11] Schimpe, M.; Naumann, M.; Truong, N.; Hesse, H.C.; Santhanagopalan, S.; Saxon, A.; Jossen, A.: *Energy efficiency evaluation of a stationary lithium-ion battery container storage system via electro-thermal modeling and detailed component analysis*, in: *Applied Energy 210*, pp. 211–229, 2018

[12] Schimpe, M.; Becker, N.M.; Lahlou, T.; Hesse, H.C.; Herzog, H.-G.; Jossen, A.: *Energy efficiency evaluation of grid connection scenarios for stationary battery storage systems*, in: *Energy Procedia 155*, pp. 77–101, 2018

[13] Schimpe, M.; Piesch, C.; Hesse, H.C.; Paß, J.; Ritter, S.; Jossen, A.: *Power Flow Distribution Strategy for Improved Power Electronics Energy Efficiency in Battery Storage Systems: Development and Implementation in a Utility-Scale System*, in: *Energies (11 (3))*, 2018

[14] Schimpe, M.; Kuepach, M.E.v.; Naumann, M.; Hesse, H.C.; Smith, K.; Jossen, A.: *Comprehensive Modeling of Temperature-Dependent Degradation Mechanisms in Lithium Iron Phosphate Batteries*, in: *Journal of The Electrochemical Society 2018 (165, 2)*, pp. 181–193, 2018

[15] Schimpe, M.; Truong, C.N.; Naumann, M.; Jossen, A.; Hesse, H.C.; Reniers, J.M.; Howey, D.A.: *Marginal Costs of Battery System Operation in Energy Arbitrage based on Energy Losses and Cell Degradation*, in: *IEEE International Conference on Environment and Electrical Engineering and IEEE Industrial and Commercial Power Systems Europe (EEEIC/I&CPS Europe) 2018*, IEEE, Palermo, Italy, 2018

[16] Truong, C.N.; Schimpe, M.; Naumann, M.; Jossen, A.; Hesse, H.C.: *Impact of sub-components on the overall performance of stationary battery systems: Insights on the prototype Energy Neighbor*, in: *International ETG Congress 2017*, IEEE, Bonn, Germany, 2017

[17] Yasuda, M.: *Sony energy storage system using olivine type battery (Presentation)*, in: *OREBA 1.0 - International Conference on Olivines for Rechargeable Batteries*, Montreal, Canada, 2014

[18] Cell Database of the Institute for Electrical Energy Storage Technology of the Technical University of Munich

[19] Konan, M.-k.: *SONY US26650FTC1 Product Specification*, Tokyo, 2010

[20] The Mobility House GmbH: *World's Largest 2nd-use Battery Storage Is Starting Up*, 2016, URL: `http://www.mobilityhouse.com/en/worlds-largest-2nd-use-battery-storage-is-starting-up/`

[21] Gatta, F.M.; Geri, A.; Lauria, S.; Maccioni, M.; Palone, F.: *Battery energy storage efficiency calculation including auxiliary losses: Technology comparison and operating strategies*, in: *2015 IEEE Eindhoven PowerTech*, IEEE, 2015

[22] Neubauer, J.; Pesaran, A.; Coleman, D.; Chen, D.: *Analyzing the Effects of Climate and Thermal Configuration on Community Energy Storage Systems (Presentation)*, in: *Electrical Energy Storage Applications and Technologies (EESAT) Conference*, San Diego, CA, USA, 2013

[23] Neubauer, J.: *Battery Lifetime Analysis and Simulation Tool (BLAST) Documentation*, 2014, URL: `www.nrel.gov/docs/fy15osti/63246.pdf`

[24] Rydh, C.J.; Sandén, B.A.: *Energy analysis of batteries in photovoltaic systems. Part I: Performance and energy requirements*, in: *Energy conversion and management 46 (11-12)*, pp. 1957–1979, 2005

[25] Rydh, C.J.; Sandén, B.A.: *Energy analysis of batteries in photovoltaic systems. Part II: Energy return factors and overall battery efficiencies*, in: *Energy conversion and management 46 (11-12)*, pp. 1980–2000, 2005

[26] Patsios, C.; Wu, B.; Chatzinikolaou, E.; Rogers, D.J.; Wade, N.; Brandon, N.P.; Taylor, P.: *An integrated approach for the analysis and control of grid connected energy storage systems*, in: *Journal of Energy Storage 5*, pp. 48–61, 2016

[27] Chatzinikolaou, E.; Rogers, D.J.: *A Comparison of Grid-connected Battery Energy Storage System Designs*, in: *IEEE Transactions on Power Electronics 2016*, 2016

[28] Magnor, D.; Soltau, N.; Bragard, M.; Schmiegel, A.; DeDoncker, R.W.; Sauer, D.U.: *Analysis of the model dynamics for the battery and battery converter in a grid-connected 5kW photovoltaic system*, in: *25th European Photovoltaic Solar Energy Conference, (PVSEC)*, Hamburg, Germany, 2010

[29] Tjaden, T.; Weniger, J.; Bergner, J.; Schnorr, F.; Quaschning, V.: *Influence of the location and user behaviour on the energy evaluation of PV storage systems (German title: Einfluss des Standorts und des Nutzerverhaltens auf die energetische Bewertung von PV-Speichersystemen)*, in: *29. Symposium Photovoltaische Solarenergie*, Bad Staffelstein, Germany, 2014

[30] Weniger, J.; Tjaden, T.; Quaschning, V.: *Comparison of various indicators for evaluation of the energy performance of PV battery systems (German title: Vergleich verschiedener Kennzahlen zur Bewertung der energetischen Performance von PV-Batteriesystemen)*, in: *32. Symposium Photovoltaische Solarenergie*, Bad Staffelstein, Germany, 2017

[31] Tjaden, T.; Weniger, J.; Messner, C.; Knoop, M.; Littwin, M.; Kairies, K.-P.; Haberschusz, D.; Loges, H.; Quaschning, V.: *Open simulation model for grid-coupled PV battery systems*, in: *32. Symposium Photovoltaische Solarenergie*, Bad Staffelstein, Germany, 2017

[32] Weniger, J.; Tjaden, T.: *Performance-simulation model for AC-coupled PV battery systems (PerModAC): Documentation V1.0*, 2017

[33] Naumann, M.; Karl, R.C.; Truong, C.N.; Jossen, A.; Hesse, H.C.: *Lithium-ion Battery Cost Analysis in PV-household Application*, in: *Energy Procedia 73*, pp. 37–47, 2015

[34] Truong, C.N.; Naumann, M.; Karl, R.C.; Müller, M.; Jossen, A.; Hesse, H.C.: *Economics of Residential Photovoltaic Battery Systems in Germany: The Case of Teslas Powerwall*, in: *Batteries 2 (2)*, p. 14, 2016

[35] Petzl, M.; Danzer, M.A.: *Advancements in OCV Measurement and Analysis for Lithium-Ion Batteries*, in: *IEEE Transactions on Energy Conversion 28 (3)*, pp. 675–681, 2013

[36] Barai, A.; Widanage, W.D.; Marco, J.; McGordon, A.; Jennings, P.: *A study of the open circuit voltage characterization technique and hysteresis assessment of lithium-ion cells*, in: *Journal of Power Sources 295*, pp. 99–107, 2015

[37] Dreyer, W.; Jamnik, J.; Guhlke, C.; Huth, R.; Moskon, J.; Gaberscek, M.: *The thermodynamic origin of hysteresis in insertion batteries*, in: *Nature materials 9 (5)*, pp. 448–453, 2010

[38] Kim, J.; Seo, G.-S.; Chun, C.; Cho, B.-H.; Lee, S.: *OCV hysteresis effect-based SOC estimation in extended Kalman filter algorithm for a LiFePO4-C cell*, in: *International Electric Vehicle Conference (IEVC)*, IEEE, Greenville, SC, USA, 2012

[39] Srinivasan, V.; Newman, J.: *Existence of Path-Dependence in the LiFePO4 Electrode*, in: *Electrochemical and Solid-State Letters 9 (3)*, A110, 2006

[40] Hu, X.; Li, S.; Peng, H.: *A comparative study of equivalent circuit models for Li-ion batteries*, in: *Journal of Power Sources 198*, pp. 359–367, 2012

[41] Bernardi, D.: *A General Energy Balance for Battery Systems*, in: *Journal of The Electrochemical Society 132 (1)*, p. 5, 1985

[42] Rao, L.: *Heat-Generation Rate and General Energy Balance for Insertion Battery Systems*, in: *Journal of The Electrochemical Society 144 (8)*, p. 2697, 1997

[43] Ye, Y.; Shi, Y.; Cai, N.; Lee, J.; He, X.: *Electro-thermal modeling and experimental validation for lithium ion battery*, in: *Journal of Power Sources 199*, pp. 227–238, 2012

[44] Forgez, C.; Vinh Do, D.; Friedrich, G.; Morcrette, M.; Delacourt, C.: *Thermal modeling of a cylindrical LiFePO4/graphite lithium-ion battery*, in: *Journal of Power Sources 195 (9)*, pp. 2961–2968, 2010

[45] Thomas, K.E.; Newman, J.: *Thermal Modeling of Porous Insertion Electrodes*, in: *Journal of The Electrochemical Society 150 (2)*, A176, 2003

[46] Vetter, J. et al.: *Ageing mechanisms in lithium-ion batteries*, in: *Journal of Power Sources 147 (1-2)*, pp. 269–281, 2005

[47] Lewerenz, M.; Käbitz, S.; Knips, M.; Münnix, J.; Schmalstieg, J.; Warnecke, A.; Sauer, D.U.: *New method evaluating currents keeping the voltage constant for fast and highly resolved measurement of Arrhenius relation and capacity fade*, in: *Journal of Power Sources 353*, pp. 144–151, 2017

[48] Gatta, F.M.; Geri, A.; Lamedica, R.; Lauria, S.; Maccioni, M.; Palone, F.; Rebolini, M.; Ruvio, A.: *Application of a LiFePO4 Battery Energy Storage System to Primary Frequency Control: Simulations and Experimental Results*, in: *Energies 9 (11)*, p. 887, 2016

[49] Lin, X.; Perez, H.E.; Mohan, S.; Siegel, J.B.; Stefanopoulou, A.G.; Ding, Y.; Castanier, M.P.: *A lumped-parameter electro-thermal model for cylindrical batteries*, in: *Journal of Power Sources 257*, pp. 1–11, 2014

[50] Notton, G.; Lazarov, V.; Stoyanov, L.: *Optimal sizing of a grid-connected PV system for various PV module technologies and inclinations, inverter efficiency characteristics and locations*, in: *Renewable Energy 35 (2)*, pp. 541–554, 2010

[51] Casanellas, F.: *Losses in PWM inverters using IGBTs*, in: *IEEE Proc., Electr. Power Appl. (IEEE Proceedings - Electric Power Applications) 141 (5)*, p. 235, 1994

[52] Kolar, J.W.; Drofenik, U.: *A General Scheme for Calculating Switching- and Conduction-Losses of Power Semiconductors in Numerical Circuit Simulations of Power Electronic Systems*, in: *International Power Electronics Conference IPEC-Niigata 2005*, Institute of Electrical Engineers of Japan, Tokyo, 2005

[53] Ponnaluri, S.; Linhofer, G.O.; Steinke, J.K.; Steimer, P.K.: *Comparison of single and two stage topologies for interface of BESS or fuel cell system using the ABB standard power electronics building blocks*, in: *European Conference on Power Electronics and Applications*, IEEE, 2005

[54] Smith, K.; Baggu, M.; Friedl, A.; Bialek, T.; Schimpe, M.R.: *Performance and health test procedure for grid energy storage systems*, in: *2017 IEEE Power & Energy Society General Meeting*, IEEE, Chicago, IL, USA, 2017

[55] Jin, X.; Vora, A.; Hoshing, V.; Saha, T.; Shaver, G.; García, R.E.; Wasynczuk, O.; Varigonda, S.: *Physically-based reduced-order capacity loss model for graphite anodes in Li-ion battery cells*, in: *Journal of Power Sources 342*, pp. 750–761, 2017

[56] Delacourt, C.; Safari, M.: *Life Simulation of a Graphite/LiFePO4 Cell under Cycling and Storage*, in: *Journal of The Electrochemical Society 159 (8)*, A1283–A1291, 2012

[57] Sarasketa-Zabala, E.; Gandiaga, I.; Rodriguez-Martinez, L.M.; Villarreal, I.: *Calendar ageing analysis of a LiFePO4/graphite cell with dynamic model validations: Towards realistic lifetime predictions*, in: *Journal of Power Sources 272*, pp. 45–57, 2014

[58] Grolleau, S.; Delaille, A.; Gualous, H.; Gyan, P.; Revel, R.; Bernard, J.; Redondo-Iglesias, E.; Peter, J.: *Calendar aging of commercial graphite/LiFePO4 cell – Predicting capacity fade under time dependent storage conditions*, in: *Journal of Power Sources 255*, pp. 450–458, 2014

[59] Naumann, M.; Schimpe, M.; Keil, P.; Hesse, H.C.; Jossen, A.: *Analysis and modeling of calendar aging of a commercial LiFePO 4 /graphite cell*, in: *Journal of Energy Storage 17*, pp. 153–169, 2018

[60] Sarasketa-Zabala, E.; Gandiaga, I.; Martinez-Laserna, E.; Rodriguez-Martinez, L.M.; Villarreal, I.: *Cycle ageing analysis of a LiFePO4/graphite cell with dynamic model validations: Towards realistic lifetime predictions*, in: *Journal of Power Sources 275*, pp. 573–587, 2015

[61] Wang, J.; Liu, P.; Hicks-Garner, J.; Sherman, E.; Soukiazian, S.; Verbrugge, M.; Tataria, H.; Musser, J.; Finamore, P.: *Cycle-life model for graphite-LiFePO4 cells*, in: *Journal of Power Sources 196 (8)*, pp. 3942–3948, 2011

[62] Schmalstieg, J.; Käbitz, S.; Ecker, M.; Sauer, D.U.: *A holistic aging model for Li(NiMnCo)O2 based 18650 lithium-ion batteries*, in: *Journal of Power Sources 257*, pp. 325–334, 2014

[63] Swierczynski, M.; Stroe, D.-I.; Stan, A.-I.; Teodorescu, R.; Kaer, S.K.: *Lifetime Estimation of the Nanophosphate LiFePO4/C Battery Chemistry used in Fully Electric Vehicles*, in: *IEEE Transactions on Industry Applications 51 (4)*, pp. 3453–3461, 2015

[64] Sarasketa-Zabala, E.; Martinez-Laserna, E.; Berecibar, M.; Gandiaga, I.; Rodriguez-Martinez, L.M.; Villarreal, I.: *Realistic lifetime prediction approach for Li-ion batteries*, in: *Applied Energy 162*, pp. 839–852, 2016

[65] Ecker, M.; Gerschler, J.B.; Vogel, J.; Käbitz, S.; Hust, F.; Dechent, P.; Sauer, D.U.: *Development of a lifetime prediction model for lithium-ion batteries based on extended accelerated aging test data*, in: *Journal of Power Sources 215*, pp. 248–257, 2012

[66] Waldmann, T.; Wilka, M.; Kasper, M.; Fleischhammer, M.; Wohlfahrt-Mehrens, M.: *Temperature dependent ageing mechanisms in Lithium-ion batteries – A Post-Mortem study*, in: *Journal of Power Sources 262*, pp. 129–135, 2014

[67] Schuster, S.F.; Bach, T.; Fleder, E.; Müller, J.; Brand, M.; Sextl, G.; Jossen, A.: *Nonlinear aging characteristics of lithium-ion cells under different operational conditions*, in: *Journal of Energy Storage 1*, pp. 44–53, 2015

[68] Ecker, M.; Nieto, N.; Käbitz, S.; Schmalstieg, J.; Blanke, H.; Warnecke, A.; Sauer, D.U.: *Calendar and cycle life study of Li(NiMnCo)O2-based 18650 lithium-ion batteries*, in: *Journal of Power Sources 248*, pp. 839–851, 2014

[69] Kuepach, M.E.v.: "Semi-Empirical Modeling of Temperature-Dependent Degradation Mechanism in Lithium-Ion Batteries (German title: Semi-empirische Modellierung von temperaturabhängigen Alterungsmechanismen in Lithium-Ionen Batterien)", Master's Thesis, Institute for Electrical Energy Storage Technology, Technical University of Munich, 2017

[70] Beck, H.-P.: *Project Report ESPEN - Potentials of electrochemical storages in power grids in competition to further technologies and system solutions*, 2016

[71] Hackl, M.: "Energy-Efficiency Optimized Load Distribution Strategies for Battery Energy Storage Systems and Their Impact on Battery Aging", Master's Thesis, Institute for Electrical Energy Storage Technology, Technical University of Munich, 2018

Acknowledgment

This thesis originates from my time as a research associate at the Institute for Electrical Energy Storage Technology (EES) at the Technical University of Munich. The achieved results have only been possible thanks to the support of various individuals, collaborations and institutions. The head of the institute, Professor Andreas Jossen, supervised and supported the research with highly helpful feedback and also enabled me to pursue my research interests abroad. The team for stationary energy systems, headed by Holger Hesse, also tremendously supported my research. Another big thank you goes out to my hosts at the institutions that I visited during my time as a researcher: Shriram Santhanagopalan and Ahmad Pesaran of the National Renewable Energy Laboratory, as well as Jorn Reniers and David Howey of the University of Oxford. I also want to thank my students Nick Becker, Markus Kuepach, Christian Piesch, and Martin Hackl whose work contributed to this thesis. A final big thank you goes to my wife Saygi, my parents, and my whole family who have all supported me tremendously.